THE PHYSICAL ORIGIN OF PRE-BREAKDOWN ELECTRON EMISSION FROM BROAD-AREA HIGH VOLTAGE ELECTRODES.

Keith Howard Bayliss B.Sc.

A Thesis submitted for the Degree
of Doctor of Philosophy.

The University of Aston in Birmingham.

July, 1984.

"THE UNIVERSITY OF ASTON IN BIRMINGHAM"

THE PHYSICAL ORIGIN OF PRE-BREAKDOWN ELECTRON EMISSION FROM BROAD-AREA HIGH VOLTAGE ELECTRODES.

Keith Howard Bayliss B.Sc.

Submitted for the Degree of Doctor of Philosophy, 1984.

SUMMARY

An investigation has been undertaken into the nature of the localised electron emission sites which cause pre-breakdown conduction between broad area electrodes separated by short ultra high vacuum gaps.

A new automated specimen scanner and an electron imaging technique have shown that emission sites are composed of many distinct electron sources (sub-sites) which in total may extend over areas as large as $\sim 1\,mm^2$. The energy distributions of the electrons emitted from individual sub-sites on copper electrodes have been measured using a high resolution spectrometer. The spectra invariably have single peaks which are shifted at least 200 m eV below the metal Fermi level and have half widths $>$ 300 m eV. Detailed analyses of the field dependence of the various spectral parameters have provided sufficient data to enable a quantitative model of the emission process to be constructed. This assumes that thin ($<$1 um) contaminated insulating layers provide the structures necessary to initiate electron emission. Conduction through the insulator, in the form of narrow filaments, then leads to local field intensification and to a "hot electron" mechanism at the vacuum interface which allows emission over the potential barrier. The model provides relationships between previously unconnected observations, particularly the amount of spectral shift and the degree of non-linearity of a Fowler-Nordheim plot, and allows the dimensions and properties of the conducting filaments to be estimated.

The validity of the model is supported by two types of in situ surface treatments: argon ion etching, which not only removes emitting sites but allows others to be initiated, and thick oxidation, which has yielded important information on the nature of the conduction processes occuring in the insulating layer.

Key Words : Prebreakdown conduction.
Hot electron emission.

CONTENTS.

CHAPTER. PAGE NO.

CHAPTER. PAGE NO.

4. Continued.

CHAPTER. PAGE NO.

LIST OF FIGURE NUMBERS.

Figure No. Page No.

CHAPTER 1.

INTRODUCTION.

1.1 Breakdown Mechanisms.

At first sight, ultra high vacuum should provide almost perfect electrical insulation, however, it can be readily demonstrated that substantial currents may flow between vacuum insulated high voltage electrodes. These are known as prebreakdown currents and are strongly dependent upon the electric field applied to the electrode gap. When this field is increased beyond a certain point an arc is struck between the two electrodes and the gap resistance effectively falls to zero. This irreversible process is known as " electrical breakdown" and, because it causes extensive electrode damage, usually represents a catastrophy when it occurs in an item of commercial equipment, such as high energy particle accelerators, X ray tubes, electron microscopes or transmitting valves etc. Thus, in order to maximise the design efficiency of such devices, the vacuum breakdown problem is best solved by discovering the fundamental physical processes which give rise to this phenomena.(1,2)

For electrodes separated by gaps < 5 mm and fields in the range 30 to 50 MV/m there is strong evidence to suggest that prebreakdown currents are responsible for initiating breakdown. For larger gaps however, where no prebreakdown currents are observed, loosely bound microparticles are assumed to be electrostatically pulled off the electrode surfaces and accelerated by the gap field to gain sufficient energy to trigger a breakdown; a process occurring at lower fields, typically $\sim$10 MV/m, than for the occurrence of continuous prebreakdown currents. This thesis however, concentrates on the nature of the prebreakdown currents since a thorough understanding of this phenomena is required before an informed programme for improving the insulating characteristics of vacuum gaps can be carried out. Therefore, the aim of this investigation was to review and extend the present knowledge of the emission processes as they occur on broad area electrodes.

1.2. Pre-breakdown Conduction.

Traditionally, as discussed in chapters 2 & 3, pre-breakdown conduction was explained in terms of a metallic type of electron field emission, in which it was assumed that the macroscopic gap field was enhanced to $> 10^9$ V/m by surface features such as sharp metal protrusions or whiskers. This model was supported by three main observations: a) electron emission was known to arise from a small number of extremely localised sites; b) the current - voltage characteristics of the emission process appeared to follow the predictions of metallic field emission theory; and c) microscopic protrusions had been observed on electrodes which were previously exposed to high fields. However, this interpretation has now been largely superseded by models of emission based on electron conduction through insulating or semiconducting surface inclusions; these are discussed in chapter 4 but see also for example Noer (1) or Latham(2). The change in thinking was brought about by recent experiments which indicated that unrealistically high geometrical field enhancement factors had to be assumed in the metallic whisker model, and that no direct observation of these whiskers could be made in the areas from which electrons were emitted. Further direct evidence against the metallic field emission theory was obtained from optical experiments and from measurements of the energy distributions of the emitted electrons.

Both of these experiments yielded results which were much more consistent with an interpretation based on insulating surface layers or inclusions. Non metallic layers and inclusions must invariably be present on nominally clean metal surfaces, where the exact details will depend on the specific history of the particular piece of metal, i.e. polishing technique, ambient atmosphere, smelting procedure or even the type of ore used etc.

Several models were originally proposed to describe the emission of electrons from such semiconducting and insulating surface layers. Early models were only of a qualitative nature, and were also unable to explain many of the subsequent experimental findings. However, further theoretical developments have since been made, so that it now seems likely that the emission takes place as a result of an electron "heating mechanism" which occurs at the ends of thin conducting channels or filaments which first penetrate through the insulating layer from the metal surface. The hot, or very energetic, electrons being produced by acceleration in the electric field which then penetrates into the insulating inclusion. The exact details of this process vary from model to model but the culmination of the above developments, which are also discussed in chapter 4, envisaged the external field penetrating into an insulating impurity which, at a certain value, produced an electron avalanche that caused it to switch from a low to a high conductivity state. This state was then seen as being formed into the insulator and then maintaining itself by a regenerative process which resulted from the combined action of electrons and holes. However, even this model will be shown to have problems when examined critically so that an alternative explanation of the various phenomena has been sought.

In fact, it will be shown in chapters 4 & 7, that an examination of the likely properties of contaminated surface inclusions with particular regard to the latest experimental findings, leads to a simpler model than the above, which has been found to account for all the present experimental results without any additional hypotheses. Thus a contaminated surface inclusion, which represents the only reasonable assumption for the structures found on broad area electrodes, would be expected to contain both donor and electron trapping centres and these, if present in sufficient numbers, lead automatically to the conditions for the relatively easy tunnelling of electrons into the insulator and for their subsequent conduction through it. The quantitative development of this model will then be shown to give many interesting relationships between the various parameters, all of which will be seen to be of the order expected for contaminated insulators.

1.3. Instrumentation.

The experimental technique which forms the major part of this study, is the measurement of the energy distribution of the electrons emitted from the localised sites on broad area electrodes. This in principle contains more basic information than the commonly measured total current, which mathematically is an integration of the energy distribution over all energies. Electron spectrometry, as explained in chapter 3, has been found to be a sensitive test of the electron emission mechanism when applied to the study of field emission from metals, semiconductors and through adsorbed atoms or molecules. Not surprisingly therefore, in the present context of emission from localised sites on broad area electrodes, this technique, in conjunction with a sufficiently detailed quantitative model, has provided a surprising amount of information on the structure of the emitting sites.

As described in chapter 5, the heart of the electron spectrometer employed here is a hemispherical electrostatic deflection analyser which is capable of providing the energy distribution directly with a resolution of <30meV. This was originally established to measure the emission from micropoint tips, but had been modified to interface it with a broad-area gap; however, further refinements were found to be necessary to this interfacing lens, and these have considerably enhanced the meaning which may be placed on the interpretation of the spectra. Several other important instrumental improvements have also been incorporated into the spectral analysis system, notably an automated specimen scanner, which allows a finer and more meaningful analysis to be made on the individual emission sites.

1.4. Experimental Techniques.

In particular, two surface treatments, viz. argon ion etching and electrode oxydation, have been used to further understand the nature of the conduction processes occurring within insulating layers or inclusions,these techniques are discussed in chapter 6. Also, consecutive sequencies of spectra recorded on single photographic frames have enabled changes with field variations to be more easily assessed and measured. Lastly, a heated specimen stage has been used to investigate the influence of elevated temperatures, and this has also furthered the range of understanding of the prebreakdown emission phenomena.

CHAPTER 2.

A REVIEW OF PREBREAKDOWN CONDUCTION BETWEEN VACUUM INSULATED HIGH VOLTAGE ELECTRODES.

2.1 Introductory Remarks.

Outlined in this chapter are a selection of results which were obtained during about eighty years of scientific endeavour into the electrical behaviour of vacuum insulated electrodes. Even now, as indicated in the review by Noer(1) and in the discussion given by Latham(2), a thorough understanding of all the aspects relating to prebreakdown electron emission is only just beginning to emerge. Most early results were seen to be consistent with the metallic whisker interpretation of the phenomena but subsequent developments have shown this model to be largely an inadequate description, as will be seen from the following historical account and many of the results presented in the proceeding chapters.

2.2. Experimental Evidence in Favour of the Metallic Microprotrusion Hypothesis.

Experiments performed with electrodes having an extended area parallel plate geometry began at the turn of the century. Early work, by Millikan and co-workers(3,4) in particular, produced some important observations even though they used a rather poor vacuum system. Thus, field emission from tungsten was ordinarily observed for fields in the range 1 to 5×10^7 V/m, but if an annealing procedure was carried out at 2700K the cooled tungsten withstood a field of 4×10^8V/m before emission. Light spots were observed on the anode suggesting that electron emission occurred from a few localised cathode sites. Emission currents were found to be independent of temperature up to 1000K, and a plot of the logarithm of the current versus the inverse field gave a straight line in all cases. Millikan concluded that emission took place from cathode regions of low work function due to chemical impurities, or from regions with a high local field produced by surface roughness.

The subsequent introduction of ultra high vacuum (U.H.V.) techniques made it possible to perform experiments in which contamination from the vacuum system or from residual gases could be eliminated or controlled, thus allowing more exact definition of the cathode surface. In particular, Boyle et al(5) undertook experiments to try and confirm the early results of Dyke et al(6,7) who had used a micropoint cathode in poor vacuum and found excellent agreement with the predictions of Fowler - Nordheim(F.N.) theory. This theory, described fully in chapter 3 , used quantum mechanics to give an expression for the current density emitted from a metal surface as electrons tunnel through the narrow potential barrier formed at the electrode-vacuum interface by the applied field. Theory predicted that a surface field in excess of 10^9 V/m was required to give a narrow enough barrier, and for non planar electrode geometries it was necessary to introduce a field intensification factor β which related the average macroscopic gap field V/D to the actual microscopic surface field F over the emission area: thus $F = \beta V/D$ where D is the pertinent anode to cathode distance and V the applied voltage. Fowler-Nordheim theory then predicts that a plot of $\ln (I/F^2)$ versus $1/F$ (an F.N. plot) will be a straight line, having a slope proportional to the inverse of β and an intercept dependent upon $\ln(a\beta^2)$ where a is the emitting area. Boyles results for crossed wire electrodes in U.H.V. gave good fits to straight lines on an F.N. plot but the field enhancement factor β was found to vary with electrode gap spacing; this they explained as due to emission taking place from surface protrusions having a very minute area $\sim 10^{15}$ m^2 over which the field was increased by the factor β. Values of β ranged from unity when the gap was a few angstroms to as high as 30 for 10 μ m. gaps and was consistent with an explanation based on the presence of small metal projections on the cathode surface.

The more practical case of disc electrodes 35 mm in diameter, which were cut from single crystal tungsten, was examined by Alpert et. al.(8) who used gap spacings of 5 μm to 4 mm. Good F.N. fits were found giving β in the range 50 - 200 which were again gap dependent. Two posibilities were then considered to explain this behaviour: firstly that microscopic protrusions existed on the cathode surface and second that changes could occur in the electric field due to electrode edge effects when the gap was large. Further evidence in favour of the microprotrusion hypothesis for emission from broad areas was obtained from electron microscope studies by Little & Smith(9) and Tomasche & Alpert(10). Shadow electron micrographs of the blunt end of a 70 micron tungsten wire showed projections of micron dimentions which were capable of providing high β factors; these had appeared on previously smooth areas after an electrical breakdown. It was also noted that very small gaps gave large current fluctuations which, if allowed to proceed for several minutes, produced a large number of whisker like projections $\sim$ 0.1 μm high on previously clean cathodes. An annealing procedure at 2000K removed the current fluctuations, allowing a straight FN plot to be taken up to gap breakdown. Results for other materials including aluminium, stainless steel, Kovar, nickel, silver and copper were reported by Little & Co-workers(9,11) as being similar to those for tungsten. They also used a fluorescent anode with a gap of 0.1mm and noted that as current flowed one or more fluorescent spots <0.2mm in diameter suddenly appeared on the anode. The cathode could then be repositioned, while in the same vacuum system, so that shadow electron micrographs could be taken. It was then found that every cathode surface had features which could give high enough β factors for F.N type emission and which were not there before the application of the electric field. Little et al (11) also noted that emission was independent of temperature up to $\sim$ 1000K and independent of illumination with visible light, thus verifying that prebreakdown emission does not originate from areas having an extremely low work function.

Brodie(12,13) made other investigations into the properties of electron emitting sites associated with a 0.125 diameter nickel wire cathode in conjunction with a 76 mm cylindrical phosphorescent anode. Elliptical spots, a few millimetres across, could then be seen on the anode as the emission current flowed, these were correlated to the emission from whiskers 7 nm to 1 μm high. However, the structure within the larger ellipses could not be related to the field emission images from single crystal nickel surfaces obtained by Gomer(14). For high fields $\sim 75\times10^7$V/m new very intense emission centres suddenly appeared, capable of providing stable milliampare currents without degration. The elliptical images were then very large having major axes up to 6 cm.

Measurements of prebreakdown currents from copper electrodes in U.H.V. have been reported by Davies & Biondi(15). O.F.H.C. copper electrodes were first metallographically polished and then electrolytically polished prior to assembly in the vacuum chamber. Tungsten heating filaments then allowed the electrodes to be baked for 20 hrs at a temperature of 850°C. Linear F.N. plots resulted that had values of β in the range 140 to 240 with no correlation to gap setting at least over the range 0.3 mm to 2 mm. Davies & Biondi(16) further reported that their I-V characteristics were independent of temperature over the range 313K to 900K.

2.3. Experimental Evidence Against the Microprotrusion Hypothesis.

From early studies of prebreakdown broad area emission, a considerable amount of experimental data has accumulated in favour of the cathode microprotrusion hypothesis. However, as the experiments were refined, a great variety of effects were seen to be at odds with this model, amongst these were: curved and variable F.N. plots, prebreakdown current noise and instabilities, variation of current over extended time intervals, ignition-hysteresis phenomena, high current and negative resistance sites and microdischarges. These effects are most common in poor vacuum, i.e. $> 10^{-6}$ mbar, as indicated in the review by Hawley & Zaky (17) but most of the phenomena still persist, if with a lower incidence, in U.H.V. baked systems with pressures $< 10^{-9}$ mbar.

Powell & Chatterton (18) obtained evidence indicating that straight F.N. plots are not necessarily representative of the conduction between unconditioned electrodes. A conditioned electrode system is one whereby the voltage hold-off capacity has been maximised through the use of one or more of a variety of procedures; see for example Latham (19). For static or d.c. voltage hold-off the most widely used technique is that due to Millikan, whereby an increment of voltage is applied and all erratic or noisy components of prebreakdown current are allowed to stabalise over a time interval of ~30 min. before the next voltage increment is applied. This process is then repeated until the required voltage has been exceeded by a safety factor, say 20%. Powell & Chatterton (18) investigated the characteristics of stainless steel, copper, tungsten and aluminium electrodes, for small gaps i.e. 1 cm in both U.H.V and poor vacuum, and found remarkable similarity in behaviour for the different materials. The general non-reproducibility and variability with time of the emission current, necessitated the use of a fast response measuring system based upon a storage oscilloscope, which enabled an I - V plot to be made in five steps over the current range 10^{-9} to 10^{-3}A with each step taking about half a second. Application of the fast measuring system verified the existence of bursts of change called microdischarges previously noted by Pivovar & Gordienko (20, 21). These occurred for all materials at a definite voltage, depending on the electrode gap, but mainly during the early stages of conduction between a pair of newly installed electrodes.

Microdischarges usually consisted of many bursts of charge giving currents from less than 1 uA to ~10 mA, rather than single pulses, and lasting from 10 uS to ~10 mS. Current conditioning enabled these events to die out harmlessly but did not reduce the steady component of current; rather the current tended to increase at a given voltage after the passage of a microdischarge, at least in the early stages. Figure (1) gives typical traces of current against time for fixed voltage and shows the phenomena known as rectangular pulse conduction. An ignition-hysteresis phenomena was also observed by Chatterton(22) for currents in the region of a few uA whereby, for steadily increasing voltage, the current would at first also steadily increase but would then rise very rapidly for very little further rise in voltage, thus giving the "ignition" effect. Upon reducing the voltage, the current then remained at a high level until a lower "extinction" voltage was reached, as shown in figures (2 & 3). Both of these effects were suppressed at current levels over 10^{-4} A while at 10^{-3} A the ignition-hysteresis could be removed altogether. This was entirely a current effect occurring at the same current value for all gaps, and known as ageing. A process known as de-ageing then took place by which the emission current would fall with time at a constant voltage; subsequently, if the current was kept below ~1 uA, a return to rectangular pulse condition would result after about 20 min. in rather poor vacuum (10^{-7} mbar). Ignition phenomena only resumed however, after de-ageing for several days or after contamination of the vacuum system, such as resulted from not filling the liquid nitrogen traps. Notably, de-ageing in a clean baked system having a pressure of 3×10^{-9} mbar took several hours, but if air was admitted at a pressure of 2×10^{-6} mbar for a few minutes the electrodes completely de-aged. Powell & Chatterton(18) explained the various instabilities in terms of variable gas coverage of an emitting microprotrusion, but similar

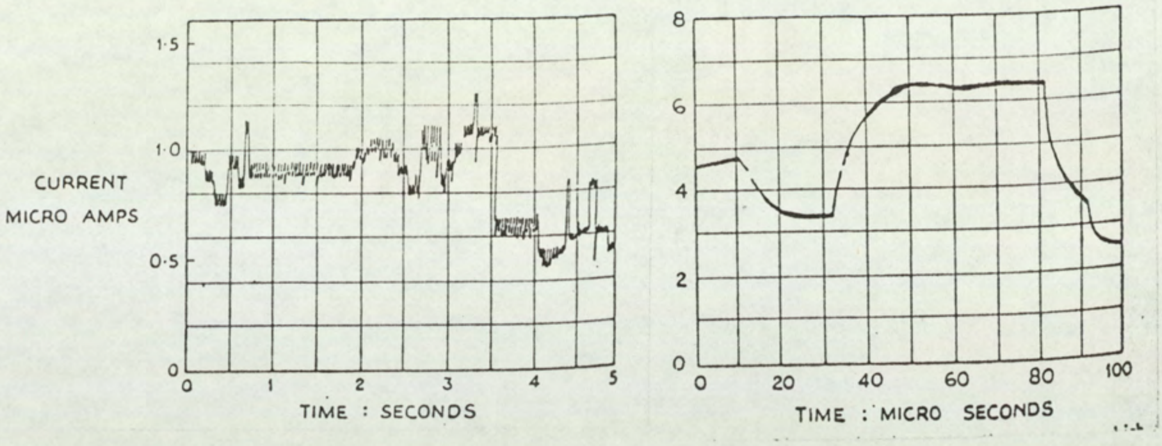

FIG 1. RECTANGULAR PULSE CONDUCTION. from Powell & Chatterton (18).

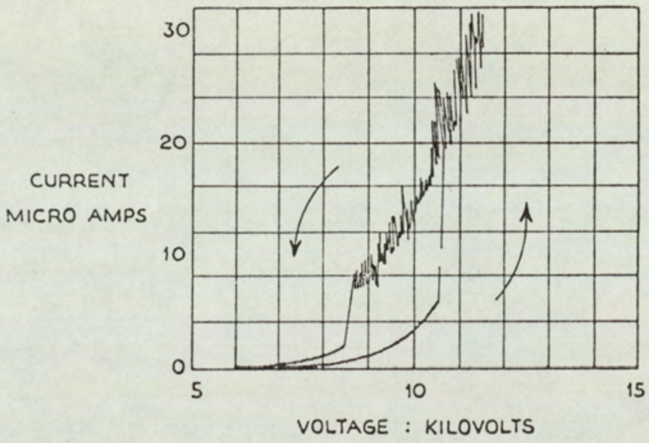

FIG 2. THE IGNITION-HYSTERESIS PHENOMENA. from Powell & Chatterton

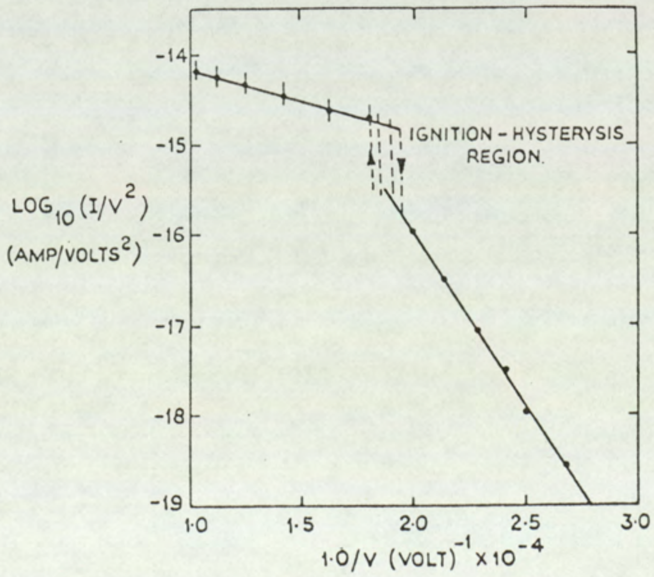

FIG 3. A FOWLER-NORDHEIM PLOT OF THE IGNITION-HYSTERESIS REGION.
from Powell & Chatterton (22).

conclusions may be drawn for variable gas coverage of almost any emitting surface. Thus, for the microprotrusion case at low currents, molecules would arrive at the tip due to field assisted surface migration and the gas coverage would increase. At higher currents, the tip temperature tends to rise increasing the positive ion sputtering of the tip which in turn tends to reduce the gas coverage. While at high values of current, the tip may become very hot and gas coverage be reduced drastically. A further assumption was that gas coverage suppresses electron emission, so that an F.N. plot under these circumstances would be expected to be non-linear as the gas coverage varied with the current.

Ignition-hysteresis effects were compared with the molecular images seen in field emission microscopes (23) where an adsorbate could suddenly increase the electron emission if its empty energy levels dipped below the Fermi level of the metal protrusion as the field was increased. Ageing was explained as the near complete removal of adsorbed gas from the emitting protrusion, while de-ageing resulted from its gradual recontamination; rectangular pulse conduction was then the result of migration of small groups of atoms across the emission zone. These results stress the need for clean baked U.H.V. systems having ultimate pressures $< 5 \times 10^{-10}$ mbar in order to minimize instabilities resulting from adsorbed gas. Similar results were reported by Hackam & Salman (24) for conditioned aluminium electrodes in a baked system at 10^{-9} mbar which gave two distinct types of F.N. plot. Short gaps i.e. <0.76 mm produced single straight line F.N. plots showing no ignition effects, but for larger gaps, i.e >0.89 mm ignition-hysteresis phenomena started to appear in the current range 2.4 to 6.6×10^{-9}A. The ignition current then increased in two stages, slowly at first to $6\text{-}10 \times 10^{-9}$A followed by a sudden jump to the range $0.26 - 6.5 \times 10^{-7}$A, all without an increase in voltage: a subsequent increase in voltage gave an F.N. plot that was definitely curved. Other non Fowler-Nordheim current relationships were revealed by Cox (25) and by

Hurley.(26) Cox made a large number of tests on 14 mm diameter copper-chromium alloy vacuum switch contacts which were set in a 6 mm plane parallel gap and under a vacuum of 2 x 10^{-10} mbar which was reached after a 250 °C. bake-out. Deconditioning to simulate in service conditions was achieved with a 14 KHz ringing discharge having a 16 KA first peak; the majority of results then gave F.N. plots with β values in the 300 to 500 range. Some tests however, produced unstable emission with the irreversible hysteresis-like I-V characteristics illustrated in figures (4 & 5). Yet other emission sites "switched on", going from a current of $<10^{-7}$A to $>10^{-5}$A with virtually no change in applied voltage. These occurred in about 1% of tests and are distinct from the ignition sites reported by Powell & Chatterton (18), because the "switch on" only occurred once even if the maximum current was limited. Other rare sites could pass the maximum available current of 0.5 mA without causing a breakdown and which had β factors of 1000 or so.

Hurley's (26) work on O.F.H.C. copper, using a pointed anode probe, showed the existance of two types of site which he termed "a" and "b" sites. The "a" sites generally gave straight F.N. plots which were characterised by β values in the range 150 to 300 with calculated emitting areas of about 10^{-16} to 10^{-14} m^2 and which produced breakdown and site destruction for currents $\sim 5 \times 10^{-5}$A. The "b" sites were quite different however, having β values in the range 10 to 150 and emitting areas from 10^{-13} m^2 to the "impossible" value of 10 m^2. A negative resistance region was also observed, such that for currents $>10^{-5}$ A, an equilibrium condition would occur that was partly determined by a 23 MΩ series safety resistor (see figure (6). If this resistor was removed and the total current then only limited by the power supply, breakdowns could occur randomly in the current range 10^{-5} to 10^{-3} A but without destruction of the emitting site.

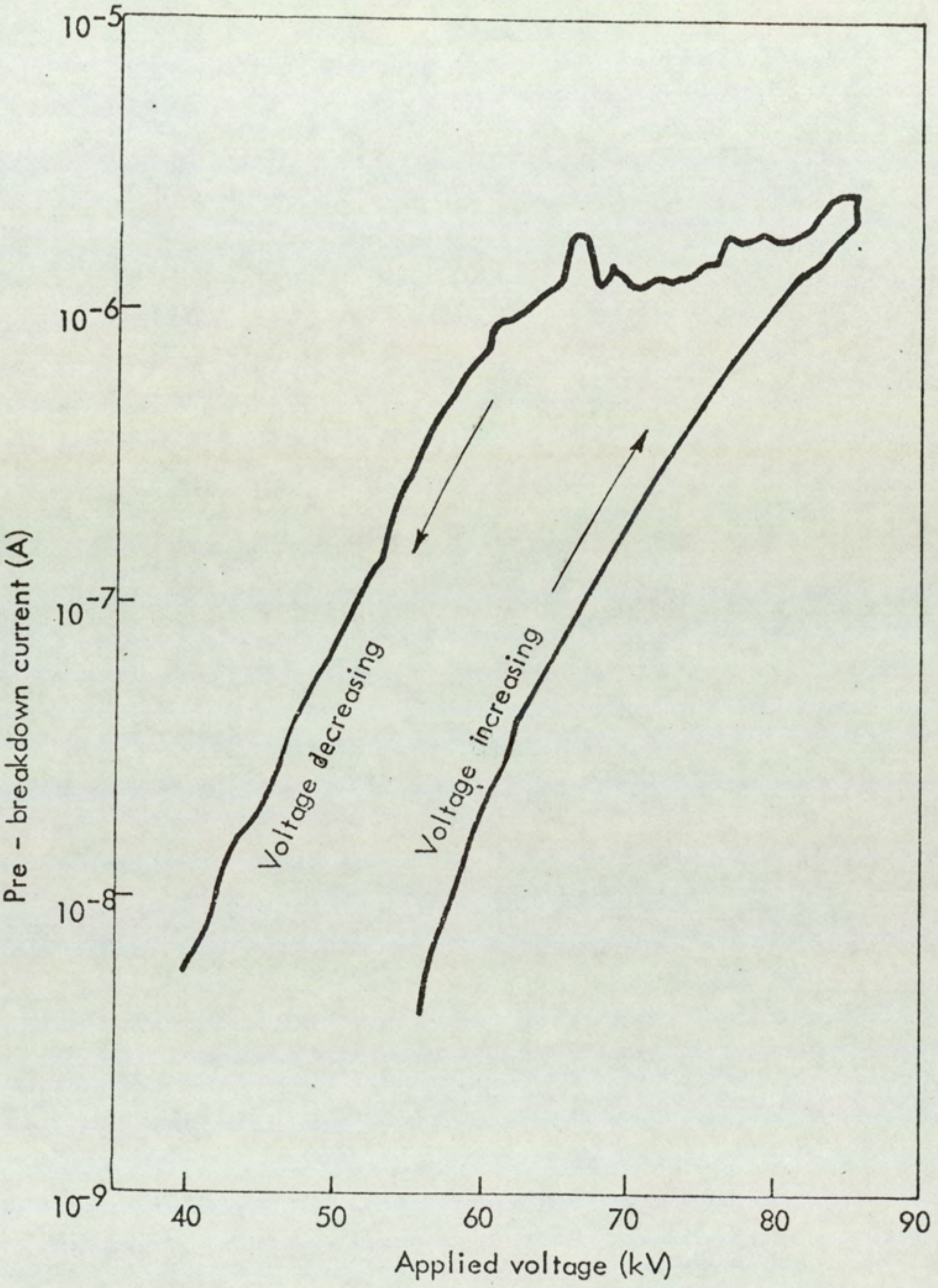

FIG 4. AN IRREVERSIBLE "HYSTERESIS-LIKE" I-V CHARACTERISTIC. from Cox (25).

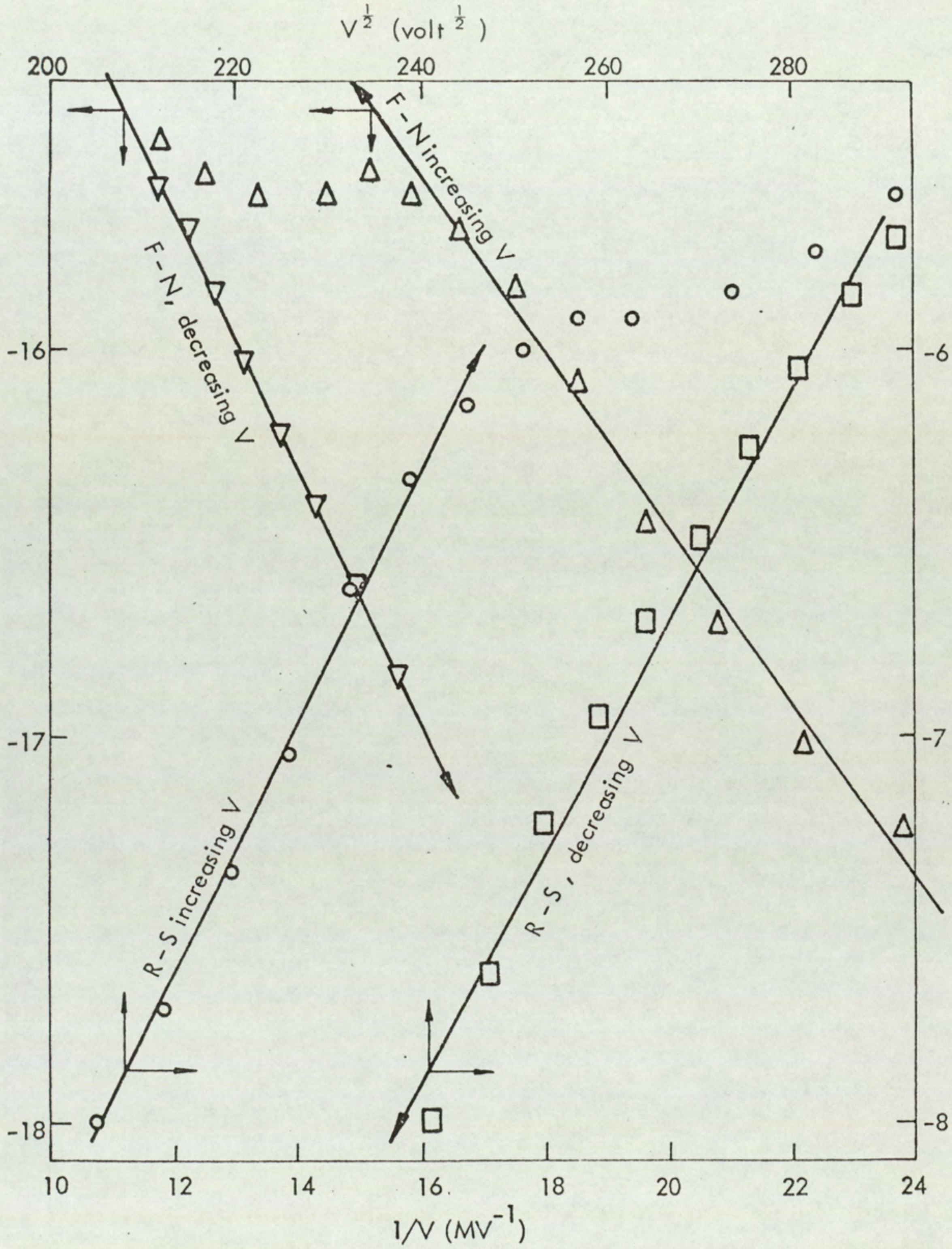

FIG 5. FOWLER-NORDHEIM & RICHARDSON-SCHOTTKY PLOTS OF THE I-V DATA SHOWN IN FIG 4. from Cox (25).

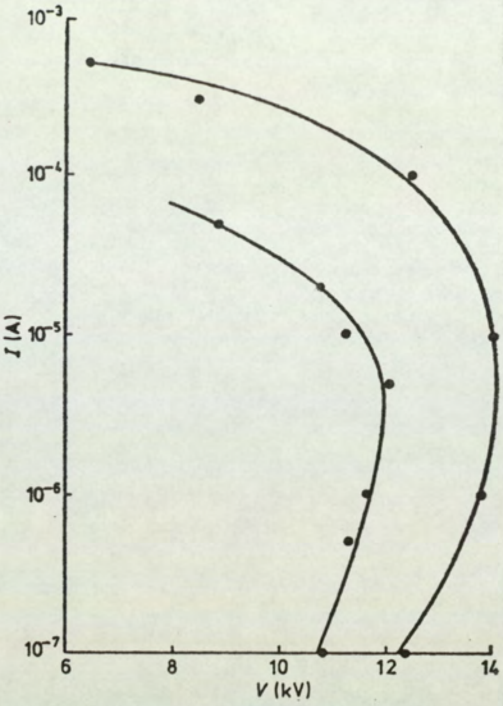

Current–voltage characteristics of typical b-sites. ●, d=0·16 mm; ⊙, d=0·32 mm. d=distance between the tip of the positive probe and the negative broad area electrode.

FIG 6. I-V CHARACTERISTICS OF TYPICAL b SITES. from Hurley (26).

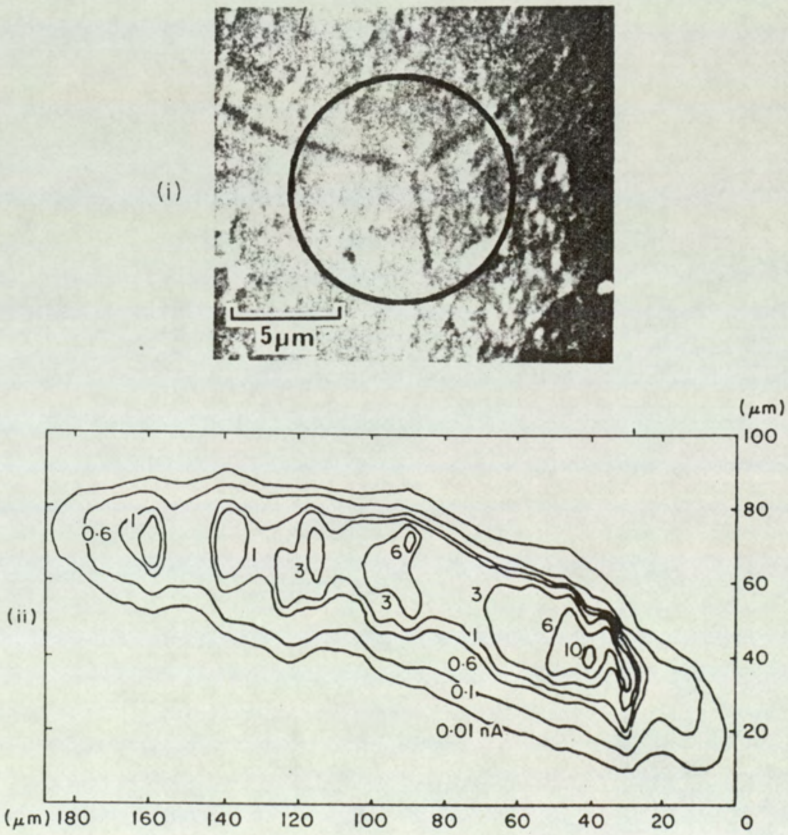

(i) A scanning electron micrograph showing the region of an electrode surface (circled) that has been identified as containing an emission site, and (ii) the complementary distribution map of the field emission current associated with this site.

FIG 7. A MAP OF THE EMISSION CURRENT IN THE ANODE PLANE. from Cox (27)

All these reports indicate that the assumption of microprotrusions being solely responsible for the prebreakdown emission from broad areas is apparently incorrect. This assumption rests essentially on the linearity of F.N. plots and on the observation that metallic field enhancing features usually exists on electrode surfaces. The first condition is seen to be only very approximately valid, while the second remains unsubstantiated since no direct evidence exists which correlates electron emission from broad area electrodes with metallic surface protrusions having a high enough β factor, at least for unconditioned electrodes. Prebreakdown conduction is also seen to be much more complicated than a simple application of Fowler - Nordheim theory would allow. Recent experimental results which are summarised below have now converged to give an alternative hypothesis; viz. that of conduction through embedded insulating impurity particles and contaminated oxide layers.

2.4. Recent Evidence in Favour of Non -Metallic Emission Involving Surface Oxide Layers and Insulating Inclusions.

The recent work of Cox,(27) Hurley and Dooley,(28) Allen and Latham (29) and Athwall and Latham (30) in particular provides a diverse body of results which cannot be explained by simple metallic emission processes. Cox & Wort (31) were the first to develope a refined method for locating and then mapping the constant current contours of emission sites on broad area electrodes which used two 0.5 mm diameter anode probe holes, one behind the other. Each site position could thus be determined to an accuracy of 0.1 mm by moving the anode assembly relative to the specimen surface. A notable early result was obtained by using this equipment to plot the emission from a simulated site consisting of a tungsten tip inserted into a planar copper surface. In fact emission was recorded from a position close to, but definitely separate from the artificial protrusion, thus showing that the most likely source of emission from a field enhancement point of view is not necessarily the actual emitter. Cox (27) then improved the facility and incorporated it into a U.H.V. scanning electron microscope (S.E.M.). With this system emitting sites were first located by scanning the specimen in a raster pattern beneath a large anode apperture. A smaller probe was then selected and the specimen positioned such that the current collected by the movable probe was maximised. By repeating this procedure for smaller and smaller specimen - anode gaps the electron trajectories from the beam centre could be ploted and the site co - ordinates determined with a resolution of $\sim$ 10 um. This area was then examined in the S.E.M. with the probe hole moved out of the way. Results showed that even though the F.N. plots for individual sites gave β values $>$100 no surface feature could be identified which could give such high field enhancement. Dust particles were found to be the cause of many emission centres, these were largely prevented by setting up a specimen cleaning bath right next to the S.E.M. and using both in a clean room, Subsequent sites were found at cracks or grain boundaries as in figure (7) or at the specimen edge despite attempts at reducing field intensification near the specimen sides by profiling the electrodes (27). Unpolished stainless steel was examined by Cox & Williams (32) using the above technique which was found to give an exceedingly strong emission with $\beta = 735$ from a 5um diameter insulating particle.

An extensive amount of data has been gathered on the breakdown initiating effects of microparticles. In particular Donaldson and Robinowitz (33) found that the thermal decomposition of glass (as used for closing vacuum chambers) generates particles having diameters between 10 nm and 0.5 um. which contained a variety of elements including sodium, potassium and boron. These particles were not removed during a system bakeout at 450°C. and were found to reduce breakdown voltage by 50% or so if present on an electrode surface. Pakrovskaya et al.(34) have demonstrated that the insulating inclusions $Fe S$, $Al_2 O_3$, $Si O_2$ and alumina silicate glass added to pure iron cathodes produce 20 - 30% degradation in breakdown voltage; large particles 50 to 500 um in diameter giving the greatest and longest lasting reduction. They then confirmed the earlier work of Maskrey & Dugdale (35) suggesting that breakdown events were localised to regions containing the inclusions. In the case of refractory $Si O_2$ particles breakdown events fused the iron near the inclusion, whereas for cathodes having the more easily melted $Fe S$ particles, it was the inclusion material which melted. More recently Farrall et al (36) have investigated the effect on voltage hold off of deliberatly contaminating copper electrodes with alumina powder. When 50 um diameter particles were present, emission currents of $\sim 10^{-5}$ A were obtained at voltages 30% lower than those required for uncontaminated surfaces prior to the occurrence of any breakdown events. Pulsed breakdowns at high current led to the eventual convergence of the emission properties for all surface treatments. Metal-insulator boundaries were later found to be associated with the breakdown events since particles showed signs of smoothing (melting) at the edges when observed in the S.E.M. Cavities were also observed which appeared to be places from which particles had been ejected.

A different type of observation which is also not consistent with the microprotrusion hypothesis, is due to Hurley & Dooley. (28) These authors carried out an investigation into the spots of light which can appear on cathode surfaces when prebreakdown current flows i.e. the same phenomena as briefly noted by Klyarfell & Pokrovskya - Soboleva(37). Again using broad area copper electrodes, the experimental technique involved observing the cathode or "K" spots of light through an image intensifier, and then to measuring their optical spectra, in a simple way, with a photo-multiplier in conjunction with a series of filters. The spectrum typically obtained, which is shown in figure (8), corresponded neither to black body radiation or to any obvious discharge spectra, but instead was suggestive of electroluminescence produced by the action of the electric field on semiconducting or insulating surface inclusions. A measurement of the applied voltage-light intensity relationship over a reasonable range of field confirmed that "K" spots obeyed the Alfrey - Taylor (38) law characteristic of electroluminescent cells. Hurley, (39) in a later experiment, demonstrated that electron emitting sites on copper electrodes are also the source of the electroluminescence. Discharges were sometimes seen to occur from within the light emitting areas and could be correlated with the onset of discharge flares and gap breakdown events(40). Hurley & Dooley examined electrodes of O.F.H.C. and high purity copper, molybdenum, stainless steel and duralumin, all of which gave similar results, but in the case of copper, straight tracks were sometimes seen originating from the "K" spots which were believed to be caused by uncharged particles being ejected from the electrode surface, as shown in figure (9).

More recently, experiments by Athwal & Latham (3) using an improved pointed anode probe technique similar to that used by Hurley(41), have also indicated that electron emission takes place from sub-micron to micron-sized impurity particles adhering to the electrode surfaces, rather than from the numerous field enhancing features, such as polishing marks, which were present on the electrode surface. Again, no projections were found capable of yielding high β factors. The technique was developed for in-situ studies in a convential S.E.M. and used three progressiely sharper anode probes to home down on-to

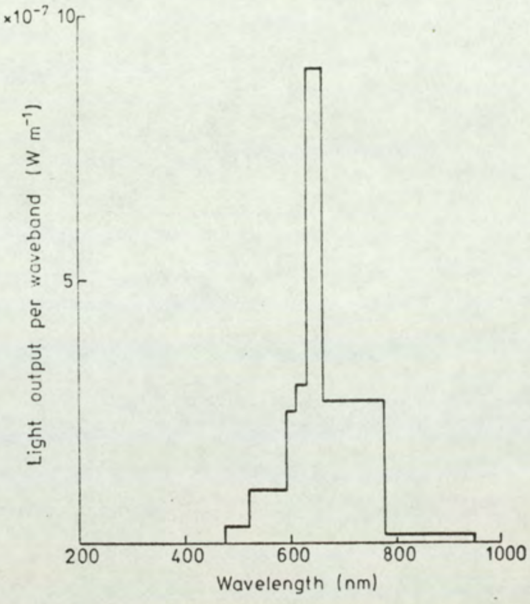

Spectrum of light emitted from a single cathode spot: 4·8 mm gap, 61 kV DC.

FIG 8. THE SPECTRUM OF LIGHT FROM A CATHODE SPOT. from Hurley et.al(28)

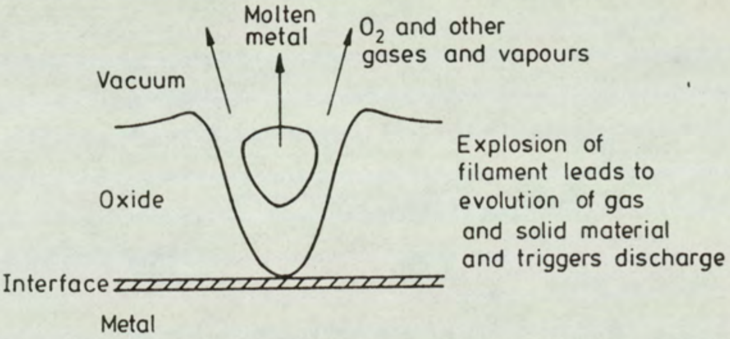

An illustration of the breakdown mechanism associated with the conducting filament model of Fig. 8.5. (From Hurley [5], with permission).

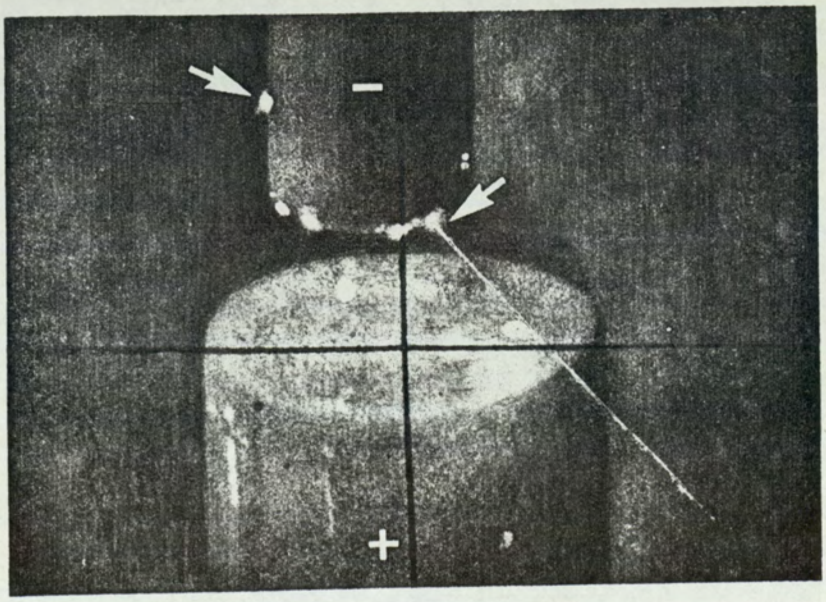

An open-shutter photograph of an electrically stressed planar high voltage gap showing both anode and cathode spots. Also shown arrowed are flares and discharge tracks emanating from cathode-spots.

FIG 9. "K" SPOTS OF LIGHT & DISCHARGE TRACKS. from Hurley & Dooley (40) an emitting area, giving an estimated resolution of 3-4 um. Subsequent X ray analysis of the emission zone, using an associated facility coupled directly to the S.E.M, showed the presence of compounds (probably oxides) of the electrode metal and sometimes foreign elements.

Early work on the electron energy distributions associated with broad area emission was published by Allen & Latham (42) at about the same time as Hurley's work on electroluminescence. This has shown that the electron energy spectrum for each emission site is indeed not compatible with emission from a metallic microprotrusion; infact, as will be shown, it is more characteristic of a semi-conducting emitter. Later work by Athwal & Latham(43) however, has indicated that even this model does not account for a great many of the known phenomena and work presented here reinforces these findings. A detailed model based on the emission of hot electrons from surface layers and inclusions has been developed which currently explains most of the phenomena; this is presented in later chapters.

CHAPTER 3.

HIGH FIELD ELECTRON EMISSION.

The first attempt to quantify the "cold" field emission of electrons (F.E.E.) from metals was due to Schottky (44), who postulated complete reduction of the potential barrier at the metal surface due to a combination of the external electric field and the electron image force potential; i.e. an extension of the mechanism that had been verified with thermionic emission under low field conditions. Application of this effect to cold-high field electron emission however, led to completely wrong predictions. A satisfactory theory was later formulated by Fowler and Nordheim who proposed a quantum mechanical model whereby electrons tunnel through the Schottky-modified potential barrier, shown in figure (10), which results when a high external field acts on a clean surface. This phenomena will now be described as it is applied to the emission of electrons from metals and semiconductors, and to emission through adsorbates, so that results may be compared with those obtained from broad area prebreakdown measurements. Temperature assisted and thermionic emission are then examined since these phenomena form the basis of the currently accepted model of prebreakdown emission, i.e. the hot electron model, and finally the measured energy distributions of the emitted electrons are compared with those resulting from Fowler - Nordheim theory etc.

3.1. Field Electron Emission from Clean Metal Surfaces.

The Fowler - Nordheim (F.N.) model of field electron emission assumes Fermi-Dirac statistics to describe the electron arrival rate at the metal surface, and a surface potential barrier penetration probability found from a solution of the Schrodinger wave equation.

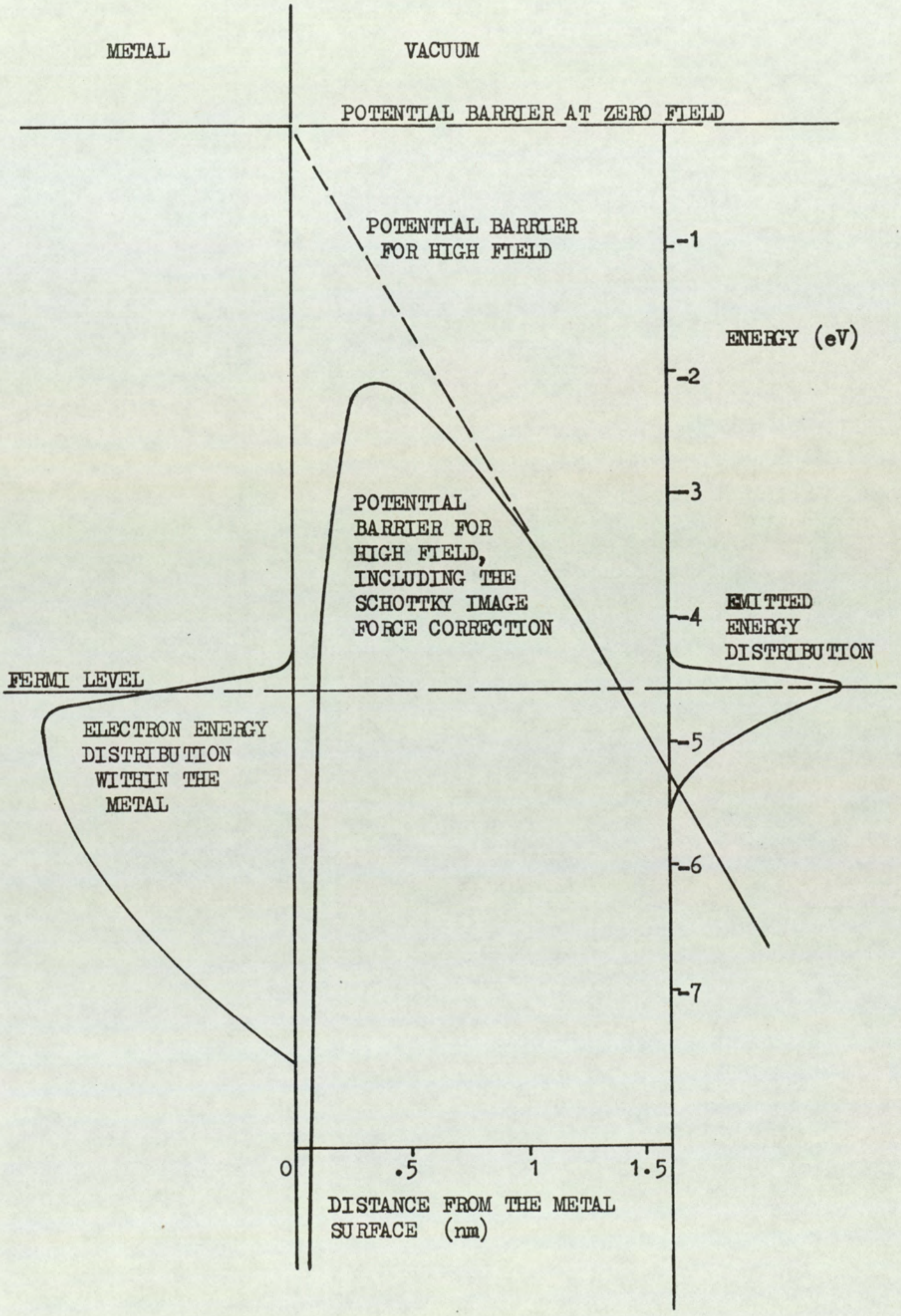

FIG. 10. A SCHEMATIC REPRESENTATION OF METALLIC FIELD ELECTRON EMISSION.

The mathematical procedure is then to fomulate the following parameters:

a). $N(W)\,dw$ = The supply function which gives the number of electrons with Z energy component in the range W to W + dw incident on the surface per second per unit area.

b). $D(W)$ = The probability that an electron with energy W will penetrate the barrier.

c). $P(W)\,dw$ = $N(W)\,D(W)\,dw$, which gives the number of electrons in the range W to W + dw penetrating the barrier (The normal energy distribution).

d). $J = e\int_W P(W)\,dw$, which gives the current emitted per unit area.

The detailed evaluation of N (W) D (W) and the approximations necessary to integrate analytically P (W) dw are an involved mathematical exercise requiring no further physical insight and modern reviews by Good & Muller (45) and Van Oostrom (46) adequately cover this.

For the low temperature approximation, i.e <300K when few states above the metal Fermi level are occupied the emitted current density is usually expressed thus

$$J = \frac{1.54 \times 10^{-6}}{\phi\, t^2(y)} F^2 \,\mathrm{EXP}\left[-\frac{6.83 \times 10^9\, \phi^{\frac{3}{2}}\, v(y)}{F}\right] \qquad (1)$$

This is known, as the Fowler-Nordheim equation where

J is the current density (Am^{-2})

F is the surface electric field (Vm^{-1})

ϕ is the metal work function (eV)

and t (y), v (y) are tabulated dimensionles elliptic functions of the (45,47) variable

$y = 3.79 \times 10^{-5} \dfrac{F^{\frac{1}{2}}}{\phi}$. For the stable current range of field emission i.e. $1 \times 10^9 < F < 6 \times 10^9$, $t(y) \sim 1$ and $v(y) = 0.956 - 1.062\ y^2$.

Substituting these approximations into the expression for J given by equation 1 and rearranging gives the most useful form of F.N. equation, viz.

$$J = 1.54 \times 10^{-6}\ \frac{10^{4.54\phi^{-\frac{1}{2}}}}{\phi}\ F^2\ \mathrm{EXP}\left[\frac{-6.53 \times 10^9\ \phi^{\frac{3}{2}}}{F}\right] \qquad (2)$$

Fowler - Nordheim theory was first tested by Haefer (48) using a point cathode with a planar anode; later, Duke et al. (49, 50) using micro point emitters having accurately known geometry and hence surface field, obtained good agreement with theory over several orders of current. Departures from F.N. theory at high current density could be accounted for by taking space charge into consideration. For simple parallel plane configurations however, they obtained a given current at fields 2 orders lower than that for the case of micro - point geometries which needed fields of $\sim 10^9\ \mathrm{Vm}^{-1}$.

If now the field is locally enhanced at some surface feature by a factor β, over an emitting area a, the resulting emission current will be $I = J a$, and for uniform field over the emitting region

$$\beta = F_{mic} \Big/ F_{mac} \qquad (4)$$

Since $F_{mac} = V/D$ for a plane-parallel electrode gap, where V is the applied potential difference and D is the electrode gap spacing,

$$F_{mic} = \beta \frac{V}{D} \qquad (5)$$

substituting this expression into equation 2 gives the F.N. equation in terms of measurable parameters thus

$$I = 1.54 \times 10^{-6}\ \frac{10^{4.54\phi^{-\frac{1}{2}}}}{\phi}\ \frac{a\beta^2 V^2}{D^2}\ \mathrm{EXP}\left[\frac{-6.53 \times 10^9\ \phi^{\frac{3}{2}} D}{\beta V}\right] \qquad (6)$$

It follows, that if the current-voltage characteristic of a gap with a single emitter is plotted in the form $\ln \frac{I}{V^2}$ Versus $\frac{1}{V}$

i.e. an F.N. plot, the result will be a straight line with slope

$$M = 6.53 \times 10^9 \phi^{\frac{3}{2}} \frac{D}{\beta} \qquad (7)$$

and intercept

$$C = \ln \left[1.54 \times 10^{-6} \; \frac{10^{4.54 \phi^{-\frac{1}{2}}}}{\phi} \; \frac{a \beta^2}{D^2} \right] \qquad (8)$$

Therefore, since D is known and ϕ for the emitter can be assumed to have the bulk metal value, the F.N. plot slope will give a measure of the emitter β factor; this may then be used with the intercept value to determine the emitting area.

For the case of a number of emitters distributed over the cathode surface, computer simulation studies by Tomasche & Alpert (51) have shown that prebreakdown current will always be dominated by one emitter, with its field enhancement factor and area reflected in the associated F.N. plot.

Early field emission experiments were mainly concerned with the field dependence of the total emission current under different surface conditions. A more basic parameter however, is the electron energy distribution of the emitted electrons, that is, the product of the energy distribution inside the emitter and the transmission probability at each energy. Thus, information about the origin of the emitted electrons and the energy dependence of their emission probability is contained in the measurable external electron energy distribution

3.2. Energy Distributions of Electrons Field Emitted from Metals.

Very early studies of the field emission of electrons were carried out using retarding potential analysers of rather poor resolution. Thus Henderson & co—workers (52,53), using a platinum wire cathode, showed that electrons emerge just below the Fermi level, whilst Muller (54,55) used a concentric anode and collector with a tungsten emitter to obtain good agreement with the theoretical energy distribution used in the derivation of the F.N. equation. This was verified later by Muller & Bahadur (56). With an improved retarding potential analyser however, Young & Muller (57) obtained an energy distribution much narrower than that assumed in the F.N. model, indicating that further theoretical work was necessary.

Now in the derivation of the F.N. equation the tunnelling probability is determined by the normal component of energy, i.e. that directed towards the surface. Hence the measured distribution was at first expected to be the distribution in normal energy of the emitted electron. This is true for a perfectly plane emitter - collector geometry but for any other geometry the transverse component of energy, conserved in the tunnelling process, is transferred to the normal direction once the electron has left the emitter. In fact Gadzuk & Plummer (58) showed that only when the distance r, of the probe hole of an analyser from the emitter, approaches the emitter radius r_o can the normal energy distribution be recorded; in the usual arrangement where $r \gg 10\, r_o$, the total energy distribution is obtained. Accordingly Young (59) used free electron theory to reformulate the F.N. equation in terms of the total energy distribution of electrons field emitted from a metal surface.
For this he defined the following new parameters :

$N(W,E)dWdE$ = Number of electrons with total energy in the range E to E + dE having a Z energy component in the range W to W + dW, incident upon the surface per unit area per second

$P\,(W,E)\;dWdE \;=\; N\,(W,E)\;D\,(W)\;dWdE$ which is the number of electrons in the given energy ranges penetrating the barrier.

$P\,(E)\;\;dE = \int_W W\,P\,(W,E)\;dWdE$, which is the total energy distribution.

$J = e\int_E P\,(E)\;dE$, which is the emitted current density .

Young showed that :

$$P(E)\;dE = \frac{4\pi md}{h^3}\;\mathrm{EXP}(-C)\;\frac{\mathrm{EXP}\left(\dfrac{E-E_f}{d}\right)}{1+\mathrm{EXP}\left(\dfrac{E-E_f}{kT}\right)}\,dE \qquad (9)$$

where

$$C = \frac{4e^{\frac{1}{2}}\;(2m\phi^3)^{\frac{1}{2}}}{3\;\hbar\;\;F}\;\;v(y) \qquad (10)$$

and

$$d = \frac{\hbar e^{\frac{1}{2}}\;\;F}{2(2m\phi)^{\frac{1}{2}}}\;\frac{1}{t(y)} \qquad (11)$$

with the other parameters as previously defined, and where $E_f = -\phi e$ with ϕ in eV.

Also $E_{max} = E_F - kT \ln\left(\frac{d}{kT} - 1\right)$ (12)

where E_{max} is the energy of the peak in the distribution so that

$E_{max} = E_F$ when $T = 0$. From equation 9

the full width at half maximum (F.W.H.M.) of the total energy distribution at zero temperature is found to be 0·693d : the expression appropriate to higher temperatures is too complex to be useful. The theory also gives the normal energy distribution which is

$$P\ (W)\ dW = \frac{4\pi m\ kT}{h^3}\ \mathrm{EXP}\left[\frac{-4\pi(2m)^{\frac{1}{2}}\ |W|^2}{3eh\ F}v(y)\right] \ln\left(1+\mathrm{EXP}\frac{E_F-W}{kT}\right)dW \qquad (13)$$

Both the normal and total energy distributions obtained by Young are shown in figure (11) for three different temperatures. Since the total energy distribution is the one directly measurable, all subsequent references to field emission energy distributions (F.E.E.D.) will mean measurements based on total energy.

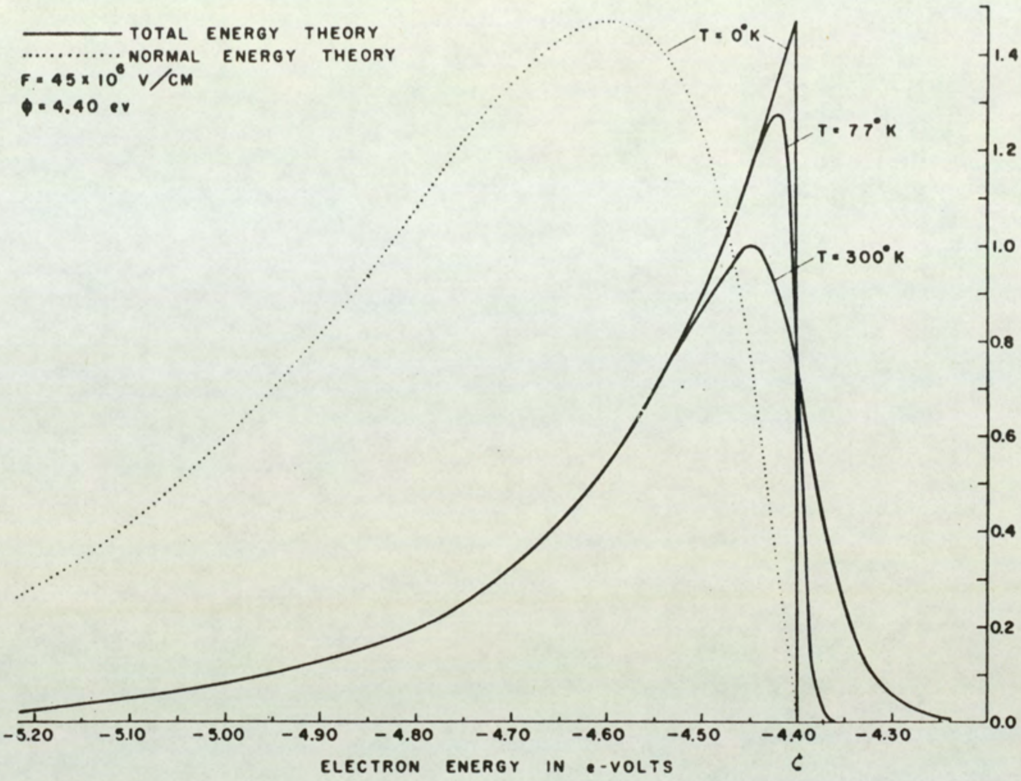

a) Fig. 2. Total- and normal-energy distributions for field emitted electrons. The 300°K curve is arbitrarily normalized.

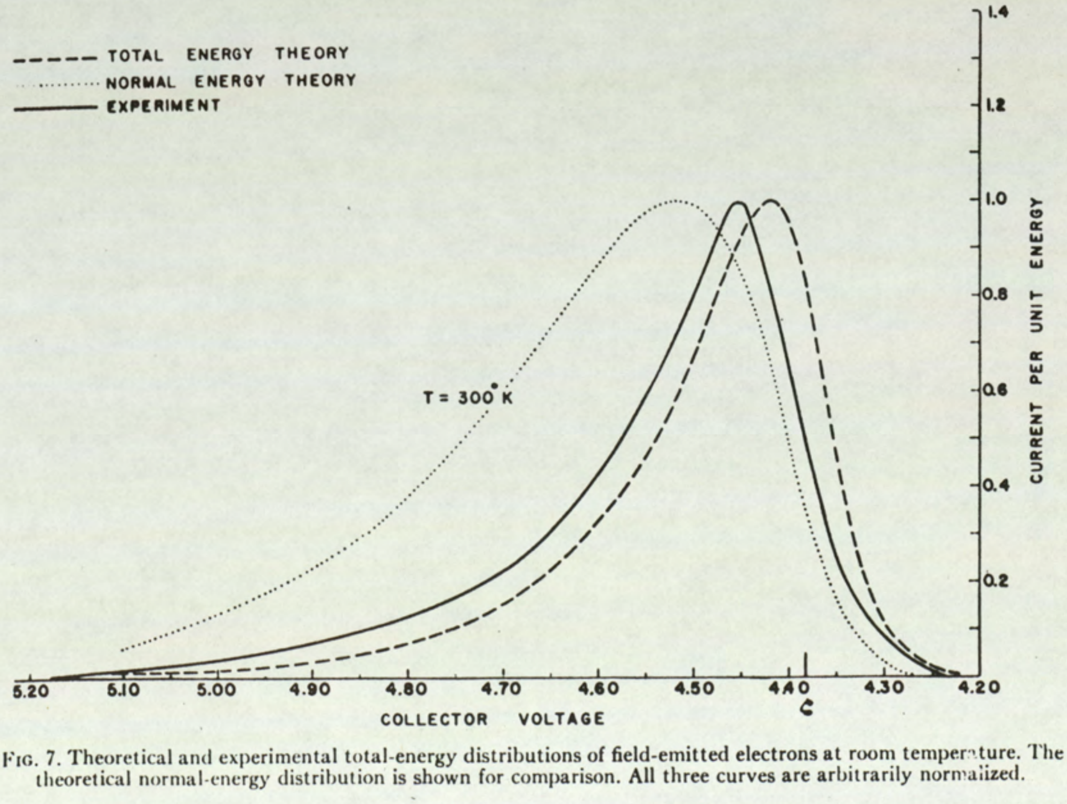

b) Fig. 7. Theoretical and experimental total-energy distributions of field-emitted electrons at room temperature. The theoretical normal-energy distribution is shown for comparison. All three curves are arbitrarily normalized.

FIG 11. TOTAL & NORMAL ENERGY DISTRIBUTIONS FROM A METALLIC EMITTER. from Young (59).

It should also be noted that under certain circumstances the non - free electron behaviour in metals shows up. Thus Swanson & Crouser(6) observed a low energy hump (the "Swanson hump") at 0.35 eV below the Fermi level, emitted from the (100) direction of a tungsten microtip. Other effects were studied by Plummer & Bell (61), again using tungsten, who predicted non free electron effects in all spectra. However, for these to be observable, the current axis of the F.E.E.D. must be plotted in logarithmic form, the "Swanson hump" being a notable exception. Later Nicolou & Modinos (62,63) developed a systematic theory for transition metal field emission, using a "Muffin tin approximation". Here the potential seen by an electron inside the metal is characterised by non overlapping spherical potentials centred on each of the crystal ions and by a constant potential outside these spheres. It is further assumed that the bulk potential ends abruptly at the surface, while outside the metal an electron sees only the applied field. Modinos (64) then goes on to calculate the expression for the total emitted current and the energy distribution, which have been shown to be in good agreement with experiment; see for example figure (12). However, low energy electron diffraction (L.E.E.D) data indicate that while the "Muffin tin approximation" is resonable for transition metals, it is not necessarily valid for other metals, and not for semiconductors where surface restructuring occurs.

Other Materials which have had their F.E.E.D's examined include molybdenum (65), platinum, copper, rhodium, iridium, palladium (66) and nickel where all deviations from free electron theory have been explained by band structure effects or local variations in the density of states at the metal-vacuum interface. Deviations from F.N. theory have also been thought to result from relaxation processes involving bulk scattered electrons (that is mechanisms for replacing

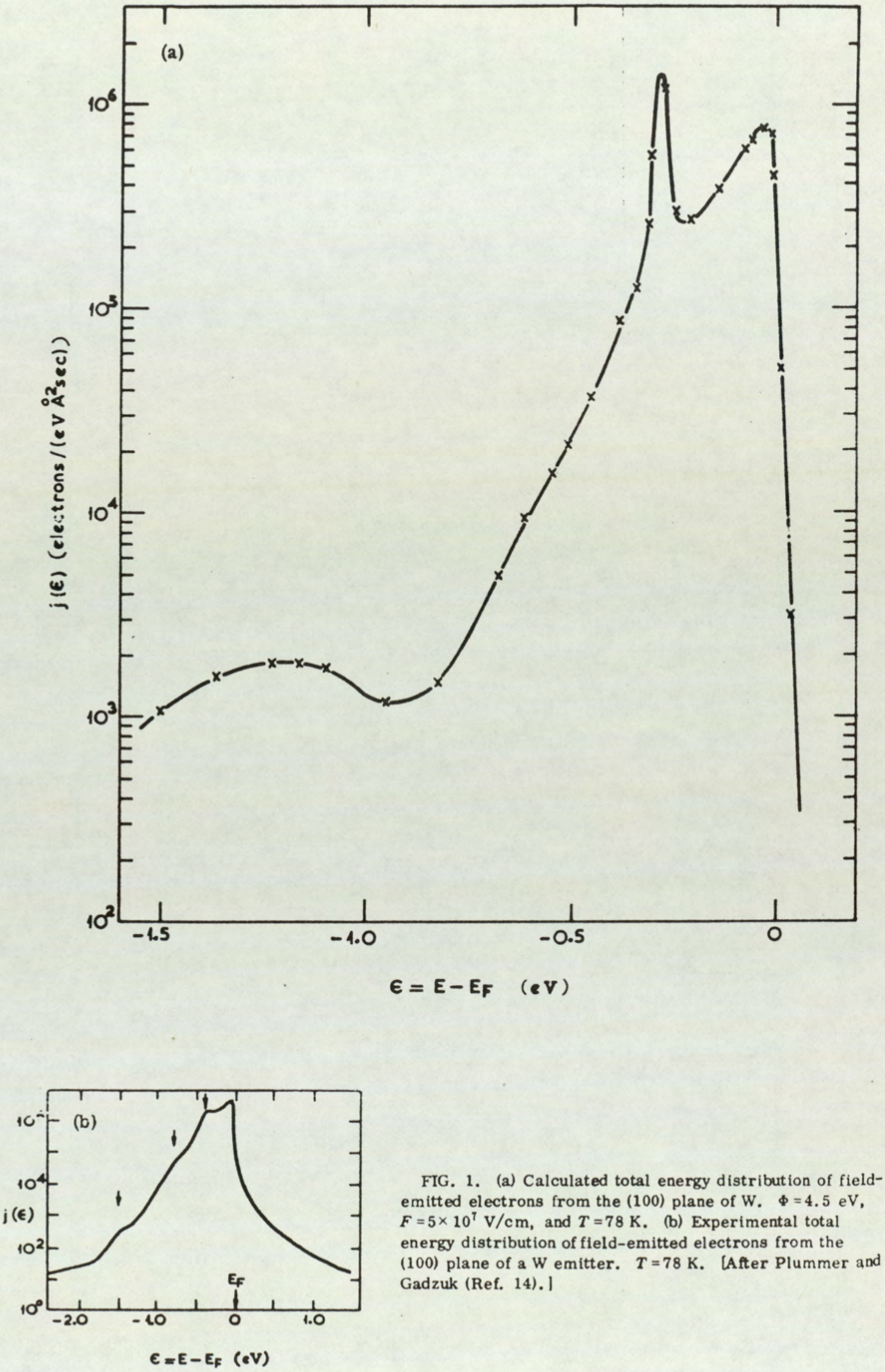

FIG. 1. (a) Calculated total energy distribution of field-emitted electrons from the (100) plane of W. $\Phi = 4.5$ eV, $F = 5 \times 10^7$ V/cm, and $T = 78$ K. (b) Experimental total energy distribution of field-emitted electrons from the (100) plane of a W emitter. $T = 78$ K. [After Plummer and Gadzuk (Ref. 14).]

FIG 12. THE ENERGY DISTRIBUTION OF A TRANSITION METAL.
from Nicolaou & Modinos (62,63).

the emitted electron) (68, 69, 70) and energy broadening due to tunnelling life - times. These phenomena need sensitive electron spectrometers for their detection and lead only to small perturbations in the resulting F.E.E.D. with little effect on the F.W.H.M. and no observable effect on the F.N. plot

3.3. Field Emmission from Semiconductors.

The theoretical treatment of the emission process from semiconductors is more complex than that from metals. This is because account has to be taken of a number of additional factors. These are: a) the more complicated energy band structure of these materials b) the presence of interband surface states; c) field penetration into the semiconductor surface layer; and d) the ohmic potential dropped within the emitter due to its higher electrical resistance. Stratton (71,72,73), in a theorectical treatment of field emission from semiconductors then assumed the following: an F.N. type surface barrier with a modified image force correction to take into account the semiconductor's dielectric constant; and surface state effects on field penetration, but not emission from these states.

Surface states arrise as a result of the sudden termination of the periodicity associated with the crystal lattice and the resulting rearrangement of surface atoms as they attempt to satisfy all their bonding electrons. Extra solutions in the wave mechanical treatment then become possible with new eigen values (energy states) made available. Inside the crystal the allowed solutions produce the well defined energy bands but at the surface the extra states may be within or overlapping these bands. Excess charge may be stored in these states, producing a field which gives rise to energy band bending inside the crystal near the surface, and in a direction determined by the details of the semiconductor and its surface structure(74).

The application of an external field will then result in the behaviour shown in figure (13). First of all further charge will be induced into unoccupied surface states; this tends to peg the Fermi level and effectively shield the semiconductor interior from field penetration until the density of available surface states drops appreciably. Field emission will then be possible from the valence band or the Boltzmann tail of electrons in the conduction band, again depending on the semiconductor details (band gap, Fermi level position, etc.,). Therefore, two peaks may be observed in the F.E.E.D. separated by the forbidden energy gap of the semiconductor, as illustrated in figure (13a). As the remaining surface states fill, the Fermi level at the surface will move relative to the energy bands in order to maintain electron thermodynamic equilibrium and field penetration will occur bending the energy bands down. This is shown in figure (13b), where both peaks now move to lower energies with respect to the Fermi level as the applied field is increased. If the field is great enough to pull the conduction band edge below the Fermi level the conduction band will become degenerate, i.e. electrons here will obey Fermi-Dirac instead of Boltzmann statistics. Field emission will probably be enhanced at this point, the major contribution to the F.E.E.D. being from the conduction band with a maximum at the Fermi level, as shown in figure (13c). The peak at the Fermi level should be "metal like", i.e. not shifting with further increase in field, though the valence band peak may shift slightly.

In addition to the above effects the Fermi level throughout the semiconductor will be distorted due to the potential dropped across the bulk resistance as the field emission current starts to flow. Also a further shift in surface Fermi level with respect to

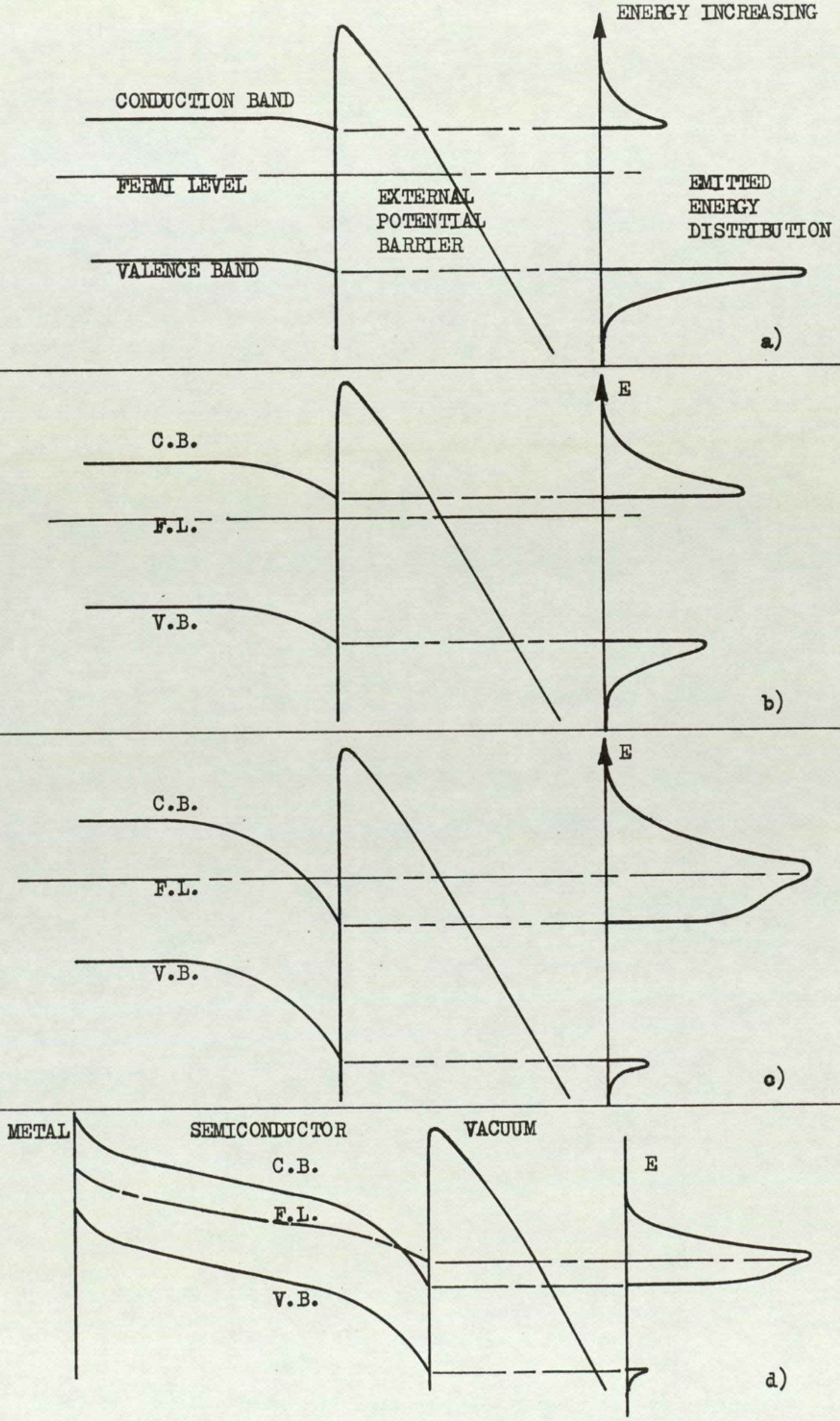

FIG. 13. STAGES IN THE F.E.E.D. FROM AN IDEALISED SEMICONDUCTOR AS THE APPLIED FIELD IS RAISED.

the directly measurable Fermi level of the metal substrate will result from band bending at the metal-semiconductor interface. This arrises from differences in the work functions of the two materials, which requires electrons to be transferred across the interface before the external field is applied in order to achieve thermodynamic equilibrium. Charge will be accumulated in the semiconductor with a sign depending on direction of electron transfer, which in turn depends on which work function is the greater. This process is further modified by the presence of "surface states" which tend to peg the Fermi level here just as at the semiconductor surface. Any of the F.E.E.D's in the previous cases (13 a-c) will thus include shifts due to both these factors, i.e. as shown in figure (13d), although the exact details for a particular semiconductor will vary. For instance, the applied field may be high enough to saturate the surface states before being high enough for field emission.

Stratton (71,72) also predicted the current-voltage charateristic to be expected from his assumptions : at low fields, emission occurs from the valence band, while at high fields emission from the conduction band predominates, both cases giving essentially linear F.N. plots. For the intermediate field case however, the current should increase much more rapidly as the conduction band population increases. Agreement between this theory and experimental current - voltage measurements was rather poor, in particular the mid-field current increase was not observed. Baskin et al.(75) then proposed that the current could be restricted by a low arrival rate of carriers at the surface due to a low conductivity depletion region just within a P type surface, or because of a low carrier concentration in the bulk of an N type semiconductor. Numerical calculations then gave qualitative agreement with experiment although the saturation currents were now smaller than expected.

Further experimental work on F.E.E.D's from semiconductors by Lewis & Fischer (76) using silicon , by Arthur (77) on germanium, Hughes & White (78) on gallium arsenide and Salmon & Braun (79) on cadmium sulphide, then showed the observed distributions to be wider and of a different shape to those predicted in Strattons theory.

The next step was taken by Modinos (80), who included emission from surface states by extending a model of the semi-conductor surface proposed by Handler (81). A uniformly dense band of surface states was proposed which extended right across the band gap and into the valence and conduction bands. An F.N. type barrier then operates on the resulting density of states function to give expression for the emission current and energy distribution. Two unknown parameters appear in these expressions; the shift of the electrostatic potential at the surface relative to its bulk value, and the surface quasi-Fermi level appropriate to the applied field. Poissons equation at the surface, together with an equation representing the replenishment of surface states from the valence and conduction bands, can then be solved to eliminate the two unknowns and give the energy distribution in terms of the semiconductor parameters as before.

Calculations by Modinos have given the F.E.E.D. for N type, P type and intrinsic germanium at 300K and for three values of external field. The intrinsic distribution is shown in figure (14); the F.E.E.D for both the types of doped germanium are almost the same as this, although the valence band edges are in different positions. This theory now predicts that for low current densities ($<10^6$ Am $^{-2}$) electrons are mainly emitted from surface states and the valence band, with an energy shift away from the Fermi level towards lower energies as the field increases. Emission from both the valence and conduction

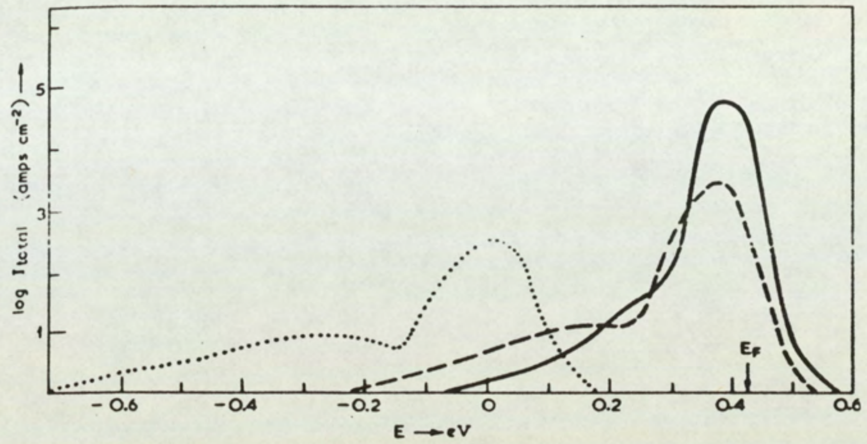

Fig. 8. Total energy distributions for $u_b = 4$. The values of the parameters are: $N_0 = 10^{14}$ eV^{-1} cm^{-2}, $E_0 = 0.05$ eV, $S = 10^{-16}$ cm^2, $\theta = 0.01$ Å^{-1}.

Solid line: $F = 0.2$ V/Å, $V_s = -14\,kT$, $E_F - F_t < kT$, $I_c = 1.9 \times 10^{-12}$ A cm^{-2}, $I_s = 1.77 \times 10^{-3}$ A cm^{-2}, $I_v = 9.98 \times 10^{-4}$ A cm^{-2}, $\log I_{total} = -2.56$.

Broken line: $F = 0.3$ V/Å, $V_s = -11.5\,kT$, $E_F - F_t < kT$, $I_c = 1.36 \times 10^{-8}$ A cm^{-2}, $I_s = 10.1$ A cm^{-2}, $I_v = 7.04$ A cm^{-2}, $\log I_{total} = 1.23$.

Dotted line $F = 0.4$ V/Å, $V_s = 4\,kT$, $E_F - F_t = 13.75\,kT$, $I_c = 1.78$ A cm^{-2}, $I_s = 7.64 \times 10^2$ A cm^{-2}, $I_v = 6.98 \times 10^2$ A cm^{-2}, $\log I_{total} = 3.169$.

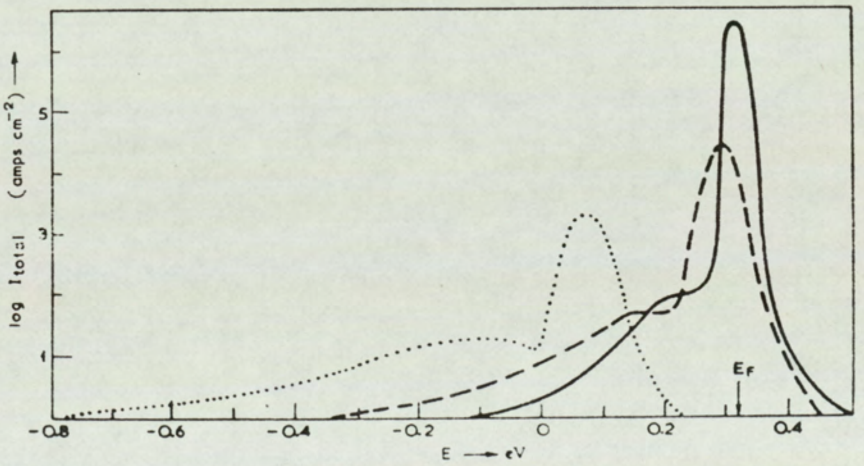

Fig. 9. Total energy distribution for $u_b = 0$. The values of the parameters are: $N_0 = 2 \times 10^{14}$ eV^{-1} cm^{-2}, $E_0 = -0.05$ eV, $S = 10^{-16}$ cm^2 and $\theta = 0.01$ Å^{-1}.

Solid line: $F = 0.2$ V/Å, $V_s = -12.5\,kT$, $E_F - F_t < kT$, $I_c = 1.56 \times 10^{-13}$ A cm^{-2}, $I_s = 1.11 \times 10^{-3}$ A cm^{-2}, $I_v = 9.02 \times 10^{-4}$ A cm^{-2}, $\log I_{total} = -2.698$.

Broken line: $F = 0.3$ V/Å, $V_s = -11.5\,kT$, $E_F - F_t < kT$, $I_c = 2.5 \times 10^{-10}$ A cm^{-2}, $I_s = 5.7$ A cm^{-2}, $I_v = 6.9$ A cm^{-2}, $\log I_{total} = 1.1$.

Dotted line: $F = 0.4$ V/Å, $V_s = -2.5\,kT$, $E_F - F_t = 7.75\,kT$, $I_c = 4.9 \times 10^{-5}$ A cm^{-2}, $I_s = 5.05 \times 10^2$ A cm^{-2}, $I_v = 6.97 \times 10^2$ A cm^{-2}, $\log I_{total} = 3.08$.

FIG 14. THE ENERGY DISTRIBUTION FROM INTRINSIC GERMANIUM. from Modinos (80).

bands increases with field but the conduction band emission is not observable in linear F.E.E.D's. for current densities $<10^7 Am^{-2}$; at higher densities degeneracy sets in making the theory inapplicable. The theory has been tested against the experimental work of Arthur(77) and Shepherd & Peria (82) on germanium, Sykes & Braun (83) on lead telluride and Richon (84) using zinc oxide, who found reasonable agreement. Significant shifts in the F.E.E.D from the Fermi level with increasing field were not noted however, possibly due to the fairly low current densities used.

3.4. Field Emmision Through Adsorbates.

Any surface not specifically cleaned will be covered by adsorbed gas atoms or molecules. In particular, field emitting tips whether deliberately manufactured or produced unintentionally on a broad area cathode will have their energy distributions considerably modified by such gas coverage; see for example Duke & Alferieft (85). Adsorbed gas atoms not only produce changes in the real work function by altering the surface barrier height, but also change the effective barrier thickness due to the presence of the adatom's attractive potential well. Electron tunnelling probabilities could thus change drastically, affecting both the F.N. plots and the energy spectra, even though the thermodynamic work function might remain constant. Quantum mechanical double-barrier potential theory (86) indicates that barrier penetration is enhanced if a tunnelling electron has the same energy as an allowed state of the potential well situated between the two barriers. Referring to figure (15), assuming a square adatom potential well with a vertual energy state near the Fermi level, electrons can then tunnel directly from a metal state to a vacuum state or go via the resonance atomic state. The resonance route is favoured because of the reduction in total barrier thickness, which then means the W.K.B phase integral used to claculate the electron transmission probability will give en enhanced transmission function. Thus F.E.E.D's will display fine structure associated with electrons tunnelling via the adatom energy levels.

Various adsorbates have been used at monolayer levels of coverage on tungsten tips to check this theory, these include hydrogen, oxygen, krypton, germanium and alkaline earth metals(58); the data being presented in terms of an enhanced resonance factor R, defined as the ratio of the electron tunnelling probabilities with and without the adatom potential well. The results for single barium atoms is pre - sented in figure (16) as reported by Plummer & Young (87) for adsorption on the (111) plane of tungsten. Plummer & Bell (61) and Swanson & Crouser (88) have also shown inelastic scattering of tunnelling electrons by polyatomic adsorbates, where the weak energy losses were attributed to W-H_2 vibrational modes excited by field emmitted electrons. An electrstatic deflection spectrometer coupled to a multichannel analyser was used here to give the high signal noise ratio necessary for the detection of these small effects. Several interesting effects have also been observed, by Swanson & Crouser (88), in the F.E.E.D. of large molecules (anthracene, pentacene and phthalocyanine) adsorbed onto various faces of tungsten or molybdenum crystals. Observations were restricted to those parts of the field emission pattern on the anode known to result from molecular adsorption, in the hope that F.E.E.D. structure could be interpreted as either resonance tunnelling or inelastic excitation of vibrational or electronic states within the molecule. In this context resonance tunnelling energy shifts Ea are given by $Ea = Eo - eFx$ where Eo is the zero shift, F the electric field and x is of the order of the molecule-substrate separation: vibrational levels on the other hand tend not to shift with field and electronic excitational shifts remain un - determined. A set of distributions for phthalocyainine adsorbed on the

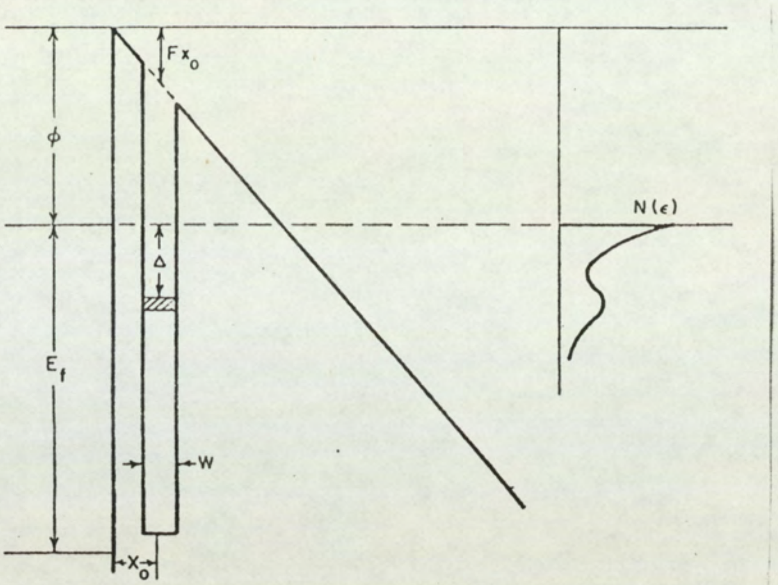

FIG 15. POTENTIAL ENERGY DIAGRAM FOR TUNNELLING RESONANCE EMISSION.

Experimental enhancement factor for single Ba atoms on the (111) plane of tungsten. The three lower curves represent cases where adsorption of electronegative gases was observed before the Ba atom arrived. The shift in the narrow peaks with field was $\Delta E/e\Delta F = 1.3 \pm 0.3$ Å, while the peak separation was 0.29 ± 0.01 eV where $\epsilon = E - E_F$.

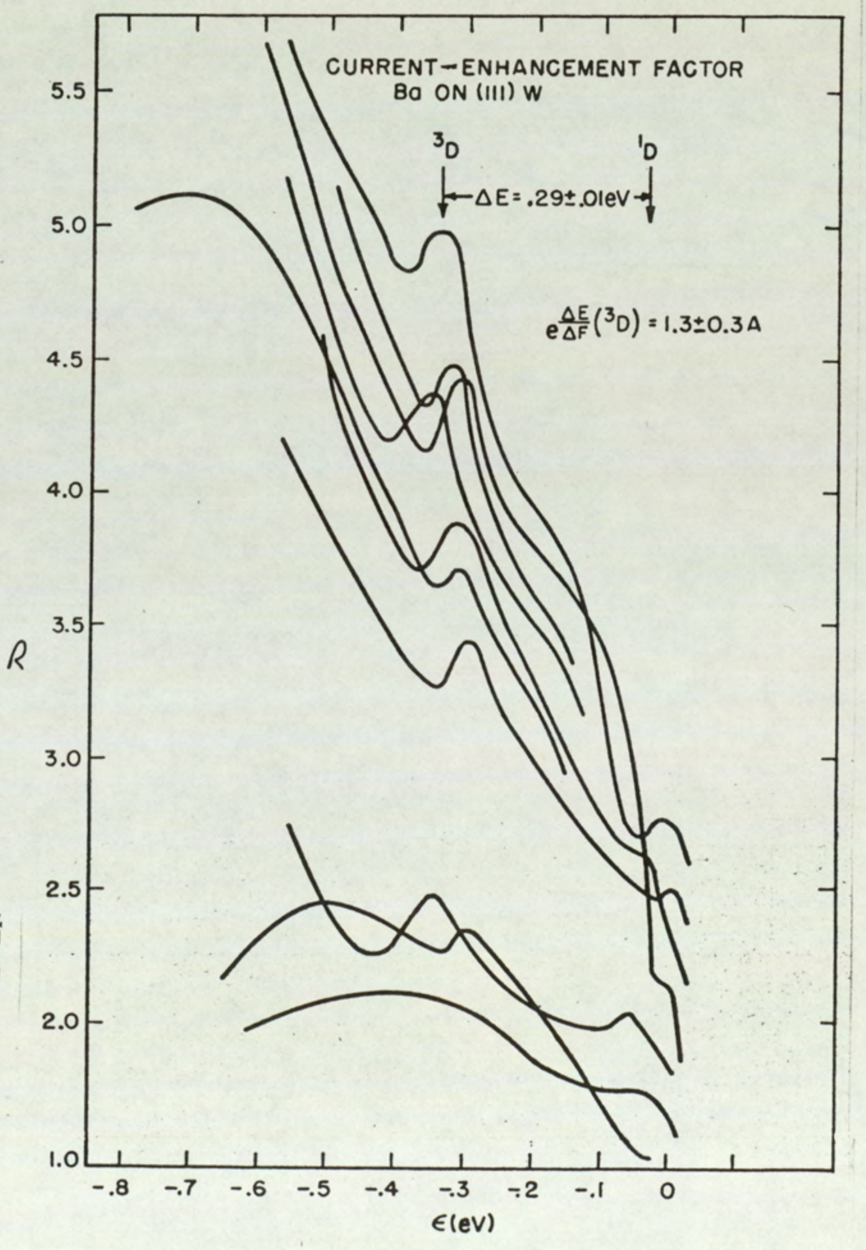

FIG 16. EXPERIMENTAL ENHANCEMENT FACTOR, ADSORBED Ba ATOMS ON W. from Plummer & Young (87).

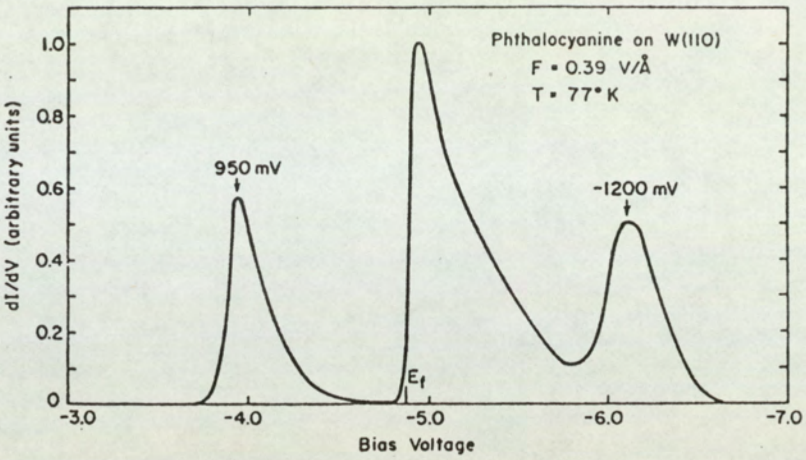

TED spectra phthalocyanine on W (110); $I_a/I_c = 540$.
Note the peak 950 mV above the Fermi level.

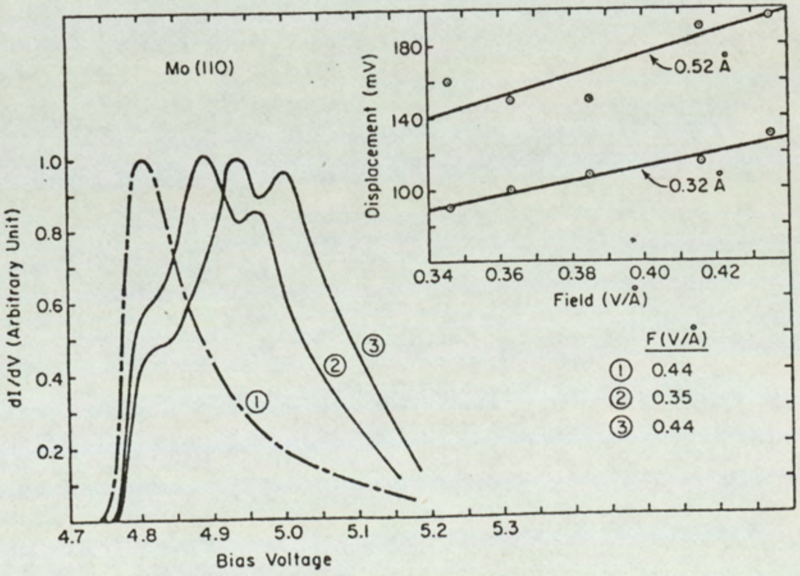

TED spectra for phthalocyanine on Mo (110); $I_a/I_c = 27$; curve 1 is clean TED.

FIG 17. ENERGY DISTRIBUTIONS FOR ADSORBED PHTHALOCYANINE ON TUNGSTEN & MOLYBDENUM. from Swanson & Crouser (88).

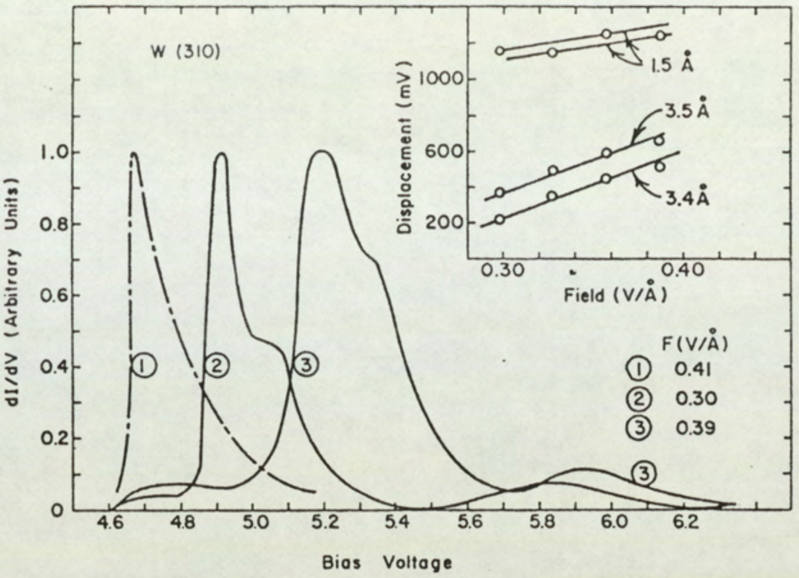

TED spectra pentacene on W (310); curve 1 is clean, $\Delta\phi = -1.7$ eV, $B = 2.0$; $I_a/I_c = 680$.

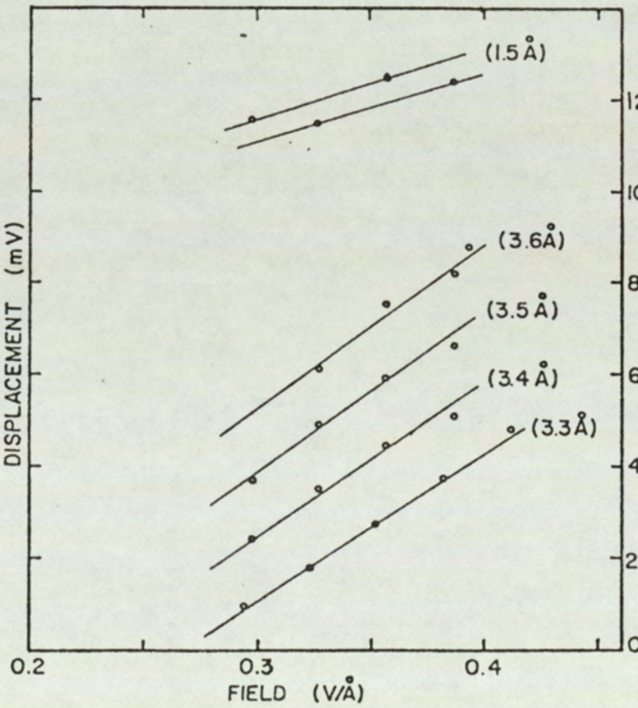

Summary of peak displacements versus field strength for pentacene on W (310); numbers in parenthesis are the slopes.

FIG 18. ENERGY DISTRIBUTIONS & PEAK DISPLACEMENTS WITH FIELD FOR PENTACENE ON TUNGSTEN. from Swanson & Crouser (88).

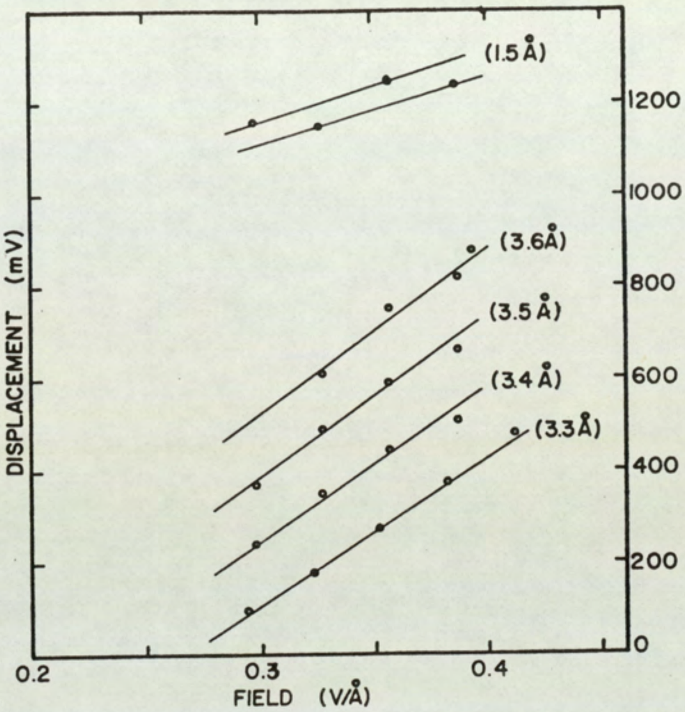

Fig. 21. Summary of peak displacements versus field strength for pentacene on W (310); numbers in parenthesis are the slopes.

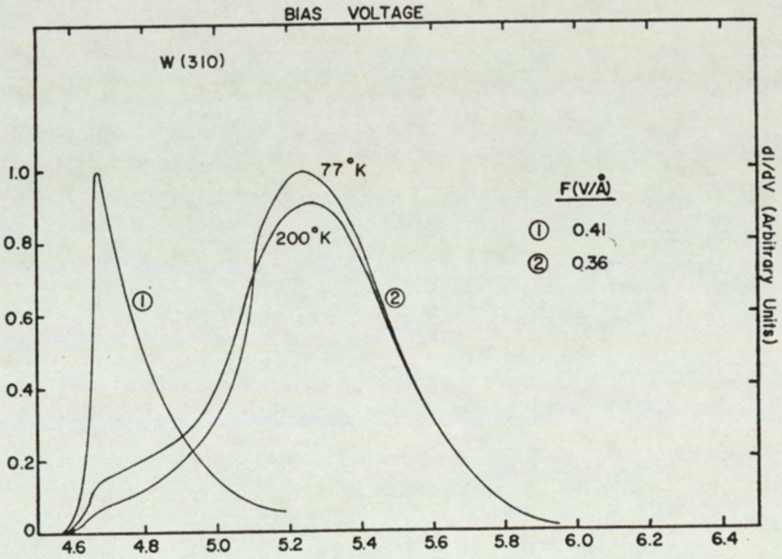

Fig. 22. TED spectra pentacene on W (310); curve 1 is clean; $\Delta\phi = -0.65$ eV; $B = -0.6$; $I_a/I_c = 5.7$. The TED is shown at 77 and 200°K.

FIG 19. PEAK DISPLACEMENTS WITH FIELD & ENERGY DISTRIBUTIONS FOR PENTACENE ON TUNGSTEN. from Swanson & Crouser (88).

(110) plane of molybdenum are shown in figure (17) where the inset gives the shifts of the peaks with field. These molecules are ~ 10 Å square hence the slope of the field effect is too small to be produced by resonance tunnelling, but could well be due to vibrational excitation. However, results for pentacene molecules, measuring 4 Å by 12 Å, suggest that resonance tunnelling is an important feature although electron-electron scattering cannot be ruled out, as shown in figure (18). An important point to note, especially when considering emission from broad area electrodes is that all the peak shifts on the F.E.E.D's through adsorbates are a linear function of applied field, as illustrated in figure (19). Further work by Swanson & Crouser indicate that the reproducibility of some of their data on other molecules was not all that good. They point out for example that it was difficult to position the probe hole over a single molecular spot, so that the resulting F.E.E.D. contained information from two molecules with different steric conformations. Also, changes in the adsorbate-substrate configuration could be brought about by thermal or field induced phenomena, thus affecting the energy distribution, while coupling between the many possible tunnelling mechanisms was difficult to handle theoretically.

3.5. T.F. Temperature Assisted Field Emission.

So far consideration has essentially been restricted to low temperature - high field electron emission, that is for $T < 300K$, where electrons in metals have on average only a small increase in energy above the Fermi level, or where only few states in an intrinsic semiconductor's conduction band are occupied. Under these conditions emission at 0K is described by the F.N. equation given earlier, and restated here in terms of the electron parameters

$$J\ (F,0) = \frac{e^2}{16\pi^2\ \hbar}\ \frac{F^2}{\phi\ t(y)}\ \mathrm{EXP}\left[\frac{-4\ (2\ em)^{\frac{1}{2}}\ \phi^{\frac{3}{2}}\ V\ (y)}{3\ \hbar\qquad F}\right] \qquad (14)$$

For slightly higher temperatures this was modified by Murphy & Good (89) to the expression

$$J\ (F,T) = J\ (F,0)\ \frac{\pi kT/d}{\sin \pi kT/d} \qquad (15)$$

on the assumption that essentially the same energy distribution applies. The limits of applicability of this equation are given by Good & Muller (45) as $d > kT$, where k is Boltzmann's constant, T the temperature and d is given by

$$d = \frac{he\ F}{(8em\phi)^{\frac{1}{2}}}\ \frac{1}{t(y)} \qquad (16)$$

with the parameters as defined previously, (N.B ϕ is in eV). For the usual operating conditions, and with the function $t \sim 1$, this limit reduces to $F > 8{\cdot}83 \times 10^5\ \phi^{\frac{1}{2}}\ T$. If now T is set equal to room temperature and $\phi = 4{\cdot}5$ eV, the lower limit for F is $5{\cdot}6 \times 10^8\ Vm^{-1}$, values as low as this are not usually encountered when using microtips. However, prebreakdown emission from broad surfaces is usually in the field range 10^7 to $2 \times 10^8\ Vm^{-1}$ even assuming reasonable β factors, i.e. < 50 which can easily be envisaged as due to surface roughness, hence straight forward "cold" emission theory would seem not to apply.

At the other extreme of high temperature and low field, electron emission is described by the well known thermionic equation due to Richardson (90)

$$J\ (\ 0,T\ ) = \frac{4\pi me}{h^3}\ k^2\ T^2\ \mathrm{EXP}\left[-\ \frac{e\ \phi}{kT}\right] \qquad (17)$$

where the pre-function constant is $1.2 \times 10^{6}\ \mathrm{AK^{-2}m^{-2}}$ for electrons having their free space mass value. This equation can be derived by making use of similar expressions for the free electron supply function to those used in the F.N. derivation, but with appropriate simplifications for high temperature - low field conditions and assuming that all emitted electrons go over the potential barrier. At slightly higher fields this must be corrected as in F.N. theory to include the Schottky (44) barrier height reduction, after which one obtains

$$J\ (F,T) = \frac{4\pi me}{h^3}\ \frac{\pi g}{\mathrm{Sin}\,\pi g}\quad k^2\ T^2\ \mathrm{EXP}\left[\frac{-e}{kT}\left(\phi - \sqrt{\frac{e\ F}{4\pi\mathcal{E}_0}}\right)\right] \qquad (18)$$

where $\mathcal{E}_0$ is the permitivity of free space and Murphy & Good (89) give

$$g = h\ e^{\frac{1}{4}}\ F^{\frac{3}{4}} \Big/ m^{\frac{1}{2}}\pi\,k\ T \qquad (19)$$

The limits to "thermionic" emission are then given by the two rather involved expressions below

$$\ln\left(\frac{1-g}{g}\right) - \frac{1}{g(1-g)} > \frac{-e}{g}\left(\phi - \sqrt{\frac{e\ F}{4\pi\mathcal{E}_0}}\right)\frac{1}{kT} \qquad (20)$$

$$\ln\left(\frac{1-g}{g}\right) - \frac{1}{1-g} > \frac{-\pi\,m^{\frac{1}{4}}\ e^{\frac{5}{8}}\ F^{\frac{1}{8}}}{h^{\frac{1}{2}}} \qquad (21)$$

These equations are presented in the form of a graph in figure (20), from which it will be seen that thermionic emission starts to occur to the upper left of the diagonal line and that the field range used in broad area emission (for reasonable β) is well to the left near the axis. Hence for even a moderate rise in electron temperature thermionic behaviour could well predominate. When g is so small that $\pi g \,/\, \mathrm{Sin}\,\pi g$ can be replaced by one the emission equation becomes Richardson - Schottky formula; the thermionic region is always bounded by the $g = 1$ line and the melting temperature of the material.

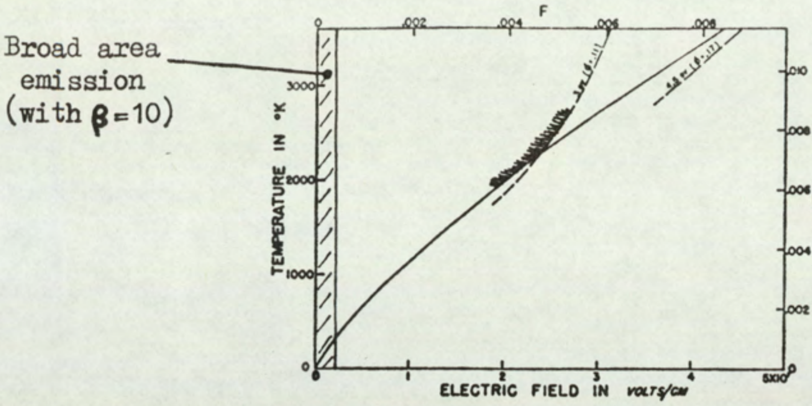

Boundaries of the thermionic emission region as given by Eq. (20), the broken lines, and by Eq. (21), the solid line. For a work function of 3 ev, the region extends from the temperature axis out to the first line encountered as indicated by the shading. For work functions of 4.5 ev and higher, the corresponding broken line lies below the solid line at these temperatures and the region extends from the temperature axis out to the solid line.

FIG 20. BOUNDARIES TO THE THERMIONIC EMISSION REGION. according to Murphy & Good (89).

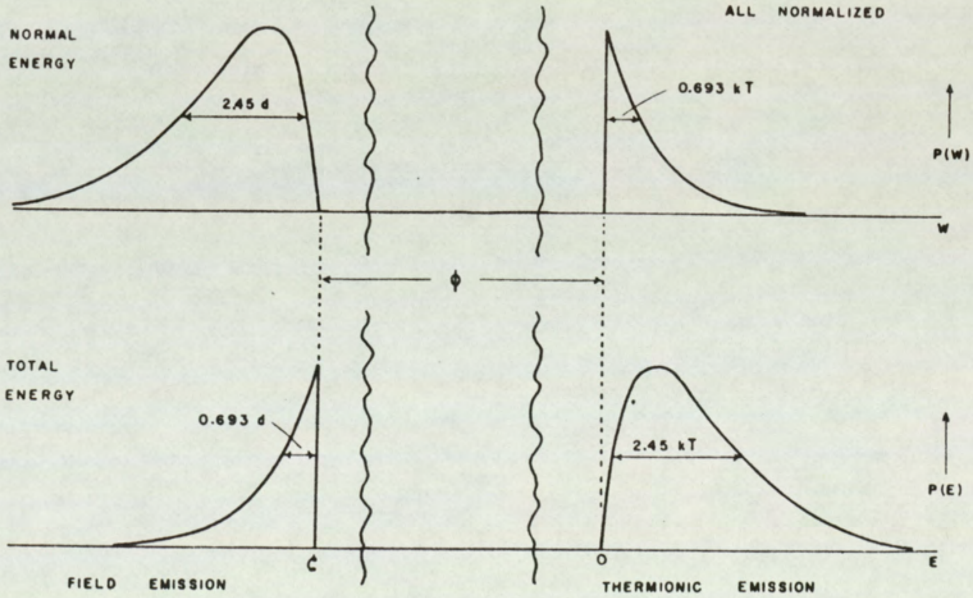

FIG 21. FIELD EMISSION & THERMIONIC EMISSION - TOTAL & NORMAL ENERGY DISTRIBUTIONS. from Young (59).

The thermionic energy distribution will extend from the top of the potential barrier tailing off exponentially with higher energies as the Fermi-Dirac supply function decreases. The total energy distribution for thermionically emitted electrons is given by Young (59) when ϕ is expressed in eV as

$$P\ (E)dE = \frac{4\pi m}{h^3} E\ \mathrm{EXP}\left[\frac{-E-\phi e}{kT}\right] \qquad (22)$$

where as for comparison the normal energy distribution is

$$P\ (W)\ dW = \frac{4\pi m}{h^3} kT\ \mathrm{EXP}\left[\frac{-W-\phi e}{kT}\right] \qquad (23)$$

Young has also shown that a remarkable mirror symetry exists between the zero temperature field emission and the zero field thermionic emission approximations when $d = kT$ as shown in figure (21). This extends even to the values for the half widths of the two sets of energy distributions.

A considerable region of the temperature field plane is still not covered by the above equations; in fact this is a particularly difficult area where analytical results are hard to come by. However, Murphy & Good (89) in their general T.F. treatment did identify an intermediate solution to the integrals involved in their derivation to obtain the following expression for the emitted current density

$$J\ (F,T) = \frac{e^2\ m^{\frac{1}{2}}}{2\pi\hbar^2}\left(\frac{kT}{2\pi}\right)^{\frac{1}{2}} t(y)^{\frac{1}{2}} F\ \mathrm{EXP}\left[\frac{-\phi}{kT} + \frac{\hbar^2 e^2\ F^2}{24m(kT)^3}\theta(y)\right] \qquad (24)$$

$$\text{where}\quad \theta(y) = \frac{3}{t^2(y)} - \frac{2\ v(y)}{t^3(y)} \sim 3 - 2v(y) \qquad (25)$$

The boundaries of this and the other emission equations are shown in figure (22) with representative energy distributions for the marked boundary points shown on figure (23). Expressions for the total

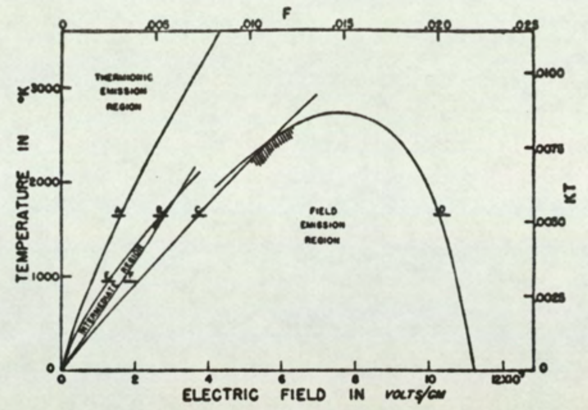

The three emission regions for a 4.5 ev work function ($\phi = 0.17$). The letters *A* to *F* indicate boundary points for which the approximate and exact energy distributions are given in Fig. 23 The points *A* to *D* are at 1700°K and *E* and *F* are at 1000°K. The values of the fields in volts/cm are as follows: *A*, 1.50; *B*, 2.50; *C*, 3.82; *D*, 10.26; *E*, 1.35; *F*, 1.74; all times 10^7.

FIG 22. BOUNDARIES TO THE THREE EMISSION REGIONS. from Murphy & Good (89).

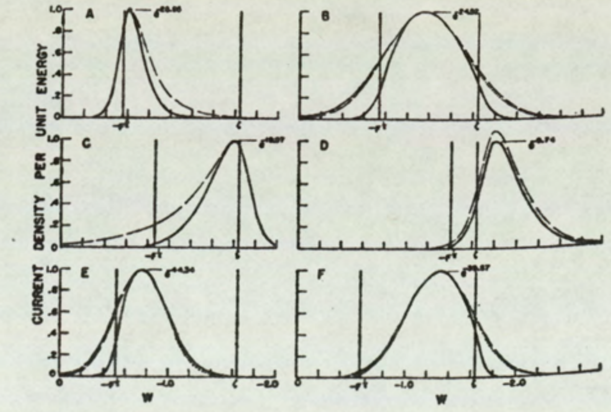

Energy distributions of the emitted current density for the six special values of temperature and field indicated in Fig. 22 and a work function of 4.5 ev ($\phi = 0.17$). The solid lines are the exact distributions according to Eq. (20). The broken lines are the approximate distributions according to Eqs. (25), (54), and (59). The dotted lines are the approximate distributions after furthermore applying the saddle-point method. The energy increases to the left. The energy at the peak of the potential $-F^{\frac{1}{2}}$ and the Fermi energy ζ are indicated by solid vertical lines. The curves are normalized to unit peak value and the actual peak values in Hartree units are given on the diagrams.

FIG 23. ENERGY DISTRIBUTIONS FOR THE PIONTS MARKED A,B,C,D,E & F IN FIG 22. from Murphy & Good (89).

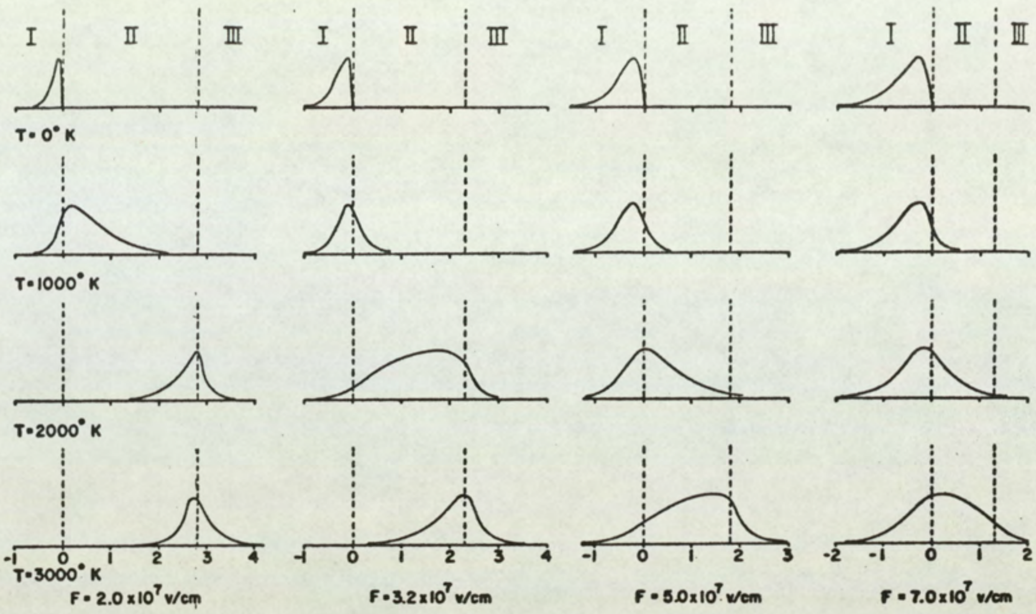

Theoretical energy distributions for emitted electrons at indicated fields and temperatures, for $\phi = 4.5$ ev, with amplitudes arbitrarily normalized to a common maximum; abscissas ϵ in ev relative to the top Fermi level at 0. Regions I, II, and III correspond to those in Fig.

FIG 24. ELECTRON ENERGY DISTRIBUTIONS AT VARIOUS FIELDS & TEMPERATURES. from Dolan & Dyke (91,92).

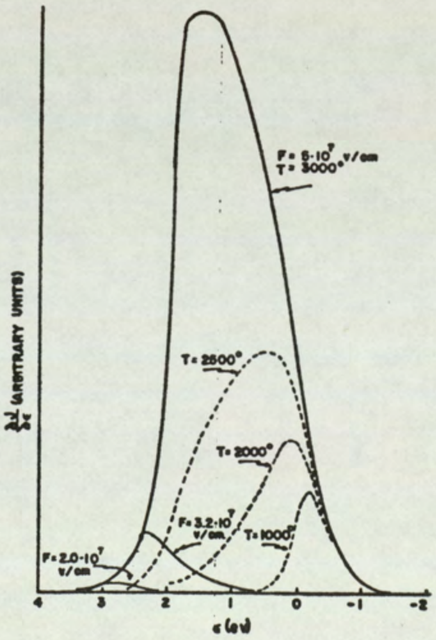

Energy distributions for emitted electrons with $\phi = 4.5$ ev and at various fields for a constant temperature $T = 3000$°K (solid curves); a constant field of 5×10^7 v/cm at various temperatures (dashed curves).

FIG 25. ELECTRON ENERGY DISTRIBUTIONS AT CONSTANT TEMPERATURE & AT CONSTANT FIELD. from Dolan & Dyke (91,92).

energy distributions in the T.F. region are equally unwieldy and difficult to handle without approximations, especially when an expression for the F.W.H.M. is required. Thus recourse is made to numerical methods and graphical plots. For example, Dolan & Dyke(91,92) have computed T.F. energy distributions, shown here in figures(24&25), where it can clearly be seen how increasing the temperature tends to move the distribution away from the Fermi level towards higher energy where finally it "sits" around the top of the potential barrier. This is a particularly marked effect at lower fields, although in figure (24) all amplitudes have been normalised and as a result disguise the actual process; figure (25) gives a better picture. At very high temperatures and fields none of the above analytic approximations are valid and the recent tabulated data Christoff (93) has to be used.

3.6. Hot Electron Emission Processes

Under certain circumstances the non-bonding electrons in a material, particularly semiconductors and insulators, can become "Hot", that is they can acquire random energy considerably in excess of that for equilibrium with the crystal lattice. This state can be quantified by an electron temperature which may be very high even though the lattice is quite cold. It then follows that emission of these electrons would be determined as much by the excess temperature as by the applied fields. An analysis of this situation for the case of the semiconductor (SiO_2 + C) has been given by Zhdan et.al. (94), who assumed a free electron F.N. type model with Maxwell-Boltzmann statistics describing electrons in the conduction band and the electron temperature being an unknown function of semiconductor field penetration. Estimates of the electron temperature θ were made from experimentally measured electron energy distributions by assuming that transmission was over the surface potential barrier,

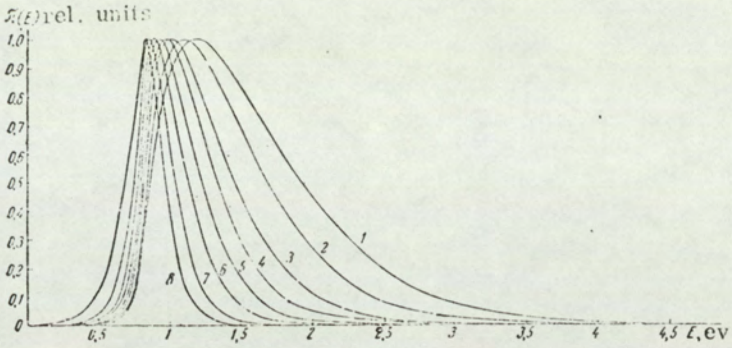

Total energy distribution of field electrons for semiconductors (theory), $F = 5.4 \cdot 10^6$ v/cm, $\chi_0 = 1.5$ ev):

1 - $\Theta = 5000°K$; 2 - $\Theta = 4000°K$; 3 - $\Theta = 3000°K$; 4 - $\Theta = 2500°K$; 5 - $\Theta = 2000°K$; 6 - $\Theta = 1600°K$; 7 - $\Theta = 1200°K$; 8 - $\Theta = 900°K$

FIG 26. ELECTRON ENERGY DISTRIBUTIONS FOR DECREASING INTERNAL FIELD & HENCE DECREASING "HOT ELECTRON" TEMPERATURE θ. from Zhdan et.al.(94).

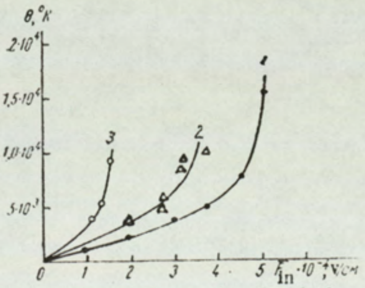

Dependence of electron temperature Θ on the value of the average internal field F_{in} in the semiconductor layer of the emitter for emitters No. 15 (curve 1), No. 25 (curve 2) and No. 4 (curve 3).

FIG 27. GRAPH OF ELECTRON TEMPERATURE AGAINST AVERAGE INTERNAL FIELD. from Zhdan et.al.(94).

and using the measured field-dependent spectral F.W.H.M. in the thermionic relation F.W.H.M. = 2.45 kθ. Their theoretical normalised energy distributions are presented in figures (26) whilst a plot of the "measured" electron temperature (θ) against internal field is shown in figure (27). As can be seen the relationship starts in a quite linear manner but then becomes very steep at $\theta \sim 5000$K. However, the actual curve depends on the particular emitter being considered where one example gave the very high temperature of 15000K for a modest penetrating field.

3.7. Emission from Broad Areas.

Emission from broad area electrodes has been shown in chapter 2 to follow an F.N. relationship only approximately, and typical results predict very unrealistic values of the field enhancing β factor. The metallic model of emission is made even more unlikely when the electron energy distribution is examined. Measurements of F.E.E.D's from broad area electrodes were first obtained by Allen & Latham (42) using ultra high vacuum conditions and the high resolution spectrometer described in chapter 5. Preliminary findings indicated three important differences in typical spectra from sites on copper electrodes compared to those from a reference tungsten microtip. Referring to figure (28) these are :

a) all electrons are emitted from states well below the bulk metal Fermi level;

b) the half width (F.W.H.M.) is considerably greater than for metallic emission processes;

c) the spectrum is more symmetrical, i.e. lacking the sharp high energy edge which characterises metallic F.E.E.D's. In fact broad area energy distributions resemble more closely those from semi - conducting tips. This led to an early model (42) explaining these results in terms of very localised semiconducting impurities

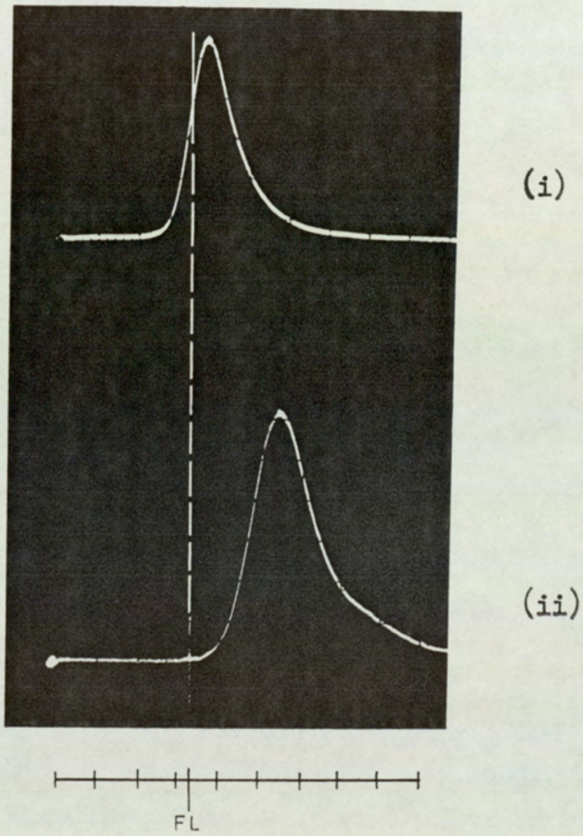

Electron energy spectrum obtained from (i) a reference tungsten emitter and (ii) a site on a broad-area copper cathode. The position of the Fermi level (FL) of each emitter is also shown. Electron energy in eV, 0·2 eV/div, is *x* axis (going from high energy to low energy left to right). Electron current per unit energy is *y* axis.

FIG 28. ELECTRON ENERGY DISTRIBUTIONS FROM A TUNGSTEN EMITTER & FROM A BROAD AREA SITE. from Allen & Latham (42).

embedded in the electrode surface. However, further work by Latham and his co-workers (95,43), particularly Athwall (96), has uncovered a considerable variety of emission effects. These include: many peaked and variable distributions, switching phenomena, very non linear F.N. plots and very non linear F.E.E.D. shifts with applied field all of which the simple semiconducting model cannot explain. Most of these effects have been explained and correlated by the work reported here using a modelbased on the emission of hot electrons from a semiconducting or insulating impurity. This hot electron emission model and its predecessors are explained in the next and subsequent chapters.

CHAPTER 4.

NON-METALLIC FIELD ELECTRON EMISSION MODELS AND CONDUCTION PHENOMENA IN THIN"INSULATING" FILMS.

From previous chapters it will be apparent that the metallic whisker model of broad area prebreakdown conduction does not satisfactorily describe the experimental data. Even the success attributed to Fowler-Nordheim theory will be shown in the following chapters to have been largely accidental, since it is extremely doubtful whether many of the published results were based on emission from single sites. When these are examined closely, each seperate source of emission current has invariably been found to give some degree of non-linearity in its associated F.N. plot. Hence no further consideration will be given to the whisker model when interpreting the present data, although it will be referred to in order to contrast it with better models.

This chapter outlines and describes the various models which have been proposed to describe conduction through "insulating" inclusions. Except for Hurley's filament model these all have at least one feature in common; this is the emission of hot electrons over the potential barrier which exists at the insulator-vacuum boundary. This proposition is necessary because the field required to obtain measurable prebreakdown currents is ordinarily too low by a factor of ~100 for barrier tunnelling to take place. The energy band diagrams used to describe electron conduction processes in insulating inclusions also bear some resemblence to each other even though the underlying mechanisms leading to these diagrams may be quite different, this is due to the necessity of providing a high surface field in the insulator to generate the hot electrons. The latter part of this chapter deals with a detailed evaluation of the electronic conduction proc -

esses in metal-insulator-metal systems, this was found necessary in order to further develope and quantify the hot electron model, which is then presented towards the end of the chapter.

4.1. An Early Band Theory Interpretation

Latham & co-workers (97,95) first developed a band theory model which interpreted early electron spectrometry results in terms of a semiconducting or insulating impurity embedded in the surface of a metal electrode, as shown in figure (29a). This was based on scanning electron microscopy experiments (27,32,98) which suggested that these micro inclusions are either oxides of the substrate metal or oxides of alien elements, which may be associated with the smelting of the substrate metal. Carbon also features strongly as an electrode contaminant and is known to accumulate at grain boundaries during the metal preparation; (99) equally it could result from electrode polishing operations when diamond paste is used.

In the absence of applied field, the idealised energy band structure would then be as in figure (29b) where the band bending at the metal-insulator interface was assumed to arise from work function differences, although no specific type of contact was mentioned. Application of a high field to the electrode surface would then result in the band structure and surface potential of figure (29c), when the field penetrates the microinclusion to the metal substrate. Electrons were then envisaged as tunnelling from the metal into the bottom of the insulator conduction band and being "heated" by 2-3 eV in the insulator bulk as a result of the penetrating field. Final emission then took place due to enhanced tunnelling through the top of the surface potential barrier by the hot electrons. To explain the second low energy peak which sometimes appeared in an electron energy spectrum,

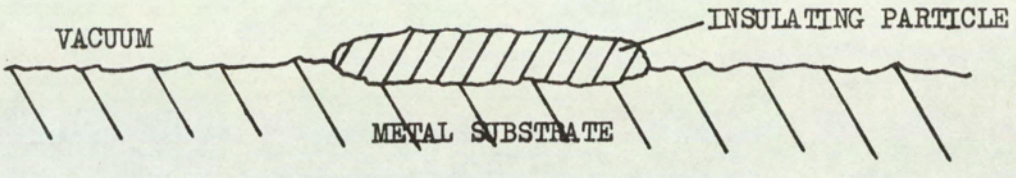

A SURFACE IMPURITY INCLUSION a)

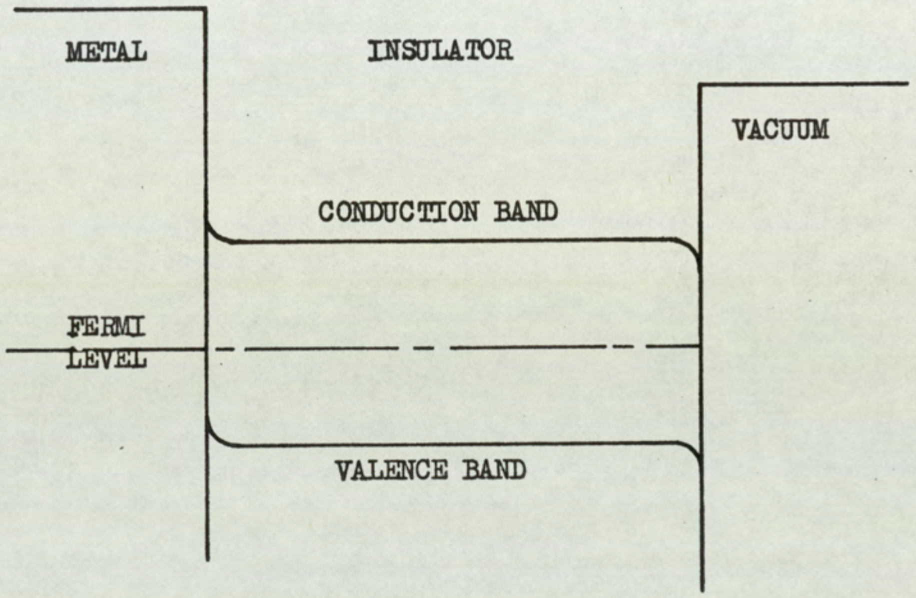

FOR ZERO APPLIED FIELD b)

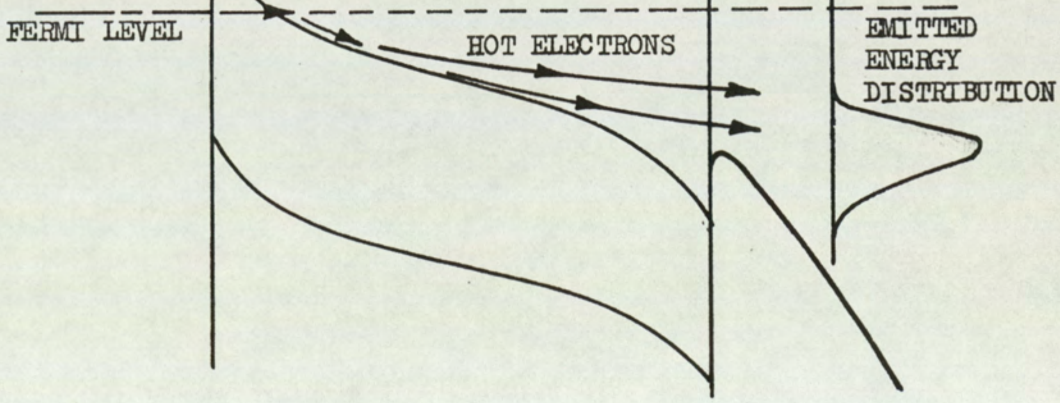

FOR A HIGH APPLIED FIELD c)

FIG.29. ENERGY BAND CONFIGURATIONS FOR A SURFACE IMPURITY INCLUSION. ACCORDING TO ALLEN et al (95).

the same authors envoked the unstable effect produced by variable surface ad-atom resonance tunnelling, as described by the model of Duke & Alferieff(85) for etched tips. It was also thought that insufficient band bending would take place at the metal-insulator contact to allow electron transfer into the insulator, so a level of interband impurity states near the bottom of the conduction band was also included in the model to facilitate this. Tunnelling electrons could then either penetrate the barrier directly or go via the energetically favoured route which included the impurity energy level.

Favourable features of this model are that a Fowler-Nordheim type I-V characteristic is maintained without having to postulate field enhancement, since the hot electrons will see a much reduced surface barrier. Also, the electron spectra will clearly be shifted below the substrate Fermi level as experimentally observed. Support for this model was further provided by Allen et al,(95) who noted that the 2-3eV acquired in the penetrating field by hot electrons was about that required to produce the electroluminescence observed by Hurley & Dooley (28).

4.2. The Filamentary Model.

An alternative explanation, based on the same impurity micro-regime as in the above model, was suggested by Hurley (41), who used the idea developed by Dearnaley (100) of electroformed conducting filaments for explaing the behaviour of some dielectric devices. Certain semiconducting and insulating materials, particularly metallic oxides, nitrides and fluorides and amorphous semiconducting glasses of nanometre to micron thickness, show a "switching" phenomena when a high field (10-100 MV/m) is applied via surface electrodes. The measured resistance may change by a factor of $\sim 10^8$ as the device changes from the non conducting "off" to the conducting "on" state. In addition, external phenomena are observed including microscopically localised electroluminescence and electron emission through thin electrodes. If the field was applied for a sufficient length of time the conducting filament became "electroformed" through the dielectric, as atoms or molecules became permantly or semi-permanantly rearranged (see Dearnaley et. al (100). Electroforming times were typically in the 1-10mS range, whereas switching times were usually $<$ 1uS. The cross sectional filament diameter was shown to vary with the length of the filaments, i.e. the film thickness, such that 40nm to 500um thick films gave filament diameters of 1nm to 50um (100,101).

Hurley's (41) emission model assumes a random distribution of surface impurity inclusions, some occurring at places where the field is locally enhanced by a factor β such as at cracks or grain boundaries. An impurity inclusion with dielectric constant ε will then have an internal electric field given by $\beta\, E/\varepsilon$ which will allow electroforming of filaments when the average field E is $\sim 10^7$ V/m and if β and ε are both about 5 to 10. Figure(30) indicates the electroformed situation; it will be seen that the filament, being essentially metal like, behaves as a whisker embedded in a dielectric which may produce sufficient field enhancement at its vacuum termination for field electron emission. Using further comparisons with the Dearnaley (102) filamentery model, Hurley supposed that high resistance spots in the electroformed filament would give rise to "hot" carriers which could then be scattered into the surrounding oxide and produce electroluminescence through impact ionisation or recombination processes, as discussed by hickmott (103). The injection of electrons from the metal substrate into the filament was assumed to ar~~r~~ise from a number of semiconductor-metal junction effects, which were also held responsible for some of the non linear F.N. plots and the shifts in the electron energy spectra which are experimentally observed.

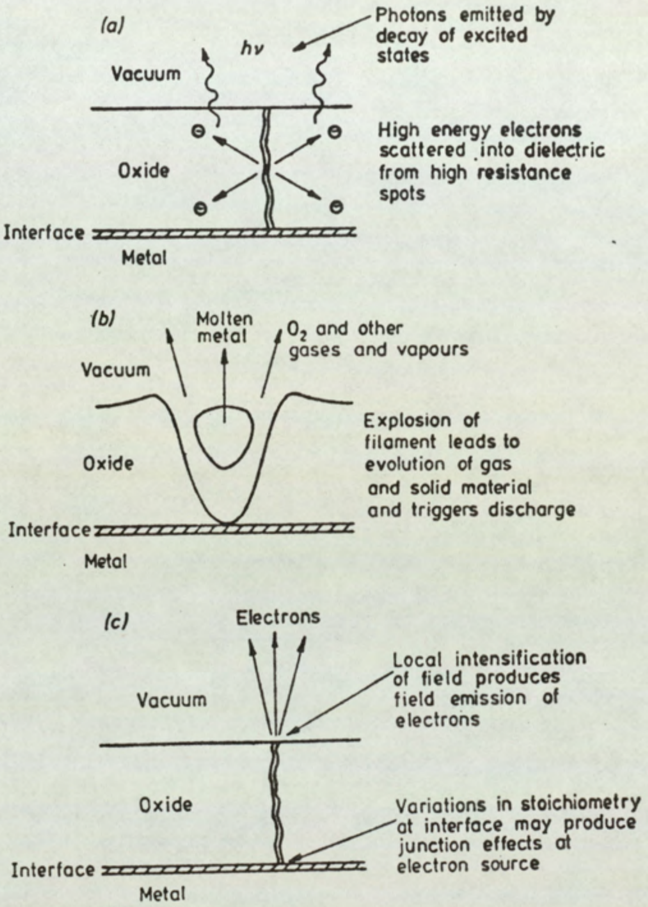

Production of electroluminescence, vacuum breakdown and electron emission from electroformed conducting filaments in oxide impurities. (*a*) Electroluminescence. (*b*) Vacuum breakdown. (*c*) Electron emission.

FIG 30. PHENOMENA WHICH MAY BE OBSERVED AS A RESULT OF THE ELECTROFORMED FILAMENT MODEL. from Hurley (41).

On the basis of this model several experimental observations can be explained. Juttner et al (104,105) demonstrated that electron emission is suppressed by "active" gases such as oxygen, carbon - monoxide and nitrogen while Hurley (41) noted that the associated electroluminescence was also suppressed by raising the ambient pressure. These effects could thus be attributed to the "poisoning" mechanism proposed by Dearnaley (102) in which absorbed gases fill the oxygen vacancies that are thought to exist in a conducting filament. Discontinuities in the I-V characteristics and marked deviation from F.N. theory could be attributed to additional filaments forming as the field was raised, or to thermal rupturing and re - forming of filaments already present. Eventual breakdown would then take place according to the thermal instability model of Cook(101) when at a certain current level, the filament temperature rose high enough to cause a molten impurity particle to be ejected into the electrode gap. Evidence for this process was reported by Hurley & Dooley(40). Current controlled "b" sites were held to be the result of filaments which either terminated short of the insulator-vacuum boundary or short of the metal-insulator junction. In both cases the emission was believed to be dependent on the metal-insulator junction, with the possibility of a reversed biased rectifying contact forming which might have exhibited negative resistance as the voltage was increased (106).

4.3. The Insulator Switching Model.

Each of the previous models is able to provide a reasonable explanation for many of the observations, but they both become very tentative and give only generalised possibilities where the experimental results are not so well explained. In particular, the energy band model does not readily explain how hot electrons are able to pass through a micron thick impurity without losing most of their energy in phonon scattering processes; it was also thought that insufficient field existed for tunnelling at the metal-insulator contact. The fiament model on the other hand offers no detailed explanation of the electron spectrometry data; it is also improbable that any filament will be thin enough to give adequate field intensification at its end without melting, since a β factor in the range 200-400 is still required for F.N. type electron emission in this case.

Athwal & Latham (43) then developed a new model to incorporate the best features of both previous models and also the new observation that emission sites usually require a lower field to maintain conduction than to initiate them. This model was based on the phenomena of Ovshinsky switching (107,108) whereby an amorphous insulator switches from low conductivity ($<10^{-7}\Omega^{-1}cm^{-1}$) to a high conductivity ($>10\Omega^{-1}cm^{-1}$) state in about lnS. Film thicknesses of 0.1 to 10um sandwiched between metal electrodes have been widely studied, requiring a potential difference of 1 to 10V across the electrodes to initiate switching. Chalcogenide glasses have been found to be the most useful materials commercially, but a large number of amorphous insulators have been investigated. (109)

Although the surface insulating impurity was assumed to be essentially amorphous so that energy band theory should strictly not be applicable, this approach is nevertheless justified if additional localised energy states are included in the energy gap. (110) Athwal & Latham applied the concepts of switching as discussed by Adler et al.(111) to modify the energy band diagram of figure (29) to that of figure (31a) where the highly distorted shape results from the superposition of the potentials due to space charges and the penetrating field, as shown in figure (31b). The space charges were seen as arising in the insulator from an excess of electrons near the vacuum

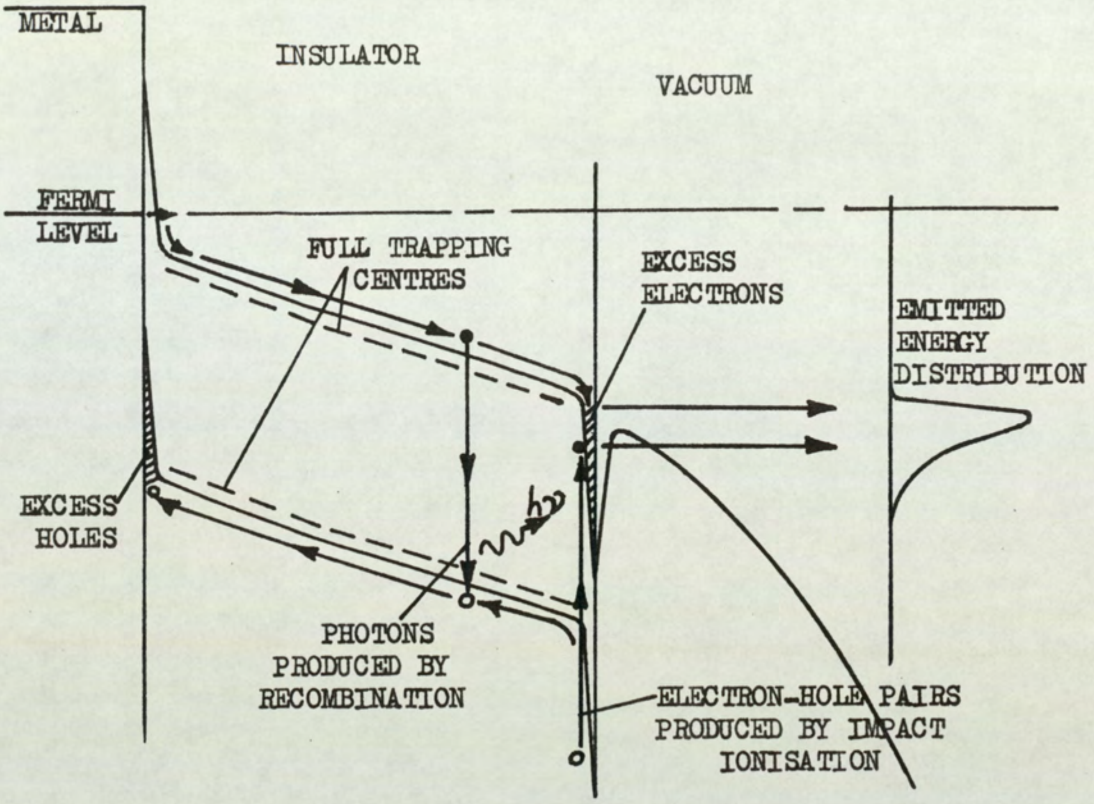

THE ENERGY BAND DIAGRAM. a)

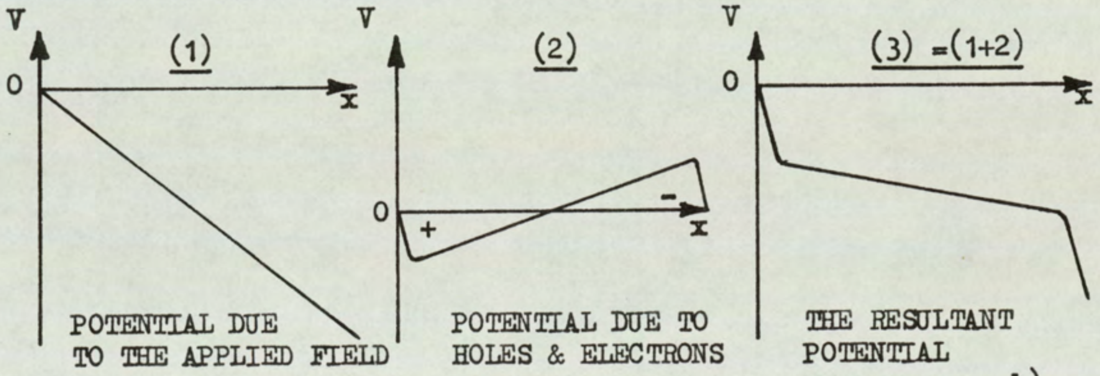

b)

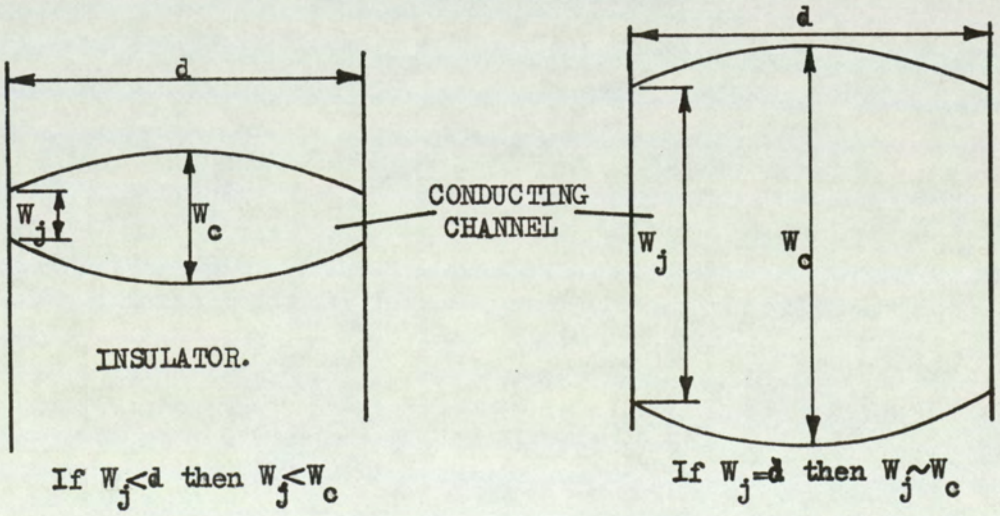

THE CONDITION FOR THE CROSS SECTIONAL WIDTH OF THE CHANNEL. c)

FIG. 31. SCHEMATIC DIAGRAMS ASSOCIATED WITH THE INSULATOR SWITCHING MODEL.

boundary and from an excess of holes close to the metal-insulator junction, in a similar manner to that envisaged in the double injection dynamic conduction model due to Mott.(112) The barrier at the metal-insulator contact would then be thin enough to allow electron tunnelling into the insulator. Rapid thermalisation, by impact with the insulator structure, enabling these electrons to cross the low field region of the insulator bulk in the bottom of the conduction band, where their lifetimes may be $\sim 10^{-8}$ S. (113) Near the vacuum boundary, the second high field region reaccelerates (heats) the electrons so that they pass over the top of the insulator electron affinity barrier and into the vacuum space. Thus, the two main objections to the original energy band model were overcome and the poisoning phenomena described by Juttner could still be accounted for in terms of electron traps or oxygen vacancies.

Conduction was believed to be started by the tunnelling of a few electrons into the insulator when the local field was above a critical value, these then suffered impact ionisation processes which induced an avalanche effect. The electrons and holes thus created would drift in opposite directions; the holes to the metal interface and the electrons to the vacuum boundary, where they would be caught in the large number of localised interband trapping levels. Hence the two internal boundary fields would be enhanced and the electron tunnelling probability increased.

For continuous conduction however, this model requires the presence of a large population of holes moving towards the metal contact; these were assumed to be generated in the high field region near the vacuum boundary from impact ionisation of the insulator lattice by the hot electrons arriving from the metal. This process was also believed to lead to electroluminescence when some of the holes and electrons recombined in trapping states.(114)

Other processes that were envisaged as producing light were the impact or field ionisation of luminescent centres at the insulator surface.

In order for a positive space charge to form at the metal - insulator contact, the electron mobility there had to be considerably greater than the hole mobility since overall charge neutrality was expected, Mott (112) had shown that these requirements lead to constant current density in the conducting channel. The current density also needed to be large enough to keep all the interband trapping states fully occupied or the channel conductivity would fall dramatically. From these considerations Mott proposed that an increase in cross channel width accompanied an increase in current. Thus in figure (31c), it will be seen that if the cross channel width W is less than the film thickness d, the current density in the bulk would have to be less than at the channel ends in order to satisfy Laplaces equation etc., and in fact may be too low for stable conduction. The two conditions, i.e. $W \geqslant d$ and constant current density j_m then lead to a minimum value of holding current given by $i_m = j_m d^2$, where the value of j_m was later found to be $\sim 10^8$ A/m^2 by Peterson & Adler. (113) However, this value is so large that in order to explain the very low current behaviour observed with broad area emission sites, Athwall & Latham (43) had to further postulate that once switched on the conducting filament underwent a forming process similar to that assumed by Hurley, by which the filament became more crystaline. Thus from the above equation for im, in order to obtain the currents which may be observed as low as 10^{-14}A, the film thickness would have to be $\sim 3 \times 10^{-12}$m which is clearly impossible. Unfortunately the two propositions of Athwall & Latham then lead to a situation where one unverified hypothesis is used to override a previous one but only where the original hypothesis breaks down. It may also be said that a crystalised (formed) filament conducting at $< 10^{-6}$A may not behave according to Mott's model of dynamic conduction, and in any case it may not be possible for the necessary quantity of holes to be produced or to reach the metal-insulator contact, due to various recombination processes. The latter fact was recognised by Athwal but the model as presented did explain in a general way a great many of the observations. In particular, the emission site switch-on and electroluminescence were features incorporated into its developement, although it may be further noted that emission sites do not always exhibit electroluminescence since this has not been seen during the series of experiments presented here, or recently by other researchers in the Aston laboratory. High current "a" sites and current controlled "b" sites clearly fit the model in a general sort of way,(25,26) while some of the non-linear F.N. plots may be explained by assuming changes in the structure of the conducting channel. For example the crystalinity may change or the channel width may be restricted by the size of the insulating surface inclusion. The shift observed in the electron energy spectrum arises from the same effects as in the simple band model, i.e. from the sum of the potentials dropped at the metal-insulator contact, at the insulator-vacuum boundary and in the insulator bulk, although it is not so clear that the correct functional relationships result from this model. The I-V functions which describe only the injection of electrons are derived in sections 4.7 & 4.8. of this chapter, these have been found to fit the experimental data quite well.

Some of the anomalous phenomena, eg. F.N. plots with sharp discontinuities and the hysteresis effects observed by Chatterton(18) etc., may be attributed to either changes in the surface barrier height brought about by gas desorption, or to the scattering of electrons out of the conducting channel into the surrounding higher resistivity material. In relation to some of these phenomena it should be emphasised that it is unlikely that emission from single sites has been investigated in the past, since it will be shown in later chapters, that what was previously considered to be a single site of emission usually consists of several sources of emission current (sub-sites) and that each of these may switch on and off at random, especially for currents $> 10^{-7}$A .

4.4. General Observations.

From an examination of the preceeding three emission models it will be noted in particular that they are all very speculative about the nature of the potentials dropped across the metal-insulator contact and across the bulk of the insulator. In fact, none of the models gives any real idea of the functional form such potential differences might take as the current is varied; although for the switching model, Athwal (96) indicated that if the current was dependent upon the potential barrier at the contact, then an approximate F.N. relationship should follow: this property was also supposed to account for the F.N. character of the emission current. However, it will now be shown that a detailed model based on the emission of hot electrons over the vacuum surface potential barrier is sufficient to account for the observed phenomena without additional complications. In order to develope this model much greater attention has to be paid to the nature of the insulator-metal contact and to the insulator bulk parameters than in the past; it will also be shown that this leads to verifiable V-I relationships for the contact and bulk potential drops, together with explanations for the non-linear F.N. plots which are often observed. In this context a great wealth of information exists in the literature of semiconductor physics and from studies on metal-insulator - metal systems in particular, concerning the electrical conductivity of metal-insulator junctions and the properties of thin imperfect insulators in general. Where in particular the excellent review article by Simmons (115) has been found most useful.

4.5. Electrical Conduction in Imperfect Insulators.

The electrical conductivety of a metal-insulator - metal system is not directly determined by the properties of the insulator, but rather by the interaction of the insulator with its metal electrodes. Three types of contact may then be formed at a metal-insulator interface which are described by Simmons (116) as: a) the ohmic contact ; b) the neutral contact; and c) the blocking contact. For all types of contact considerations of thermodynamic equilibrium and continuity of electrical potential demand that the Fermi levels of the insulator and metal electrode be continuous across the interface, and that the energy difference between the insulator vacuum and Fermi levels far from the interface will be equal to the insulator work function ϕ_I. Therefore, in the absence of surface states the interfacial barrier height will be

$$\phi = \phi_M - X \qquad (1)$$

where ϕ_M is the metal work function and X the insulator eletron affinity.

4. 5.a) The Ohmic Contact (Mott-Gurney Contact)

An ohmic contact is achieved when the electrode work function ϕ_M is smaller than the insulator work function ϕ_I, as shown in figure (32a). Thermodynamic equilibrium at the junction then means that electrons are injected into the conduction band of the insulator from the metal, giving rise to a negative space charge region and an induced field within the insulator. This space charge region extends a small distance into the insulator and is called an accumulation region because it acts as a charge reservoir capable of supplying

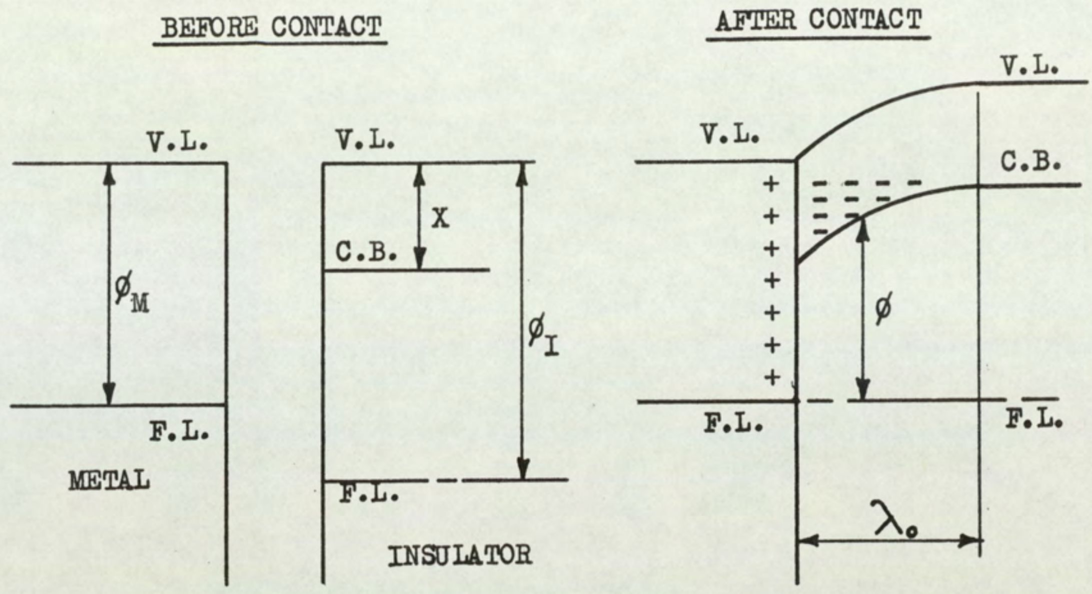

a) FORMATION OF AN OHMIC CONTACT $\phi_M<\phi_I$ a)

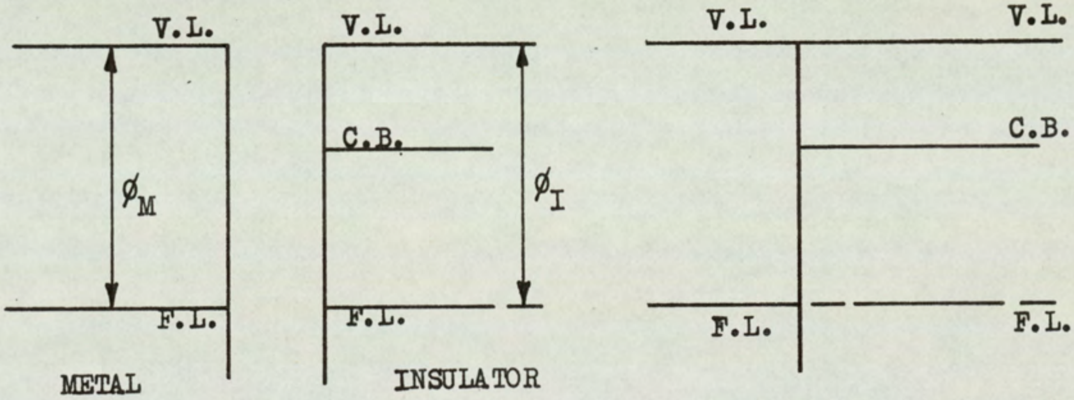

b) FORMATION OF A NEUTRAL CONTACT $\phi_M=\phi_I$ b)

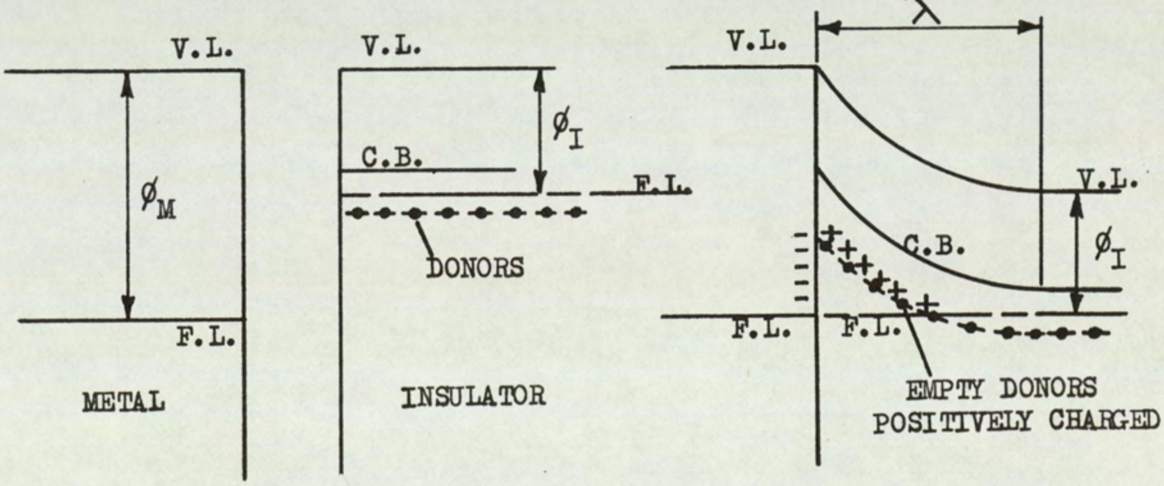

c) FORMATION OF A BLOCKING CONTACT $\phi_M>\phi_I$ c)

FIG. 32. ENERGY BAND DIAGRAMS SHOWING THE FORMATION OF THE THREE TYPES OF METAL-INSULATOR CONTACT. V.L.=THE VACUUM LEVEL, F.L.=THE FERMI LEVEL AND C.B.=THE INSULATOR CONDUCTION BAND.

electrons to the insulator bulk as required by bias conditions. The conduction process is thus limited by the rate at which electrons can flow through the bulk of the insulator, rather than by the rate of electron supply from the electrode, and the conduction is therefore bulk limited. However, from the band diagram of figure (32a) it will be seen that the conduction band edge, well into the insulator, is raised above the metal Fermi level, in contradiction to the electron energy spectral data for broad surface emission assuming negligible potential drop in the insulator bulk. Hence this type of contact need not be considered further.

4.5. b) The Neutral Contact.

If $\phi_M = \phi_I$ the vacuum and Fermi levels of the insulator and electrode line up naturally without the necessity for charge transfer and a neutral contact results. The band diagram of figure (32.b) indicates that, in this case, the conduction band is flat right up to the interface since there is no space charge within the insulator to bend the bands. For an initial bias voltage, the elctrode is capable of supplying the current flowing in the insulator and the process is bulk limited; moreover the field in the insulator is constant so that the conduction is ohmic. As the voltage is raised however, a limit is reached to the current that can be supplied by the electrode, this is the saturated thermionic (Richardson) current for electrons passing over the interfacial barrier. Calculations indicate that for this type of contact at room temperature, the saturated current will be much lower than observed for broad area emission unless the barrier height is less than 0·5 eV, which is unlikely for insulators.

4.5.c) The Blocking Contact (Schottky Barrier)

Blocking contacts occur when $\phi_M > \phi_I$, as shown in figure (32.c), so that electrons flow from the insulator to the metal in order to establish thermal equilibrium. As a result a positive space charge region is created in the insulator which, because it is devoid of conduction electrons, is known as a depletion region. A local field then exists within the insulator causing the bottom of the conduction band to bend downwards until the bulk Fermi level lies ϕ_I below the vacuum level. An intrinsic insulator however, contains such a low density of electrons that it would have to be very thick in order to provide the positive space charge required to satisfy the above condition. Hence the conduction band of an intrinsic insulator barely slopes downward, especially when surface states are involved, and so an essentially neutral contact results.

To achieve marked band bending the insulator has to be doped, i.e. be impure, as would be expected for the surface layers and inclusions found on broad area electrodes; under these circumstances the resultant donor centres can provide the free electrons at an energy level E_D just below the conduction band edge. From figure (32c) it will be noted that the free electron density at the metal insulator interface is much lower than in the bulk of the insulator, hence the rate of flow electrons will be determined by the flow over or through the barrier and therefore the conduction will be contact limited.

The shape of the potential barrier within the insulator may be found by solving Poisson's equation at the contact for a constant donor density N_D throughout the insulator. That is —

$$\frac{d^2\phi}{dx^2} = \frac{e}{\mathcal{E}\mathcal{E}_o} N_D \qquad (2)$$

with the boundary conditions $\phi = \phi_M - X$ at $x=0$ & $\frac{d\phi}{dx}=0$ at $x=\lambda$ where ϕ is the potential (in eV) at distance x from the metal interface, e is the electronic charge, $\mathcal{E}_o$ the permitivity of free space and $\mathcal{E}$ the dielectric constant of the insulator, while λ is the width of the depletion region.

Solving equation 2 $$\phi = \phi_M - X + \frac{e N_D}{\mathcal{E}\mathcal{E}_o}\left[\frac{x^2}{2} - \lambda x\right] \qquad (3)$$

and since $\phi = \phi_I - X$ when $x = \lambda$

one has $$\lambda = \left[\frac{2\,\mathcal{E}\mathcal{E}_o}{e\,N_D}\left(\phi_M - \phi_I\right)\right]^{\frac{1}{2}} \qquad (4)$$

The following table gives a few values for λ assuming $\phi_M - \phi_I = 2$ eV and $\mathcal{E} = 5$.

N_D (m^{-3})	10^{21}	10^{23}	10^{25}	10^{27}
λ (m)	10^{-6}	10^{-7}	10^{-8}	10^{-9}

When a bias voltage V_c is applied to the insulator, most of it will be absorbed across the depletion region since this has a much lower electron density and hence conductivity than the insulator bulk. Therefore

$\phi = \phi_I - X + V_c$ at $x = \lambda$ and equation 4 is modified to (5)

$$\lambda^2 = \frac{2\mathcal{E}\mathcal{E}_o}{e\,N_D}\left[\phi_M - \phi_I + V_c\right] \qquad (6)$$

The electric field F_o at the metal-insulator interface is given by $F_o = \frac{-1}{e}\frac{d\phi}{dx}$ which from equation 3 with ϕ_I & ϕ_M in eV gives

$$F_o = \left[\frac{2e\,N_D}{\mathcal{E}\,\mathcal{E}_o}\left(\phi_M - \phi_I + V_c\right)\right]^{\frac{1}{2}} \qquad (7)$$

Thus, for reasonable impurity doping levels etc., i.e.

$N_D = 10^{24}\ m^{-3}$ and with $\mathcal{E} = 4$, we have even for very low applied voltages, $\lambda < 250\overset{o}{A}$ and $F_o > 10^8$ V/m. Such a high value of internal field will increase further as the applied voltage is raised and will then be more than sufficient to promote electron tunnelling when $F_o \sim 10^9$ V/m and the barrier width at the metal Fermi level is reduced. The barrier width at the Fermi level λFL is given by equation 3 when $\phi = 0$ and $x = \lambda$FL. Hence-

$$\lambda_{FL} = \lambda - \left[\lambda^2 - \frac{2\mathcal{E}\mathcal{E}_o}{e\,N_D}\left(\phi_M - X\right)\right]^{\frac{1}{2}} \qquad (8)$$

and then the voltage required to pull the conduction band down to the metal Fermi level is obtained when λFL just equals λ giving finally $Vc = \phi_I - X$, as would be expected even by just examining figure (32c). Thereafter, as pointed out by Simmons,(116) substantial electron tunnelling will take place when $\lambda FL < 50\overset{o}{A}$ which corresponds to a value of Vc of about 1·7 to 2·5 V depending on the insulator parameters. The conduction band edge will then be $Vc - \phi_I + X$ below the metal Fermi level, or $\sim$.2 to 1V.

4.6. Energy Band Models for the Insulator.

In addition to impurity or doping levels, a realistic description of an imperfect insulator must include the effects of electron traps. The insulating structures occurring on broad area electrodes will at best be polycrystaline and may in fact be mainly amorphous. For crystalite sizes of 100Å, trapping densities as high as $10^{24}\ \mathrm{m}^{-3}$ are easily possible due to grain boundary defects alone and any further disrupting influences, such as polishing strains or dislocations, will only increase this number.

If now a simple insulator model is assumed, containing N_T traps and N_D donors positioned at energies E_T and E_D below the conduction band with the Fermi level at energy E_F , several possible band diagrams may be drawn as shown in figure (33a). For each diagram, the relationship is given between the various parameters, assuming non- degenerate positioning of the Fermi level with respect to the donor and trapping levels (117). These systems have been analysed by Simmons (118) who noted that it was only system II which allowed a wide degree of flexibility between the values of N_D and N_T; the extremes of the range of variation are given by

$$N_D = N_T \ \mathrm{EXP}\pm\left[\left(E_D - E_T \mp 4\,kT \right) \Big/ kT\right] \qquad (9)$$

where T is the absolute temperature and k Boltzmann's constant. Simmons also calculated the ratio of the insulator conductivities with traps σ_T and without traps σ_o to be

$$\frac{\sigma_T}{\sigma_o} = \mathrm{EXP}\left[\frac{-E_T}{2kT}\right] \qquad (10)$$

which, if $E_T = 0{\cdot}75$ eV predicts σ_T/σ_o to be 10^{-7}; i.e. the traps have reduced the conductivity by 10^{-7}. Similar conclusions can be arrived at for the other energy band configurations.

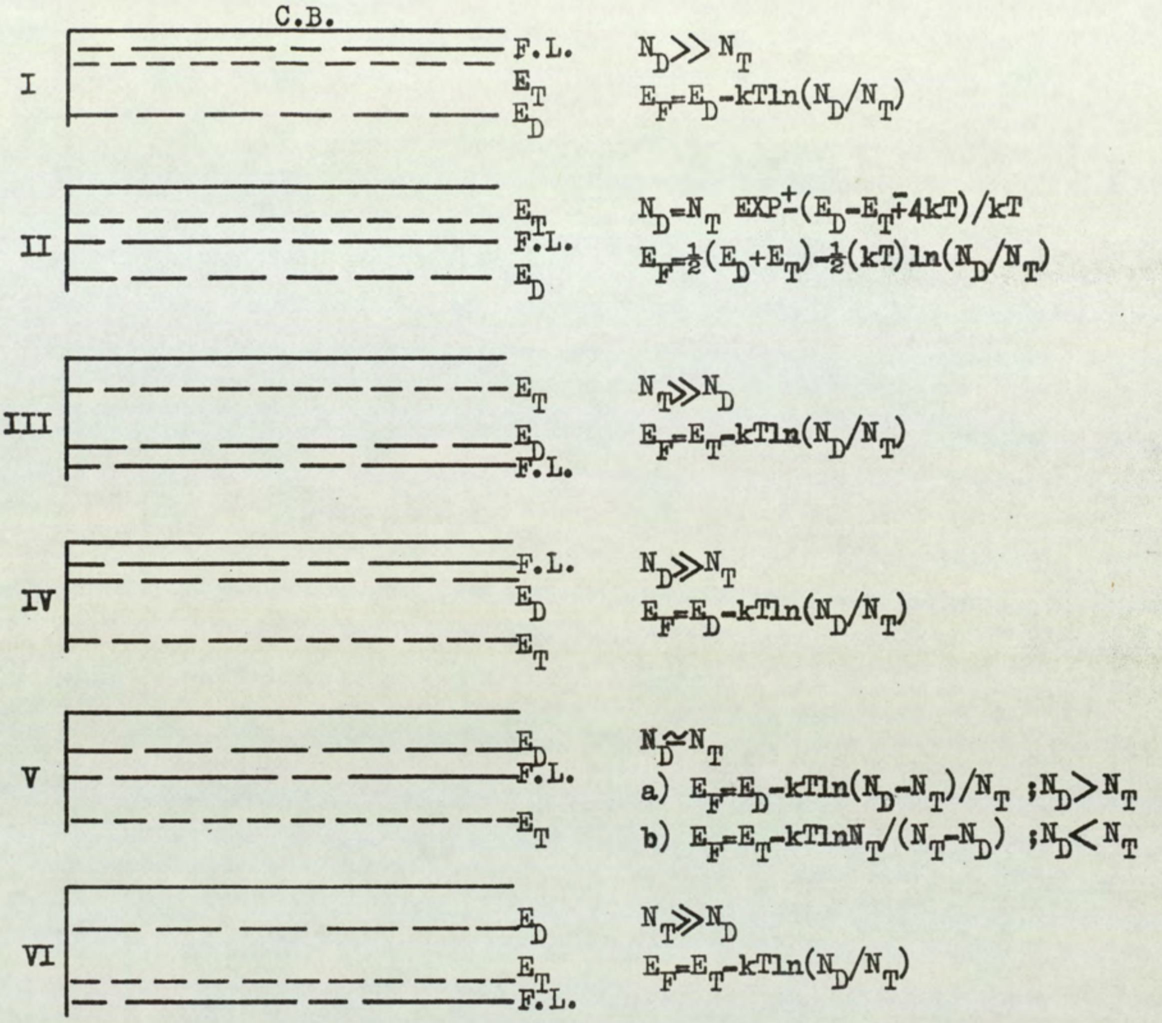

FIG.33. INSULATOR BAND MODELS.
The relationships between N_D, N_T and E_F alongside each diagram are the conditions for that particular energy configuration, assuming $n < N_T$ and non-degenerate positioning of E_F.

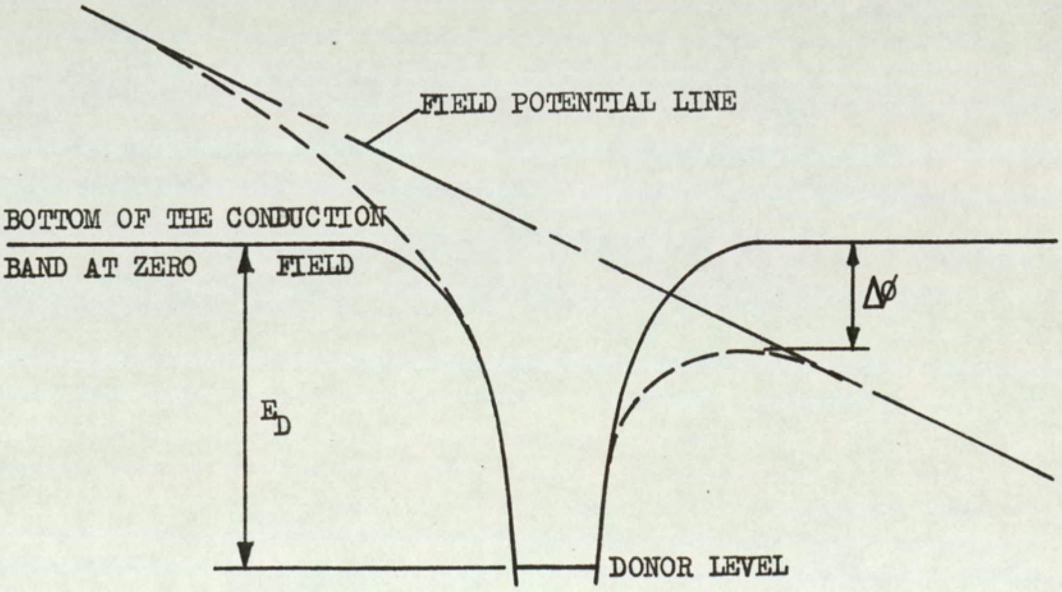

FIG.34. THE POOLE-FRENKEL EFFECT AT A DONOR CENTRE.

In the contact depletion regions associated with insulators I to III of figure (33a), and provided $N_D > 10^{23}$ m^{-3}, both donors and traps may be assumed to be empty since they are above the Fermi level and as a consequence positive charge density ($\equiv N_D$) will exist there. The situation is then the same as for a metal-insulator contact having a single donor level, so that the preceeding equations describing a blocking contact remain unaltered, as has also been shown by Simmons (117).

4.7. J-V Characteristics For a Metal-Insulator System.

The electrical conduction characteristics for an imperfect insulator may now be conveniently split into three voltage ranges: a) low voltages, where the process is thermally controlled, i.e. the Richardson-Schottky effect; b) intermediate voltages, where the process is electrode limited and contact tunnelling or impact ionisation take place and c) high voltages, where bulk processes become important which eventually override the contact processes to give bulk limited conduction.

4.7.a) The Richardson-Schottky Effect.

This process requires electrons to gain sufficient energy from random thermal effects to surmount the metal-insulator contact barrier ϕ_o. A field dependency is then introduced because an increasing field at the metal-insulator interface reacts with the electrode image force causing the barrier height to be reduced below ϕ_o, thus allowing more current to flow. The relavent relation is then obtained from equation 18 of chapter 3·5 i.e.

$$J = AT^2 \, \mathrm{EXP}\left[-\frac{e}{kT} \left(\phi_o - \beta_s F^{\frac{1}{2}} \right) \right] \qquad (11)$$

where $\beta_s = \left(\dfrac{e}{4\pi\varepsilon_o\varepsilon^{*}} \right)^{\frac{1}{2}}$ (12)

and F is the field given by equation 7. In equations 11 and 12 $\mathcal{E}^*$ is the high frequency dielectric constant and A has a value of $1 \cdot 2 \times 10^6$ $A/m^2/K^2$ assuming that the effective electron mass m* is equal to the free electron mass m. However, at room temperature this effect should be negligible for the barrier heights to be expected for metal-insulator systems, i.e. 1V, and furthermore, broad area emission shows no change in magnitude with temperature down to 77 K, thus indicating that this conduction mechanism is insignificant at ambient temperatures

4.7.b) Contact Tunnelling and Carrier Multiplication.

When the field at the metal-insulator interface is high enough to reduce the width of the barrier at the metal Fermi level to about 50Å or less, electron tunnelling will take place. Then, for $V_c > \phi_o$, the barrier at the interface may be considered to be approximately triangular, so that the simple Fowler-Nordheim expression i.e. equation 1 of chapter 3.1., may be used to arrive at the current density tunnelling through the contact barrier. This is

$$J = \frac{1 \cdot 54 \times 10^{-6}}{\phi_o} F_o^2 \ \mathrm{EXP} \left[- \frac{6.83 \times 10^9 \ \phi_o^{\frac{3}{2}}}{F_o} \right] \qquad (13)$$

where F_o (V/m) has a value again given by equation 7 such that

$$J = \frac{5 \cdot 56 \times 10^{-14}}{\mathcal{E}^* \ \phi_o} N_D \left(V_c + \phi_M - \phi_I \right) \mathrm{EXP} \left[-3.61 \times 10^{13} \left(\frac{\phi_o^3 \ \mathcal{E}^*}{N_D (V_c + \phi_M - \phi_I)} \right)^{\frac{1}{2}} \right] \qquad (14)$$

of particular note here is the fact that $(V_c + \phi_M - \phi_I)^{\frac{1}{2}}$ replaces the usual V-term associated with F.N. metal-vacuum tunnelling. This equation gives a sharply rising current dependence with applied voltage, and hence a rapidly falling contact resistance which is essentially independent of temperature.

However, a slight temperature dependence does result if electrons tunnel through the barrier indirectly, i.e. via donor or trapping centres within the depletion region (117). These processes can modify the transparency of the barrier quite markedly and will normally be associated with the absorption or emission of a lattice phonon, since the components of momentum for an electron entering a donor level or trap state will, in general, not be compatible with the occupancy of these centres. The probability of an indirect transition then depends on the temperature through the quantum occupation number of the excited phonon states (117). A second temperature-dependent process would be the indirect tunnelling of an electron into a trap followed by thermal activation over the reduced barrier existing at the trapping centre.

In addition to contact tunnelling the high field existing in the depletion region also makes it possible for an electron to gain sufficient energy to cause impact ionisation of the insulator lattice. According to Simmons (115,117) this requires the energy gain before collision to be $> 1\cdot5E_G$, where E_G is the energy band gap of the insulator, and the mean free path of the electron in the insulator to be long enough, that is, for a typical ionisation energy of 5eV and for field of $\sim 10^8\ Vm^{-1}$, a mean free path of the order of 500Å is required. However, measurements by Braunstein et. al. (119) and by Schuermeyer (120) indicate that the electron mean free path in amorphous insulators is only a few tens of angstroms; in addition it will be shown in a later chapter that the contact potential drop for the insulating inclusions on broad surfaces is <3V, indicating that this process does not play a major role at the metal-insulator contact in this case.

4.8. Bulk Conduction.

For an insulator containing both donors and traps, the bulk conduction equation is

$$J = eun \frac{V_b}{d} \qquad (15)$$

where V_b is the voltage dropped across the bulk, d is the insulator thickness, u the electron mobility and n is the volume density of electrons which is given by

$$n = N_c \, \mathrm{EXP}\left[-\frac{E_F}{kT}\right] \qquad (16)$$

where N_c is the effective density of states in the insulator. The value of E_F for the particular arrangement of donors and traps assumed for model II of figure (33a) was calculated by Simmons(118) by assuming that the number of ionised donors is the same as the number of occupied traps, i.e. $N_D \, \mathrm{EXP}-(E_D - E_F)/kT = N_T \, \mathrm{EXP} - (E_F - E_T)/kT$ hence

$$2\,E_F = E_D + E_T - kT \ln\left[\frac{N_D}{N_T}\right] \qquad (17)$$

The number of electrons in the conduction band will then be negligible when compared to the number in trapping states but they will none the less be responsible for the bulk conductivity which will therefore be given by

$$J = eu \frac{V_b}{d} \; N_c\left(\frac{N_D}{N_t}\right)^{\frac{1}{2}} \mathrm{EXP}\left[\frac{-(E_D + E_T)}{2kT}\right] \qquad (18)$$

When the applied field is further raised however, this equation needs to be modified in order to take into account the interaction of the field with the Coulombic barriers associated with donors and traps. These barriers result repectively from the attractive force that exists between a donor centre or a charge trap (i.e. charged when empty and neutral when full) and an electron as shown in figure (34). The barrier height reduction is then known as the Poole-Frenkel effect.(121) This process is the bulk analogue of the Schottky effect at an interfacial barrier, and since the potential energy in a Coulombic field ($-e^2/4\pi\varepsilon\varepsilon_0 x$) is four times that due to image force effects, the Poole-Frenkel reduction of the Coulombic barrier $\Delta\phi_{PF}$ in a uniform field is twice that for the Schottky effect at a neutral contact. Hence

$$\Delta\phi_{PF} = \left(\frac{e}{\pi\varepsilon\varepsilon_0}\right)^{\frac{1}{2}} F^{\frac{1}{2}} \equiv \beta_{PF}\left(\frac{V_b}{d}\right)^{\frac{1}{2}} \quad \text{eV.} \tag{19}$$

and then the bulk conduction equation is

$$J = J_o \, \text{EXP}\left[\frac{e}{kT}\beta_{PF}\left(\frac{V_b}{d}\right)^{\frac{1}{2}}\right] \tag{20}$$

If these traps are assumed to be neutral and shallow (i.e. just under the bottom of conduction band) Simmons (116) has shown that

$$J = J_o \, \text{EXP}\left[\frac{e}{2kT}\beta_{PF}\left(\frac{V_b}{d}\right)^{\frac{1}{2}}\right] \tag{21}$$

and at high fields in both these equations the exponential term dominates the linear dependence of J_o on V_b.

4.9. Contact-Limited to Bulk Limited Transition.

If the insulator contains a high donor density ($N_D > 10^{24} m^{-3}$) and a high trap density ($N_T > 10^{25} m^{-3}$) the depletion region will be very thin and its bulk conductivity will be low in spite of the high donor density (see equation 18.) Under these conditions an electrode-limited to bulk-limited transition may be observed. During the initial voltage application electrons tunnel into the insulator conduction band and the current rises very sharply with applied voltage. At this stage most of the voltage appears across the contact, since the contact resistance is much higher then the bulk, and the J-V characteristic will be virtually thickness - independent. Electrode limited conduction will not continue indefinitely however, because the bulk resistance falls much less rapidly with increasing voltage than the contact resistance. Thus at some voltage V_T, the contact and bulk resistances will be equal and the applied voltage will be split equally across each region. Subsequent increases in voltage will appear mainly across the bulk, and as a result the current will cease to rise as sharply as for the initial phase, since it will now be controlled by bulk processes which will be thickness dependent. Curves showing contact to bulk limited transitions are shown in figure (35), where the plots are of the form logI versus $V^{\frac{1}{2}}$ in order to display the linear region of the Poole-Frenkel effect. The dashed and dot-dashed lines represent the behaviour predicted by the bulk and contact equations repectively, while the full lines give the combined (series) effect of both to show the form of the characteristics which may actually be measured. It follows that in order to obtain the true bulk characteristic from observed data, it is necessary to extrapolate the contact limited line to higher currents and subtract its effect from the measured data.

4. 10. The Hot Electron Model in Outline

4.10.a Filament-Switch on.

It will now be apparent from the preceeding discussion that emission from an electrode surface through an insulating layer cannot begin to occur until the field at the metal-insulator junction reaches a value at least high enough for electron tunnelling to take place. Thus the potential at the vacuum-insulator interface, due to the penetrating field plus the contact potential, must be sufficient to depress the conduction band edge below the metal Fermi level, as shown in figure (36b). From equation 8, the contact voltage necessary to do this is $V_C \gtrsim \phi_I - X$, which in this case will be equal to the electrostatic potential difference across the

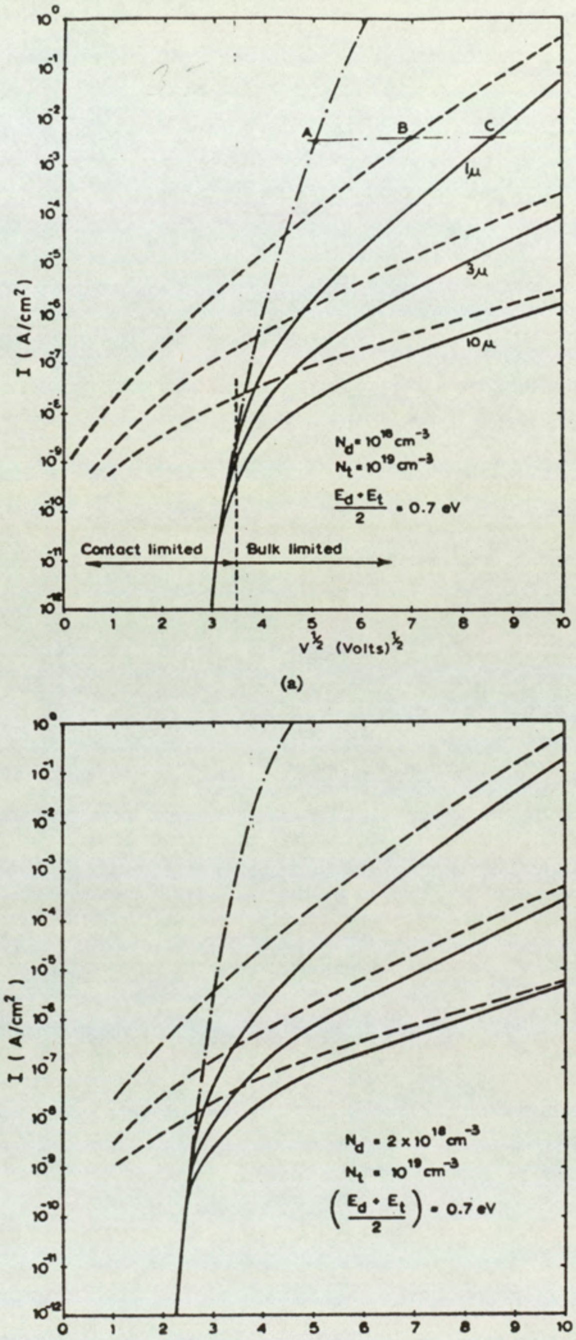

(a)

(c)

FIG 35. PLOTS SHOWING CONTACT TO BULK LIMITED TRANSITIONS IN M.I.M. DEVICES. from Simmons (116).

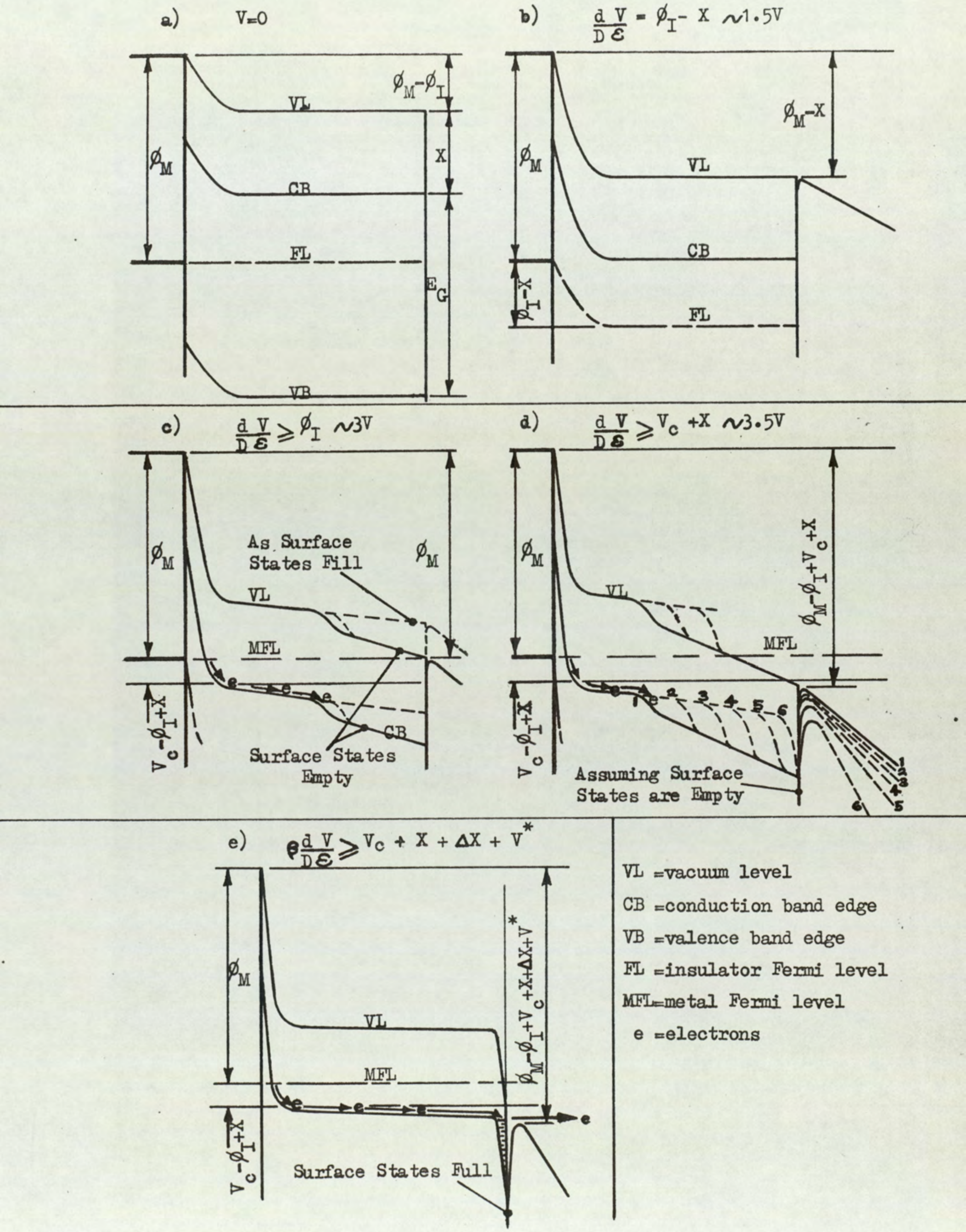

FIG 36. STAGES IN THE "SWITCH ON" OF A CONDUCTING FILAMENT AS THE APPLIED VOLTAGE IS RAISED.

insulator due to the penetrating field, i.e. $V_C = \frac{d}{\mathcal{E}}\frac{V}{D}$ where D is the inter-electrode gap, V the applied anode voltage and d the thickness of the insulator with dielectric constant $\mathcal{E}$. Hence

$$\frac{d}{\mathcal{E}}\frac{V}{D} \gtrsim \phi_I - X \qquad (22)$$

which for the usual gap of 0·5mm, and assuming sub-micron thick surface layers having $X \sim 1.5$, $\mathcal{E} \sim 3$ and $\phi_I - X \sim 1.5$ eV, gives a tunnelling initiation voltage between ∼3 and ∼9 KV. Following the application of a voltage greater than this, electrons will begin to tunnel into the insulator where they then start to fill empty electron traps which exist just below the bottom of the conduction band. However, this process cannot continue for long because the position of the conduction band edge will rise towards the metal Fermi level in responce to the negative charge added to the insulator. Even increasing the applied voltage to a value such that the vacuum surface barrier is depressed down to the metal Fermi level, as in figure (36c) will probably not produce a continuous emission current, since the vacuum barrier peak will again rise above the metal Fermi level as additional electrons flow into the insulator to fill empty surface states. In order to initiate a continuous emission current, the peak of the vacuum surface barrier must first be depressed below the level of the conduction band at which substantial electron tunnelling takes place from the metal, as shown in figure (36d). The conduction band edge at the metal contact will be $\sim V_C - \phi_I + X$ below the metal Fermi level under these conditions (where V_c is the contact potential drop) so that the vacuum barrier peak needs to be depressed an amount given by

$$\frac{d}{\mathcal{E}}\frac{V}{D} + \phi_M - \phi_I \gtrsim \phi_M + V_c - \phi_I + X \quad \text{or} \quad \frac{d}{\mathcal{E}}\frac{V}{D} \gtrsim V_c + X \qquad (23)$$

which, if the previous values are used for $\mathcal{E}$, d, X and D, and with V_c estimated from spectra to be $\sim 2V$, gives a filament switching voltage between ~ 7 and ~ 16 KV. Values of this order are typical for copper electrodes with sub-micron to micron sized surface inclusions, eg Athwall (96) and Donaldson & Robinowitz(33); smaller inclusions will of course require higher voltages and very thin robust oxide layers, such as occur on stainless steel or aluminium electrodes, will need even higher voltages, as seems in-fact to be the case experimentally. When the vacuum barrier peak is depressed down below the metal Fermi level, a strong electric field will exist in the insulator bulk and electrons will gradually migrate towards the vacuum surface under the action of this field. As a result the bottom of the conduction band will progressively rise as a high field domain sweeps across the developing conducting channel, as indicated in figure (36d - 1,2,3, 4,5,6). When stages 5 and 6 are reached the insulator surface field will have become considerably enhanced relative to the average field in the insulator, since the rate of change of potential is then very high near the surface. This greatly enhanced field will not end abruptly at the vacuum surface however, since severe field distortion would be produced, rather, continuity of the field lines means that the vacuum field just outside the insulator will also be enhanced. The surface potential barrier will then be thinned and depressed to such a level, as the effect of stored negative surface charge is overcome, that electrons are able to escape from the insulator, as also indicated in figure (36d). Escaping electrons then reduce the charge stored near the insulator vacuum surface, which in-turn further lowers the potential barrier relative to the insulator bulk conduction band edge, and a regenerative situation then sets in such that a large current would be able to flow. However, a substantial current may still be maintained even with the applied voltage reduced, since the vacuum field over the filament and the average field in the **filament** will have become enhanced by a factor β, due to the potential distribution in the insulator then being maintained by the flowing current. This is shown in figure (36e) and also in figure (99) of chapter 7, and thus represents an alternative explanation of the site "switch on" effect to that given by Athwal & Latham(97) which has the advantage of requiring no further hypotheses (such as filament "forming") to describe the "on" state.

4.10 b) Stable Conduction.

Following the early switching events outlined above a continuous stream of electrons will tunnel through the metal - insulator barrier to suffer phonon interactions with the insulator lattice and be thermalised into the bottom of the conduction band. For a parabolic minimum in the energy-momentum relation, these electrons would then have a F.W.H.M. to their energy distribution of $\sim 1{\cdot}5$ kT, which at room temperature amounts to a negligible 0·04 eV when compared to the typical F.W.H.M. of a measured spectrum. Donor centres distributed throughout the insulator ensure that the bulk conductivity is non zero, and so electrons will arrive at the high field region in the filament tip to be accelerated towards the vacuum interface. Further extensive electron-lattice interactions take place, which may be sufficiently energetic to produce impact ionisation, which in-turn can lead to light production when the resulting holes recombine with free or trapped electrons. As a result of these processes a pool of hot electrons will be established very close to the vacuum surface such that the enhanced electron temperature enables most electrons at the vacuum surface to escape over the energy barrier, in a form of Richardson-Schottky thermionic emission, as first suggested by Latham (122).

Latham's original idea assumed that the population of hot electrons obeyed Maxwell-Boltzmann statistics so that the emitted current density would then be given by the Richardson - relation, i.e.

$$J = A \; Te^2 \; \mathrm{EXP} \left[- \frac{e X}{kTe} \right] \qquad (24)$$

where Te was the enhanced electron temperature, X the height of the potential barrier at the vacuum interface (the electron affinity) and the constant $A = 1{\cdot}2 \times 10^6 \; A / m^2 / K^2$ if the electrons had their free space mass value. In addition, Latham assumed that the kinetic energy gained by the electrons as they were accelerated in the penetrating field was approximately given by the entire potential difference across the insulator, i.e. $e \, \Delta V \sim \frac{e}{\mathcal{E}} \frac{d}{D} V$ and that this was equal to the average knetic energy of the pool of hot electrons, i.e. $e \, \Delta V = \frac{3}{2} kTe$. This then lead to

$$Te \sim \frac{2}{3} \; \frac{e \; d \; V}{k \, \mathcal{E} \, D} \qquad (25)$$

and hence

$$J = A \left(\frac{2}{3} \; \frac{e}{k} \; \frac{d}{D \, \mathcal{E}} \right)^2 V^2 \; \mathrm{EXP} \left[- \frac{3}{2} \; \frac{D \, X}{d \, V} \right] \qquad (26)$$

so that a plot of $\ln {}^{J}/_{V^2}$ against ${}^{1}/_{V}$, which is equivalent to an F.N. plot, should have been a straight line as approximately observed experimentally. This hypothesis thus provided the means of interpreting mathematically the general ideas incorporated into the energy band diagrams which were discussed earlier. However, the supporting assumptions leading to equation 25 expressing Te in terms of the insulator parameters and the applied field have been found to be over simplified. Latham (122) also assumed that the emitted electron energy distributions which are obtained from insulating inclusions on broad area electrodes were of a similar shape and orientation to the thermionic distribution, and this is not the case. A much more detailed derivation of the quantities to use in equation 24 which results from the insulator band model of figure (36e) is presented in chapter 7, where it is shown that this again leads to an emission J-V equation having a similar field dependence as the conventional F.N plot. This analysis is also shown to be in conformity with the results of previous and current research and to explain several of the other apparently unrelated experimental observations, such as the marked non-linearities often seen in F.N. plots at high current.

CHAPTER 5.

A SPECTROMETER FOR STUDYING THE ENERGY DISTRIBUTIONS OF ELECTRONS EMITTED FROM BROAD AREA ELECTRODES.

5.1. Types of Spectrometer.

In principal there are two main types of spectrometer which can be used to investigate the electron energy distributions of field emitted electrons; these are the retarding potential and the electrostatic deflection analysers. However, since the retarding potential analyser is now less favoured, it is only necessary to consider briefly it's mode of operation and opperational dis-advantages, in order to highlight the advantages of the electrostatic deflection instrument which is used throughout this investigation.

A popular design for the retarding potential analyser is that due to Van-Oostrom (123), here shown symplified in figure (37). Thus a thin wire with sharply etched tip having an end radius of ~ 100 nm forms the field emitter, which enables high fields $> 10^9$ Vm^{-1} to be created at moderate accelerating potentials, i.e. 0·5 - 5 KV. Emitted electrons are then retarded by lens L to an energy of a few eV and focused on the collector electrode. A slowly increasing ramp voltage Vc applied to collector C enables high energy electrons to be collected at first for low Vc, and then eventually all electrons if Vc goes high enough, where a typical plot of collector current Ic against collector voltage Vc is shown in figure (38). This is known as an integral plot because it is necessary to differentiate the curve in order to obtain the distribution of energies in the emitted electron current. This method of detection has several

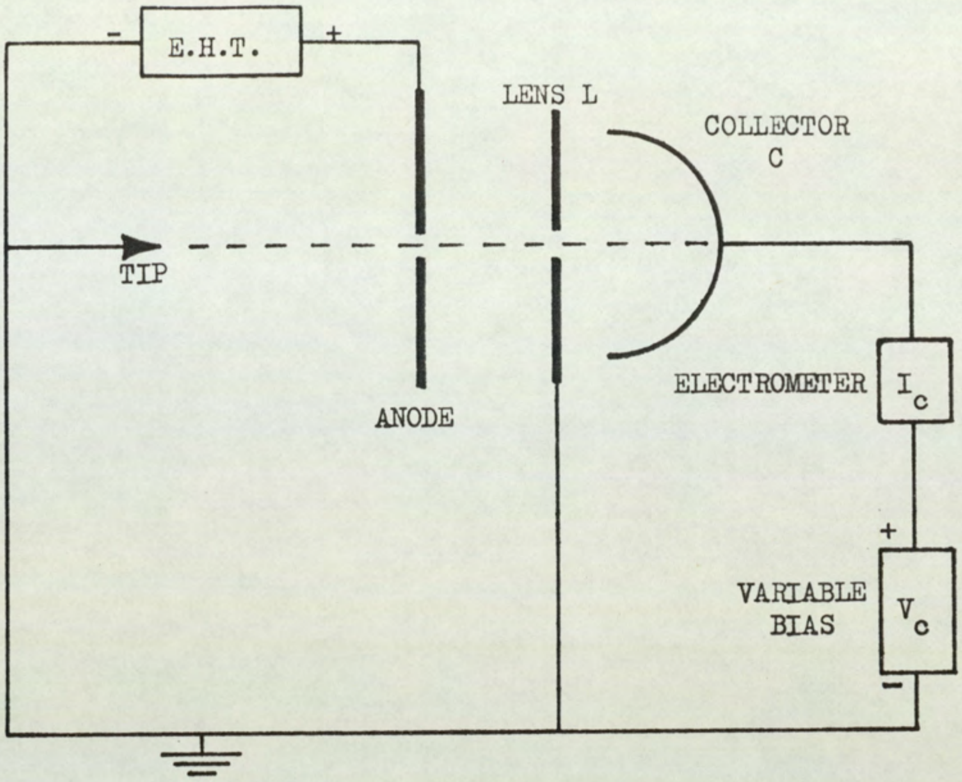

FIG.37. SCHEMATIC DIAGRAM OF THE ESSENTIAL FEATURES OF A RETARDING POTENTIAL ANALYSER.

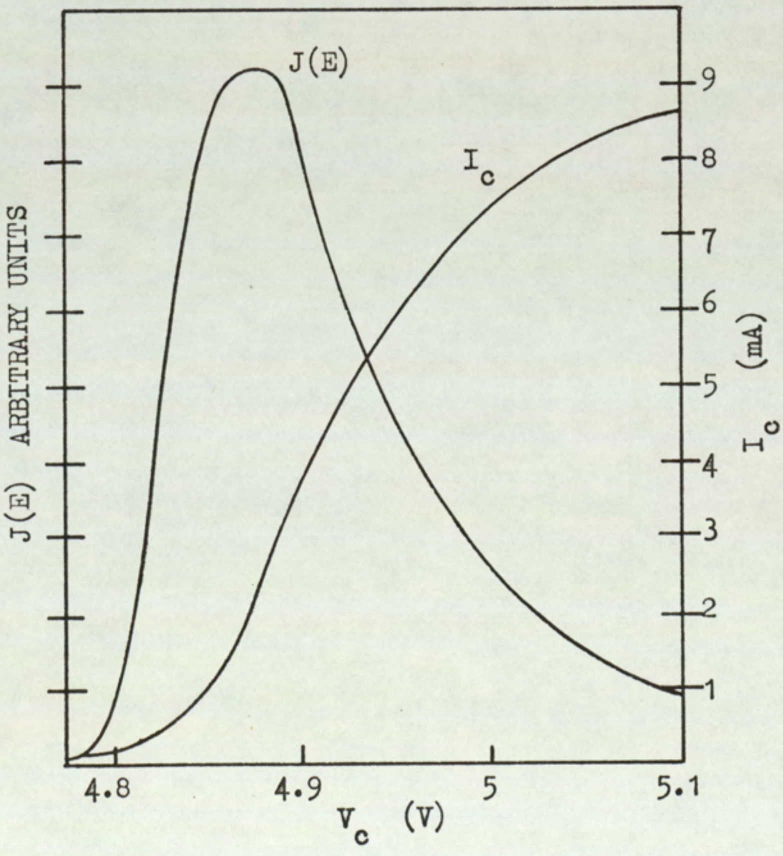

FIG.38. PLOT OF INTEGRAL CURRENT I_c, AND CORRESPONDING DIFFERENTIAL CURVE J(E), AS OBTAINED FROM A RETARDING POTENTIAL ANALYSER, BOTH AS FUNCTIONS OF RETARDING VOLTAGE V_c.

dissadvantages: firstly figure (38) indicates that the low energy part of the integral plot gives a relatively low increase in Ic and hence a poor signal to noise ratio; also the low slope leads to greater errors in the differentiation process. Secondly, electron detection at the collector using an electrometer imposes strict limits on the sensitivity attainable. In terms of the required resolution, which needs to be $\sim$ 20 meV for distributions having half widths of 200 meV, it follows that an overall resolving power of 10^5 is required for 2 KeV electrons arriving at the anode. Since the retarding potential analyser can only achieve this around the peak of the distribution, it is only of limited use in field emission studies where the low energy tail of a distribution often contains important information. Deflection analysers on the other hand are not only able to give this resolution over the entire energy range, but give a direct energy distribution output via an electron multiplier thus achieving much greater sensitivity and gain and also allowing higher scan speeds. Kuyatt and Plummer(124) were the first to use such a deflection instrument for measuring F.E.E.D's. Their instrument used an energy disspersive element that consisted of two concentric spheroids of 25mm mean radius giving 135° beam deflection. The analyser developed in the Aston Field Emission Laboratory is very similar to this but uses 50 mm hemispheres and 180° deflection which not only requires a less complicated electron optical design for the input and output lenses, but also gives other advantages that are discussed below. Details of the design and its perfomance when measuring F.E.E.D's from tungsten microtips has been given elswhere by Braun et. al.(125); Allen and Latham (126) later added a special interfacing lens in-order to study the energy distributions of electrons emitted from broad areas, which has subsequently been refined and improved as part of the research programme reported in this theses.

5.2. The Deflection Analyser: Principle of Operation and Design Parameters.

Referring to figure(39) the heart of the analyser is the energy dispersive element consisting of two concentric hemispheres with a potential difference ΔV across them. This arrangement allows electrons with kinetic energy E, which are focussed at input aperture B, to pass between the hemispheres in great circles and be refocussed at the exit aperture C; as first given by Purcell(127). Electrons with energies outside the pass range $E \pm \Delta E$ of the analyser collide with one of the hemispheres and are either trapped there or emerge diffusely at C. If now the voltage at B is altered (ramped) that part of the energy distribution with energy E will also vary; therefore a graph of the current emerging from C against the ramp voltage will produce the electron energy distribution. Effectively, a window ΔE wide is made to scan the distribution, so that the most exact results will be obtained using a small pass width ΔE. However, ΔE is linearly dependant on the pass energy E, hence a small kinetic energy at the entrance aperture B is required. A lens system is therefore necessary to retard the highly accelerated field emitted electrons having energies of KeV into the analysing energy range of a few eV and to focus an image of aperture A onto B (fig. 39). An output lens then reaccelerates the elctrons emerging at C and focusses them onto aperture D, thereby preventing any scattered electrons at C from passing D in any geat numbers. An electron multiplier collects all electrons accelerating away from D and produces the analyser output signal.

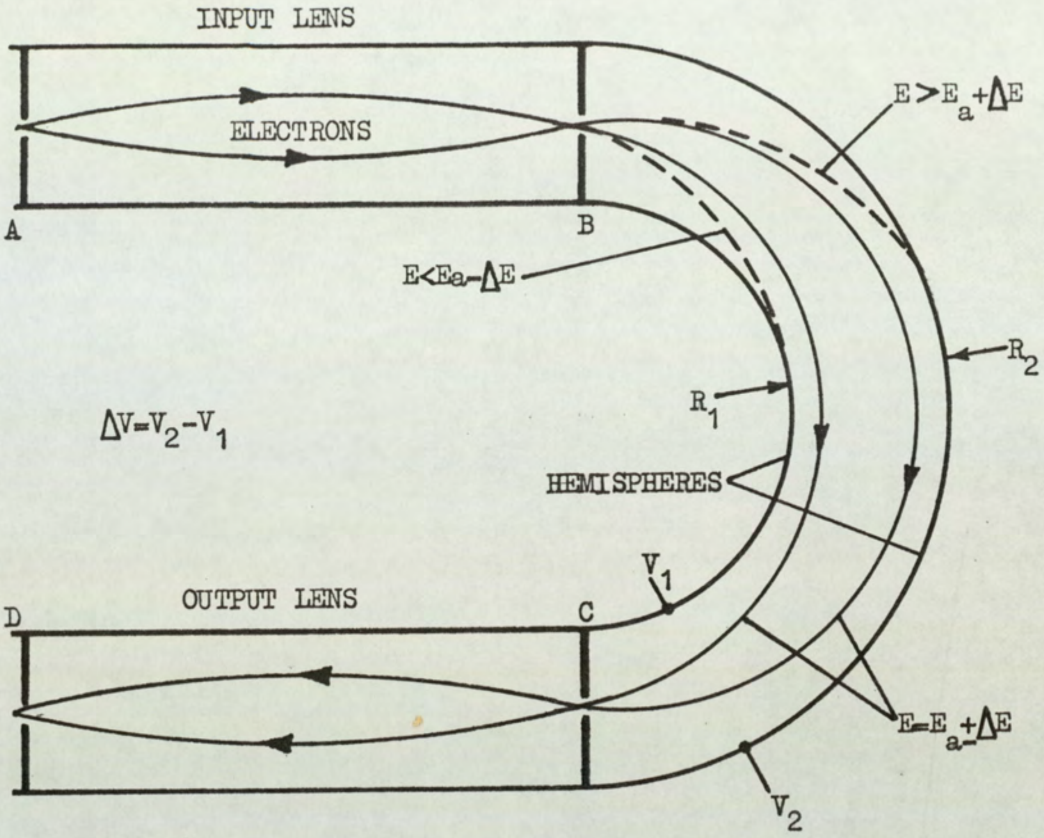

FIG.39. THE PRINCIPLE OF THE HEMISPHERICAL DEFLECTION ANALYSER

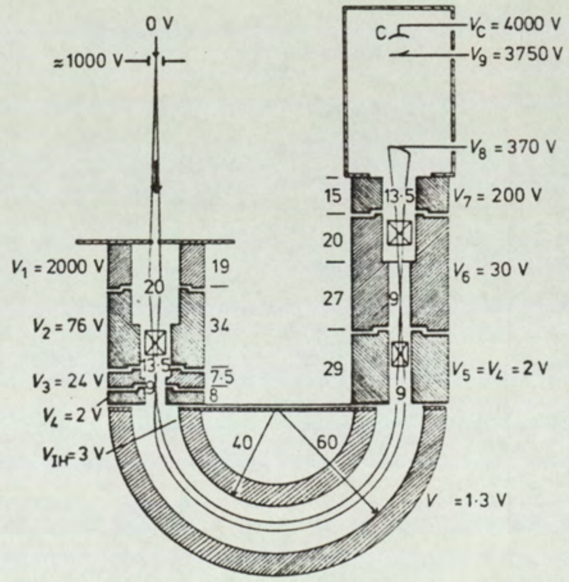

Figure 4 Essential features of the electron optical system. Lengths and internal diameters are shown to the nearest 0·5 mm. Deflector plates are contained in elements 2, 5 and 6. Also shown is a set of experimental operating voltages appropriate to an analysing energy of 2 eV; the voltages are given relative to a hypothetical stainless steel electrode outside whose surface the transmitted electrons would just come to rest. V_8 and V_9 are the voltages on the first and last dynodes of the electron multiplier and V_C is the voltage on its collector C.

FIG.40. DESIGN FEATURES OF THE UNMODIFIED ELECTRON SPECTROMETER.
FROM BRAUN et al (125).

5.3. Design Features of the Hemispherical Analysing Element.

Practical design equations for the hemispherical analyser were given by Kuyatt and Plummer (124) and may be summarised as follows.

a) An electron will move in the mid sphere between the two hemispheres if : $mv^2 = eF_oR_o$, where e is the electronic charge, m the electronic mass, v the electron velocity and F_o is the electric field at radius R_o. From the electrostatic potentials at the mid point of, and immediately outside the hemispheres, and the voltage ΔV across them, the potentials V_1 on the inner hemisphere (radius R_1) and V_2 on the outer hemisphere (radius R_2) can then be calculated, given the analysing energy E.

$$\Delta V = \frac{E}{e}\left[\frac{R_2}{R_1} - \frac{R_1}{R_2}\right] \qquad V_1 = \frac{E}{e}\left[\frac{R_2}{R_1} - 1\right] \qquad V_2 = \frac{E}{e}\left[\frac{R_1}{R_2} - 1\right]$$

b) The resolution is given by :

$$\frac{\Delta E}{E} = \frac{Z}{2R_o} + \frac{\alpha^2}{2}$$

where Z is the input and output slit width and α is the beam angular spread.

To minimise broadening of the transmission function, the input lens is designed so that $\alpha^2 = Z/4R_o$ and therefore $\frac{\Delta E}{E} = \frac{5}{8}\frac{Z}{R_o}$.

c) The minimum deviation of the beam Zm from the central path is given by :

$$\frac{Z_m}{R_o} = \frac{\Delta E}{E} + \left[\alpha^2 + \left(\frac{Z}{R_o} + \frac{\Delta E}{E}\right)^2\right]^{\frac{1}{2}}$$

These equations show that for the best resolution, the smallest pass width ΔE for given energy E is required, and that E, Z and α should be as small as possible with Ro as large as possible. But very low energy electrons are difficult to control because of stray magnetic fields and hemisphere surface potential patch effects (128), while decreasing the aperture size also reduces the total electron transmission through the analyser thus requiring more sensitive detecting equipment. From all these considerations, the Aston analyser was designed to have the following parameters :

$E = 2$ eV Resolution ~ 25 meV

$Z = 1$ mm $R_o = 50$ mm

$Z_m = 5$ mm $R_1 = 40$ mm $R_2 = 60$ mm

$\Delta V = 1{\cdot}67$V $V_1 = +1.0$V $V_2 = -0.67$V

A mu-metal shield was fitted over the whole analyser to screen against magnetic fields, and a subsequent investigation indicated that the electron spectrum was not altered by further shielding against the earths magnetic field using Helmholtz coils.

5.4. The Input and Output Lenses.

When used for analysing the electron emission spectrum of field emitting tips, the spectrometer input lens system needs to fulfil the following criteria :

1) To decelerate the electrons from an energy of ~ 2 KeV to 2 eV at the entrance aperture B.

2) To focus the beam of electrons into the entrance aperture with a small angular divergence.

3) To be capable of operating over the input energy range 1 to 4 KeV and analysing energy range 1 to 18 eV.

These criteria were satisfied by using a three element lens designed by Heddle et al.(129) followed by a fixed ratio lens, all having different diameters so that the overall length of 70 mm was not excessive. Fine beam steering was achieved with

X - Y deflector plates in one of the lens elements.

The output lenses reaccelerate the electron beam from the hemispheres to 200 eV and collimate it into the electron multiplier through a further set of X - Y deflecter plates.

A complete layout of the electron optical system in the spectrometer is shown in figure (40).

5.5. Electrical and Electronic Systems.

Figure (41) shows the original electronic circuitry used for obtaining the lens control voltages, the scan voltage and signal output; i.e. prior to the modifications made during this present research programme. In particular, the lens voltages were supplied from a single fully adjustable 2MΩ resister chain so that the lens voltage ratios, and hence their focussing properties remained constant as the anode voltage V_1 was varied through the range 1 to 5 KV. The voltage ΔV across the hemispheres was adjustable to accommodate analysing energies from 2 eV to 18 eV; the former being used for high resolution work, while the latter higher voltage enabled easier beam alignment, for initial setting up at greater signal strength but low resolution.

The energy scan is still achieved through a versatile ramp generator giving a switched amplitude of 1, 2, 5 or 10V with a continuously adjustable starting voltage, enabling the hemisphere mid potential V_4 to be ramped over these ranges starting anywhere between 0 and 15V, with a scan time variable between 10 mS and 100 S. By ramping the hemisphere mid potential V_4 energy scanning is achieved whilst keeping the voltage across the hemispheres and the anode potential V_1 constant. This approach has the important advantage of having no effect upon the analyser resolution or upon the emission process and only a negligible effect upon the lens focussing properties. Hence at any particular ramp voltage all

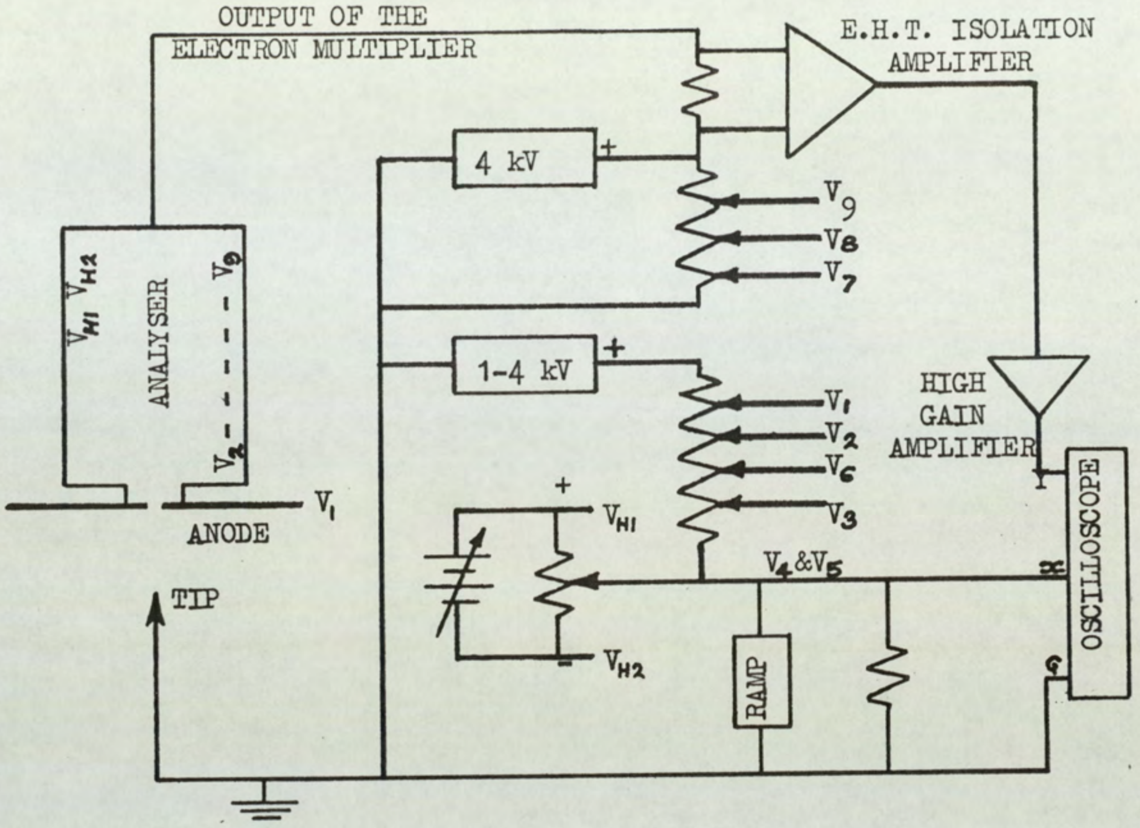

FIG.41. SCHEMATIC DIAGRAM OF THE ORIGINAL VOLTAGE SUPPLY AND SIGNAL PROCESSING ARRANGEMENTS FOR THE ANALYSER.

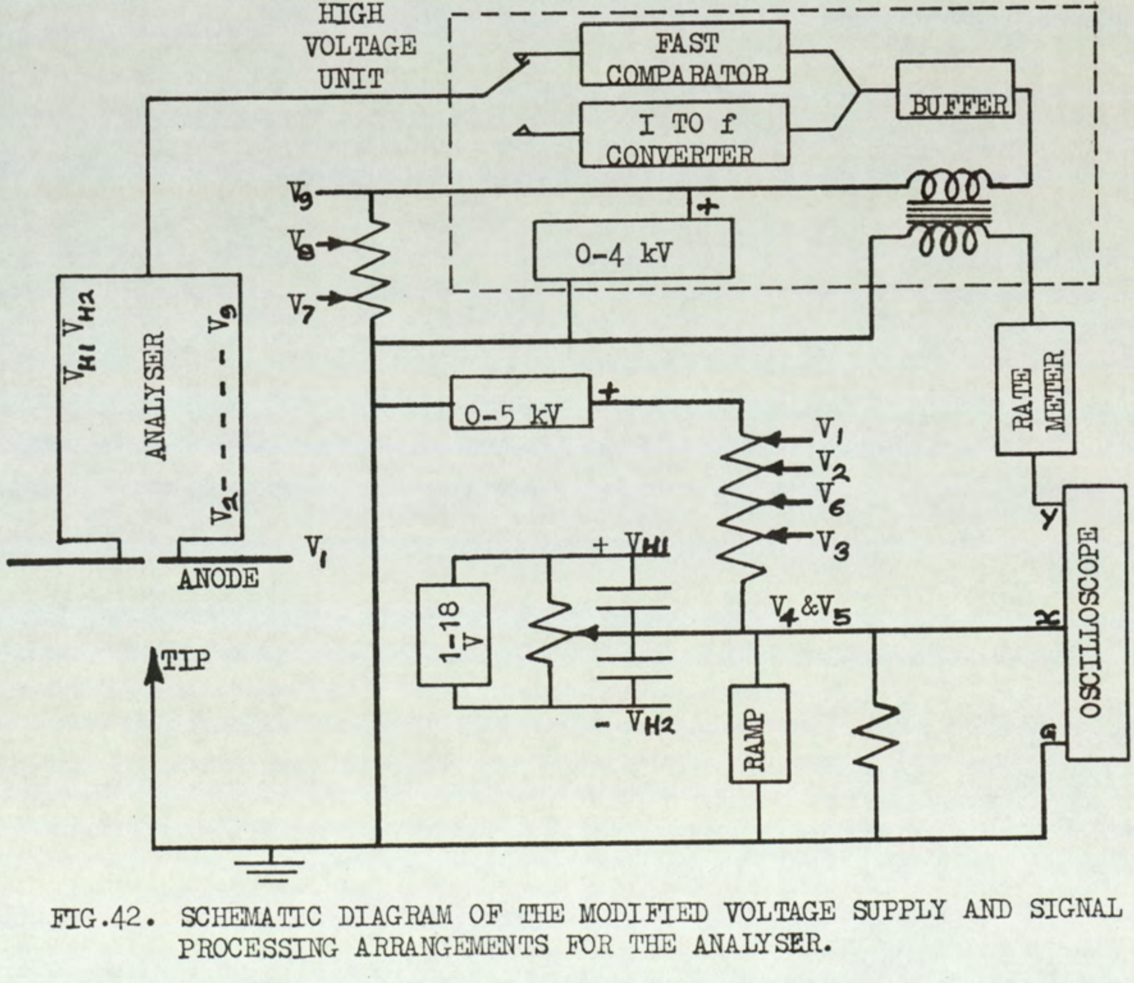

FIG.42. SCHEMATIC DIAGRAM OF THE MODIFIED VOLTAGE SUPPLY AND SIGNAL PROCESSING ARRANGEMENTS FOR THE ANALYSER.

electrons will have their potential energies altered, such that the analyser pass energy will only be equal to the kinetic energy of electrons from a particular part of the initial electron energy distribution. For a different ramp voltage another point in the distribution will give electrons at the analyser pass energy. Thus the plot of the analyser output signal against ramp voltage will recreate the energy distribution.

5.6. Modifications to the Detection System.

Since the old high voltage isolation amplifier was beginning to fail and because the gain of the electron multiplier was rather low, it was decided to up date the entire electron detection system in anticipation of future automatic signal processing methods. The major modification to the detection system consisted of the replacement of the old electron multiplier (Twentieth Century EP 25), isolation amplifier and high gain amplifier, with a new higher gain electron multiplier (Mullard B318AL/01) and a combined signal processing / high voltage unit, giving an output in pulses of constant amplitude at a controlled rate. This system is shown in figure (42). The old electron multiplier with a gain of 2.5×10^5, was replaced by a channeltron having a gain $\sim 5 \times 10^7$, feeding directly into the unit specially designed for electron multiplier systems (Brandenburg model 494). Contained is this unit are the first electronic stages for signal processing, operating at the electron multiplier output potential of 1 to 4 KV, together with the high potential generator. Two modes of operation are then possible. The output current from the channeltron can either be fed directly into an anoloque current to frequency converter, or can be fed directly into a fast comparator which detects the individual current pulses produced when single electrons arrive at the channeltron input. Either way, the circuit output consists of pulses at a rate determined by the channeltron input current. The information contained in this pulse stream is brought to ground potential without degradation by a pulse transformer. This method of isolation does not suffer from the disadvantage of drift which is associated with D.C. isolation amplifiers, or from the restrictions of leakage current and minimum signal frequency associated with high voltage capacitors. Pulses can also be transmitted over quite long distances (several metres in this case) without much trouble. At the far end of the cable a rate meter (Nuclear Enterprises NE 4672) reproduces a voltage signal proportional to the pulse rate as the final analyser output, fed to the Y amplifier of a storage oscilloscope. The only other circuit modification worthy of particular note was the replacement of the battery supplying the hemisphere voltage ΔV with a mains powered stabilised voltage source together with the inclusion of large capacitors connected between the hemispheres and their mid - potential rail. Previously any 50 Hz interference picked up by the hemisphere supply lines tended to modulate the electron stream transmitted through the analyser, thus producing effects on the resulting energy spectrum which could be mistaken for multipeaked fine detail.

5.7. Estimation of Spectrometer Calibration.

Since an electron at the Fermi level of an earthed piece of metal is taken to have zero potential energy, electrons at rest outside the metal will have an energy equal to the metal work function. Thus for the analysing hemispheres with a work function ϕ and mid potential V_4, the kinetic energy E, just outside the hemispheres, of any electron emitted at the Fermi level will be given by $E = eV_4 - \phi$

where E is the fixed analysing energy for the system(normally 2 eV) and V_4 is the ramp voltage. Therefore, to calibrate the analyser, a field emitter having a known Fermi level position on its energy distribution, will enable the scan voltage V_4 at the Fermi level to be measured and hence ϕ calculated.

Young (59) has indicated that for a clean tungsten emitter at $\sim 300^{\circ}$K, the Fermi level occurs 73% up the high energy slope of the distribution; Braun et al (125) used this to obtain the measured value of ϕ for this instrument which is $4{\cdot}26 \mp 0{\cdot}03$ eV. With E = 2eV (depending only on the hemisphere potential $\Delta V = 1{\cdot}67$V) This gives a value for V_4 at the Fermi level for any subsequent emitter of 6•26V.

5.8. Resolution Determination.

Young and Kuyatt (130) established the following criteria for assesing the resolution from field emission spectra. Assuming a Gaussian transmission function for an energy analyser of the form:

$$G(E) = \frac{0{\cdot}939438}{(FWHM)} \text{EXP} \left[- \frac{2{\cdot}772588\, E^2}{(FWHM)^2} \right]$$

where (F W H M) is the full width at half maximum of the transmission funtion, the effect on the field emitted energy distribution P(E) dE is given by the convolution :

$$J(E) = \int P(E_1)\, G(E_1 - E)\, dE$$

The resolution is then defined to be the difference in energy ($\Delta J(E)$ between the levels 10% and 90% up the high energy edge of the F.E.E.D. Resolution defined in this way is particularly sensitive to variation in the F.W.H.M. of the transmission function, although figure (43) indicates that a low temperature is required if meaningfull results are to be obtained.

This approach of course presumes a well calibrated and easily reproducible energy distribution from a tungsten micropoint; infact Braun el.al.(125) showed the high energy slope to be very dependent on surface contamination, and only obtained a distribution close to the theorestical value after thorough cleaning by field desorption. They then found a high energy slope width of 0·11 eV against a theoretical value of 0·10 eV. Using figure (43) this gives an analyser F.W.H.M. of 50 m eV. However, a rather large peak displacement indicated that the emitter was still not fully cleaned, hence they finally conclude the F.W.H.M. to be $<$ 30 m eV. especially since a low temperature is required for meaningful use of figure (43).

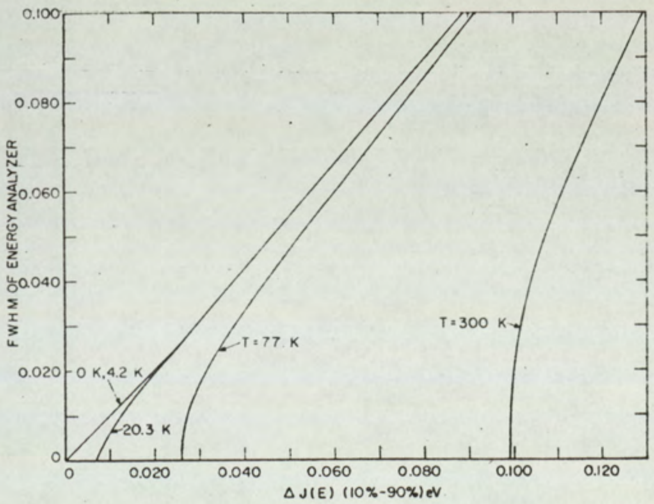

FIG. 5. FWHM of energy analyzer as determined from the high energy edge of its measured E.D. at various temperatures: FWHM vs measured energy difference between the 10 and the 90% points on the E.D. leading edge. φ and F—same as above. Note that temperatures considerably below 300 K are needed for meaningful resolution determination.

FIG 43. THE PLOT OF ANALYSER F.W.H.M. AGAINST THE HIGH ENERGY EDGE OF ITS MEASURED ENERGY DISTRIBUTION. from Young & Kuyatt (130)

5.9. Modifications for Broad Area Measurements.

Originally Braun et.al.(125) developed the spectrometer for use on laboratory fabricated field emitting tips T, as indicated in figure (44a). This simple arrangement was all that was required since the high field is produced as a result of the tip geometry : the maximum voltage at the anode A being the analyser lens voltage V_1 in figure (42), i.e. ~5 KV.

To excite the emission processes observed for broad areas however, it is necessary to use fields up to 30 MVm^{-1}, that is 15 KV across the standard gap of 0•5mm. Allen and Latham (126) solved this problem by designing an interfacing lens,using a graphical field plotting technique, as shown in figure (44b). The test gap was established between a specimen and the anode A_1 which was capable of taking a potential of 10 KV; the lens structure L connected directly to the analyser anode A then focussed the emitted electrons into a parallel beam and decelerated them from an energy of ~10 KeV down to ~2 KeV at the analyser input. Focus adjustment was undertaken by varying the analyser anode potential from 1 to 5 KV.

This lens proved satisfactory for earlier work but has been found during this study to suffer from some design over simplifications. Paramount amongst these was the assumption that a "single" emitting region produced electrons all emenating from an effective point source: this was found not to be the case, as will be shown in the experimental section, and in consequence, the interfacing lens has been refined as shown in figure (44c). Here the major modification was the replacement of the analyser entrance aperture anode A (hole diameter 1mm), with a smaller aperture anode (hole diameter 0.2mm) having a phosphor coating applied to

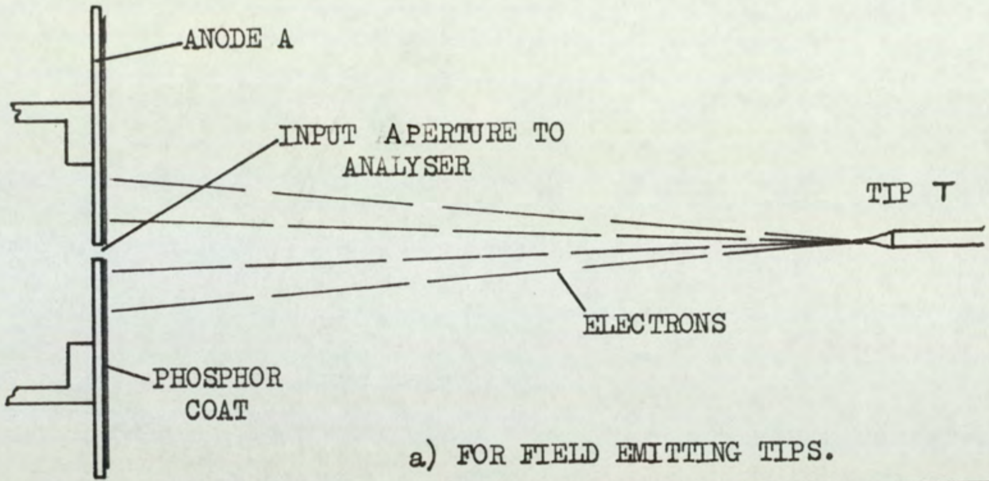

a) FOR FIELD EMITTING TIPS.

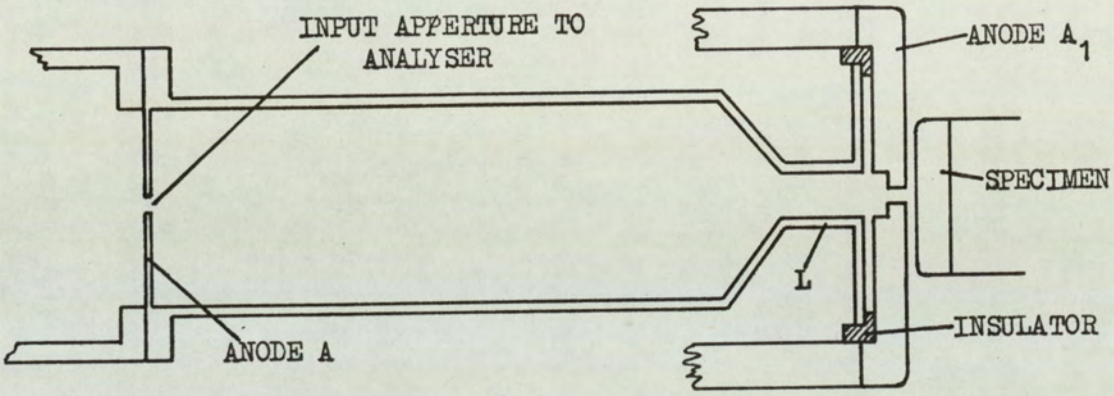

b) AS ORIGINALLY USED FOR BROAD AREA ELECTRODES.

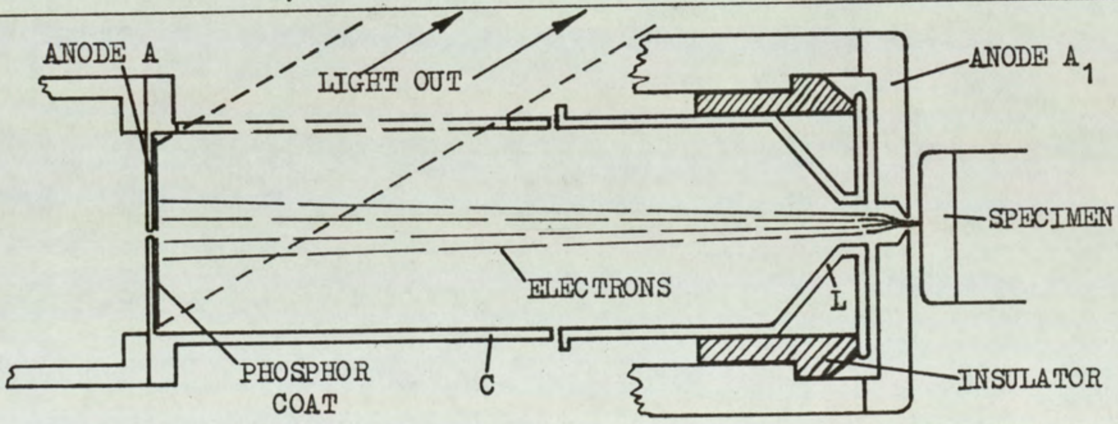

c) FOR BROAD AREA ELECTRODES, AS MODIFIED TO VIEW THE ELECTRON IMAGES.

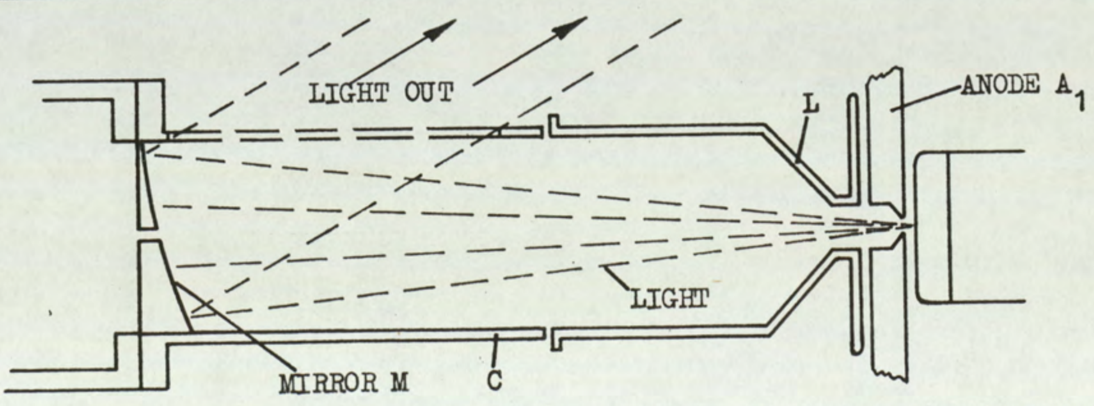

d) FOR BROAD AREA ELECTRODES, AS MODIFIED TO VIEW THE EMITTED LIGHT.

FIG.44. INTERFACING ARRANGEMENTS BETWEEN THE SPECTROMETER AND EMITTER

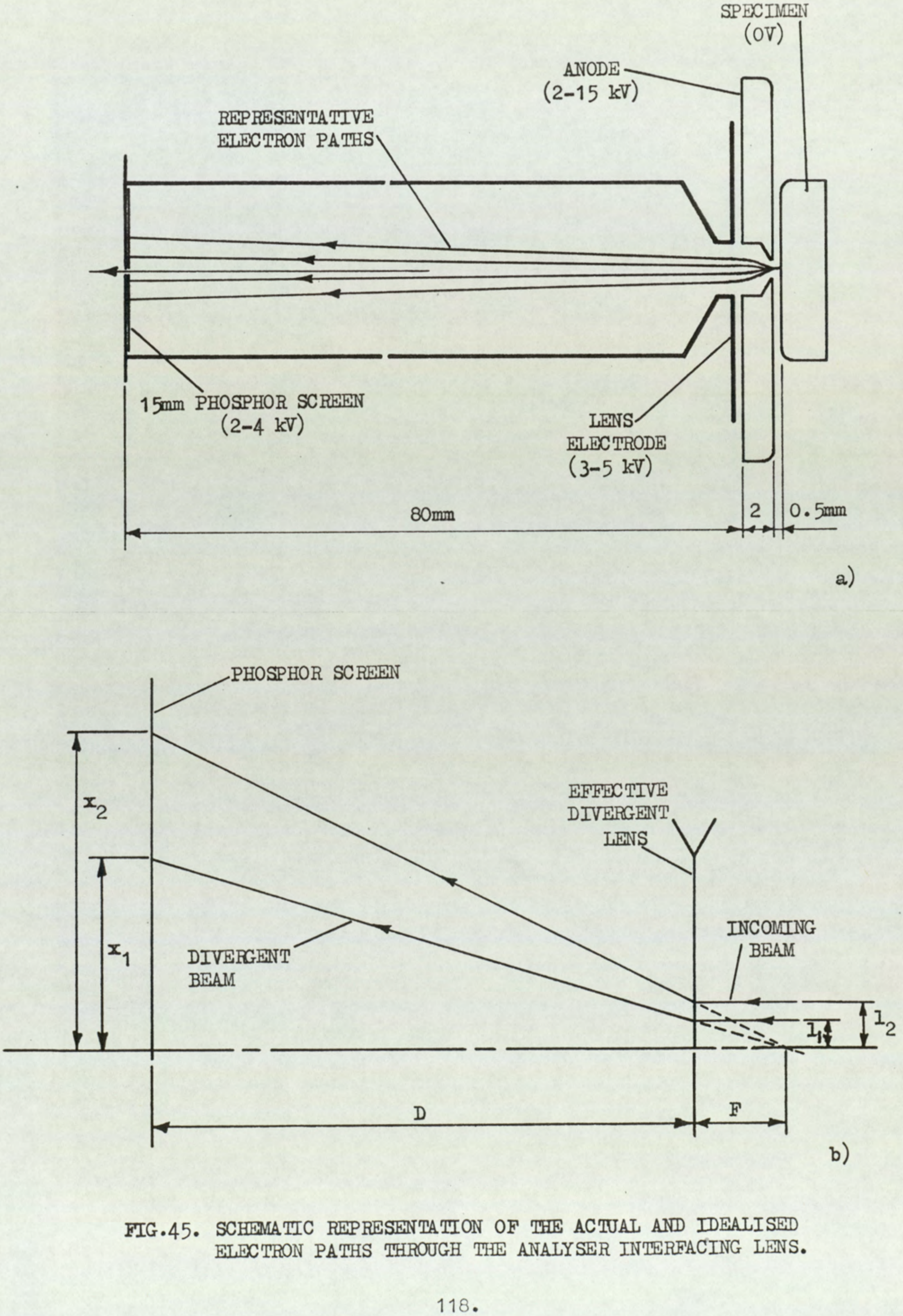

FIG.45. SCHEMATIC REPRESENTATION OF THE ACTUAL AND IDEALISED ELECTRON PATHS THROUGH THE ANALYSER INTERFACING LENS.

one side. This naturally cut down electron transmission into the analyser but this was more than off-set by the new electron multiplier detector. The electrical connection between lens L and anode A was broken to allow a separate high voltage to be applied to L giving better focus control , and a hole was cut in the side of cylinder C enabling the phosphor screen deposited on anode A to be viewed. Further refinements included a reduction in the length of the narrow section of lens element L and chamfering of the back face of anode A_1. Both of these measures being attempts to minimize any secondary electron emission or possible interference with the electron optical path, since some aberration had been detected earlier. A re-design of the lens support insulator resulted in the important experimental advantage that $V \sim 15$ KV could be applied to anode A_1 without trouble.

5.10. Properties of the Modified Input Lens.

An examination of the imaging properties of the high voltage gap-input lens electrode system for the usual operating voltages, ie. V-anode 3 to 10 KV, V-lens 2·5 to 3·2 KV and V-screen 2·5 to 3·5 KV (see figure 45a) revealed the following characteristics. A point emission source on the specimen cathode gave a divergent electron beam which then produced a projection image on the screen at the analyser input electrode, i.e. similar to that described by Juttner (131) for electron emission from millimetre radiused tips. This mode of operation is consistent with the following observations: a) The image focus was not affected by reasonable changes in the electrode voltage, although the magnification varied considerably and b) there was no reversal of image motion with respect to specimen motion; that is both the image and specimen moved up or down together. These properties can be understood by reference to figure (45b) which shows idealised electronoptical paths for the overall divergent lensformed by the combined action of the fields associated with the anode-specimen and anode-lens gaps. This approximation assumes that the electron beam just in front of the anode probe hole is parallel and perpendicular to the anode face. Hence the calculations below are only a first order estimate since the actual arrangement is an "emersion" system where the emitted electrons are never outside the influence of the lens electrostatic field even near the specimen surface. From figure (45b) it will be seen that for each ray

$$\frac{l_1}{F} = \frac{x_1}{D+F} \quad \& \quad \frac{l_2}{F} = \frac{x_2}{D+F} \qquad (1)$$

Hence the magnification

$$M = \frac{x_1}{l_1} = \frac{x_2}{l_2} = \frac{D}{F} + 1 \qquad (2)$$

giving $x_2 - x_1 = M\left(l_2 - l_1\right)$ (3)

under these conditions the image is always in"focus" for any magnification.

Since $D = 80$ mm and $F = 1$ to 3 mm, as estimated from the apperture and lens geometries (the exact value depends on the focus voltage), equation 2 gives a range of values for M from 28 to 81. A check was made on this esstimate by noting the amount of specimen movement necessary to drive the undistorted image shape across the 15 mm diameter phosphor screen. Thus by setting V-anode = 7 KV, V-screen = 2·8 KV and V-lens = 2·7 KV this gave a measured value for M of 58. Because figure (45) assumes an approximately parallel input beam, it follows that the image size should be independent of the specimen-anode spacing. This behaviour was infact observed over a gap range 0.3 to 2 mm, although of course the image brightness varied at the same time, making further checks difficult.

An additional very useful property of the lens was that variations in the anode voltage alone, over the usual range, did not significantly alter the emission image size. In fact this was to be expected because the strength of the converging section of the input lens depends on the voltage difference (Vanode—V lens), whereas the elctron kinetic energy depends on the difference (Vanode—V specimen) and the two effects tend to cancel each other out.

All these measures enabled a proper examination of the spatial distribution of electron density at the spectrometer input, which was found immediately to consist of emission from a number of sub-centres (usually ~ 5) associated with a single site, as will be shown in chapter 6.

5.11. Modifications Enabling Combined Optical and Electronic Measurements.

As the interfacing lens was being re-designed, an additional factor to be born in mind was the easy conversion to the layout shown in figure (44d). Thus the coated anode A has been replaced with an anode having again a 1 mm diameter hole but also a machined and polished spherical mirror M set at an angle to the lens centre line. This arrangement allowed electrons from a site to pass as before but also allowed any light emitted from the same site to hit the spherical mirror and be transmitted out in an approximate parallel beam.

It was hoped by this means to extend the rather crude measurements of the optical properties of emission sites, since here there is no doubt that both the electronic and any optical phenomena originate from the same small area. To date however the results have been disappointing there being no sign of any light emitted from the specimen surface, at least just using the naked eye in a dark room.

5.12. Analyser Calibration and Resolution Following the Broad Area Modifications.

Checks on the analyser calibration and operational resolution following the original broad area modifications of Allen & Latham were made by Athwal,(96) who used a tungsten micropoint emitter embedded in a re-entrant divot machined in a standard broad area electrode. This structure attempted to simulate as closely as possible the actual fields encountred in broad area measurements while hopefully obtaining the energy spectrum associated with a clean tungsten tip. This proved to be only partially successful as it was not possible to thoroughly clean the tungsten emitter. However, the spectrum gave the correct position for the Fermi level and a high energy slope width of 0·12 eV; which from the Young-Kuyatt (130) criteria gives a resolution of $\sim$80 m eV, i.e. apparently indicating that resolution had been considerably degraded. However, from other charateristics of the spectrum, in particular a rather high half-width, Athwal concluded that this was due to contamination similar to that pointed out by Braun et al (125), and that the modifications had produced no significant changes in calibration or resolution. This has subsequently been repeated and the conclusions found to be reasonable after an adequate system bake out.

5. 13. The Specimen Manipulator.

In order to analyse the energy distribution of electrons emitted from sites found on broad area electrodes, it is obviously necessary to first locate a site and position it axially oposite the probe hole in the anode (A_1 of figure 44); i.e by scanning the specimen in a systematic manner in-front of the anode. This was originally accomplished by Allen & Latham(98,126) by using a very slow semi manual specimen scanning arrangement that effectively produced a T.V. type raster pattern of the probe hole current detector over the whole specimen surface. In this system the scanning motion was transferred to the specimen holder via a single control rod passing through a bellows system into the vacuum chamber. The specimen manipulator was constructed from three "Microcontrol" type MR" translation stages : one for adjusting the gap setting (the Z co-ordinate) and the other two providing the scanning motion across the anode face (x and y co-ordinates). A rotary drive (V.G. - R.D.I) and an adjustable hinge provided adjustment of the specimen face such that it could be set parallel to the anode prior to scanning. Further alignment corrections could be made by rotation and tilt of the manipulator base plate until, at the neutral scan position, the probe hole was oposite the specimen centre and also a constant gap was maintained during scanning. A schematic diagram of all these possible movements is presented in figure (46). However this has now been upgraded to include motor drives in both the x - y dimensions via cams and gear boxes, and 10 KΩ specimen position sensing potentiometers, thus converting the system to fully automatic operation using an electronic motor controlled design for this particular application. This effectively produced a spiral

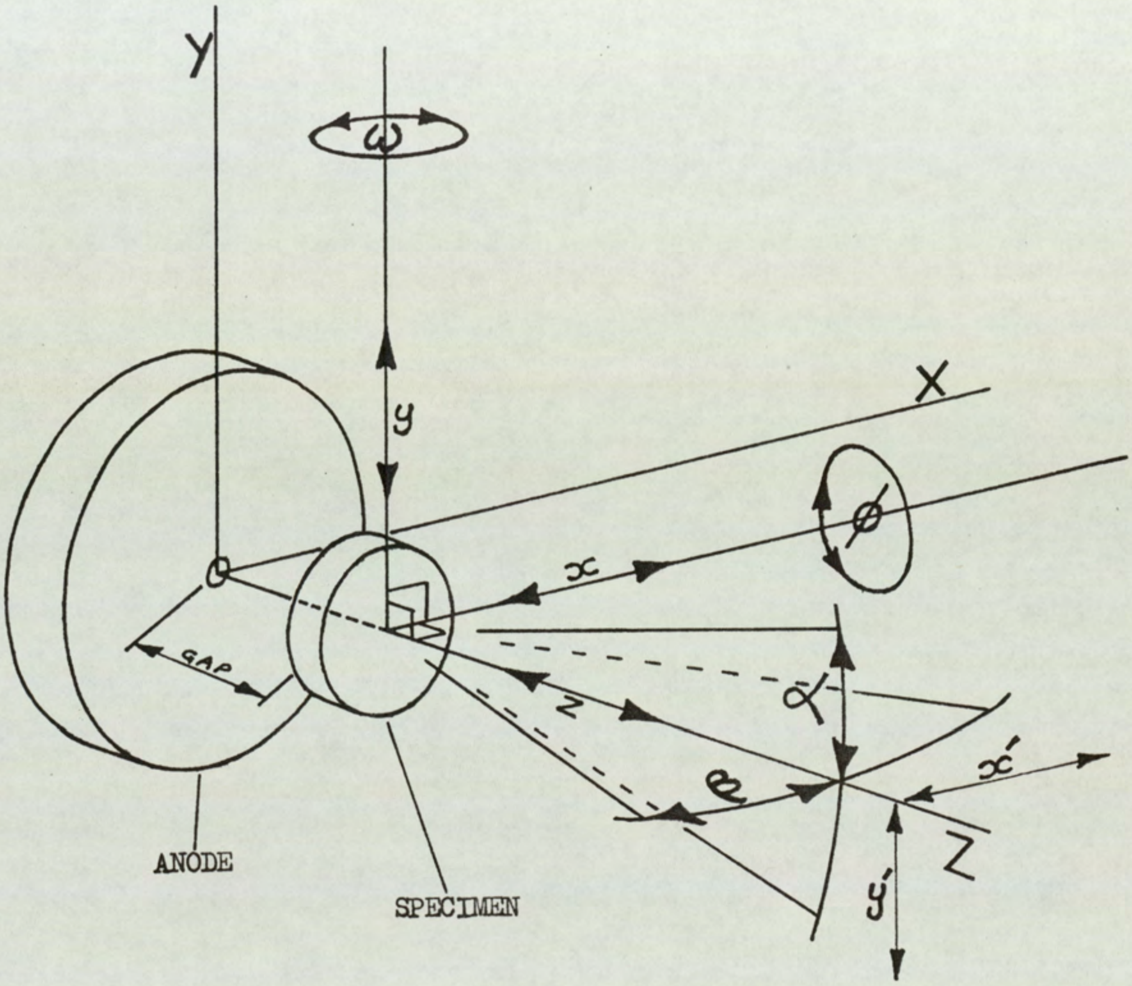

X,Y,Z are the rectangular Cartesian co-ordinates of the anode plane.

x,y,z are the rectangular Cartesian co-ordinates which determine the specimen position.

α & β are adjustment angles to allow x & y to be set parallel to X& Y.

x'&y' are linear adjustments to allow the specimen and anode centres to coincide when x=0=y.

ϕ & ω are rotation adjustments to allow the specimen face to be set parallel to the anode face.

FIG.46. SCHEMATIC DIAGRAM SHOWING POSSIBLE ADJUSTMENTS TO THE SPECIMEN POSITION IN RELATION TO THE ANODE FACE.

scanning motion of the probe hole over the circular specimen face which allowed much greater operator freedom, smoother scanning and a considerable saving of time.

5.14. Electronic Motor Control Circuity.

The complete unit shown in figure (47) generates the control waveforms for the two motors that give the specimen stage x and y motion. Specimen position is then determined either from seperate x - y controls using cartesian co-ordinates for manipulations around a known site position, or from a spiral generator using polar co-ordinates to provide the entire information for specimen surface-scanning. A brief description of the servo loop motor controller is now presented.

5.14.a) The Motor Drive System.

This circuit was designed using cheap and readily available components capable of providing the necessary output power ,ie (∼ 1/5 H.P.) Thus referring to figure (47), the motor field winding is fed at 220 V.D.C. from the bridge rectifier system D_1; adjustment of R_1 setting the rated field current. The motor armature is then fed with current pulses from the triac T_1, which is triggered in such a way that either part of the positive, or part of the negative, half circle of the main supply is used to provide shaft speed control in both directions. R_2 , C_2 , L_1 then filter out the motor commutation "spikes" and together with R_3 , C_3 - C_4 prevent false triggering of the triac. The gate control voltage of the triac is generated by IC_1 such that the triac is fired whenever the voltage (+ve or -ve) at point A reaches approximately $\pm$ 0·6V, as set by the foreward voltage of the two series silicon diodes (eg D_5 - D_6). Point A carries a voltage waveform which is produced by the summation of an effective d.c. signal from the specimen position loop amplifier IC_2 and the

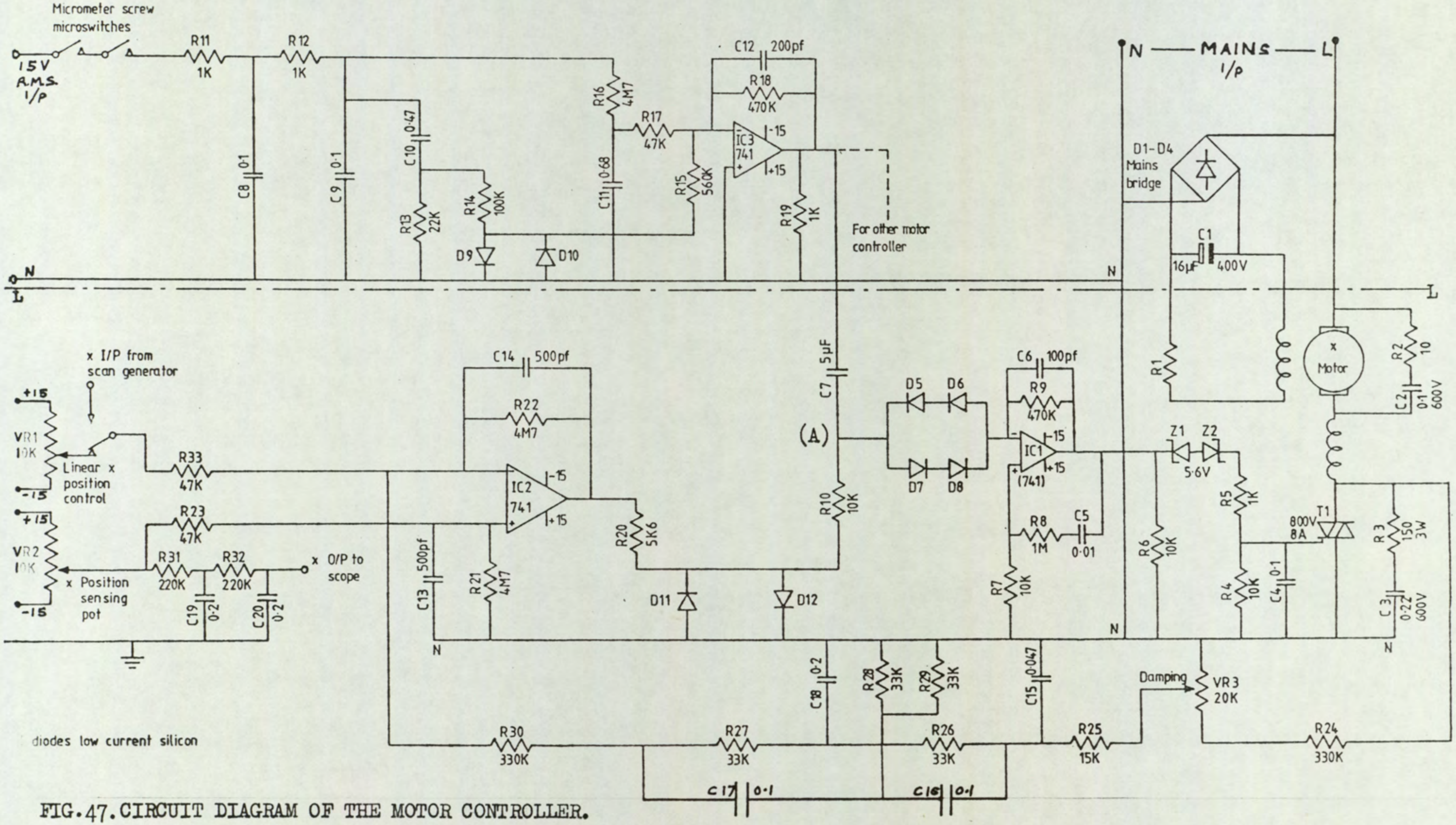

FIG.47. CIRCUIT DIAGRAM OF THE MOTOR CONTROLLER.

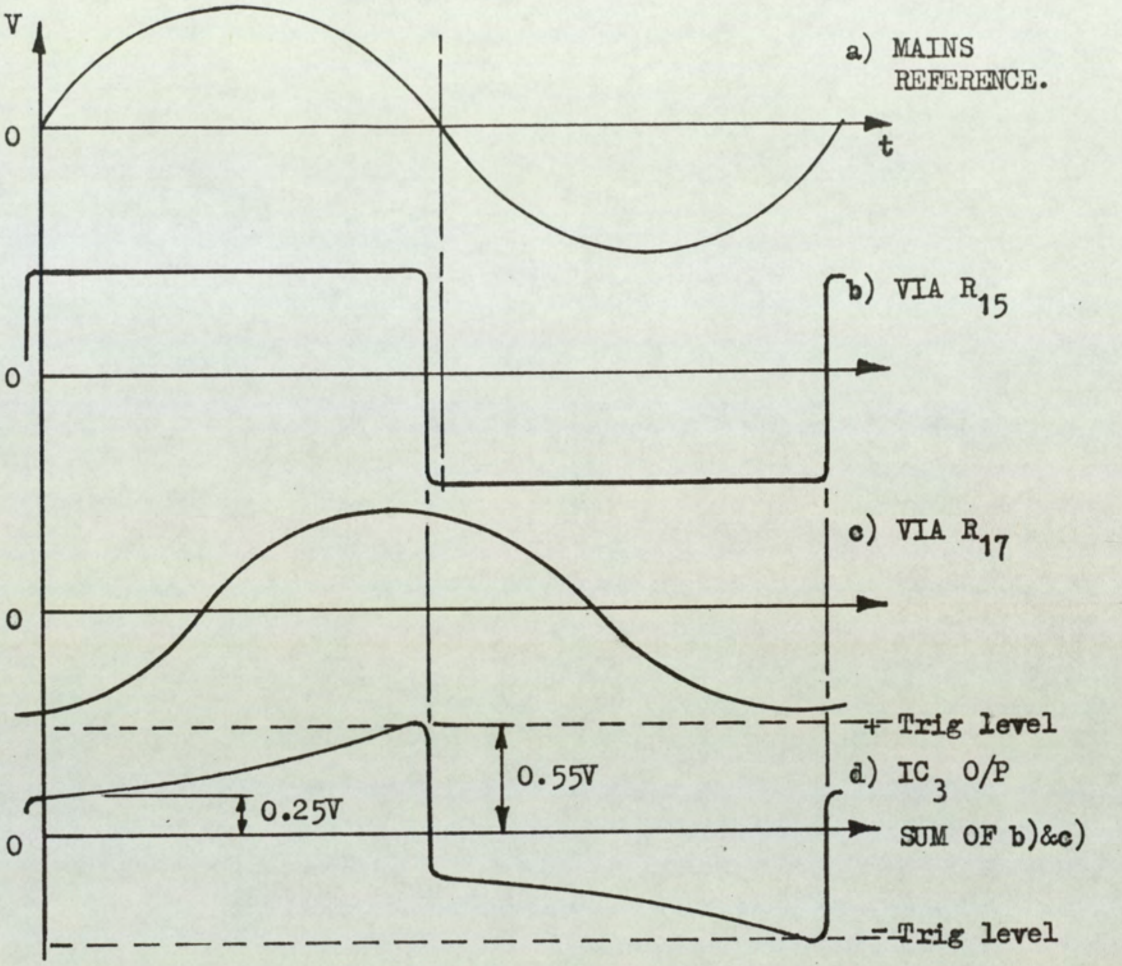

FIG.48. TRIAC TRIGGER VOLTAGE WAVEFORMS.

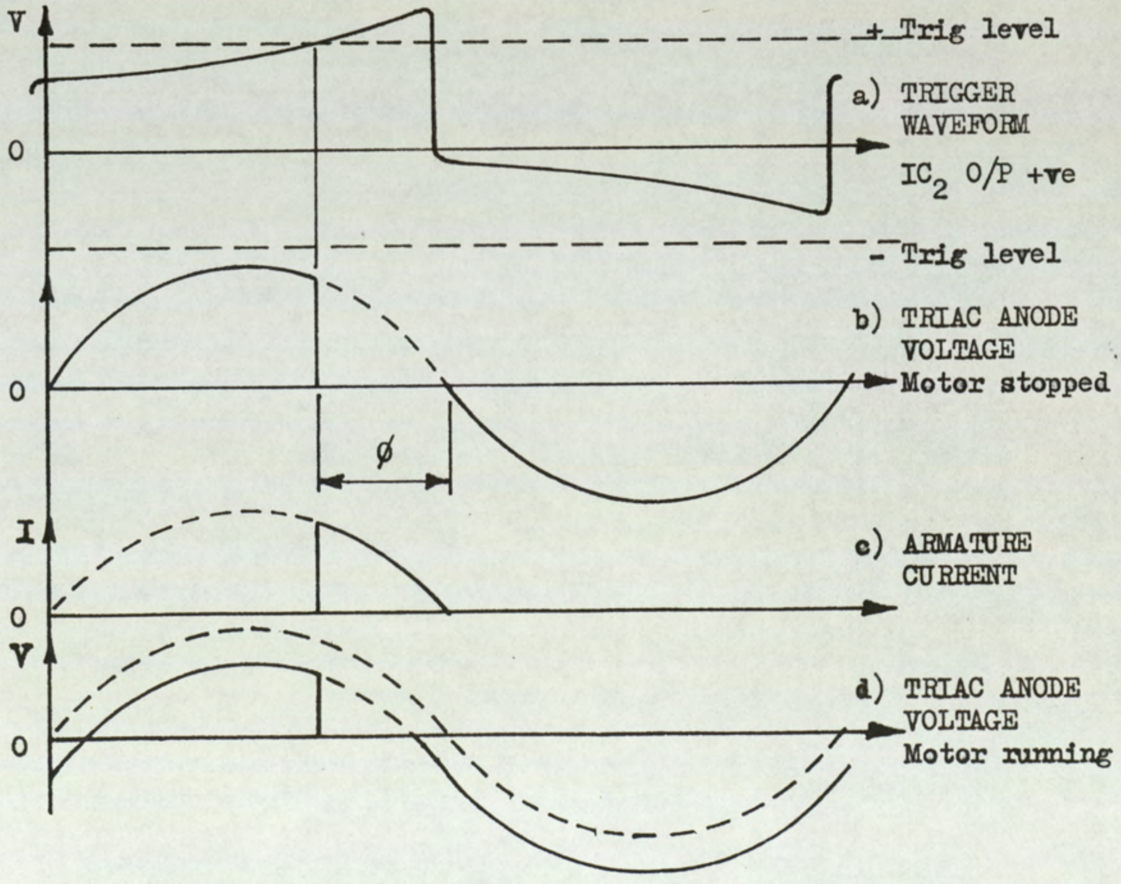

FIG.49. CONTROL AND DAMPING VOLTAGE WAVEFORMS.

waveform fed via C_7 from IC_3.

The output of IC_3 is generated as follows. A 15V R.M.S. voltage in phase with the mains supply (figure 48a) is first filtered and then passed to two phase-shift netwrks: firstly components C_{10}, R_{13} give a sine wave with a few degrees phase lead relative to the voltage in figure (48a), which is then clipped and fed to IC_3 via R_{15}; secondly, R_{16}, C_{11} produce an $\sim 85^\circ$ phase lag signal (figure 48c) which is also fed to IC_3. The output of IC_3 is then so proportioned by R_{15} - R_{18} and C_{12} to appear as in figure (48d).

The differential amplifier IC_2 forms the standard error amplifier in the position control loop but it's output voltage is limited to values inside the range $\pm$ 0.6V by D_{11} - D_{12} irrespective of large "over voltage" inputs, this prevents the entire wave form at A being lowered or raised so much as to be outside the half cycle control range. The output of IC_2 then either raises or lowers the d.c. level of the waveform at point A (figure 47) to give control of triac firing angle ϕ as shown in figure (49b & d). Thus, as the potential set by VR_1 is varied, the motor adjusts the position of the specimen stage, and hence the slider of the position detector VR_2, until the potential difference (VR_1 - VR_2) tends to zero. The potentiometer VR_1 thus functions as the specimen stage x position control.

Control loop damping is provided by tapping off a small fraction of the triac anode voltage through R_{24} and VR_3; the voltage at VR_3 - slider is then passed through a 50 HZ rejection filter R_{26} - R_{29}, C_{16} - C_{18}, and to the differential amplifier IC_2 through R_{30}. Hence the triggered triac anode voltage if the motor is not running might be as in figure (49b). However, as the motor shaft turns, the wave form changes to that shown in figure (49d) where, for a constant triac firing angle, the whole profile has been depressed negatively by the back E.M.F. of the running motor. This E.M.F. is directly proportional to the motor speed and, after filtering by R_{26} etc., provides the damping voltage required for the servo control loop. The filter needs very high rejection at 50 Hz and the bridged T circuit shown has proved quite satisfactory. Ideal values for the sharpest tuning are given by:

$$\omega = 100\,\pi = \frac{1}{CR} \qquad C = C_{16} = C_{17} \qquad R = R_{26} = R_{27} \qquad 2C = C_{18}$$

$$\frac{R}{2} = R_{28} \text{ in parallel with } R_{29}$$

The potential at VR_2 - slider gives a direct measure of the specimen stage x position when fed to an amplifier of an oscilloscope, where the filter R_{31} - R_{32}, C_{19} - C_{20} removes any 50 Hz components picked up from neutral to earth.

5.14.b) The Y Drive System.

This is identical to the x drive system so that only those components shown below the line (L - L) in figure (47) needed to be duplicated. It follows that all x labels in figure (47) should be rewritten in terms of y for this system.

5.14.c) The Spiral Scan Generator

Instead of using the voltage derived from the slider of VR_1 in figure (47) an independent controlling voltage of comparable amplitude can be used to drive the specimen stage to any available x position; likewise for the specimen stage y position. Thus, by applying the correct x and y voltages simultaneously to the two motor controllers this provides a means of spirally scanning the surface of a specimen. A suitable circuit for generating the necessary x - y voltages to give a linearly decaying spiral is shown in figure (50). This is an anologue computer arranged to solve the second order differential equation

$$\frac{d^2Z}{dt^2} + \frac{k}{CR}\frac{dZ}{dt} + \frac{1}{C^2R^2}Z = 0 \qquad (4)$$

$$\text{with } Z = 0 \text{ and } \frac{1}{CR}\frac{dZ}{dt} = r \text{ at } t = 0 \qquad (5)$$

Here Z is a parameter from which x and y can be derived and is of the form

$$Z = A\,e^{-at}\,\text{Sin}\,(wt) \qquad (6)$$

$$\text{where } A = \frac{CR\,r}{w},\quad a = \frac{k}{2CR} \text{ and } w^2 = \frac{1}{C^2\,R^2} - \frac{k^2}{4C^2\,R^2} \qquad (7)$$

so that if k is small enough $w = \frac{1}{CR}$ and the Sin term of equation 6 remains a good approximation even if k then varies.

Solution of equation 4 is accomplished by coupling two integrators (IC_1 RC) and (IC_2 , RC) and a summing amplifier IC_3 into a feed back loop such that the decay term k is determined by R_5 , $D_1 - D_2$. The potential divider formed by R_5, $D_1 - D_2$ then makes k a function of the magnitude of $\frac{dZ}{dt}$, since the resistance presented by $D_1 - D_2$ is decreased as the current through R_5 increases. As a result k then varies in exactly the right way, due to the exponential nature of the diode's foreward conduction characteristic, to offset the e^{-at} term of Z in equation 6. The function Z then becomes approximately

$$Z = A\ (1 - K)\ \text{Sin}\ (wt) \qquad (8)$$

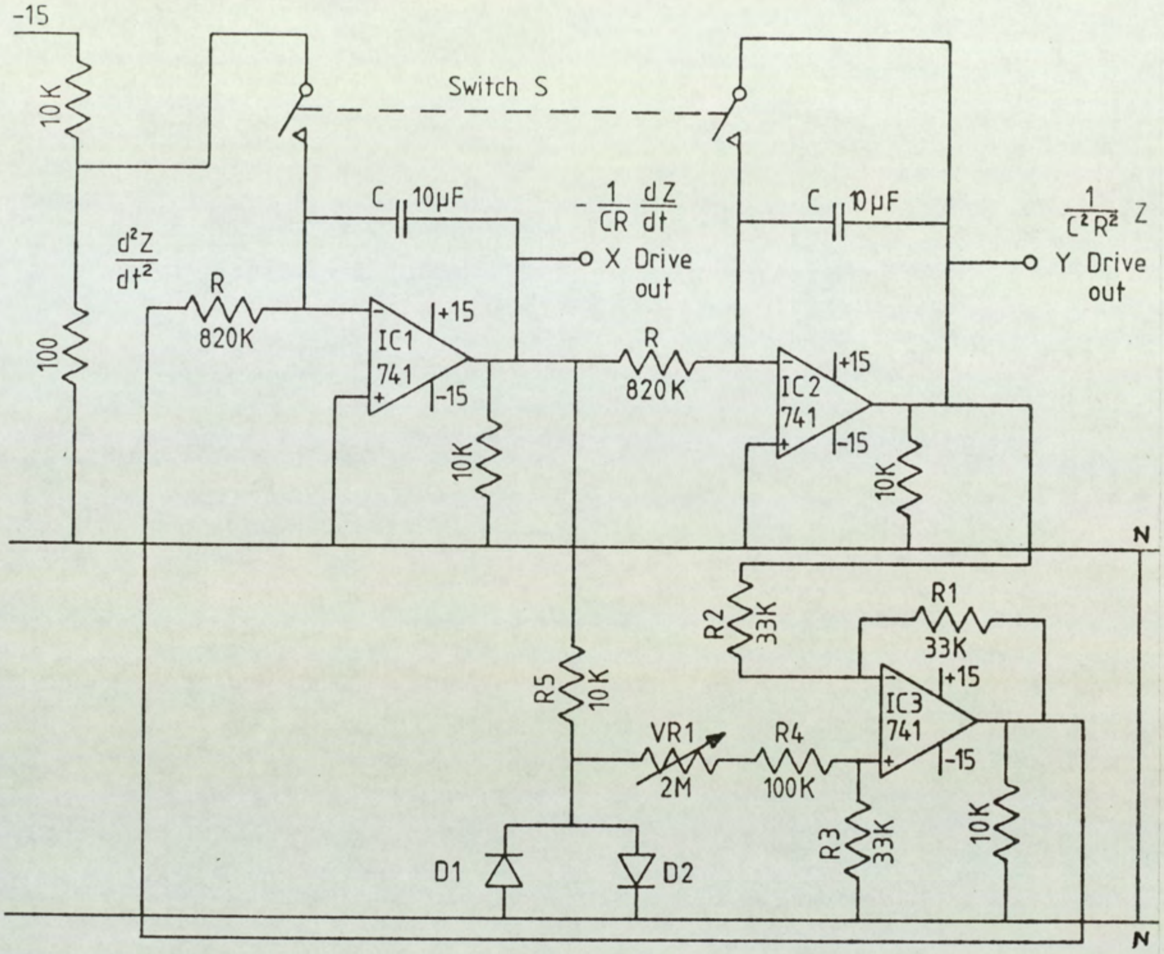

FIG. 50. CIRCUIT DIAGRAM OF THE SPIRAL SCAN VOLTAGE GENERATOR.

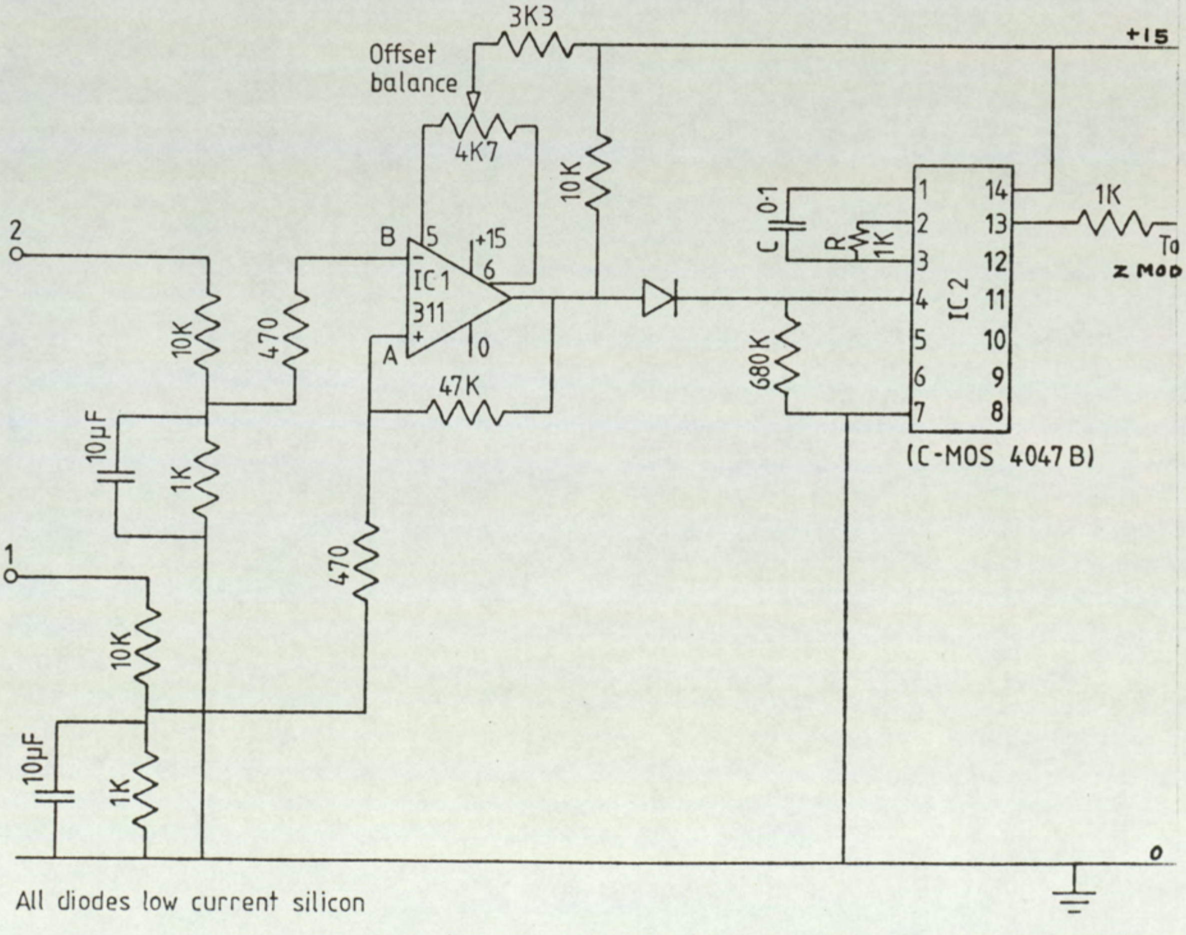

All diodes low current silicon

FIG. 51. CIRCUIT DIAGRAM OF THE OSCILLOSCOPE "BRIGHT UP" AND THRESHOLD DETECTOR.

for $0 < Kt < 1$ and $Z = 0$ for $Kt > 1$, (9)

where K is a new parameter adjusted by VR_1

The x and y outputs which determine the specimen stage position via the motor controller have the form

$$y = Z = r(1 - Kt)\,\mathrm{Sin}\,(wt) \qquad (10)$$

$$x = -\frac{1}{CR}\frac{dz}{dt} = -r(1 - Kt)\,\mathrm{Cos}\,(wt) + \frac{K}{w}\,r\,\mathrm{Sin}(wt) \qquad (11)$$

$$\text{giving } x = -r(1 - Kt)\,\mathrm{Cos}\,(wt) \text{ since } K/w \ll 1 \quad . \qquad (12)$$

These are the cartesian equations for a linearly decaying spiral starting with a radius r. In polar form (R,θ),

$$R^2 = x^2 + y^2 \text{ and } \mathrm{Tan}\,\theta = \frac{y}{x} \text{ giving } \theta = -wt \qquad (13)$$

and $R = r(1 - Kt)$. Close to the origin, as Kt approaches 1, the approximations for Z are no longer valid since k gets larger and the solution then takes the form of a heavily damped second order system going zero very quickly.

The spiral is started by closing the switch S, setting $y = o$ and $x = r$ (the maximum output for IC_1) and upon opening S the spiral is generated

5.14.d) Site Detection and Scope Bright-Up Circuit.

The preceeding circuits allow the surface of a specimen to be spirally scanned in a search for the microscopically localised electron emission sites which could be anywhere on the electrode surface. This scanning facility when used in conjunction with an oscilloscope, having a blanked out trace which is synchronized with the position of the probe hole as it moves over the specimen surface, thus allows a "picture" of the spatial site distribution to be built up in the manner of a radar viewer. Hence a point will be reached during a scan when electrons from an emitting site will be oposite the probe hole in the anode. These electrons then pass through this hole and are collected by the electrode assembly immediately behind the back face of the anode to give a signal on an in-line electrometer. An output voltage proportional to this current, together with a voltage representative of the total emission collected by the anode from all sites on the specimen are used as follows in the circuit of figure (51). Fractions of these two voltages are fed into the comparator IC_1 so that point A receives the voltage from the site detection electrometer and point B the voltage from the total specimen current electrometer. With no site current detected, B is more positive than A and the comparator output is zero. When A goes more positive than B, indicating a site oposite the probe hole, the comparator switches to + 15V and energises IC_2; this then generates a 15V square wave, with a frequency determined by C-R, which is fed to the capacitively coupled Z mod oscilloscope input to produce a trace. This approach is necessary because a d.c. Z mod signal would only produce a single "blip" during the whole time a site current was detected. Any detected site current above a certain threshold typically 10^{-9}A, as determined by the electrometer settings, will then result in a stored bright area on the oscilloscope screen. The technique thus records the current distribution in the anode plane and its spatial resolution will be determined initially by the anode probe hole diameter, but ultimately by the spot size of the oscilloscope trace in relation to the screen diameter. In the present system the anode probe hole is 1 mm in diameter to allow sufficient current to be transmitted for recording the electron spectra; the scope spot size is $\sim 0{\cdot}4$mm and the "picture" diameter 64 mm. The specimen has a diameter of 14 mm so that the oscilloscope spot size represents 0.1 mm on the specimen surface. This is a tenth of the probe hole diameter so in this case it is the probe hole which limits the spatial resolution to the rather poor value of ~ 1 mm. However, to-wards the end of the present experimental programme a simple circuit modification was discovered which enabled the resolution to be greatly improved. This is described in chapter 6 where it is also shown to lead to a resolution limited by the oscilloscope spot size, i.e. ~ 0.1 mm. in this case.

5.15. Further Instrumental Improvements.

Prior to embarking on the experimental programme described in the following chapters, several other improvements, which are described below, were made to the equipment in order to remove uncertainties in the high voltage gap setting and to reduce the time taken to load new specimens into the vacuum chamber. Specimen loading had been a lengthy process requiring the removal of the specimen holder with its bellows assembly through one large vacuum flange and the associated electrical connections through another. Accidental "flash overs" from the specimen had also been quite common because the specimen support rod tended to bend under the force of attraction which arose between the specimen and the anode when a high electric field was applied. Thermal expansion of the specimen during heating experiments again tended to reduce the high voltage gap thus making electric field measurements less accurate. These difficulties were overcome by redesigning the specimen holder and by making the support rod more rigid with additional bearings; a capacitance bridge was also designed in-order to sense changes in the gap.

15.15a Heated Specimen Holder.

Several factors had to be born in mind when designing this new holder. Firstly, it had to be rigid under the action of the applied field, and to have the electrical connections running down the central support rod to enable easy removal of the specimen assembly through one small vacuum flange. Secondly, the exposed area of metal when looking directly at the face of a fixed specimen needed to be just the specimen face itself. This was necessary so that measurements of ion etching currents as described in chapter 7, could be related directly to the specimen area, although this still meant that calculated etching rates were averaged over the whole specimen face.

The specimen heater needed to be capable of reaching a temperature of $\sim 1000\ ^{o}C$ and provision had to be made for a thermocouple to measure the specimen temperature. Finally, the back face of the holder had to be accurately parallel to the active specimen face and polished to a mirror finish in order to enable easy alignment of the specimen and anode when setting the high voltage gap, as also outlined in chapter 7.

The completed specimen holder is shown in figure (52) but with an added bearing to the central support rod removed. Figure (53) gives a sectioned diagram of the holder, where in particular a spiral coil of tungsten wire has been used for the heater, which was insulated from the clamp plate (at the back of the specimen) and the holder body by two mica washers. This arrangement proved very effective; even though the mica washers decomposed at $\sim 700^{o}C$ their insulating properties remained unaltered provided that the heating assembly was not subsequently disturbed during specimen changes.

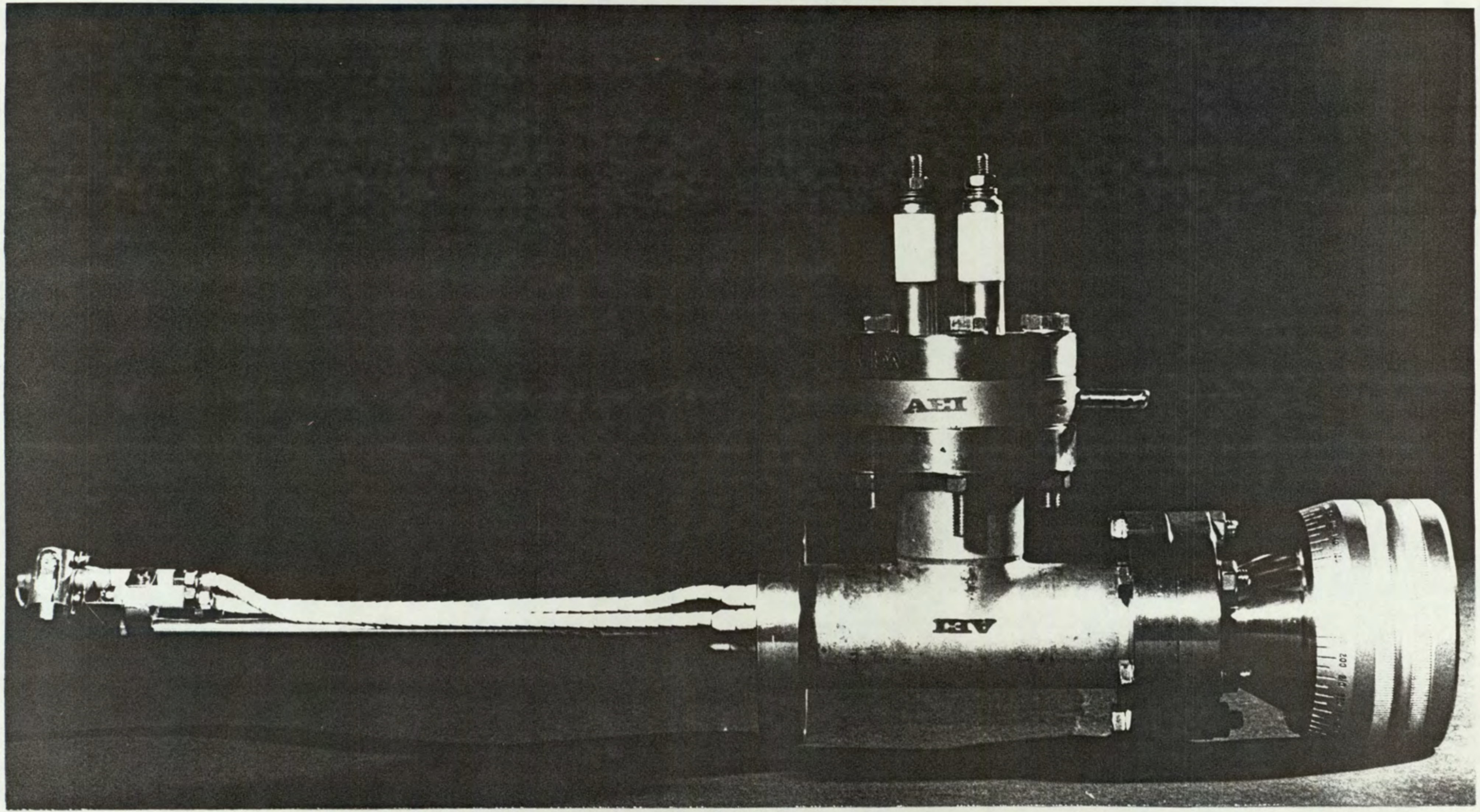

FIG 52. THE SPECIMEN HOLDER AND "FEED IN" STRUCTURE.

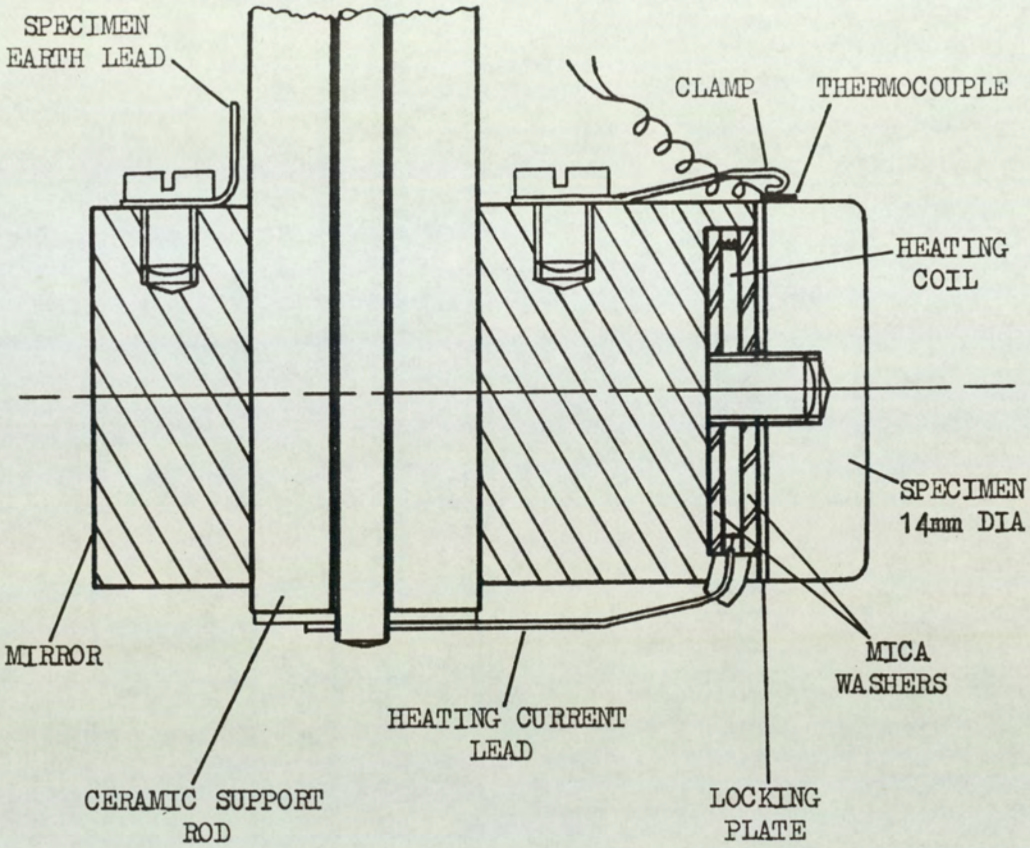

FIG.53. SECTIONAL DIAGRAM OF THE HEATED SPECIMEN HOLDER.

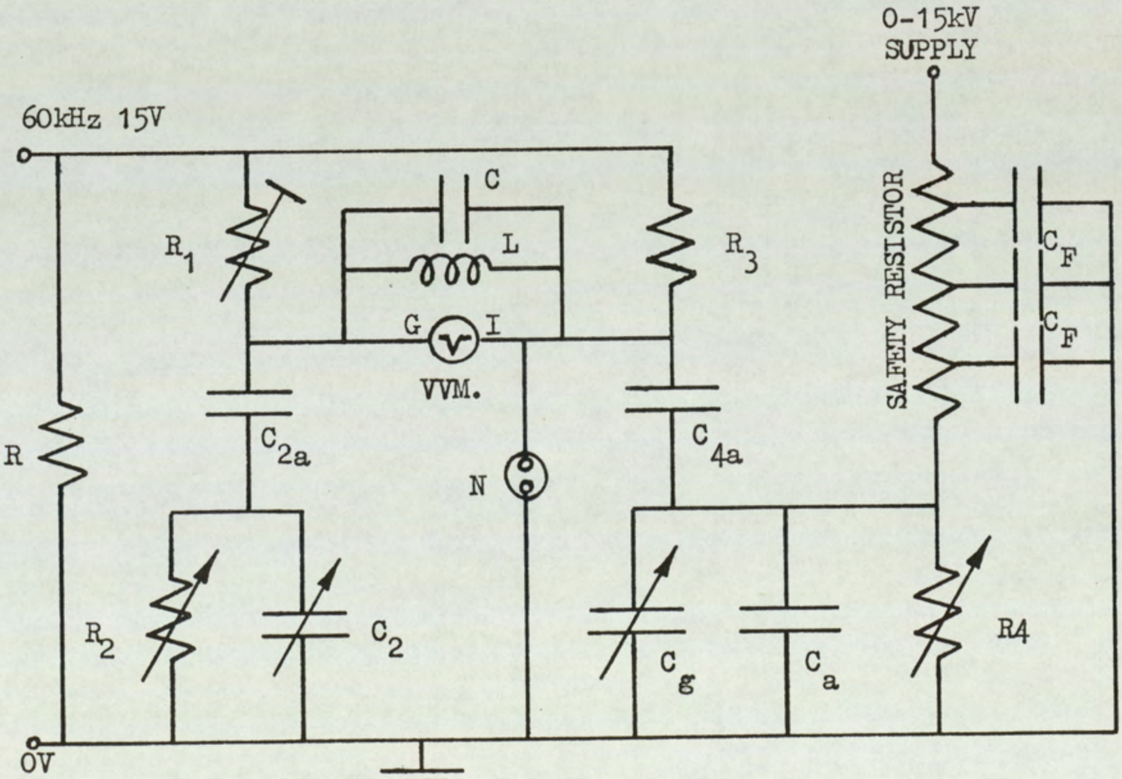

FIG.54. CIRCUIT DIAGRAM OF THE CAPACITANCE BRIDGE

5. 15b) Capacitance Bridge.

Since the electrode arrangement (specimen-gap-anode) forms a natural capacitor, the most obvious way for detecting changes in the gap width is a capacitance bridge. The only difficulties with this appart from the high voltage at the anode, are that the gap capacitance is only about 3 pF which is also a small fraction of the total from anode to ground, and any noise on the high voltage line might upset a sensitive detector. Figure (54) shows the final circuit diagram of the bridge and it will be seen that at balance, i.e. zero detected signal on the valve volt meter (VVM), $Z_1 Z_4 = Z_2 Z_3$ where

$$Z_1 = R_1 \quad \& \quad Z_2 = -\frac{j}{\omega C_{2a}} - \frac{j R_2}{\omega R_2 C_2 - j} \tag{14}$$

$$Z_3 = R_3 \quad \& \quad Z_4 = -\frac{j}{\omega C_{4a}} - \frac{j R_4}{\omega R_4 C_4 - j} \tag{15}$$

and where C_4 equals the gap capacitance in parallel with anode to ground capacitance, i.e. $C_4 = C_g + C_a$. If in addition the none varying components are related by the equation

$$\frac{R_1}{R_3} = \frac{C_{4a}}{C_{2a}} \tag{16}$$

then for balance

$$C_4 = C_2 \frac{C_{4a}}{C_{2a}} \tag{17}$$

and

$$R_4 = R_2 \frac{C_{2a}}{C_{4a}} \tag{18}$$

This circuit was chosen for its relative symplicity since the component values at balance are independent of the supply frequency and the capacitance balance equation is not a function of the resistance values. Here, resistor R_4 represents the combined effect of the electron stream between the specimen and anode, the high voltage line filter, and any stray conductances through the anode support insulators etc.,

In operation the bridge is first balanced for a 0·5 mm gap, any suspected changes in gap can them be checked and compensated for by very small movements of the gap micrometer screw, keeping the milivoltmeter reading as small as possible.

A convenient supply frequency of 60 KHz was used, and since this was the only frequency to be detected, an L - C band pass filter tuned to 60 KHz was placed across the high impedance detector. This had a $Q \sim 50$ and dynamic impedance at 60 KHz of ~ 1 MΩ with a very low impedance at other frequencies which effectively shunted all noise signals to ground. The inductance L also allowed the d.c. charging current for the high voltage isolation capacitor C_{4a} to bypass the detector. To give added circuit protection against gap "flash over", a neon N conducting at ~ 70V, isolates the low voltage circuity. Rather surprisingly, the high voltage supply had a considerable ripple voltage with frequency components including 60 KHz; however this was very conveniently removed by placing capacitors C_F at intervals along the IOMΩ safety resistor thus forming a low pass filter. Values for Z_1 and Z_3 were made quite low at 50 Hz in order to place the "earthy" side E of the milivoltmeter (V.V.M) effectively at earth potential, thereby removing mains born interference. Also, the whole input circuit (all connections to **I** on the meter) was screened right up to the vacuum chamber since the unscreened bridge could detect hand movements at ~ 1 foot away. In this way a 0·01 mm change in gap could be detected with 10 Va.c. supply. It should be added that this level of modulation to the high anode potential had no effect on subsequent electron energy distributions since $(60\ \mathrm{KHz})^{-1}$ is many orders of magnitude smaller then the time constant of the detection system used with the spectrometer.

CHAPTER 6

EXPERIMENTAL TECHNIQUES AND RESULTS

6.1. Preliminary Procedures.

The standard specimen shape adopted for this series of experiments was a thick disc having a diameter of 14 mm and a thickness of 5 mm, with a 1 mm radiused edge in-order to minimise field enhancement effects. Unless otherwise stated, the routine surface preparation started with a series of grinding operations over the active face, the radiused edge and the cylindrical sides, followed by a series of conventional metallographic diamond polishes to a surface finish of 1um. Preparation was completed by cleaning in an ultrasonic methanol bath for ~15 min. In order to minimise any contamination from stray dust particles picked up during handling, the specimen was given a final rinse with methanol immediately prior to assembly into the vacuum chamber. It should also be noted that from time to time the anode was also given a similar set of polishes and cleaning operations to remove any accumulated contamination. An optimum operating pressure of $\sim 2 \times 10^{-10}$ mbar could be achieved following an over night bake out at ~220℃ and subsequent filling of the liquid nitrogen traps.

Parallel alignment of the active specimen-face and the anode had previously been achieved by using an autocollimating telescope to simultaneously view the reflecting surfaces of the anode and the back face of the specimen holder, e.g, Allen (98), Allen & Latham (97) and Athwal.(96) Accurate alignment being assumed when the images of the two cross wires were exactly superimposed. This procedure however, was found to be unsatisfactory because polishing the specimen and anode inevitably resulted in the flat faces becoming slightly convex; in fact the surfaces tended towards natural non field enhancing Rogowski - like (132) profile, with the anode which had the larger diameter acquiring the least face curvature. Hence the specimen alignment depended on which part of the anode surface the telescope happened to be pointing at. A simple remedy to this problem was merely to view the specimen holder and anode mirror surfaces by eye, such that an image of the eye, as seen reflected from both surfaces, was as nearly continuous as possible. This quick procedure then resulted, after suitable adjustments, in an alignment of the electrode surfaces to better than 1°. Accurate setting of the specimen gap was best carried out as follows. The capacitance bridge was first balanced for a dummy specimen at a standard gap of 0·5 mm from the anode:, this was accomplished by first touching the dummy specimen against the anode (checking for an electrical contact) and then adjusting the gap to 0·5 mm using the Z micrometer screw. Any subsequent specimen could then be " non - destructively" positioned at the correct gap simply by rebalancing the bridge to the same capacitance setting, i.e. proving that all electrical connections to the anode remained unchanged. A check could always be made on the gap setting after an experiment by noting the micrometer reading necessary to contact the specimen with the anode.

The electrical connections used to obtain and map emission sites were as shown in figure (55), where appropriate voltages are taken from the electrometers to activate the scope bright-up circuit when scanning a specimen, as described in chapter 5.14d. To initiate a site the anode voltage was raised in ~1 KV steps, with a pause of ~5 min. between each step, so that any delayed switch on effects or microparticle activity

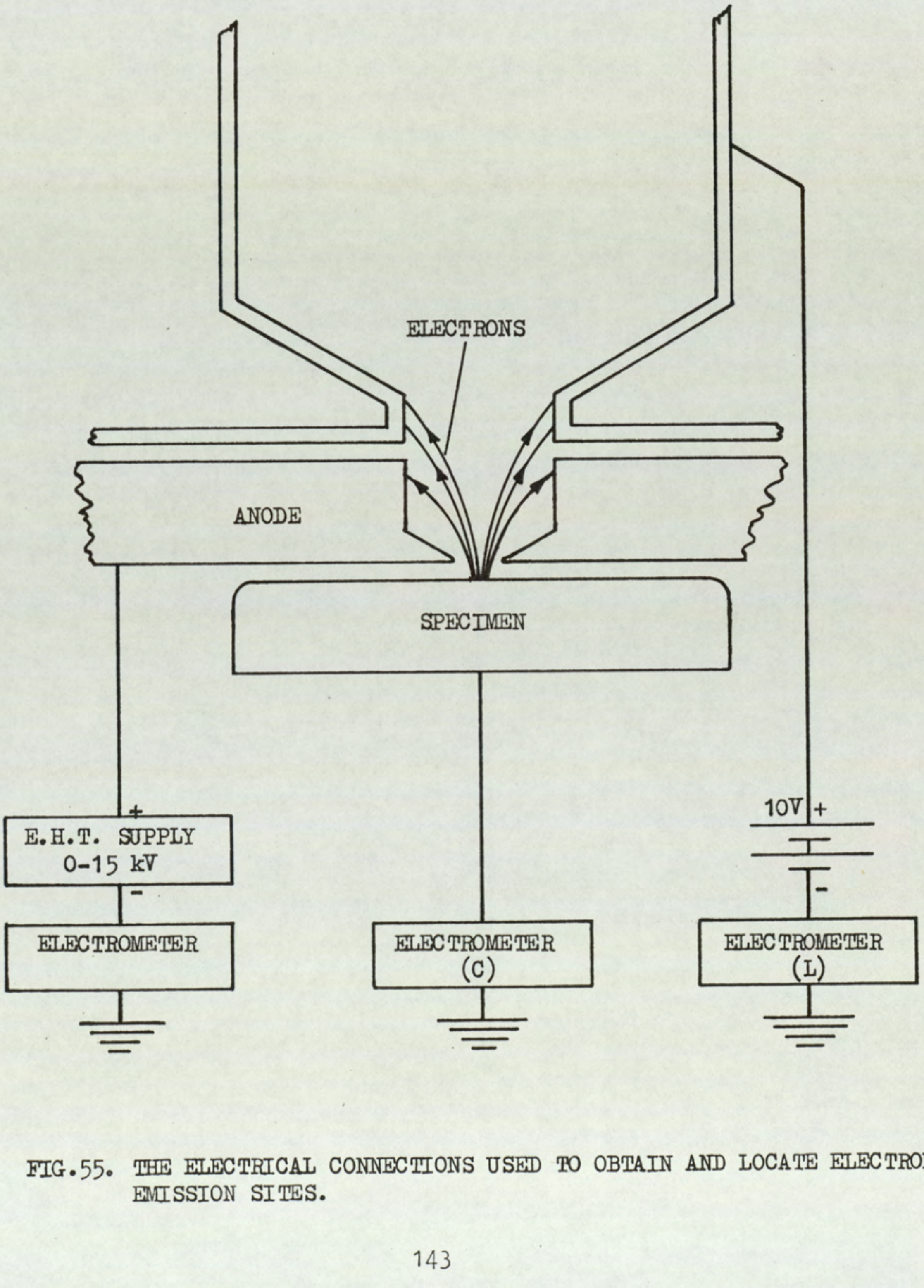

FIG.55. THE ELECTRICAL CONNECTIONS USED TO OBTAIN AND LOCATE ELECTRON EMISSION SITES.

could be detected at the lowest possible anode voltage and "flash-over" events avoided. Even so, the most common occurence was a gradual rise in current to $\sim 10^{-10}$A as the voltage was raised to $\sim$ 9 - 11 KV, with then a very sudden "switch on" such that the current would subsequently remain at $\sim 10^{-7}$A even when the voltage was reduced to 5 - 6 KV. Very low current phenomena could be examined using the electrometer C of fig. (55) connected in the earth lead. This was switched out during spectral measurements to avoid spurious "volt drops " in the electrometer input line.

Having thus obtained one or more sites, these could then be surface mapped automatically using the spiral scanning facility described in chapter (5.14), and then examined individually for their electron energy spectrum and I.V. data etc., I.V. data was obtained by recording simultaneous values of anode voltage and the current transmitted by the anode probe hole detected by the electrometer L connected to the lens electrodes. This procedure of course assumes that all the electrons emitted from a single site are detected via the probe hole; more will be said later about this important consideration. Spectral measurements were recorded with the electron lens electrode reconnected to a 0-5 KV high voltage source to give the necessary focus control.

6.2. Early Results Recorded Prior to the Modifications to the Interfacing Lens.

These results are presented in order to give some idea of the type of measurements carried out before it was realised that the input lens needed modification. They are consistent with all previous experiments on broad area electrodes, and underline the variability of the data and indicate some of the anomalous phenomena which were being observed. It was in-fact as a consequence of studying some of these "oddities" that questions were raised concerning the nature of the electron beam entering the analyser. As will be seen some of the very early spectra are shown inverted; this is because circuit modifications were being carried out that necessitated amplifier changes which gave a phase invertion for this particular set up.

6.3. Spectra From Various Materials.

Figure (56) shows the energy spectra obtained from copper, aluminium and N type silicon, each for two values of applied field. The usual single peak observed for copper at low fields is seen in figure (56a) while (56b) shows a double peaked spectrum often seen as the field was raised. Similarly for aluminium, figures (56 c & d) except that it was much more difficult to obtain stable emission without causing a microdischarge; this was probably due to the continuous ∼ 3 nm thick surface oxide layer inhibiting emission in some way. The degree of complexity shown here as the field was only slightly increased could not be satisfactorily accounted for from any simple property of a single emission site, such as molecular coverage or gas adsorption, since this behaviour persisted even after the thorough heating or field desorption. The N type silicon spectra were in every way similar to those of other materials, where the low field spectra are also occasionally multipeaked. Although figure (56e) suggests that emission is coming from the silicon conduction and valence bands (E gap for Si = 1·1 eV), this was probably not the case, as metals have produced similar results at particular fields. Unfortunately this sort of qualitative comment was about all that could be said prior to the input lens modifications. Spectra obtained for lead are shown in

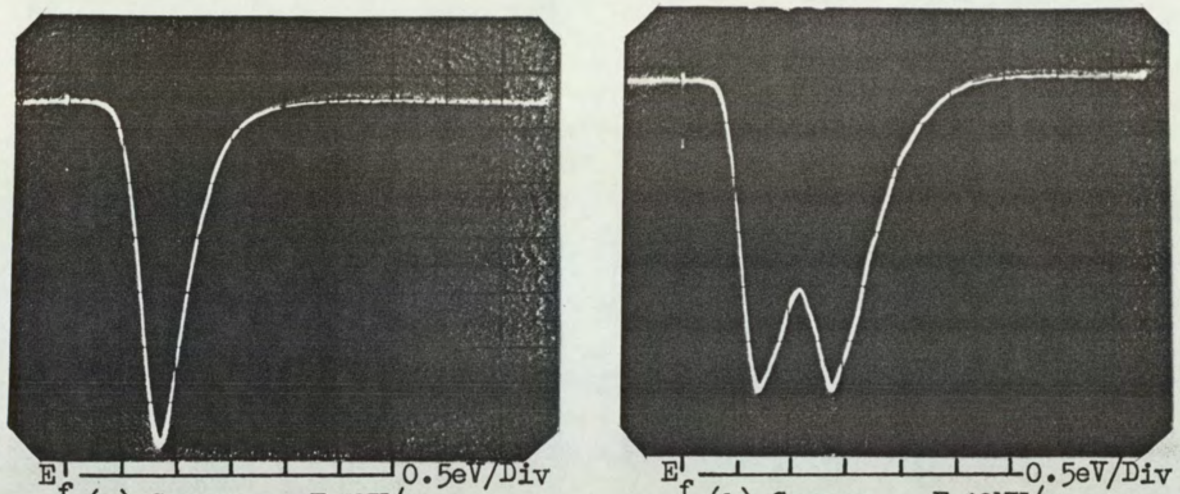

(a) Copper F=8MV/m

(b) Copper F=10MV/m

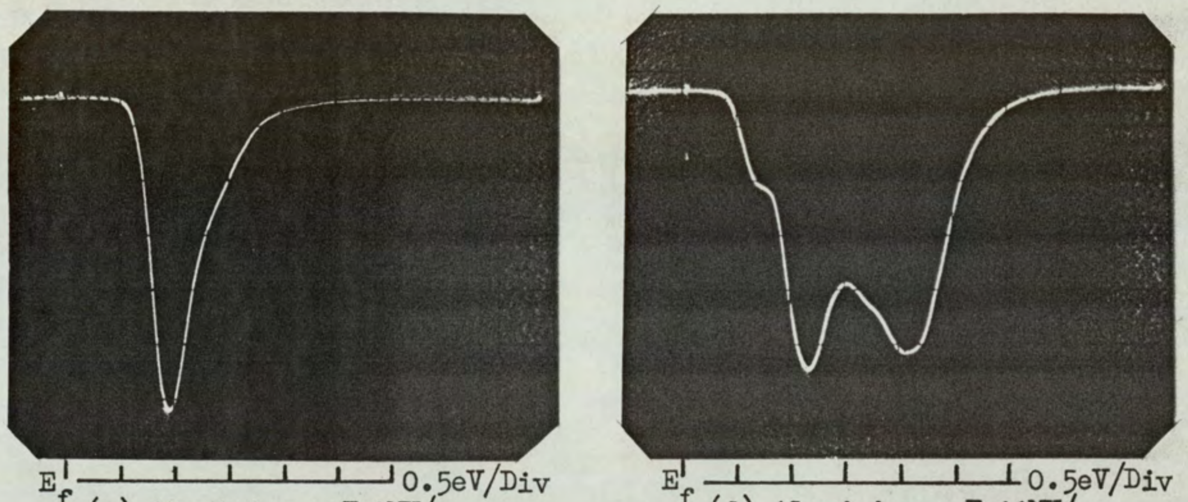

(c) Aluminium F=9MV/m

(d) Aluminium F=11MV/m

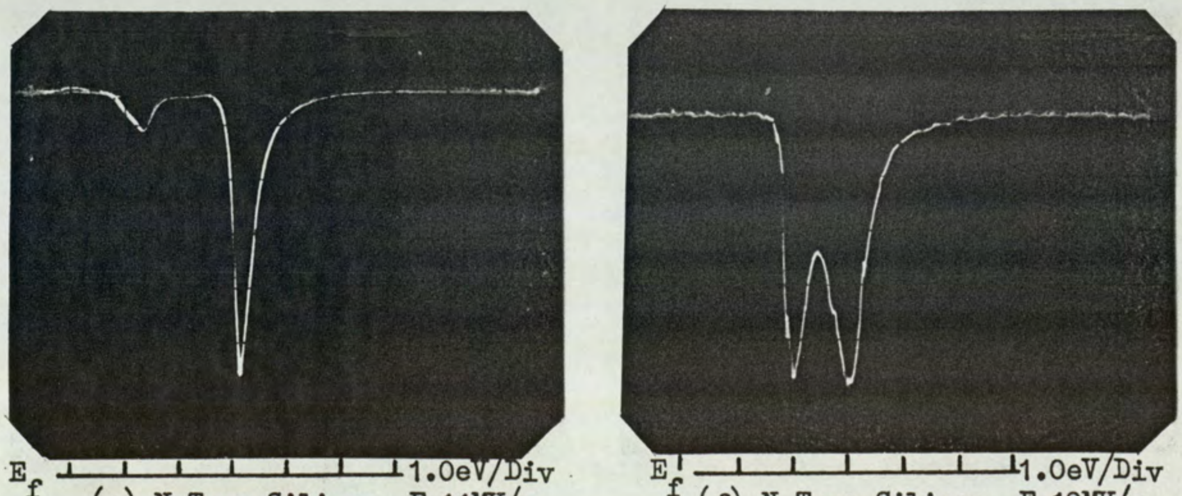

(e) N Type Silicon F=11MV/m

(f) N Type Silicon F=12MV/m

E_f=Fermi level position. Energy decreasing left to right.

Y axis = current per unit energy (inverted) arbitrary units.

FIG 56. SPECTRA FROM VARIOUS MATERIALS.

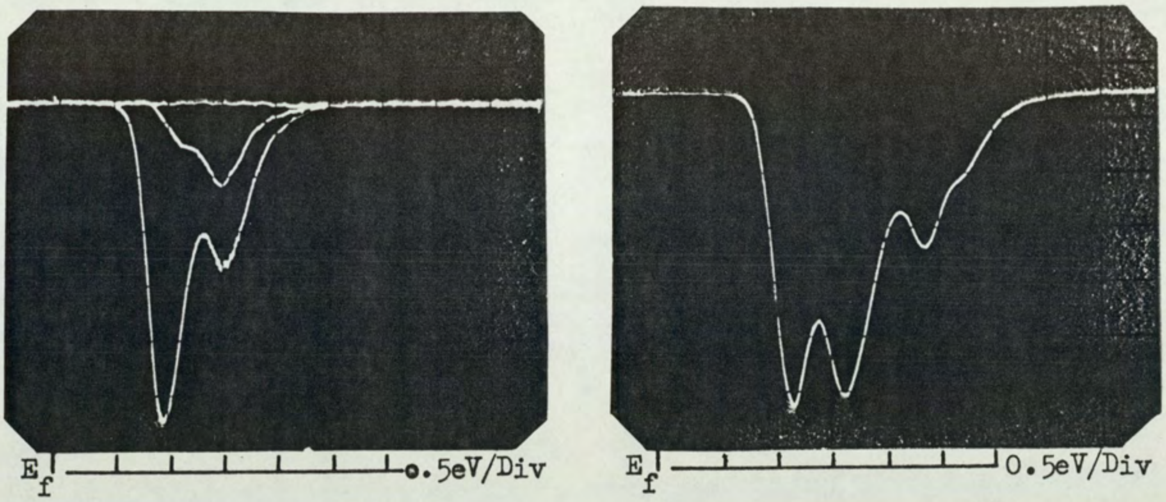

(a) Lead F=8MV/m (b) Lead F=9MV/m

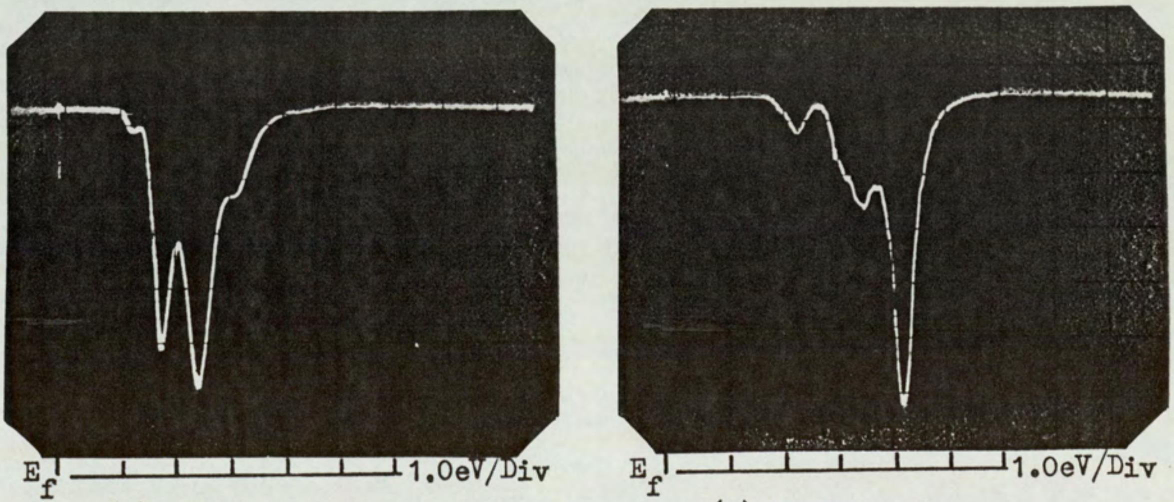

(c) Oxidised Copper (d) Oxidised Copper

Both (c&d) F=9MV/m . Only the input lens focus voltage has been changed.

Y axis, current per unit energy, (inverted) arbitrary units. Energy decreasing left to right. E_f=Fermi level position.

SPECTRA FROM VARIOUS MATERIALS: SHOWING CHANGES PRODUCED BY ALTERATIONS TO THE INPUT LENS FOCUS VOLTAGE

FIG 57.

figure (57):- (57a) shows two distributions taken for the same field but with slightly different input lens focus voltages while (57b) shows the spectrum at a higher field. Two traces for heavily oxidised copper are shown in figure (57c & d) both at the same field, but again with a small change in lens focus voltage. Similar changes in the spectrum could be brought about solely by small changes to the specimen position relative to the anode probe hole. These findings indicated that further attention needed to be given to the affects of the input lens on the electrons entering the analyser. One definite finding from these results however, was that heavily oxidised specimens produce very complex multipeaked spectra which have considerable peak - shifts with applied field i.e. several volts. The lead specimen was not deliberately oxidised but unlike the other materials, it was impossible to diamond-polish without producing a thick oxide layer, as noted by the very matt surface. Since there was very little difference in the general characteristics of the spectra from the various metals, it was decided to use copper for subsequent experiments as this metal was easy to work, usually produced emission sites in a convenient field range, and has been the subject of extensive previous studies, e.g. Athwal (96).

6.4. The Temperature Dependence of Spectra.

Spectra are shown in figure (58) which were obtained from an unoxidised copper specimen at constant field over the temperature range 20 to 700°C; the specimen having been first degassed for 3 hrs. at 800°C and a pressure of $< 10^{-6}$ mbar. This spectral sequence started with a single peaked spectrum shifted 1 eV from the Fermi level which gradually broadened

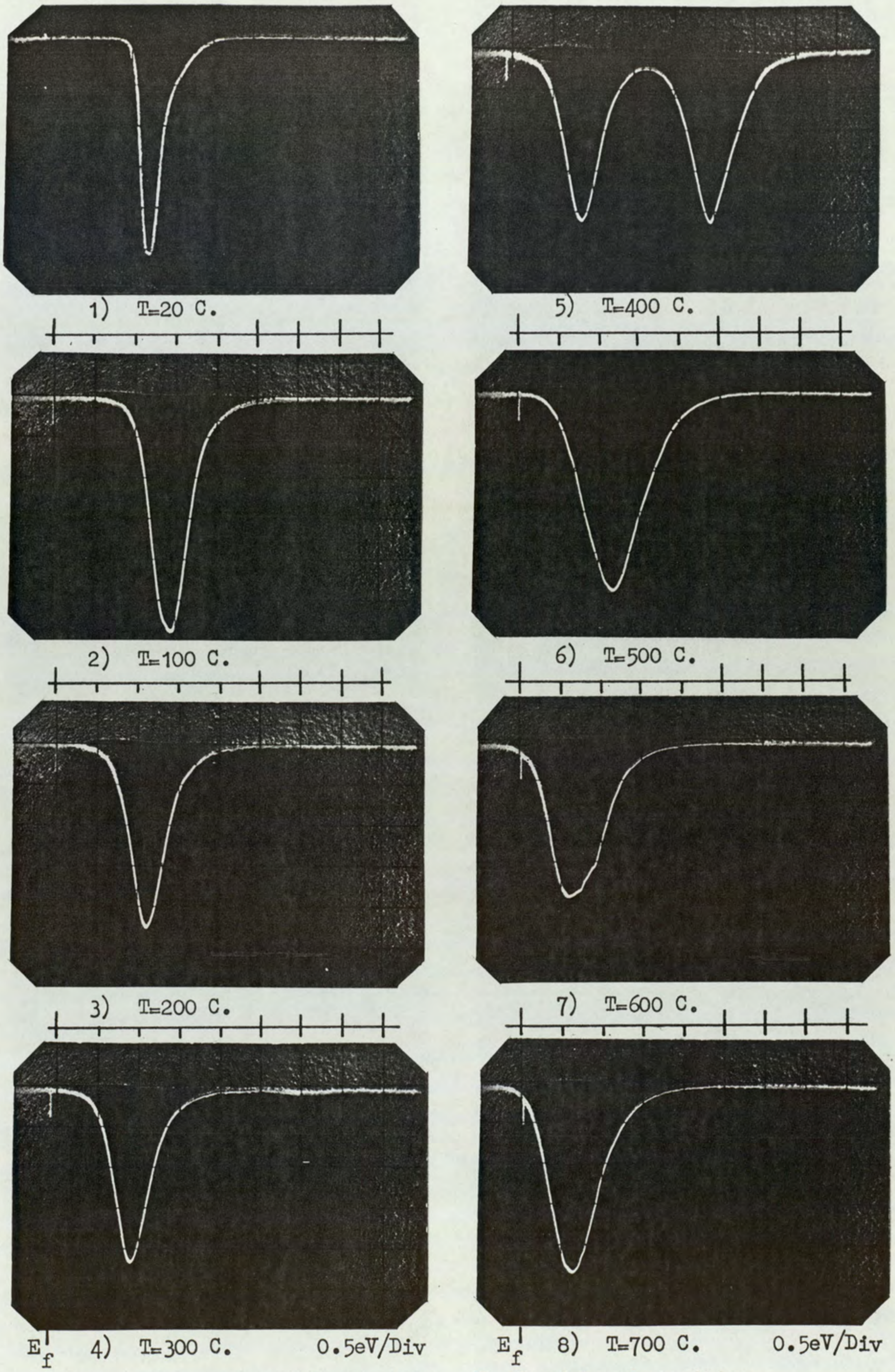

1) T=20 C.

2) T=100 C.

3) T=200 C.

4) T=300 C.

5) T=400 C.

6) T=500 C.

7) T=600 C.

8) T=700 C.

Energy decreasing left to right. E_f=Fermi level position.
Y axis = current per unit energy (inverted) arbitrary units.

SEQUENCE OF SPECTRA FROM ONE SPECIMEN AT CONSTANT FIELD, VARYING TEMPERATURE
FIG 58.

and moved slightly nerer to the Fermi level as the temperature was increased. However, at a temperature of $\sim 300^{\circ}C$ (plate 4) a second peak can be seen developing which, by $\sim 400^{\circ}C$ (plate 5), was equal in amplitude to the original peak. This second peak had a shift which decreased with temperature, such that by $500^{\circ}C$ (plate 6) it had merged into the first peak; however, a slight double peaked behaviour was still discernable at $600^{\circ}C$ (plate 7). The emission from this site was in other respects rather unique, in that it was very stable over the full temperature range for several hours; in fact attempts to reproduce this result have so-far been unsuccessful.

6.5. A Half-Oxidised Copper Specimen

A routinely prepared specimen was heated on a hot plate, in air, to a temperature of $\sim 200^{\circ}C$ while the colour changes associated with the growing thickness of oxide were noted. The specimen was allowed to cool in isolation as soon as a dark blue-purple colour appeared over the whole surface. This procedure was found to give a reproducible mean oxide thickness of $\sim 3 \times 10^{-7}$m as measured using an ellipsometry technique. The oxide layer from half the specimen surface was then removed in a nitric acid bath taking care not to etch the polished copper surface underneath or reveal the crystal grain boundaries. An ultrasonic wash in distilled water was followed with a methanol bath as usual.

It was hoped by this means to check whether emission sites form preferentially at the boundary of an oxide layer. This seems not to be the case from this experiment but this is not conclusive since the electron detection sensitivity during the surface scan had to be kept rather low. Luckily two sites were found on this specimen, one in each region, as shown in figure (59) with their associated F.N. plots shown in ficure (60). Here, the spectral trace for site B i.e figure (59 b) consists of six superimposed spectra which were obtained by increasing the field by a small amount i.e. ~ 200 V in each case. Site A, in the unoxidised half, gave typical results for metals having only ambient oxide coverage, while site B indicated that something associated with thick oxide layers was giving very large peak shifts in the energy distribution and producing a "kink" in the F.N. plot. This has been seen often and is a general characteristic for thick oxide layers, as it is their tendency to produce quite stable spectra. It is also interesting to note that several kinked F.N. plots were obtained by Athwal (96), which were almost identical to that obtained from site B, except that they were recorded from an "unoxidised" specimen with the change in slope occuring at somewhat high fields. Lastly it has to be pointed out that a better fit to the "F.N." points of site A would be a curved line bending downwards at higher fields (18,24,25) this is very often the case and will be discussed in detail later.

6.6. Fowler-Nordheim Plot for an Anomalous "Switch On" Site.

Figure (61) shows an F.N. plot obtained from a site having an unusual switch-on characteristic. Thus provided the applied voltage did not exceed ~ 5 KV, a straight line was produced (61a) for both increasing and decreasing voltages. If however the voltage was allowed to rise above this value, into the region marked with arrows, the emission eventually switched to the higher conducting state, shown by the line (61b), and remained on this curve for all subsequent changes in voltage down to a very low value i.e.<300 V. If however, the voltage was taken to zero for a short time, i.e. ~30S, the sequence of

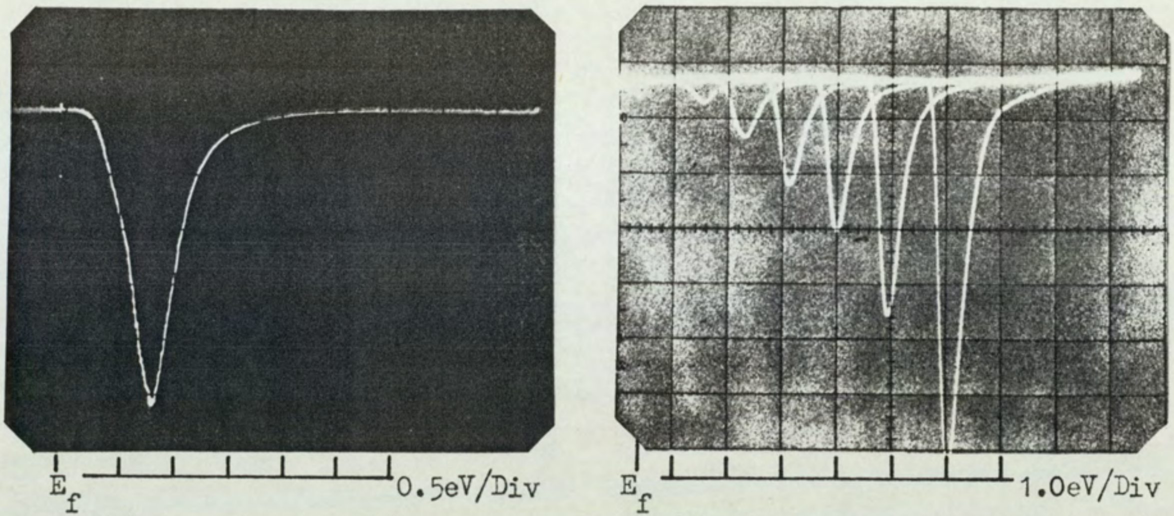

(a) Site A F=12MV/m   (b) Site B F in range 6-9MV/m

E_f=Fermi level position. Energy decreasing left to right; Y axis current per unit energy (inverted) arbitrary units.

ELECTRON ENERGY SPECTRA

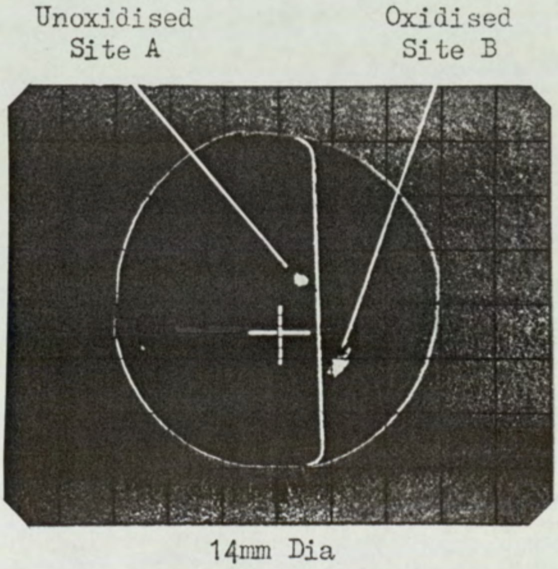

(c) Site distribution over the specimen surface.

Copper : half oxidised.

SPECTRA AND SURFACE SITE DISTRIBUTION FOR A HALF OXIDISED SPECIMEN.

FIG 59.

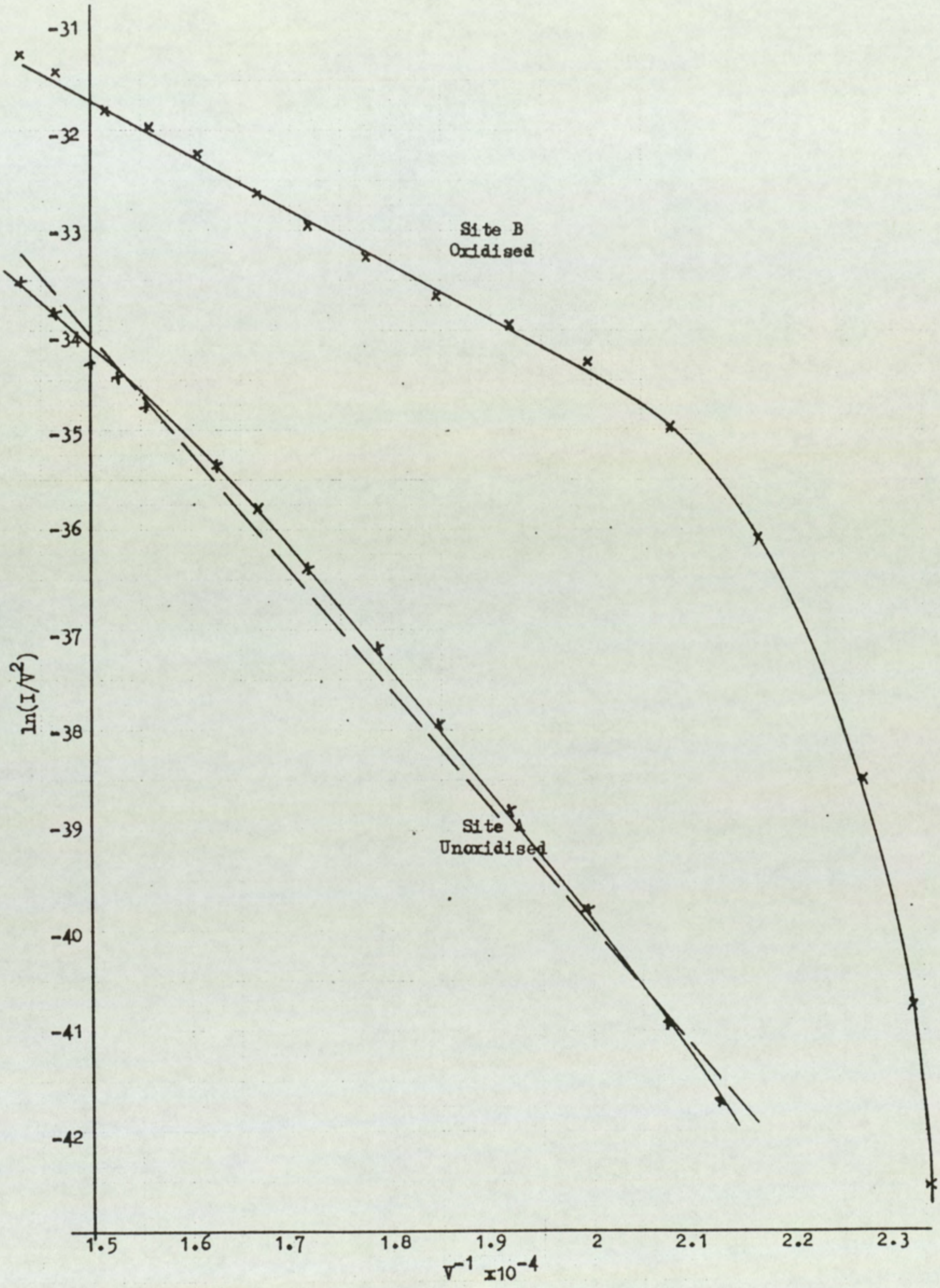

FOWLER-NORDHEIM PLOTS FROM A COPPER SPECIMEN: HALF OXIDISED.

FIG 60.

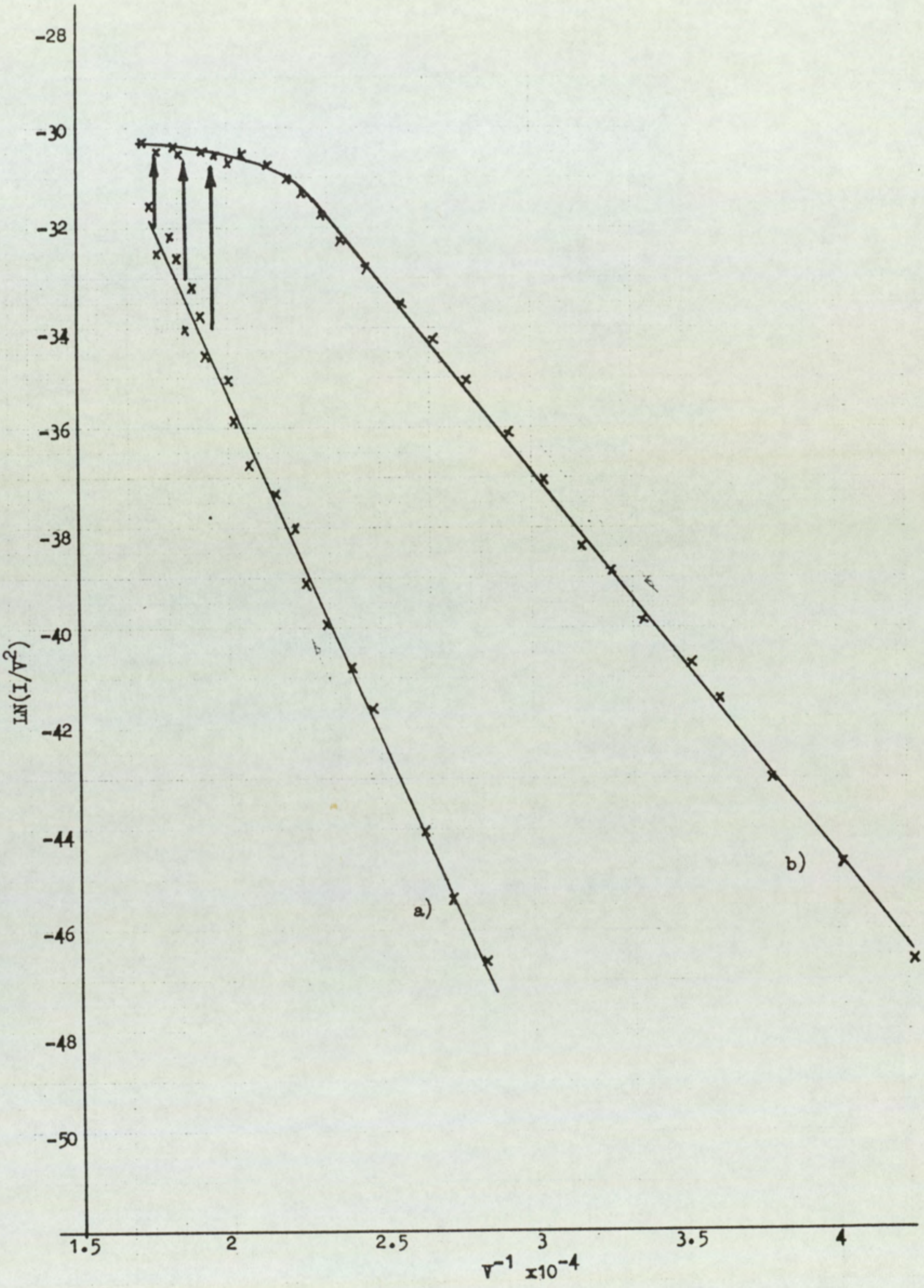

FOWLER-NORDHEIM PLOT FOR A "SWITCH ON" SITE.

FIG 61.

events would re-occur starting on line a. The sort of switch-on behaviour observed here for line b) alone is typical, apart from the field values, of sites found on copper; usually a large field $> 20\ \mathrm{MVm}^{-1}$ ($V \sim 10$ KV) needs to be applied before substantial current flows, the site then remains in a high conductivity state which enables the field to be reduced while still retaining a relatively high emission current. The simplest explanation of figure (61) would appear to be that the observed emission came from two closely-spaced sites which were not resolved by the anode probe hole - lens assembly. One of the sites, either having a low value of switch on field and then a fairly low emission current or simply not showing switch on behaviour at all.

6.7. Argon Ion Etching.

A saddle field ion source of the type described by Franks (133) had been installed in the vacuum chamber by Athwal (96), who also checked the alignment and verified that a fairly uniform beam impacted the specimen when it was correctly positioned as indicated in figure (62). The etching rate maybe calculated from the sputtering field, i.e. ~ 5 atoms per ion for copper bombarded with 8 KeV argon ions (134), as employed here, and gives a value of ·1 um of copper removed per hour from a 14 mm diameter specimen face with a total beam current of 1 uA. However, Fitch (135) has indicated that this value must be treated with caution, due to the presence of a high proportion (40%) of neutrals and multiply charge ions in the beam, and also because secondry electron emission from the specimen can give a false value for the ion current. According to Davidse & Maissel who used a 3 KeV. rf. ion source giving a beam containing only 2% of neutrals, an insulating surface inclusion or the surface oxide of a

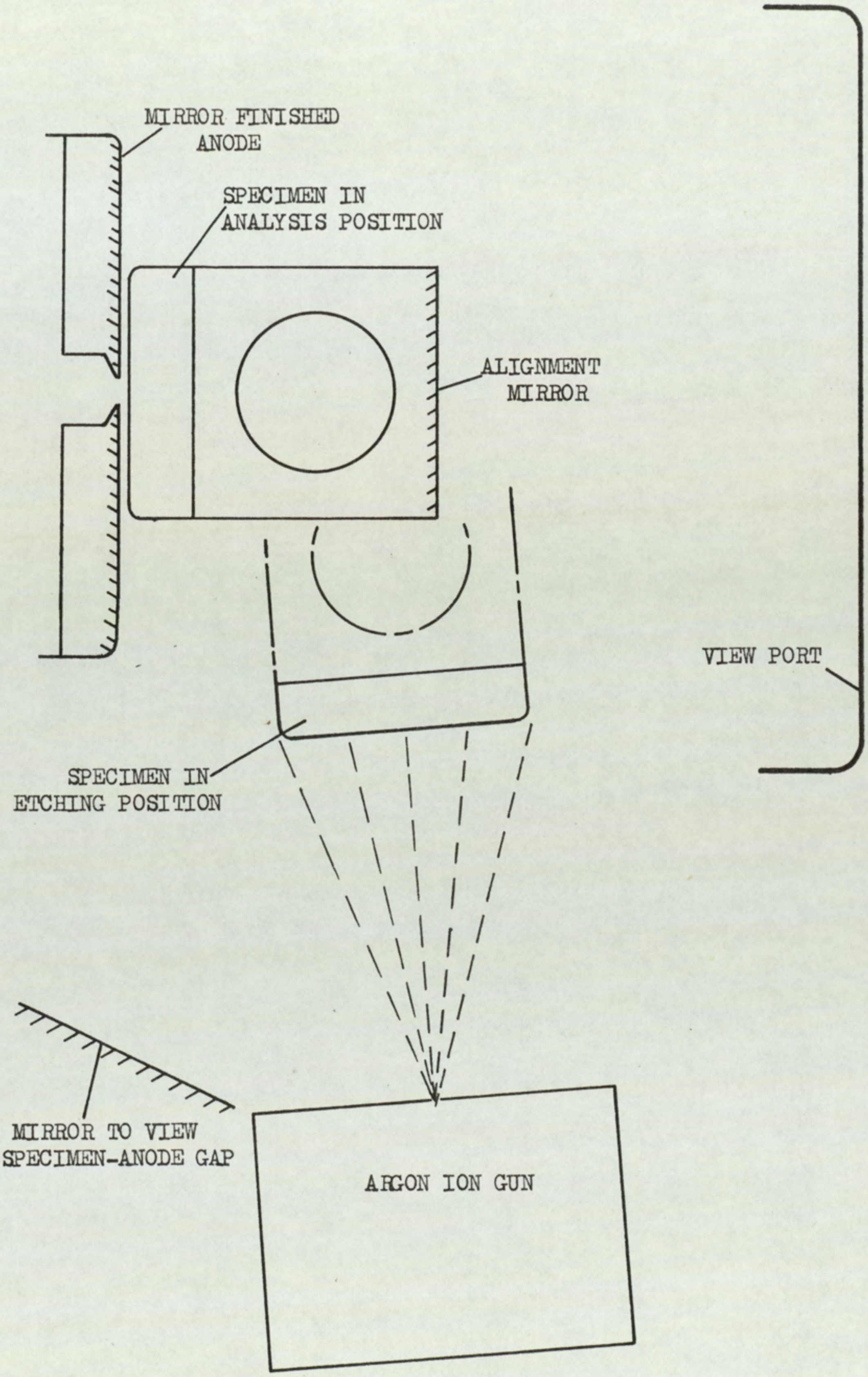

FIG.62. SCHEMATIC DIAGRAM SHOWING THE POSITION OF THE SPECIMEN DURING ION ETCHING AND FOR EMISSION SITE ANALYSIS.

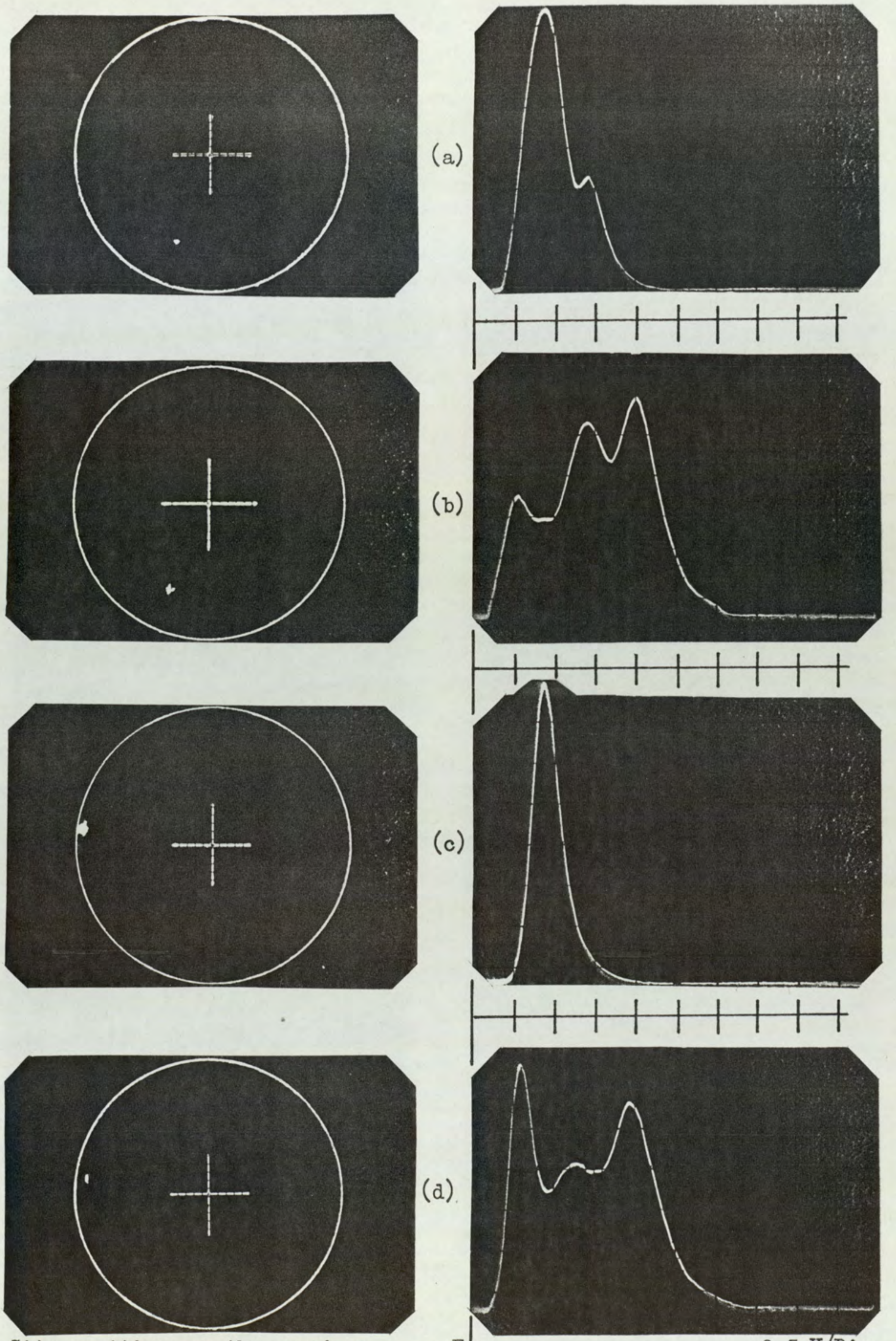

Site positions on the specimen surface at intervals during argon ion etching.

Spectra for each emission site. Y axis = current per unit energy, arbitrary units. Energy decreasing left to right. E_f=Fermi level.

FIG 63. RESULTS FROM AN ARGON ION ETCHING EXPERIMENT.

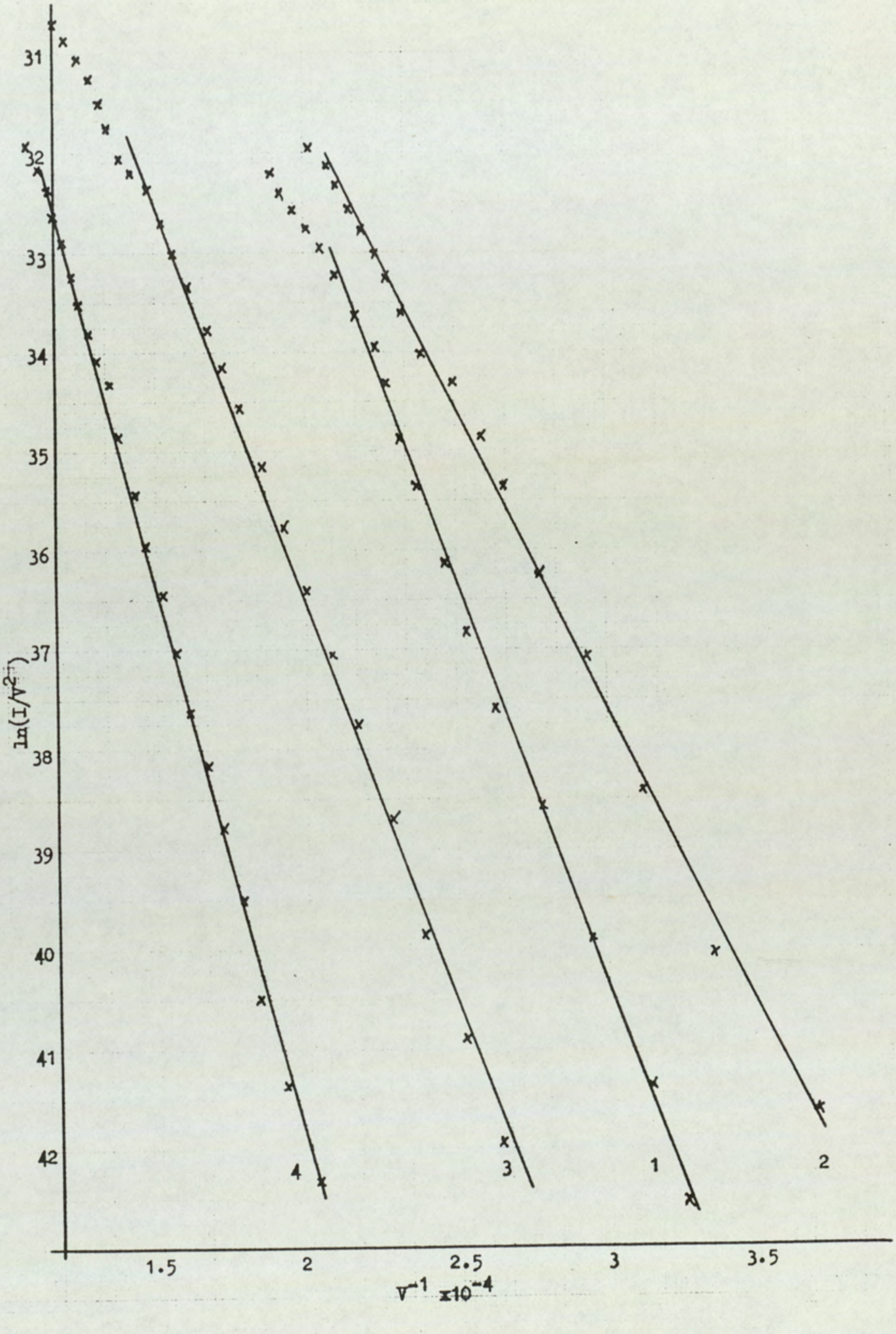

FOWLER-NORDHEIM PLOTS OBTAINED DURING ARGON ION ETCHING.

FIG 64.

specimen will typically have a sputtering yield of •3 to •8 molecules per ion. Since the actual composition of any electron emitting impurity is unknown it is reasonable to assume the impurity etching rate for 8 KeV ions to be at least •8 molecules per ion; that is 1 u A sputters ~ 16 nm per hour.

The findings of an argon ion etching experiment, using 8 KeV ions and an etching current of •1 mA are displayed in figure (63). In this particular case, a standard copper specimen initially gave no emission for anode voltages up to 10 KV. However, after etching the surface for 1 hour a site was detected in the lower left hand quadrant, as shown in figure (63a) with its corresponding electron energy spectrum; this site was found to give a current of 10^{-7}A at 5•2 KV. A second 1 hr. - etch apparently enlarged the emitting area of the site as shown in figure (63b), although it now required 8 KV to give a site current of ~10^{-7}A. After a third 1 hr etch the original site was apparently eliminated but a new one was created in the upper left hand quadrant as shown in figure (63c), which emitted ~10^{-7}A for only 5 KV. A fourth 1 hr. etch resulted in an apparently smaller area of emission as indicated in fig (63d) now requiring ~ 9•4 KV for a site current of ~10^{-7}A.

At each of the above stages of observation the I-V characteristics of the site were recorded and the corresponding F.N.plots are shown in figure (64). It can be seen from these that within the resolution of the facility there was apparently no consistent trend resulting from ion etching, although from the electron spectra it does look as if etching always tends to complicate the emission from a given site. It is clear, as might be expected, that prolonged etching can remove emission sites, but more importantly it also appears that sites can be created by ion etching. Assuming that such sites are not the result of metallic whiskers, which is reasonable since their spectra are certainly not of a simple metallic type, two other possible explanations of new site formation can easily be imagined. Either additional inclusions are uncovered from just below the specimen surface, or the etching process severely disrupts the ever present surface oxide layer making it prone to emit in some way.

6.8. Later Results Recorded After Modifying. the Analyser Interfacing Lens.

Following the analyser input lens modifications, as outlined in section 9 of chapter 5, it was immediately found that emission sites were imaged as clusters of light spots on the phosphor screen at the entrance apperture of the spectrometer. Thus figure (65a) shows such an emission cluster for the site shown in figure (65c) which was found using the spiral scanning facility. Each ~~group of~~ emission spot will henceforth be called a sub-spot and the actual emitting region on the specimen surface will be called a "specimen site" or "sub-site " to avoid confusion. Hence, five sub-spots can be seen in figure (65a) occupying the whole 15 mm diameter phosphor screen, together with the superimposed dark central hole of the analyser input apperture. Each sub-spot was positioned over the input apperture in turn to record its electron energy distribution, these are shown in figure (65b) at the current relative current amplitudes. Sub-spots 1 & 2 produced the same spectral curve although this can be seen to consist of two peaks that are not quite resolved. No difference at all could be found in the spectra from sub-spots 3 & 4, whereas sub-spot 5 gave a spectrum much nearer to the Fermi level. Lowering the focus voltage to a value well below the usual operating range, merged the spots together and gave the energy distribution shown in figure (65d), which corresponds to what had previously been called "the emission site energy distribution" under all "focus" conditions prior to the lens modifications .

A similar procedure was carried out for a second specimen to produce the data of figure (66a-e). Here the specimen site positions are shown in the scan image of figure (66c), where site A was found essentially to be a single specimen site that gave the emission image of figure (66a) which had three sub-spots giving the individual spectra shown in figure (66b). These could be fused together to give the aggregate spectra of figures (66d or f), depending on which part of the defocussed image was allowed to cover the analyser input apperture. Site B consisted of several specimen sites covering a large area which produced only a blurred image due to its complexity, and which then gave the very complicated energy spectrum shown in figure (66e).

Individual image spots varied in visual size from $\sim$1 mm to $\sim$5mm in width, although electrons could invariably be detected by the spectrometer at distances approximately twice the visible spot "width" from the spot centre, sometimes enabling double peaked spectra to be obtained from dark spaces between spots. Thus figure (67) gives a series of such spectra for constant amplifier gain over a range of applied fields. For low fields, the spectrum seems to consist of a main peak having subsidiary

a) Emission image spots at the analyser input

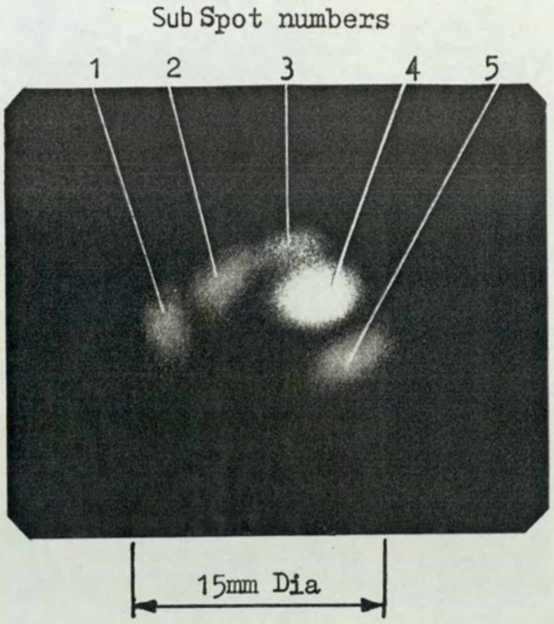

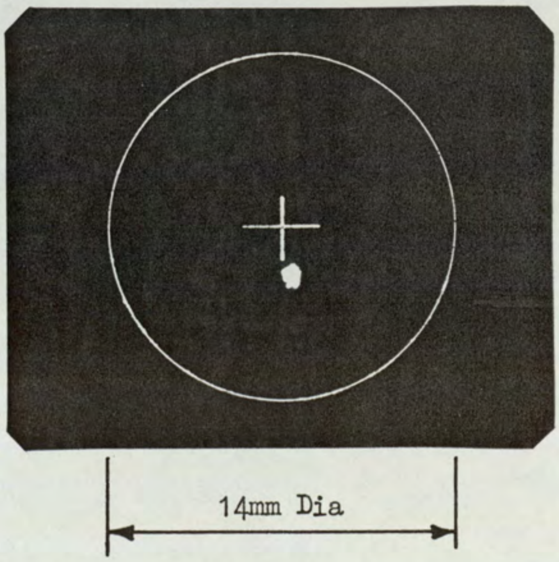

c) Site position on the specimen surface

b) Spectra for individual image spots (at constant field) .

Energy range and axis details as for d) below.

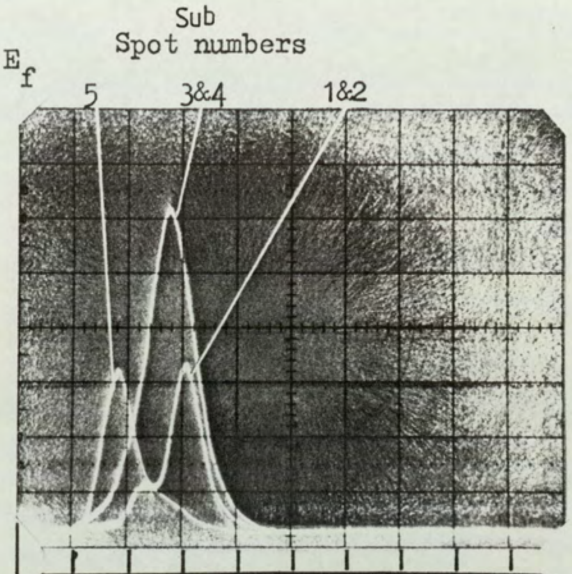

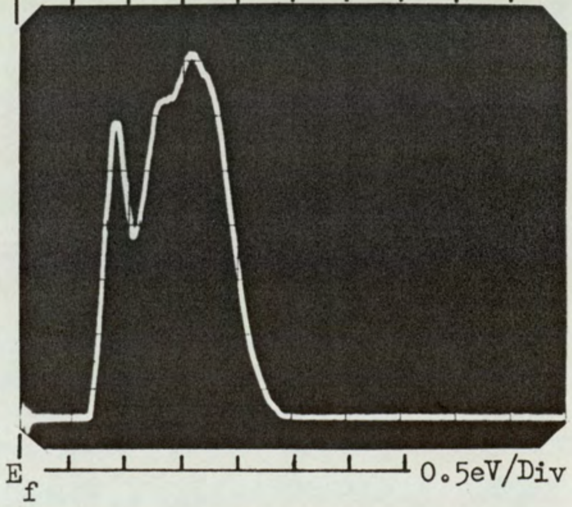

d) Spectra when all spots overlap
E_f=Fermi level position
Energy decreasing left to right.
Y axis current per unit energy arbitrary units.

SPECTRA RESULTING FROM THE EMISSION IMAGE SPOTS AT THE ANALYSER INPUT.

FIG 65.

a) Emission image spots at the analyser input, for site A.

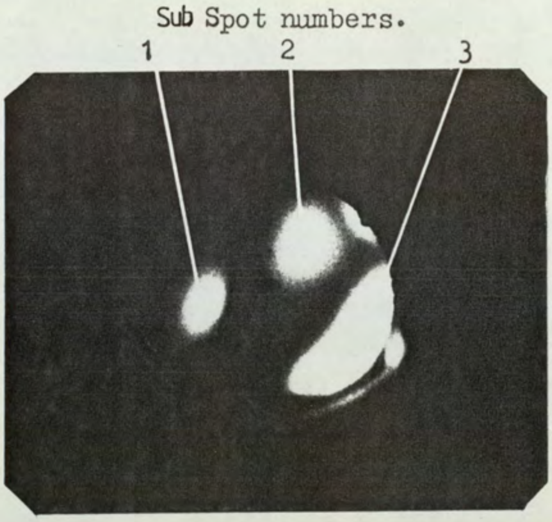

b) Spectra from individual image spots, for site A (at constant field). Energy range and axis details as for (d&f) below.

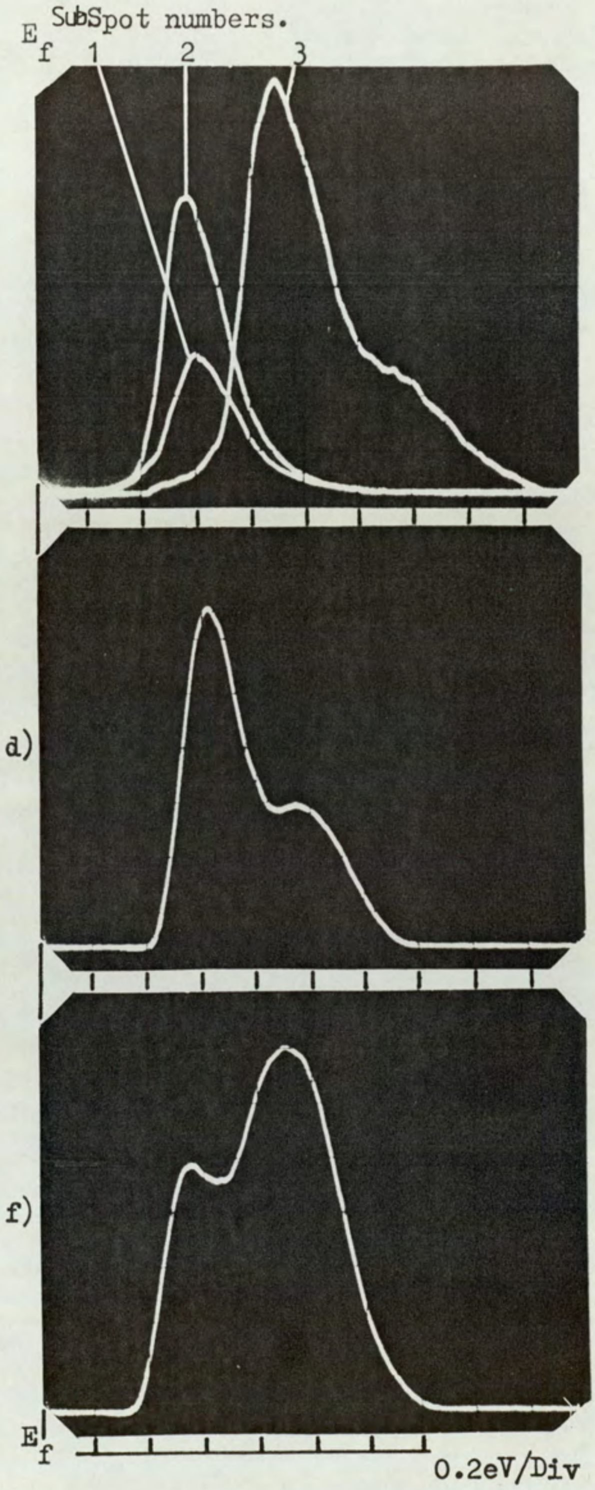

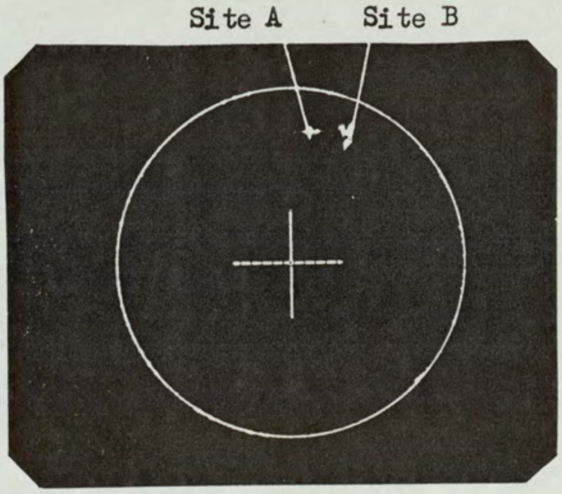

c) Site positions on the specimen surface.

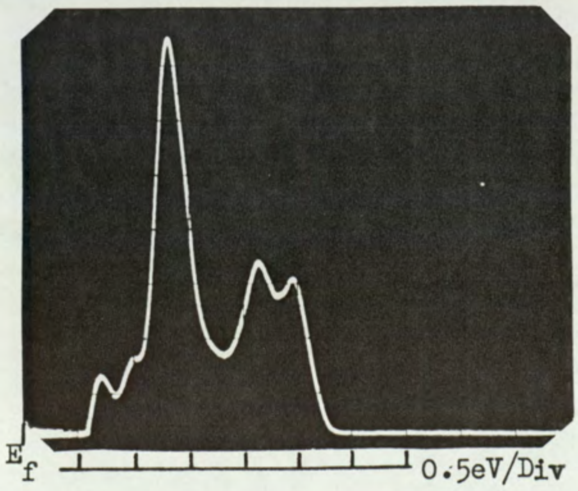

e) Composite spectrum for site B

(f&d) Typical spectra when all spots overlap, depending on which part of the emission image pattern falls over the analyser input hole.
Y axis current per unit energy, arbitrary units.
Energy decreasing left to right.
E_f=Fermi level position.

FIG 66. SPECTRA FROM EMISSION IMAGE SPOTS AT THE ANALYSER INPUT.

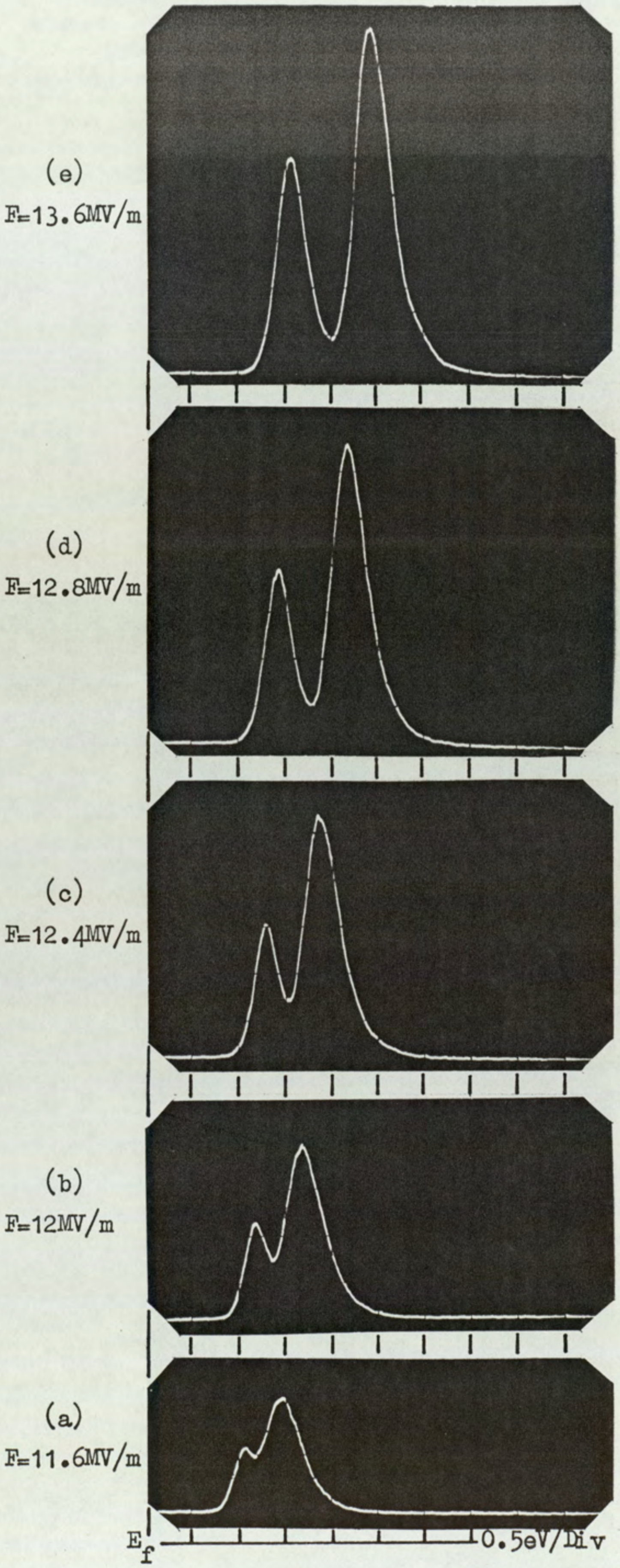

Y axis, current per unit energy arbitrary units.
Energy decreasing left to right. E_f=Fermi level.

FIG 67. COMBINED SPECTRA FROM TWO NEARBY SUB SITES AT PROGRESSIVELY INCREASING FIELD.

"hump" on its high energy edge, which then seems to slowly transform into a double peaked spectrum at higher fields. In-fact this shows that the spectra from neighbouring subsites on a specimen can have different spectral shifts from the Fermi - level at a given field,and furthermore that this shift may be a unique function of applied field for each sub-site. This sequence of spectra also indicates that the shift tends to depend directly on the sub-site current, i.e. the area under the curve, so that a large peak is shifted more than a smaller one. Thus an explanation is provided for the observation of Athwal (96) that in multipeaked spectra the subsidiary peaks "grow" on the high energy edge of the main peak as the field is increased. That this is only a trend however, can be seen from an examination of the multipeaked spectra presented here, i.e. some show the main peak nearest the Fermi level. Care was thus needed when interpreting the multipeaked spectra that were still occassionally obtained with the modified lens.

As explained in section 10 of chapter 5 the interfacing lens, operated under normal voltage conditions, produces a magnification of ∼60. Therefore since each emission image group occupied approximately the whole area of the phosphor screen which is 15 mm in diameter, the diameter of the whole electron beam entering the anode probe hole from a typical specimen site was ∼·2 mm. This value agrees well with the maps of emission current in the anode plane produced by Cox (27) and shown in figure (7) of chapter 2. It could thus be assumed that a negligible fraction of the emitted electrons were collected by an anode having a probe hole diameter of 1 mm. It may also be noted however, that such a large hole in conjunction with an electrode gap of 0·5 mm, results in a field reduction at the specimen surface on the lens axis of $\sim 15\%$. Accordingly, account has been taken of this effect in all subsequent calculations.

Since essentially all the electrons emitted from a specimen site pass through the anode probe hole, the method used to measure site currents described earlier in section 1 would enable accurate F.N. plots to be made for the whole site. From a fundamental point of view however, this procedure is relatively meaningless as each site consists of several sub-sites and each sub-site may have different characteristics. Accordingly the following method for measuring the current emitted by each sub-site was addopted for later measurements. This involved selecting a specimen site which produced not only a single image spot on the phosphor screen, but also a single peaked spectrum; both properties being maintained over a wide range of anode voltage. Hence the current measuring method previously used on collections of sub sites could be applied in this case to give reliable readings for a single sub site. Concurrently with these measurements a series of energy spectra were taken with the gain settings of the electron multiplier adjusted such that known relative spectral amplitudes were maintained over the whole sub - site current range. Since the area under the energy distribution is proportional to the emitted current, measurements of the areas of the above spectra enabled a comparison to be made between the measured sub-site currents and these areas. The spectral areas were then found to be proportional to the sub-site current with an uncertainty of $\sim\pm$ 15%. An absolute current calibration of the spectral areas could then be made by estimating the emission image size on the phosphor screen at particular currents. Repeating this for several sub-sites at various currents revealed an accuracy no better than to an order of magnitude. This however, is less important for subsequent calculations than the 15 % value quoted above for relative magnitudes, since a knowledge of the absolute value of current is only necessary when considering emission area, as explained later.

6.9 A Detailed Investigation For Copper and Oxidised Copper Specimens.

Several standard copper specimens were surface scanned to locate the emission sites in the usual way. In each case a stable sub-site emission spot was centred on the analyser input hole and a series of calibrated spectra were taken from the lowest detectable current $\sim 5 \times 10^{-13}$A to the limit of site stability at typically $\sim 5 \times 10^{-8}$A, by varying the applied anode voltage in 100 V steps. Figure (68) shows typical emission image spot patterns recorded from several specimens in this stable current range, where a given pattern would be expected to remain unchanged for at least 30 min. For sub-site currents approaching 10^{-7}A however, the spot pattern might change once in 10s, with the appearance or dissappearance of image spots, or the break-up of a large spot into several smaller ones; although the overall pattern would still be recognisable. At currents of the order of 10^{-7} to 10^{-6}A the whole emission site might change once in two seconds, frequently to a completely different pattern, while at higher currents each sub-spot would flicker on and off independently once or twice a second.

A specimen could be oxidised insitu by raising its temperature, while still under U.H.V. and with its site position held fixed, and then letting air into the vacuum chamber for a short time $\sim$ 30s, followed by an immediate pump-down. The temperature rise and oxidation time were kept as for the previous hot-plate experiment described in section 5 so that a definite average oxide thickness could be assumed. The specimen could then

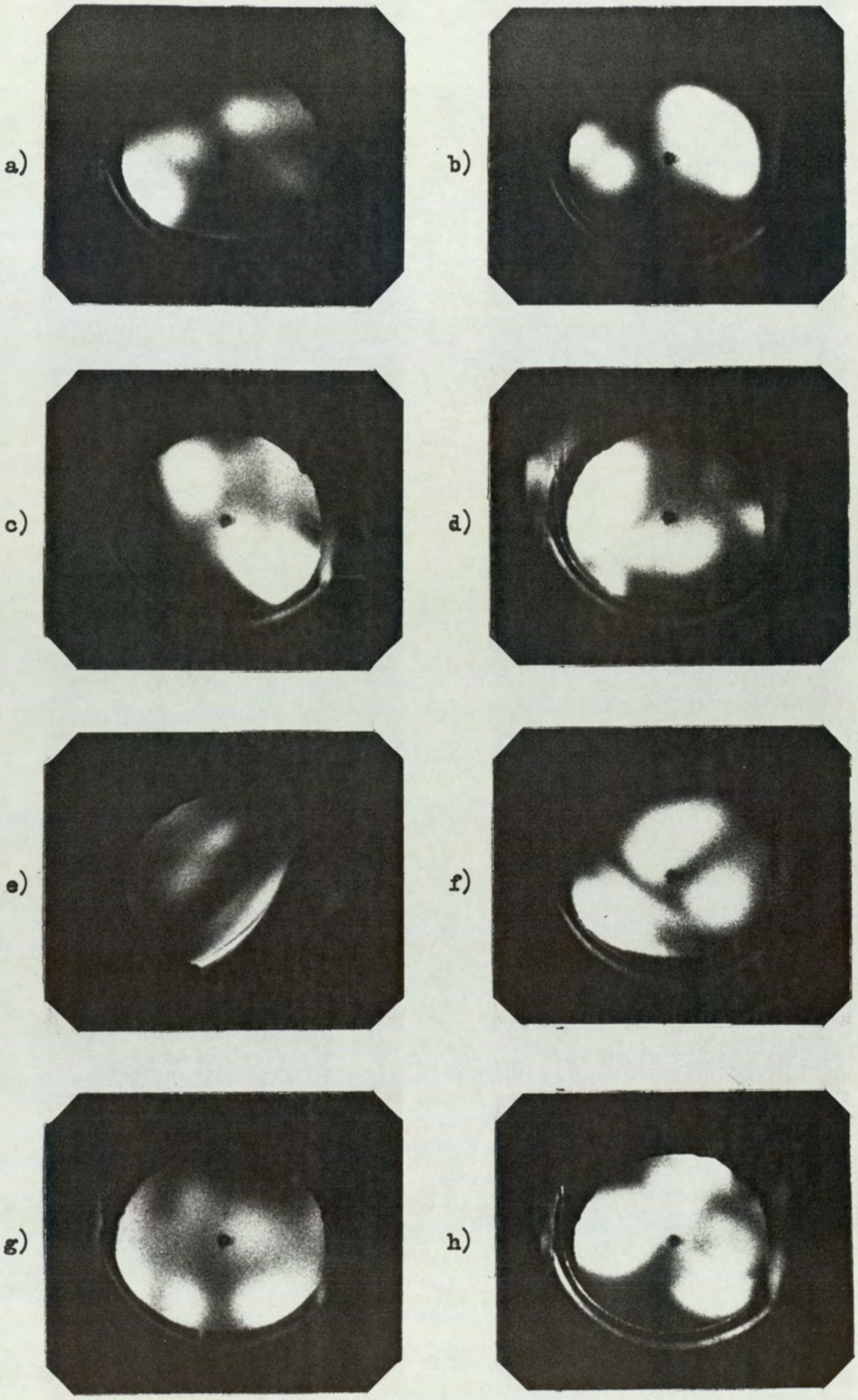

Diameter of the phosphor screen 15mm
Central input hole diameter 0.3 mm.

FIG 68.
TYPICAL ELECTRON IMAGE SPOT PATTERNS, AT THE ANALYSER INPUT FACE.

be repositioned to the correct gap and the sub-site emission pattern re-examined. Emission invariably resulted from the same site but the distribution of sub-site spots was usually different, often much more complicated. The resulting sequences of spectra obtained from these two specimens are shown in figures (69) & (70) for specimen 1, and in figures (71) to (73) for specimen 2.

The effects of a small temperature rise was also investigated, for both unoxidised and oxidised specimens, by continually monitoring the sub-site spot pattern and the electron energy spectra. It was found that specimen heating had a negligible effect on an unoxidised specimen's electron energy spectrum over a wide temperature range, i.e. up to 300°C, however, the spot pattern was found to become very unstable for temperatures in excess of 150°C. A similar instability existed for the oxidised case, but in addition as the temperature was raised a marked decrease in spectral shift was observed. This is shown in the sequences of spectra which were recorded from a single sub-site on specimen 3, i.e. figures (74) to (76), these were taken in the stable current range and at a fixed raised temperature.

It was particularly noted that the spectral shift recovery time when the oxidised specimens were cooling was much greater than the thermal time constant of the specimen plus holder. Thus the cool-down time from a temperature of $\sim 80^{\circ}C$ was about 20 min. but the thermally reduced spectral shift lasted for several hours. The higher the temperature the greater the reduction in shift and the longer the shift relaxation time on cooling. Upon heating however, changes in spectral shift were in step with the specimen temperature. The considerable amount of data contained in the spectra of figures (67) to (76) is analysed in the next chapter.

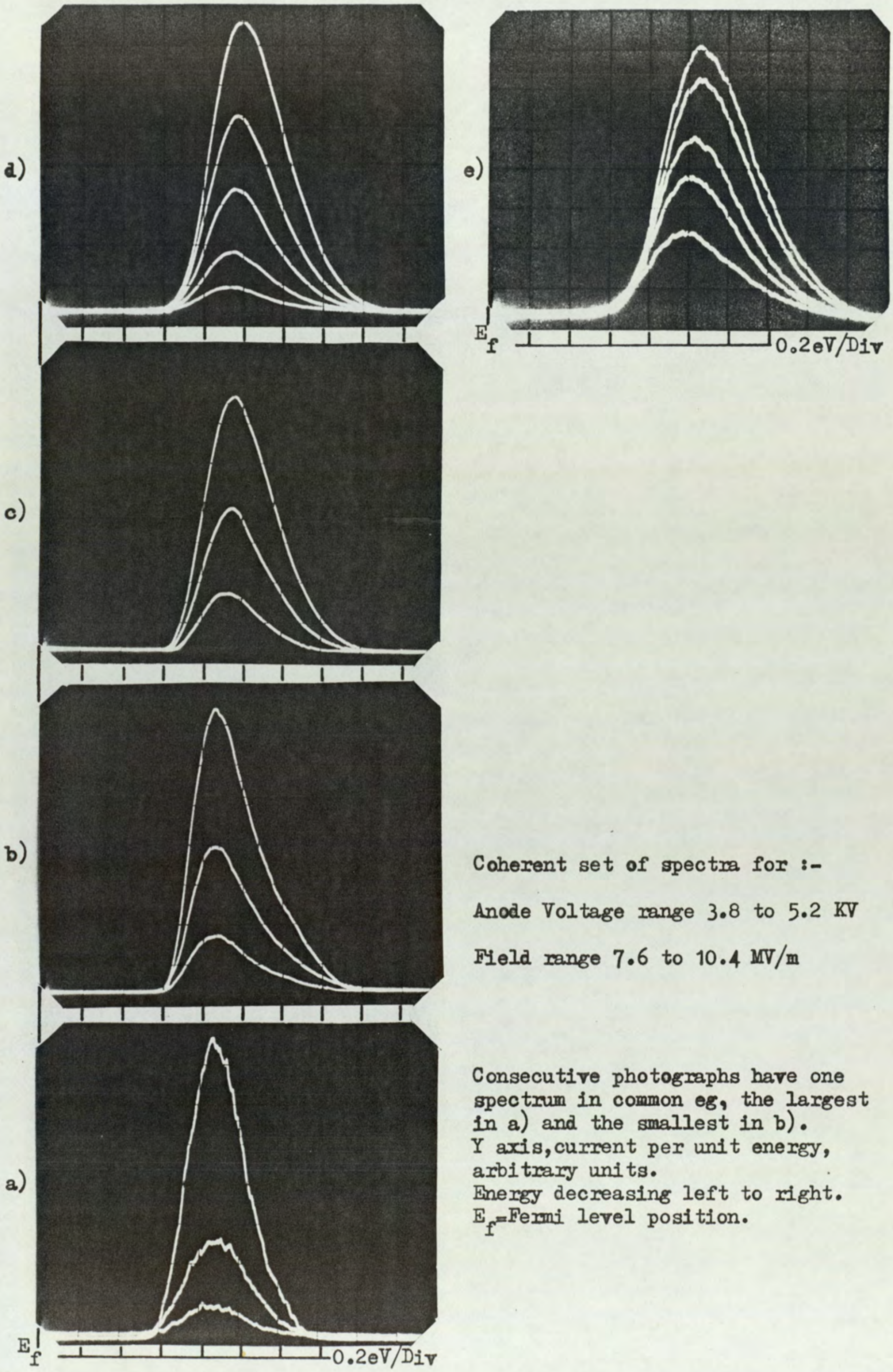

Coherent set of spectra for :-

Anode Voltage range 3.8 to 5.2 KV

Field range 7.6 to 10.4 MV/m

Consecutive photographs have one spectrum in common eg, the largest in a) and the smallest in b).
Y axis, current per unit energy, arbitrary units.
Energy decreasing left to right.
E_f=Fermi level position.

FIG 69. SEQUENCE OF SPECTRA FOR SPECIMEN (1), UNOXIDISED.

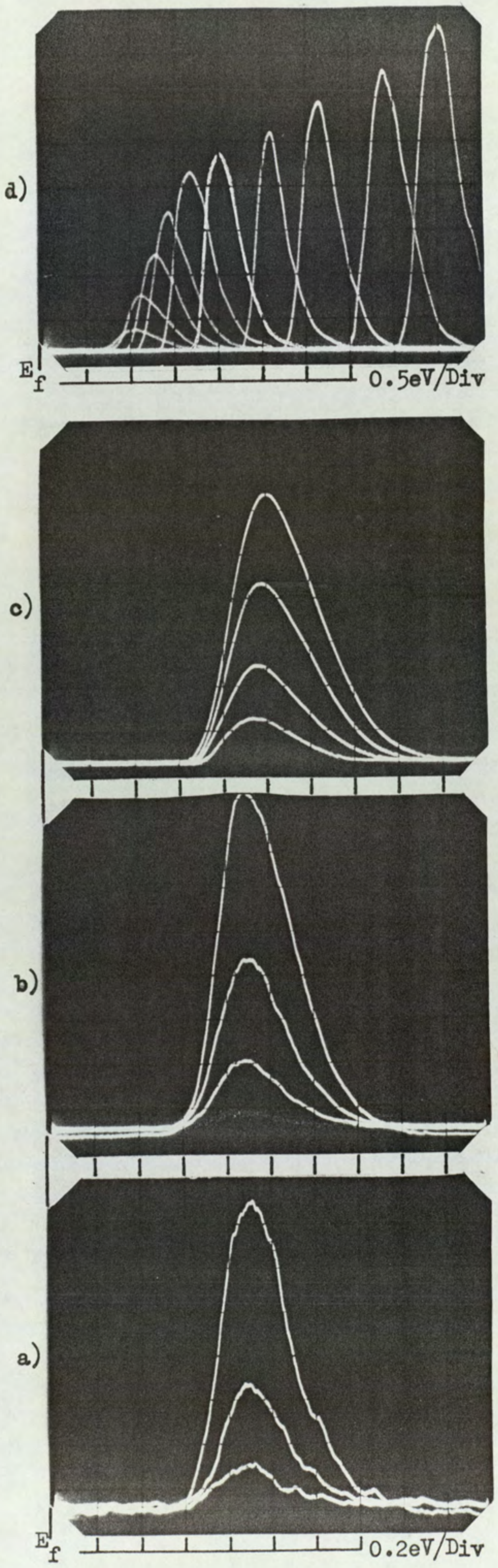

Coherent set of spectra for :-

Anode Voltage range 3.8 to 5.4 KV

Field range 7.6 to 10.8 MV/m

Consecutive photographs have one spectrum in common eg, the largest in a) and the smallest in b).
Y axis, current per unit energy, arbitrary units.
Energy decreasing left to right.
E_f=Fermi level position.

FIG 70. SEQUENCE OF SPECTRA FOR SPECIMEN (1),OXIDISED.

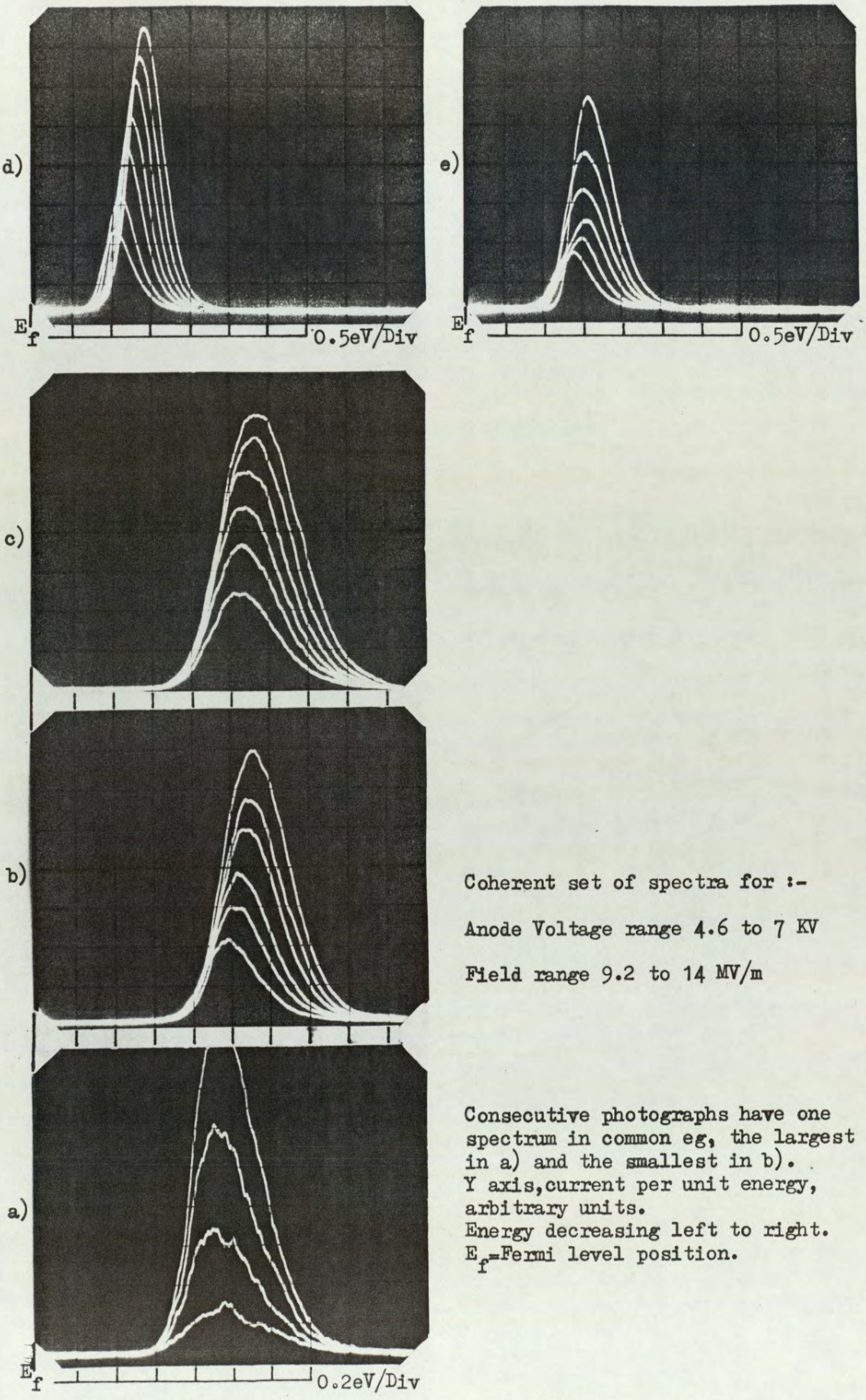

Coherent set of spectra for :-

Anode Voltage range 4.6 to 7 KV

Field range 9.2 to 14 MV/m

Consecutive photographs have one spectrum in common eg, the largest in a) and the smallest in b).
Y axis, current per unit energy, arbitrary units.
Energy decreasing left to right.
E_f=Fermi level position.

FIG 71. SEQUENCE OF SPECTRA FOR SPECIMEN (2), UNOXIDISED.

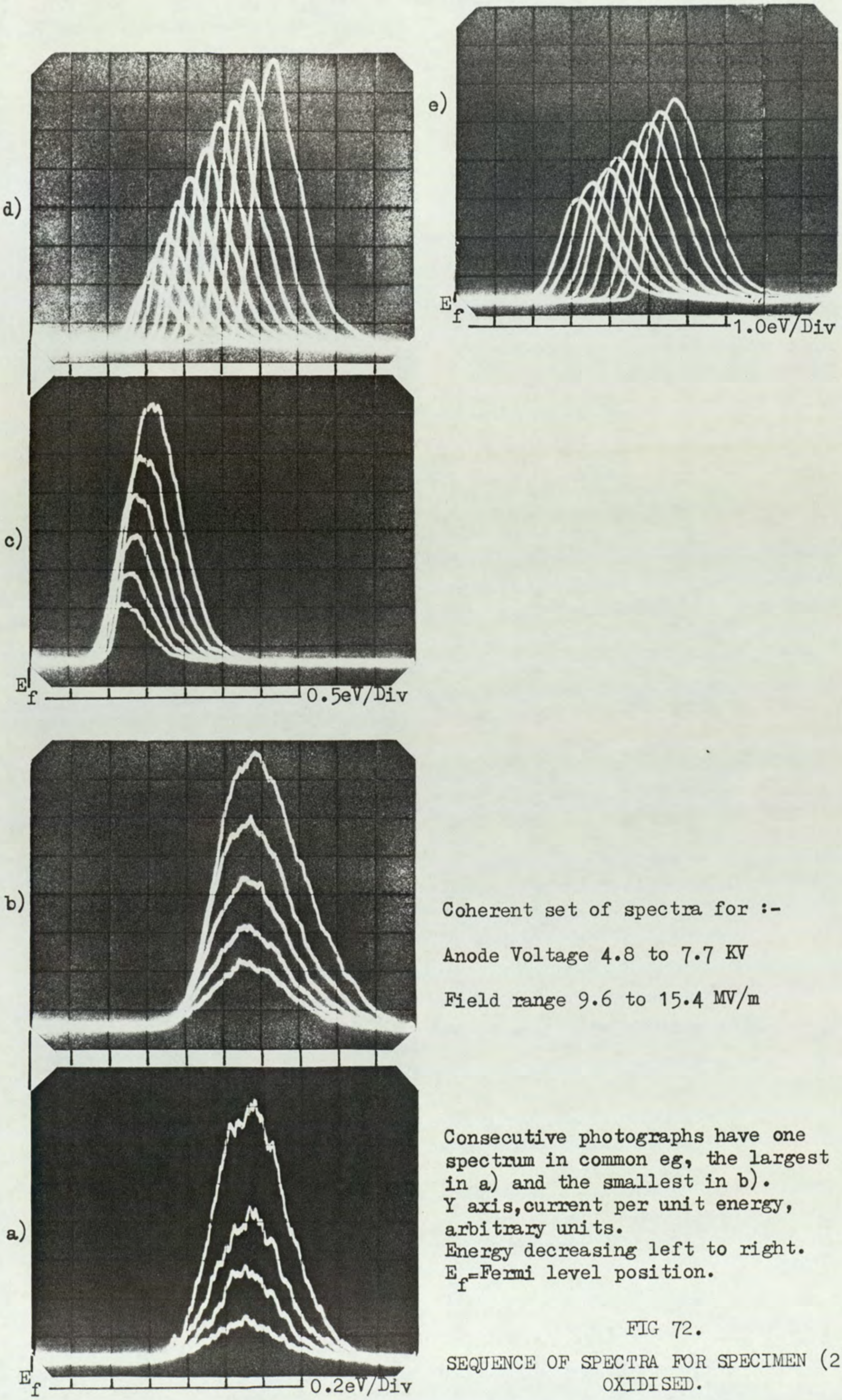

Coherent set of spectra for :-

Anode Voltage 4.8 to 7.7 KV

Field range 9.6 to 15.4 MV/m

Consecutive photographs have one spectrum in common eg, the largest in a) and the smallest in b).
Y axis, current per unit energy, arbitrary units.
Energy decreasing left to right.
E_f=Fermi level position.

FIG 72.

SEQUENCE OF SPECTRA FOR SPECIMEN (2) OXIDISED.

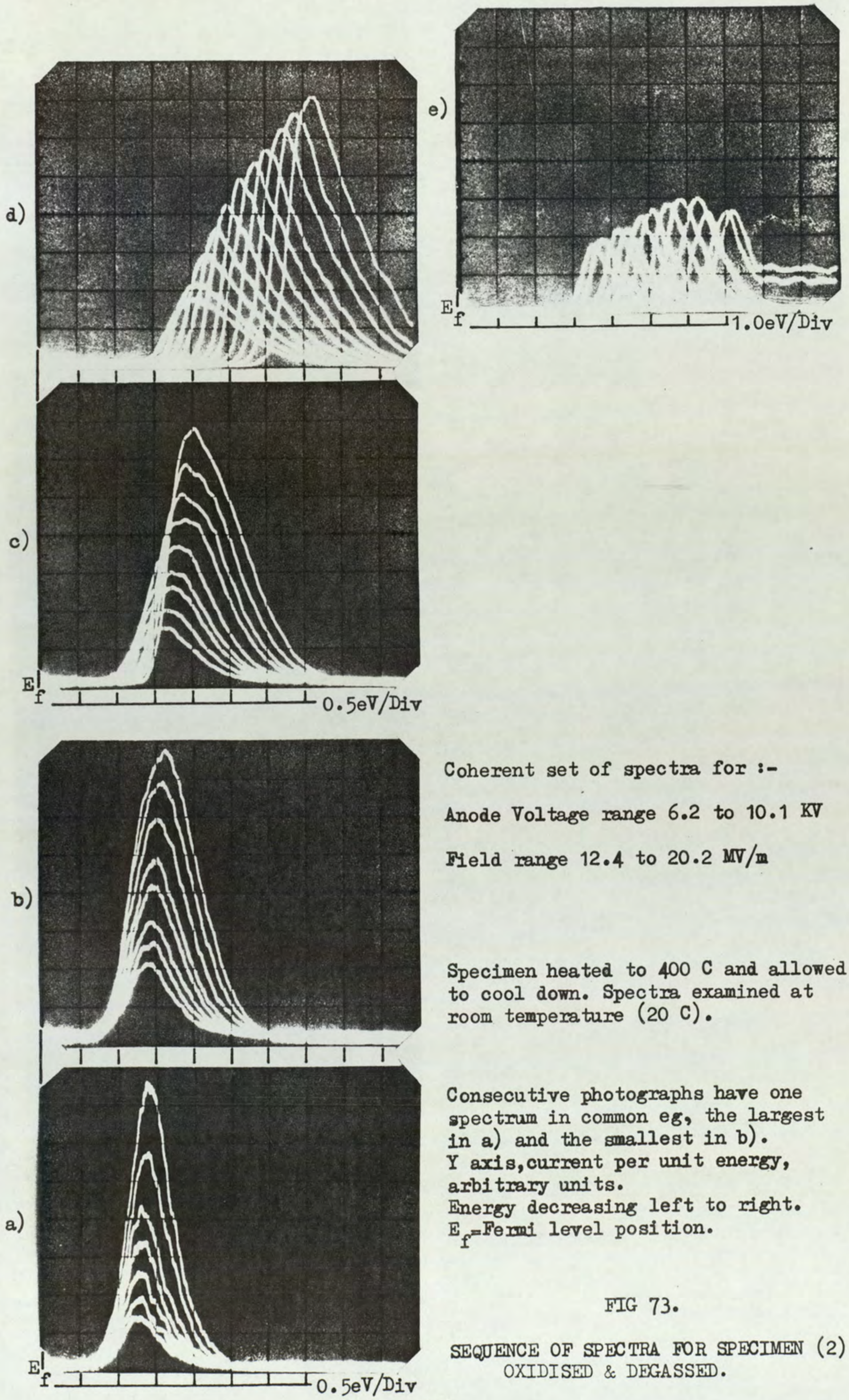

Coherent set of spectra for :-

Anode Voltage range 6.2 to 10.1 KV

Field range 12.4 to 20.2 MV/m

Specimen heated to 400 C and allowed to cool down. Spectra examined at room temperature (20 C).

Consecutive photographs have one spectrum in common eg, the largest in a) and the smallest in b).
Y axis, current per unit energy, arbitrary units.
Energy decreasing left to right.
E_f=Fermi level position.

FIG 73.

SEQUENCE OF SPECTRA FOR SPECIMEN (2) OXIDISED & DEGASSED.

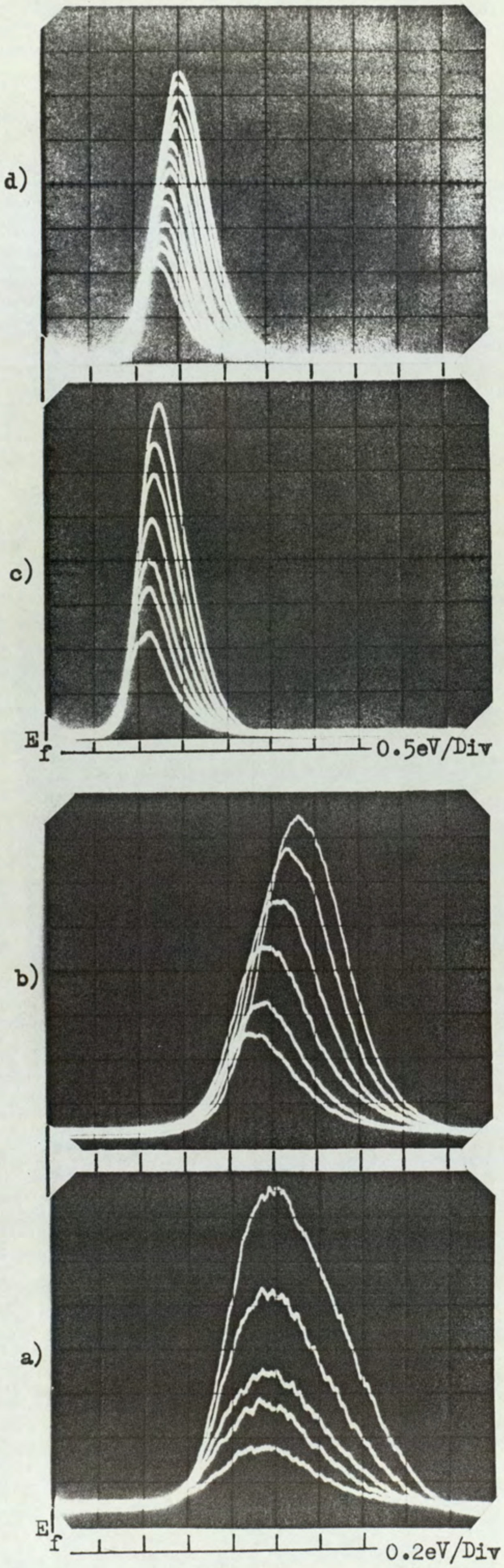

Coherent set of spectra for :-

Anode voltage range 5 to 7 KV

Field range 10 to 14 MV/m

Consecutive photographs have one spectrum in common eg, the largest in a) and the smallest in b).
Y axis, current per unit energy, arbitrary units.
Energy decreasing left to right.
E_f=Fermi level position.

FIG 74.

SEQUENCE OF SPECTRA FOR SPECINEN (3) UNOXIDISED.

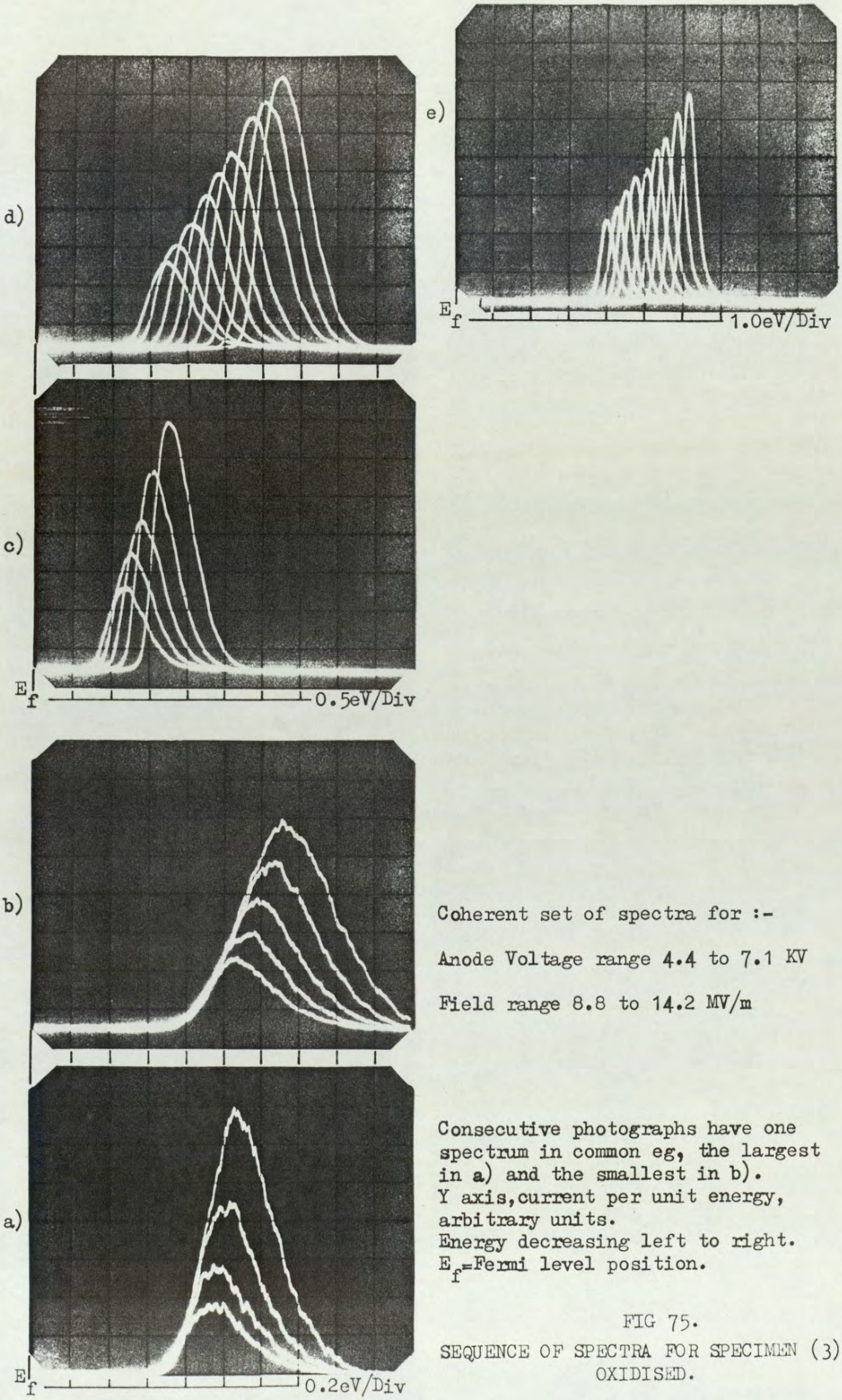

Coherent set of spectra for :-

Anode Voltage range 4.4 to 7.1 KV

Field range 8.8 to 14.2 MV/m

Consecutive photographs have one spectrum in common eg, the largest in a) and the smallest in b).
Y axis, current per unit energy, arbitrary units.
Energy decreasing left to right.
E_f=Fermi level position.

FIG 75.
SEQUENCE OF SPECTRA FOR SPECIMEN (3) OXIDISED.

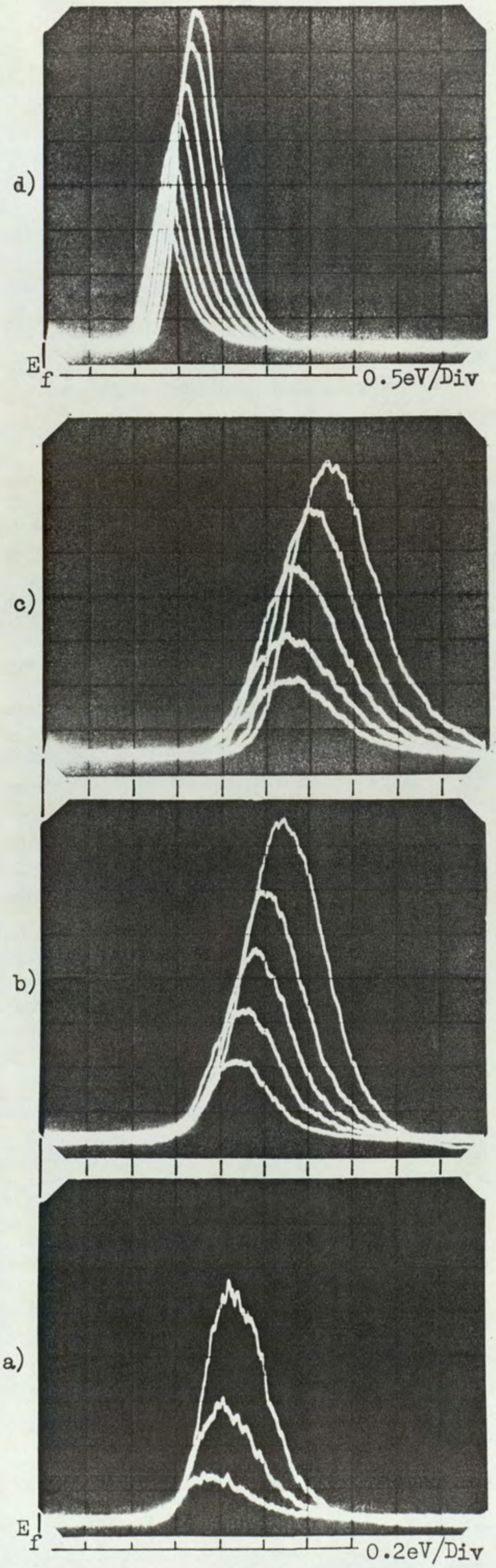

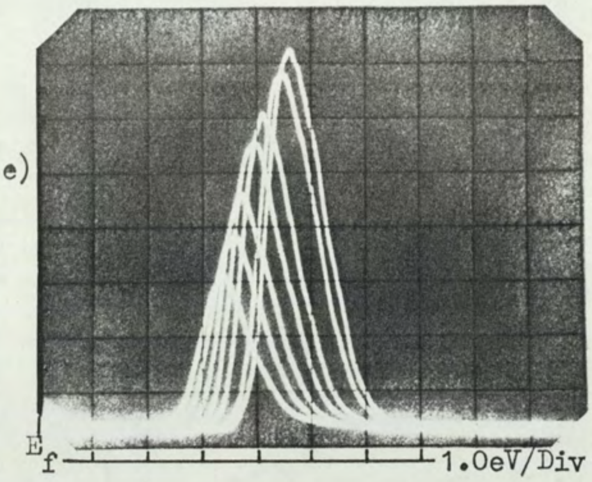

Coherent set of spectra for :-

Anode Voltage range 4.4 to 6.5 KV

Field range 8.8 to 13 MV/m

Specimen heated to 80 C and all spectra examined at this temperature

Consecutive photographs have one spectrum in common eg, the largest in a) and the smallest in b).
Y axis, current per unit energy, arbitrary units.
Energy decreasing left to right.
E_f=Fermi level position.

FIG 76.
SEQUENCE OF SPECTRA FOR SPECIMEN (3) OXIDISED.

6.10 Circuit Adaptation For the High Resolution Location of Emission Sites.

Towards the end of the present experimental programme it was realised that a simple circuit modification would considerably improve the resolution of the specimen scanning facility. As previously stated in chapter 5.14d this was limited to the anode probe hole diameter, or to the scanned picture size in relation to the oscilloscope trace spot diameter, which-ever was the poorest. In fact, the anode probe hole limited the scanning resolution to $\sim$ 1 mm. In order to increase the spatial resolution the circuit was modified by re-connecting the analyser input lens electrodes so that the system was set to record the electron energy spectrum; thus , when an emission site passed in front of the probe hole it produced it's spectral signal for a brief period. However, this signal was not displayed directly by the oscilloscope but was fed to the threshold detector in order to generate the scope bright-up signal. Everything else was connected as before for site scanning, so that now a site was detected if it produced a sufficiently large electron energy spectrum. A marked increase in spatial resolution was thus achieved, approximately given now by the resolution of the analyser input hole divided by the lens magnification, or the oscilloscope spot size, which ever was the poorer. Since the lens can resolve two electron beams separated by $\sim$10 μm in the anode plane it is clear that the oscilloscope spot size in relation to picture diameter is now the limiting factor, this then makes the overall resolution $\sim$100 um. The resulting picture appearing on the scilloscope screen during site scanning then represents the distribution of electrons in the anode plane rather than at the specimen surface. A further advantage of this arrangement was that the detector gain could be greatly increased;

previously this had been kept low because the electrometer which was used to detect the site currents tended to saturate for several seconds if the sensitivity was high and a large current was subsequently deted.

Early results using the improved system are shown in fig. (77); thus figure (77a) shows sites detected using the high gain high resolution detector, while figure (77c) shows the same area scanned at the same field but using the earlier electrometer detector. It would appear that a considerable amount of information has been lost in the past, and that what were thought to be isolated sites seem in fact to be associated with **localised areas which are milimetres** across that **are** particularly prone to electron emission. It must of course be remembered that this method of site detection makes all sites seem equally emissive.

It so happened that the large emitting area shown in figure (77a) could be identified by eye as being rather darker than the surrounding shiny copper surface; usually nothing in particular can be seen even in a conventional scanning electron microscope. In this case Auger electron analysis could be carried out because the site could be identified from its secondary electron image shown in figure (77b). The resulting Auger readout is shown in figure (78), where the large agglomeration had the following constituents:

ELEMENT	% CONCENTRATION.
S	2·54
Cl	3·29
C	44·22
O	11·89
Cu	38·06

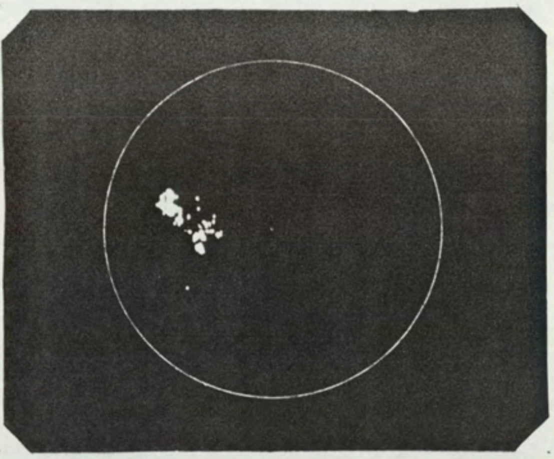

a) Site positions on the specimen surface (high resolution scan). Specimen A. F=10MV/m.

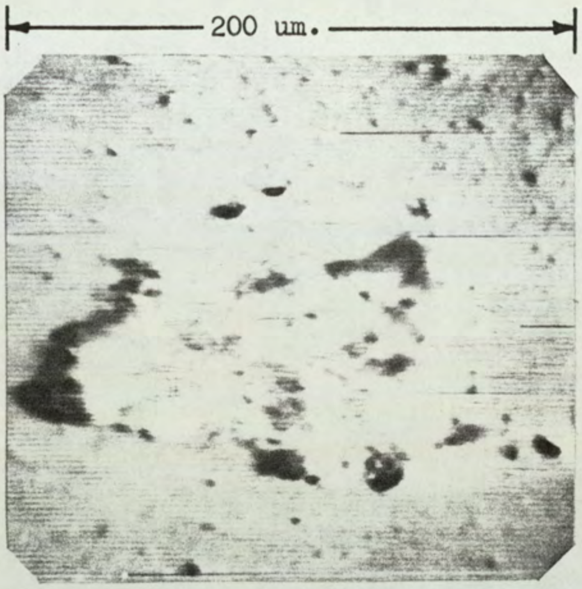

b) Electron image of the upper site on the surface of specimen A. As seen prior to Auger analysis.

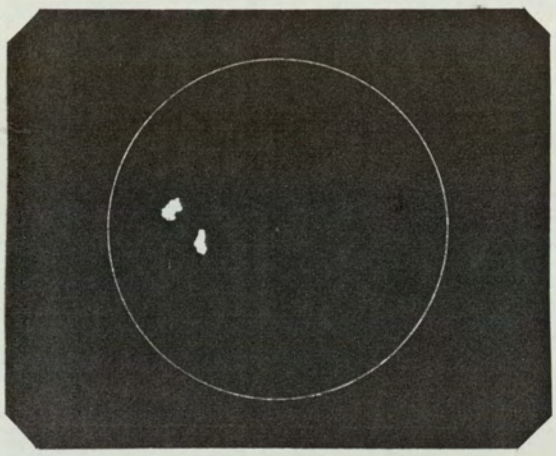

c) Site positions on the specimen surface (low resolution scan). Specimen A. F=10MV/m.

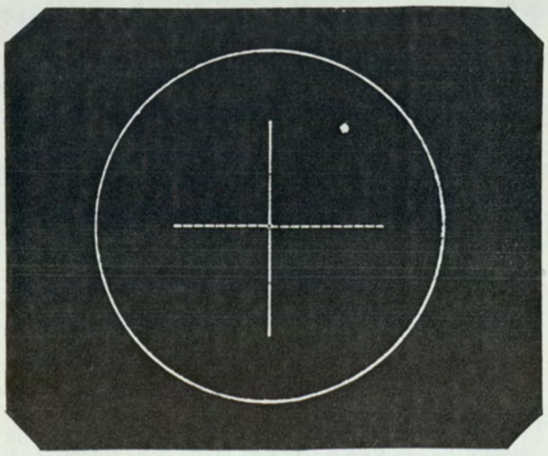

d) Site positions on the specimen surface (high resolution scan). Specimen B, F=12MV/m, I=1uA.

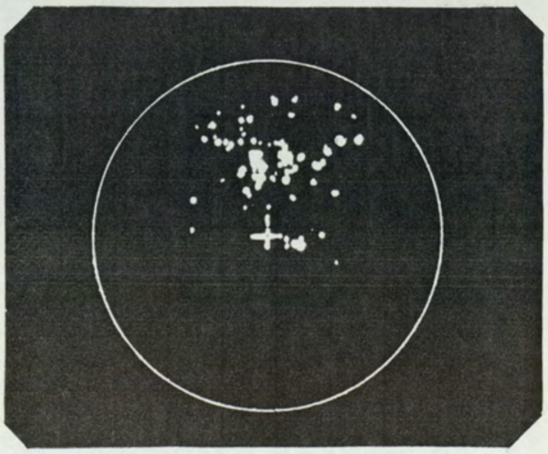

e) Site position on the specimen surface (high resolution scan). Specimen B, F=12MV/m, I=40uA.

FIG 77.

A COMPARISON OF HIGH AND LOW RESOLUTION SURFACE SCANNING TECHNIQUES.

FIG 78.

ASTON AUGER/X.P.S.
ANALYSIS

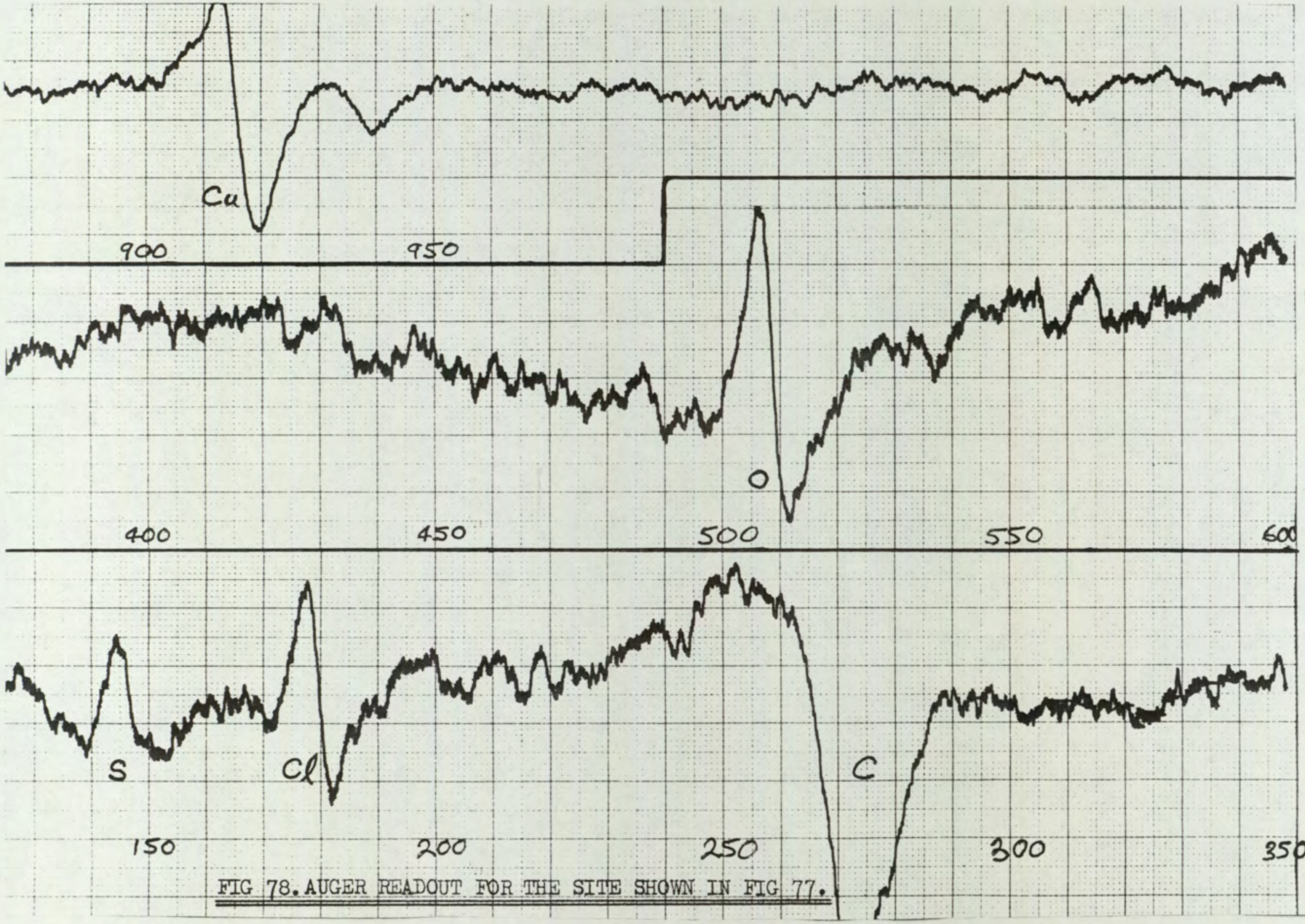

DATE 8-6-83
SPECTRUM Nº 1
SAMPLE Nº 1
PREPARATION —
ETCH 0
ETCH VOLTS
TECHNIQUE AES
PRESSURE 5×10⁻⁹T
SOURCE
VOLTAGE 5kV
SPOT SIZE 4 (<5μ)
CURRENT 300μA
MODE FRR
RESOLUTION LO
MAG. HI
SCAN
KE/BE 100
START
SCAN WIDTH 250
SCAN TIME 100S
SENSITIVITY 0·2mV
T.C. 10S
% BACKOFF
MULT. VOLTS 5-75
PREAMP MODE
MOD. 3v p-p

FIG 78. AUGER READOUT FOR THE SITE SHOWN IN FIG 77.

This data therefore suggests that its likely composition was a mixture of copper compounds (mainly copper oxide) and carbon. The presence of such a large amount of carbon is quite surprising unless it originated from the stainless steel anode during a previous microdischarge. It can however be said with certainty that such a large surface feature was not present before the specimen assembly was fitted into the vacuum chamber. In this regard, carbon, when added deliberately to an electrode surface has always been found to produce copious electron emission, but a thorough analysis of this effect has so far not been carried out. These findings indicate that more use could have been made of the Auger facility except for the fact that it's spatial resolution was only $\sim$ 20 um, which was not sufficient for re-locating micron sized sites if no definite feature could be identified, as is usually the case.

Lastly, figure (77d) shows a high resolution surface scan for another specimen which had been oxidised as previously described. This at first revealed a single site giving $\sim$ 1 uA for an anode voltage of $\sim$ 6 KV. However, over a period of two days experimentation sites seemed to "switch on" spontaneously at intervals, with no obvious cause or other effects, so that a second high resolution scan at 6 KV but now at a current of $\sim$40 uA gave the picture shown in figure (77e). From a retrospective examination of the specimen it was evident that microdischarges were the cause of the great proliferation of sites , since stainless steel could clearly be seen when the surface was viewed under an optical microscope; this was later confirmed by Auger analysis. Whether emission was enhanced by the local stainless steel layers or by the severely disrupted thick oxide film remains open to conjecture at present however.

CHAPTER 7.

DATA ANALYSIS IN TERMS OF A DETAILED HOT ELECTRON MODEL.

In this chapter the data obtained from the series of electron energy spectra given in section 9 of the previous chapter will be analysed in terms of a quantitative hot electron emission model. The basic assumptions of this model were outlined in chapter 4-section 10 where they were also compared with the assumptions made for earlier hot electron models and with those of other emission models. However, in order to benefit fully from the instrumental and observational improvements introduced in chapters 5 & 6 it is necessary to develope the hot electron model in much greater detail than has hitherto been the case. In this context, previous results were principally discussed on a qualitative basis when referring to emission models, and even then largely in terms of F.N. plots which fundamentally should only apply to the direct field emission of electrons from metals. The recent quantitative hot electron model proposed by Latham(122) provided the link between the earlier energy band models of emission through insulators and the fact that experimental results approximately follow the linear F.N. relationship. However, this model has been shown to be over simplified, and it does not directly relate to the energy band diagrams which best describe the characteristics of the insulating inclusions, hence it was of only limited practical use.

This more rigorous developement of the model however is still based on electron conduction from the metal substrate through a single layer of imperfect insulator, since the detailed structure of any emission site is unknown. Therefore, this layer will be held to account for the effects due to surface oxide coverage and to possible surface inclusions, without distinguishing between the two.

7.1. The Hot Electron Emmission Model in Detail.

Referring to the energy band diagram of figure (79), this represents stable electron conduction through a localised region of an insulating layer on the surface of a metal electrode, following the primary switching events as discussed in chapter 4. 10a. The potential at the insulator vacuum surface will then be equal to the contact potential ($\phi_M - \phi_I$) plus the surface potential due to the electric field within the insulator. An electric field penetrating into a non conducting insulating layer will produce a surface potential given by-

$$\frac{d}{\varepsilon}\,\frac{V}{D} \qquad (1)$$

with the parameters as given below, but the presence of a conducting filament will increase the field around the conducting region and may also change the dielectric constant slightly. Hence the insulator vacuum surface potential for a conducting filament will become

$$\frac{d}{\varepsilon}\,\beta\,\frac{V}{D} + \phi_M - \phi_I \qquad (2)$$

in the absence of trapped surface charge, where ϕ_M and ϕ_I are the metal and insulator work functions respectively (in eV), ε is the insulator dielectric constant and d its thickness, while D is the specimen-anode gap, V the applied voltage and β is the conducting channel field intensification factor. Under stable current conditions, however, electrons will be trapped throughout the insulator at trapping centres, also at its vacuum surface in surface states and possibly at the bottom of the conduction band where the vacuum surface barrier is too wide for electron tunnelling.

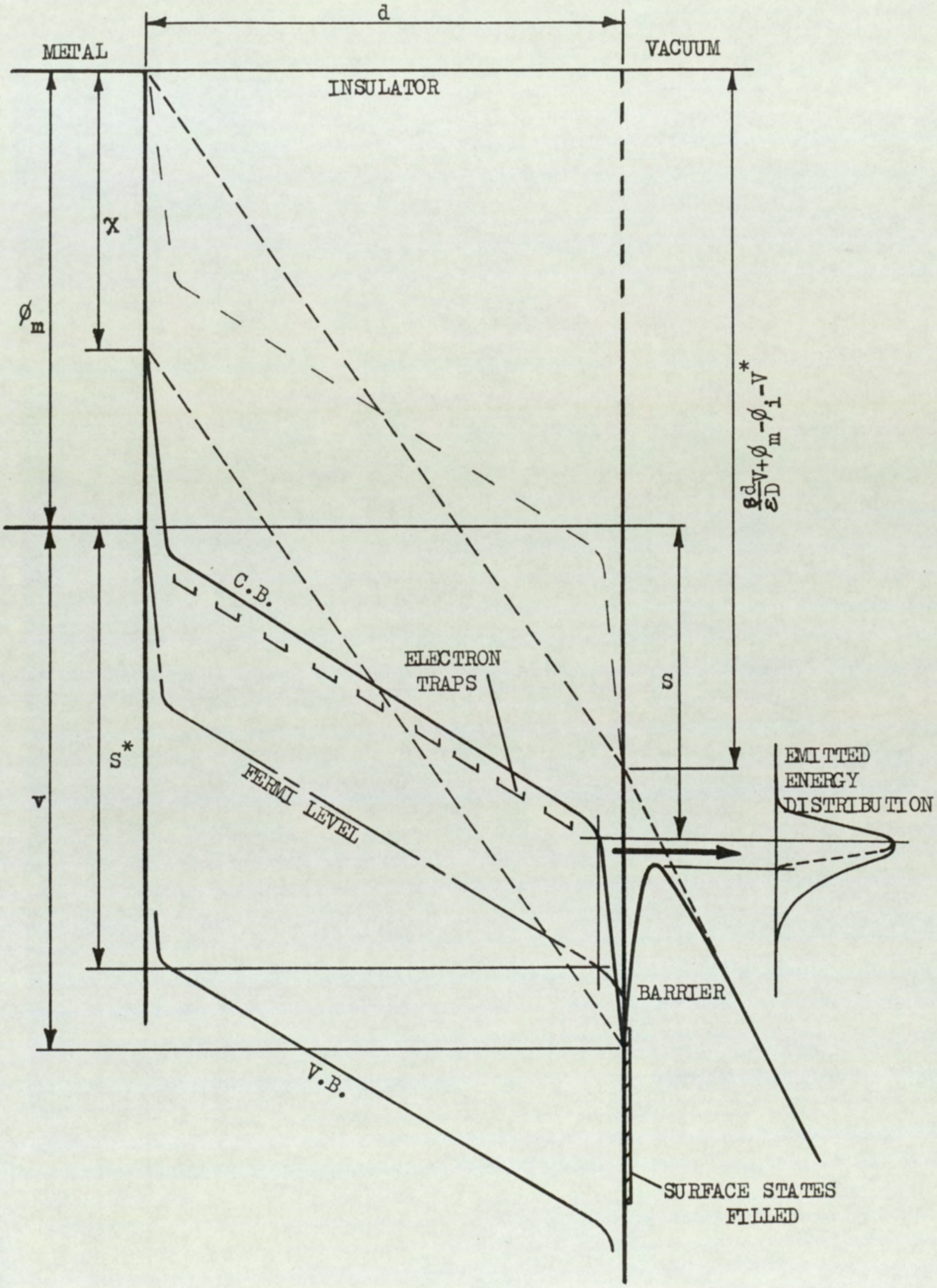

FIG.79. ENERGY BAND DIAGRAM FOR THE HOT ELECTRON MODEL OF AN ESTABLISHED CONDUCTING FILAMENT.

The insulator surface potential then becomes

$$\frac{d}{D}\frac{\beta}{\varepsilon} V + \phi_M - \phi_I - V^* \qquad (3)$$

where V^* represents the effect of the stored negative charge produced by electrons trapped at the vacuum surface etc. V^* would be expected to vary with field as the position of the Fermi level at the insulator vacuum surface changes, but for simplicity of analysis this will be considered constant so that the results will then represent only a first approximation to the actual case.

With regard to the vacuum potential barrier, in the absence of electron image forces and surface contamination, this will have a height equal to the insulator electron affinity X, since the unmodified barrier peak and the insulator surface vacuum level are at equal energy under these conditions. The Schottky image force correction then reduces this except for a further correction due to the dielectric nature of the emitting surface. Stratton (71) gives this correction as

$$\left(\frac{\varepsilon^* - 1}{\varepsilon^* + 1}\right)^{\frac{1}{2}} \qquad (4)$$

where ε^* is the high frequency dielectric constant since emitted electrons only spend a very brief period close to the insulator surface. However, at the end of a conducting channel the surface electron density will be assumed to be high enough for this correction to be insignificant, and the image force barrier height reduction term will then be as for a metallic emitter.

The barrier height (in eV) will then be

$$X^* - \left(\frac{e\,\beta\,V}{4\pi\mathcal{E}_0 D} \right)^{\frac{1}{2}} \qquad (5)$$

where e is the electronic charge, $\mathcal{E}_0$ the permitivity of free space and X^* represents a modified X due to surface contamination. Figure (80a) then shows an enlarged region around the surface potential barrier that is believed to exist at the insulator - vacuum interface together with a typical emission spectrum. It is also assumed that the spectral peak is positioned opposite the bottom of the conduction band at a point just before the band bends into the high field surface region. This is because electrons are fed into the surface region at the knee in the conduction band where they are accelerated by the high field towards the vacuum interface. An enhanced probability for emission will then result there, if the conduction band knee is closer to the vacuum surface than a few times the hot electron mean free path length in the insulator, i.e. ~10 to 50 nm.

Referring again to figure (79), S is the measured shift of the spectral peak from the metal Fermi level, while **v** represents the calculated difference in energy between the conduction band edge at the vacuum surface and the metal Fermi level. Hence from the geometry of figure (79) **v** is given by

$$v = \frac{d\,\beta}{D\,\mathcal{E}}V + \phi_M - \phi_I - V^* - \phi_M + X \qquad (6)$$

or

$$v = \frac{d\,\beta}{D\,\mathcal{E}}V + X - \phi_I - V^* \qquad (7)$$

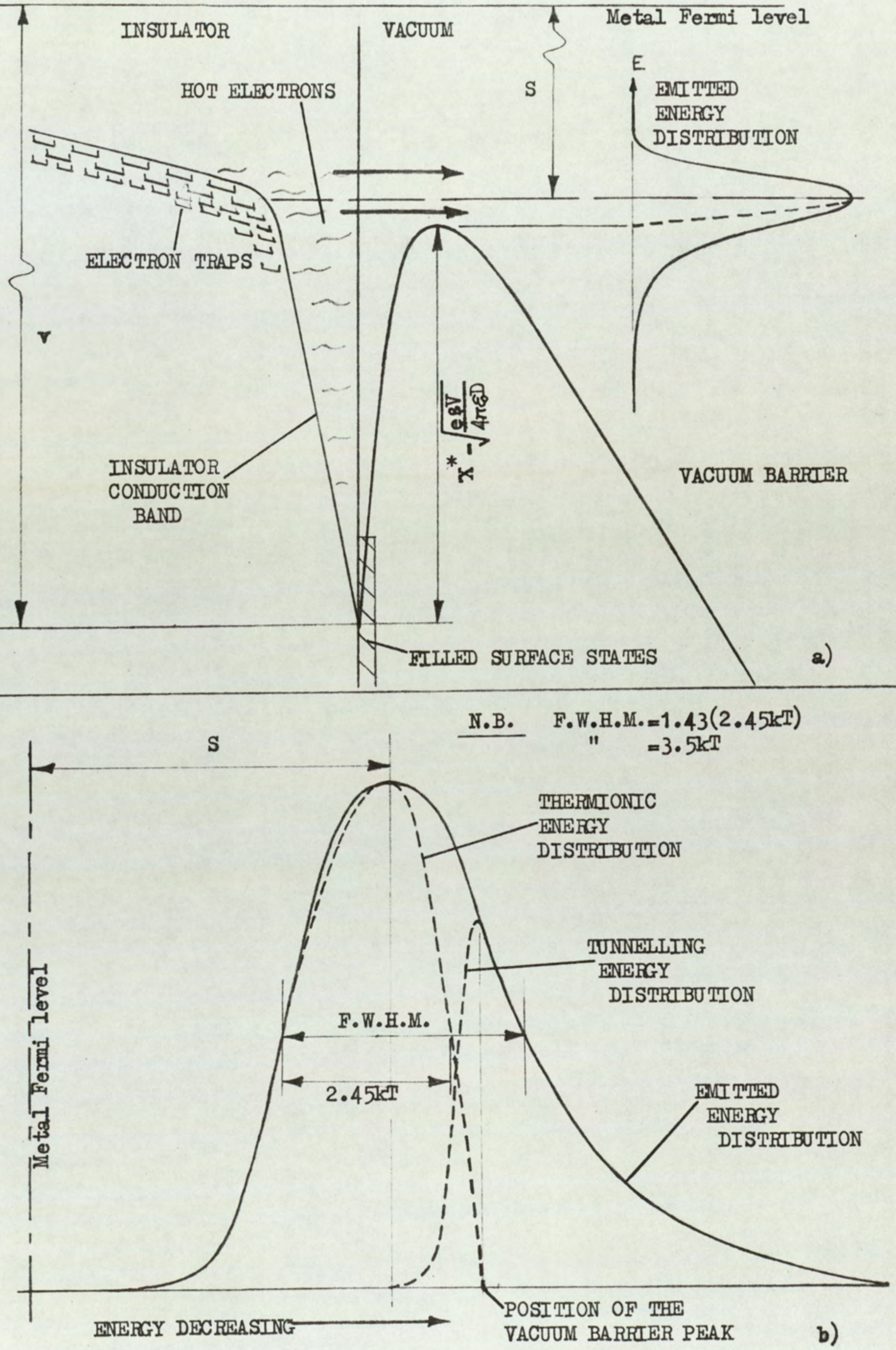

N.B. F.W.H.M. = 1.43(2.45kT)
" = 3.5kT

FIG.80. SCHEMATIC DIAGRAMS OF, a) THE REGION ARROUND THE VACUUM BARRIER AND b) THE COMPONENT SPECTRA OF THE EMITTED ENERGY DISTRIBUTION

Since most electrons lose energy S (eV) in traversing the insulator bulk the energy available for generating hot electrons near the vacuum surface, with respect to the conduction band bottom will be

$$\Delta E = v - S \qquad (8)$$

However, a large proportion of this energy will be lost as the electrons react with the insulator lattice in an attempt to thermalise down to the lattice temperature T_0. A Boltzmann gas of electrons at temperature T will have a mean kinetic energy given by $\frac{3}{2}kT$, where k is Boltzmann's constant, and this will be equal to the ambient kinetic energy $\frac{3}{2}kT_0$ if there is no additional input of energy to the electrons. The extra energy available to electrons in the insulator-vacuum surface region is ΔE, and it will be further assumed that the resulting temperature T of the hot electrons is a linear function of ΔE as indicated by the data given by Zhdan et.al. (94) in chapter 3.6. Hence equating energy terms $\frac{3}{2}kT = M^* e \Delta E + \frac{3}{2}kT_0$, where M^* is an unknown constant. Replacing M^* by the constant M this equation may be written as

$$kT = M e \Delta E + kT_0 \qquad (9)$$

In order to obtain further information about the hot electron temperature it is first necessary to appreciate that an actual emission spectrum is composed of a thermionic component corresponding to electrons going over the barrier, and a field emission component corresponding to electrons tunnelling through the barrier. These components are shown in figure (80b) by dashed lines : the thermionic component was calculated from equation 22 in chapter 3.5. which was then subtracted from a typical emission spectrum to give the tunnelling component. It will be seen that the thermionic distribution fits the high energy slope of the measured energy spectrum very well, except for the small region just off the peak. The measured spectrum has a relatively greater electron emission at this point, presumably reflecting the slightly enhanced emission probability which results from the closeness of the insulator conduction band knee to the vacuum surface, as explained earlier.

The classic Richardson electron energy distribution (90) for thermionic emission has a F.W.H.M. given by 2·45 kT. This expression however assumes an essentially "black body" emission showing no internal structure effects of the emitter, so that a higher value results when these effects, such as non free electron behaviour, are taken into account. (137) In this case, a simple function for the F.W.H.M. of most measured spectra may be obtained with reference to figure (80b), where it will be seen that the measured F.W.H.M. is $\sim$1·43 times the super imposed thermionic F.W.H.M. Hence the measured F.W.H.M. in eV will be given by

$$\text{F.W.H.M.} \sim 1{\cdot}43 \quad (2{\cdot}45\ kT)\,/e = 3{\cdot}5\ kT/e \qquad (10)$$

while for non typical spectral shapes such as in the results of figure (73) chapter 6, a separate proportionality constant may be calculated in a similar manner for that particular geometry. A more accurate method of deriving this relation for the entire series of spectra which were obtained as the applied field was varied, would have been to fit a thermionic component to each measured spectrum in turn and then to calculate an individual factor of proportionality for each : in this way the slight variation in the shape of the spectrum with field would be overcome. However, it was decided that the amount of work involved was not justified by the accuracy of the experimental data.

Following the above observations on the spectral components in the emitted energy spectrum, it will also be seen that the Richardson-Duschman relation for thermionic emission, i.e. equation 17 of chapter 3.5., is only applicable to the total emitted current here provided it is realised that this procedure results in an error to any calculated emitting areas of about 30%, due to the correction required for the tunnelling component. This relation is

$$I = 1{\cdot}2 \times 10^{6} \quad aT^{2}\ \mathrm{EXP}\left[-\frac{e\phi}{kT}\right] \qquad (11)$$

where I is the current emitted from area a and ϕ is the barrier height in eV.

Various relationships may now be calculated as follows : equations 7, 8, and 9 may be substituted into equation 10 to give

$$\mathrm{F.W.H.M.} = 3{\cdot}5\,M\,(v - S) + 3{\cdot}5\,kT_0 / e$$

$$\text{or F.W.H.M.} = 3{\cdot}5\,M\left(\frac{\beta d}{\mathcal{E} D} V - S - \phi_I - V^{*} + X\right) + 3{\cdot}5\,\frac{kT_o}{e} \qquad (12)$$

which on re-arranging in terms of the constants

$$M_1 = 3{\cdot}5\,M \qquad (13) \qquad\qquad B = \frac{\beta\ d}{\mathcal{E}\ D} \qquad (14)$$

$$C_1 = 3{\cdot}5\,M\left(X - \phi_I - V^{*}\right) + 3{\cdot}5\,\frac{kT_o}{e} \qquad (15)$$

reduces to an equation of a straight line thus.

$$\mathrm{F.W.H.M.} = M_1\ (BV - S) + C_1 \qquad (16)$$

This equation then relates measurements of spectral F.W.H.M. to the peak shift S and the applied voltage V, and treats (BV - S) as a single independant variable. A convenient method of solution for this equation is to programme a computer to give a least squares fit to the data for an assumed value of B, and to calculate a regression coefficient R (138) indicating the closeness of fit to a straight line. Data giving a graph of negative slope will produce an exact fit to a staight line if the value of the regression coefficient R is - 1. Values between -•98 and - 1 indicate quite good fits to straight lines. Other B values can be tried until the value of R is maximised and the optium straight line found, from which values can then be assigned to the other constants M_1 and C_1. If now a further constant G is defined as

$$G = V^* + \phi_I - X - \frac{kT_o}{Me} = - \frac{C_1}{M_1} \qquad (17)$$

and the various parameters are substituted into the Richardson - Duschman relation of equation 11 one has

$$I = 1{\cdot}2 \times 10^6 \, a \frac{e^2 \ M^2}{k^2} (BV - S - G)^2 \ \mathrm{EXP} \left[\frac{-X^*}{M(BV - S - G)} \right] \qquad (18)$$

It can now be shown that this equation gives an approximately straight line when experimental I - V data is presented in the form of a Fowler - Nordheim plot. Thus, if the shift data is not included the terms inside the square brackets can be written as

$$B \left(V - \frac{G}{B} \right)$$

and since V is about twice as large as G/B this can always be set proportional to V for a sufficiently restricted range of V, as is the case for normal experiments.

Hence

$$I = \text{Constant} \times V^2 \ \text{EXP} \left[\frac{\text{Constant}}{V} \right]$$

which is of F.N. form and will give a straight line when represented as a plot of ln $^{I}/_{V^2}$ against $^{1}/_{V}$. The most exact expression for the emitted current obtainable from this model includes the Schottky barrier height reduction given by equation 5 so that equation 18 becomes

$$I = 1{\cdot}62 \times 10^{14}\ a\ M^2\ (BV - S - G)^2\ \ \text{EXP} \left[\frac{-X^* + \left(\frac{e\beta V}{4\pi\mathcal{E}_o D} \right)^{\frac{1}{2}}}{M\,(BV - S - G)} \right] \qquad (19)$$

This expression now relates the spectral measurement of current, (i.e. area), to peak shift S and the applied voltage.

The easiest method of solving this equation is to firstly take logarithms, i.e.

$$\ln \frac{I}{(BV - S - G)^2} = \ln 1.62\text{x}10^{14}\ a\ M^2 + \frac{1}{M} \left[\frac{-X^* + \left(\frac{e\beta V}{4\pi\mathcal{E}_o D} \right)^{\frac{1}{2}}}{BV - S - G} \right] \qquad (20)$$

and then to define the additional constants thus

$$M_2 = \frac{-X^*}{M} \quad (21) \qquad C_2 = \ln(1.62\text{x}10^{14}\ a\ M^2) \quad (22) \qquad W = \frac{\beta}{(X^*)^2} \quad (23)$$

so that

$$\ln \frac{I}{(BV - S - G)^2} = M_2 \left[\frac{1 - \left(\frac{W\,e\,V}{4\pi\mathcal{E}_o D} \right)^{\frac{1}{2}}}{BV - S - G} \right] + C_2 \qquad (24)$$

which is an equation to a straight line with a dependent variable

$$\ln \frac{I}{(BV - S - G)^2} \equiv \underline{\text{H.E.}} \quad \ln \frac{I}{f\,(V, S)} \qquad (25)$$

and an independent variable

$$\frac{1 - \left(\frac{W\,e\,V}{4\pi\varepsilon_0 D}\right)^{\frac{1}{2}}}{BV - S - G} \equiv \underline{\text{H.E.}} \quad F(V, S) \qquad (26)$$

N.B. the H.E. functions defined on the R.H.S. are used to label the graph axes of the next section. In order to solve this equation reasonable values must be assigned to G, W and B based on the values obtained from the F.W.H.M. graph. Unfortunately the measurement of F.W.H.M. has a rather high uncertainty and the change in spectral shape with field was not taken into account, so that the values of M_1, C_1 and B are only approximate. A least squares fitting procedure giving the best straight line to the above equation can then be carried out by optimising B as before for equation 16. Results can then be compared with those obtained from the F.W.H.M. graph and with data from the standard F.N. plot, which can be generated using the above equation by setting $S = G = 0 = W$ and $B = 1$.

Before this data is examined however, a further relationship will be derived between the emitted current and the spectral shift voltage S. From figure (79) it will be seen that if the knee in the conduction band bottom is very close to the vacuum surface, then the total drop in energy in (eV) from the metal Fermi level to the insulator Fermi level measured beneath the knee, i.e. S^*, will be equal to the voltage dropped by the metal - insulator contact plus that dropped by the insulator bulk. As the insulator

Fermi level is ($\phi_I - X$) below the conduction band edge by definition we have

$$S^* = S + \phi_I - X \qquad (27)$$

This assumes that Fermi level position in relation to the bottom of the conduction band is only slightly affected by any injected electrons or those which have become trapped in the insulator bulk. In the very narrow high field region just before the insulator vacuum interface however, a marked shift in the Fermi level position would be expected, due to the large number of electrons trapped in surface states and the pool of hot electrons. The relationship derived for S^* also implies that the potential dropped in the high field region close to the vacuum interface does not affect the spectral shift voltage S, **this** is **not the case** in all previous hot electron models. Thus by assuming a typical value for $\phi_I - X$, a functional plot of S^* against I should reveal information about the insulator contact and bulk parameters. Here $\phi_I - X$ has been set equal to 1•5 eV in all calculations.

From chapter 4 it was noted that for the type of blocking contact assumed, a plot of

$$\ln \frac{I}{V_c} \text{ versus } V_c^{-\frac{1}{2}}$$

should be a straight line if the conduction is contact-limited. On the other hand if the insulating layer is thick enough, bulk-limited behaviour is described by a linear plot of

$$\ln I \text{ versus } V_b \text{ and here } S^* = V_c + V_b .$$

If the thick insulating layer has in addition a large defect population, a contact-limited to bulk-limited transition may occur in the voltage range usually measured. This will subsequently be shown on a ln I versus $S^{*\frac{1}{2}}$ plot as the smooth intersection of the straight bulk-limited line with an almost straight line representing the contact-limited region. The contact-limited line will also tend to a straight line on this plot for the lower voltages and will be very steep.

7.2. Data Analysis

Having derived the equations which quantify this particular hot electron emission model, they may now be used to analyse the data obtained from the individual emission spots of the three copper specimens which were presented in figures(69) to (76) of chapter 6. Hence the plots of figures(81) to (88), refer to the data obtained from specimen (1) while figures (89) to (96) refer to the data obtained from specimen (2). Most of the data for specimen (3) is not presented in graphical form because it would only duplicate the other two sets of plots, however, additional data for specimen (3) is presented in figure (98). The various plots associated with specimens (1) and (2) will be discussed in parallel since the interpretations are the same, while the physical implications will be discussed in a later section of this chapter.

Thus the graphs shown in figures(81) and (89) result from a conventional F.N. treatment of the data, where it will be seen that the plots are only approximately linear, as is often the case for unconditioned electrodes. Previously the points obtained from the unoxidised specimens would have been considered to give quite good fits to straight lines, but this is not justified on statistical grounds since the outer points would all lie below the line while the central points would all lie above it.

The lines for the oxidised cases all show a "saturation" effect at the higher values of current which has also often been seen for "unoxidised" specimens $^{(18, 27, 96)}$ but was not properly explained. The field intensification factors (β) quoted on the F.N. graphs refer to the best fit straight lines taking all the points into account.

It will now be shown that the present hot electron model does not suffer from these non linear difficulties since a plot based on equation 19 gives excellent straight lines in all cases. Thus the plots of figures (82 & 83) and figures (90 & 91) show nothing but random fluctuations about the best fit lines , having R values close to -1,which resulted from use of the same data as in the above F.N. plots; there being no need to introduce complications such as space charge effects to try to explain the overall results.

The graphs of figure (84) and figure (92) indicate how the spectral F.W.H.M. relates directly to applied anode voltage, where again the "unoxidised" plots are very slightly curved and the "oxidised" plots have a marked change in slope at higher currents and a rather odd kink. On analysis these marked slope changes were found to occur at the same anode voltage as the previous F.N. plots changed slope; while the kinks might in fact be artifacts of the process of F.W.H.M. determination, since there are also changes in the spectral shapes at these points. The same F.W.H.M. data is displayed in figures (85 & 86) and figures (93 to 95) but now using equation 16 from the hot electron analysis. Reasonable straight lines result for the "unoxidised" cases, there being no sign of the curvature, while for the oxidised cases all the points have at least moved towards the best fit straight lines and thereby increased the regression co-efficients, just as in the other hot electron plots. However, some rather curious loops have developed in these plots which, if they are not simply characteristics of the shape independent relationship between kT and the spectral F.W.H.M. used in deriving equation 10, could result from small changes in the stored surface charge of the conducting channel. This is expressed in this hot electron analysis as V^* which has been assumed to be constant for simplicity, but this may not be the case when the Fermi level at the vacuum surface suddenly changes, as might in fact occur when a contact to bulk-limit transition takes place within the insulator. It should be noted in the case of the degassed-oxidised specimen, that the shape of the emission spectrum was non typical and that the low energy tail was much more pronounced at all anode voltages. Thus as may be seen from an examination of figure (73) in chapter 6 in conjunction with figure (80b) this set of spectra is best described by the relation F.W.H.M. = $4{\cdot}5\ kT/_e$ rather than $3{\cdot}5\ kT/_e$ due to the higher proportion of low energy electrons in the energy distribution.

Figure (87) and figure (96) are particularly interesting since they show obvious contact-limited to bulk-limited transitions for the oxidised cases. The unoxidised cases simply show the gently curving plots with steep slopes characteristic of contact-limited behaviour, although even here, bulk-limited behaviour might have occurred if the currents had been increased sufficiently. The fact that the ten lowest current readings of specimen (1) - unoxidised did in fact give a contact-limited characteristic is illustrated by the linear plot of figure (88), assuming that $\phi_M - \phi_I = 1{\cdot}5$ eV.

The contact to bulk-limited plots of figure (96) indicate that a small change has taken place in the contact behaviour of specimen (2) durring heating and degassing. This may be due to changes in the insulator work function or electron affinity or possibly the donor

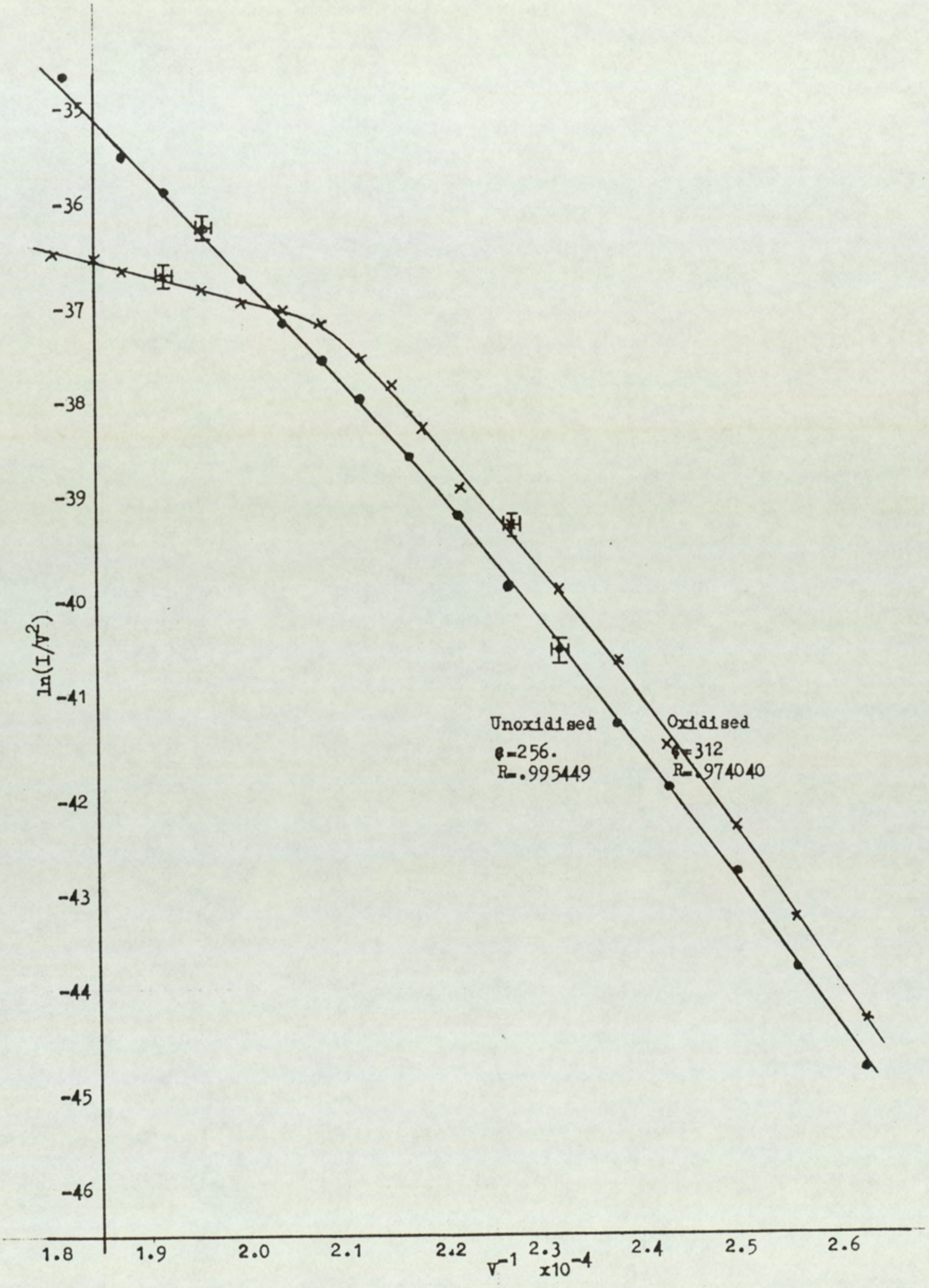

FOWLER-NORDHEIM PLOTS FOR SPECIMEN (1).

FIG 81.

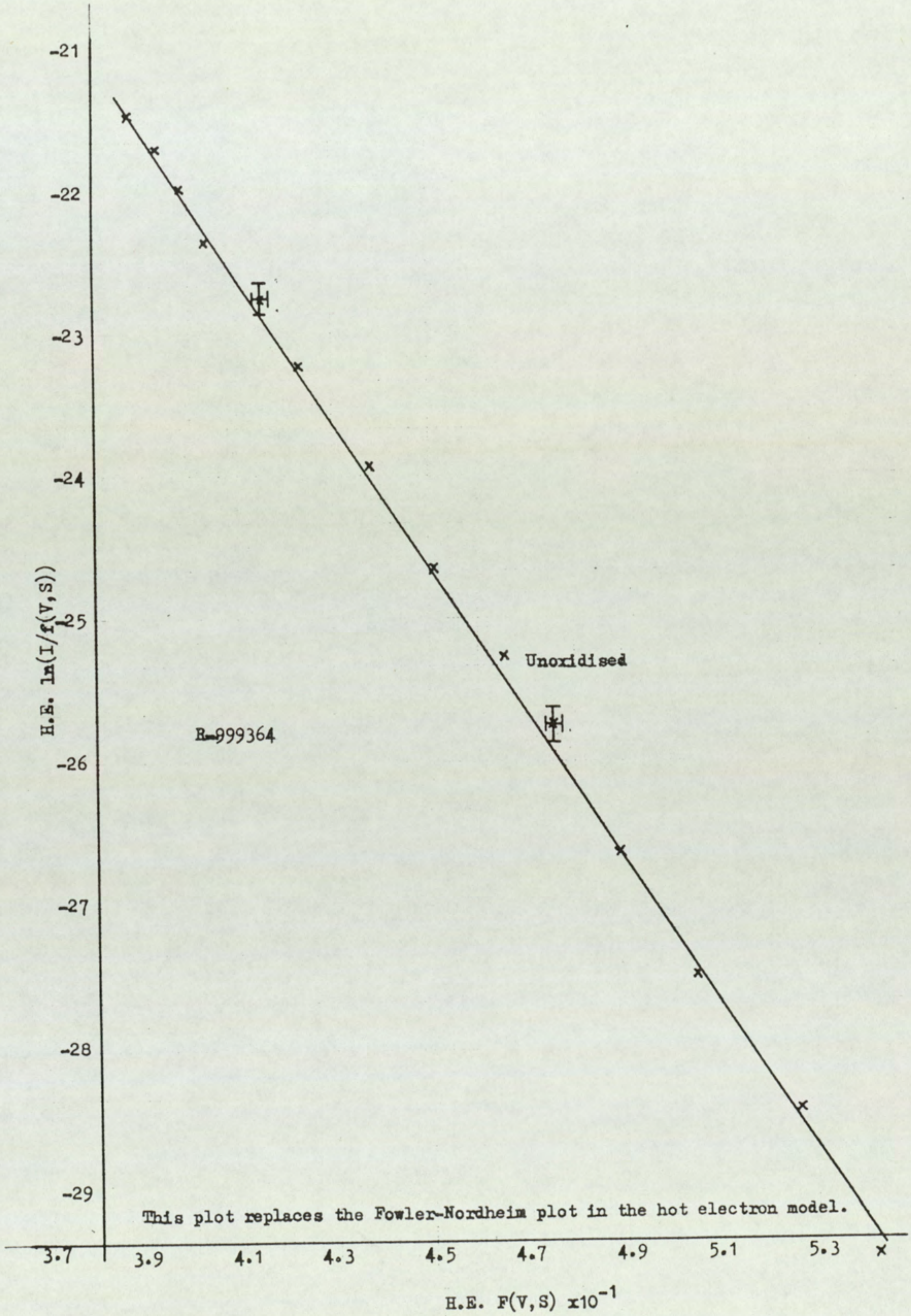

This plot replaces the Fowler-Nordheim plot in the hot electron model.

"HOT ELECTRON" PLOT FOR SPECIMEN (1) UNOXIDISED.

FIG 82.

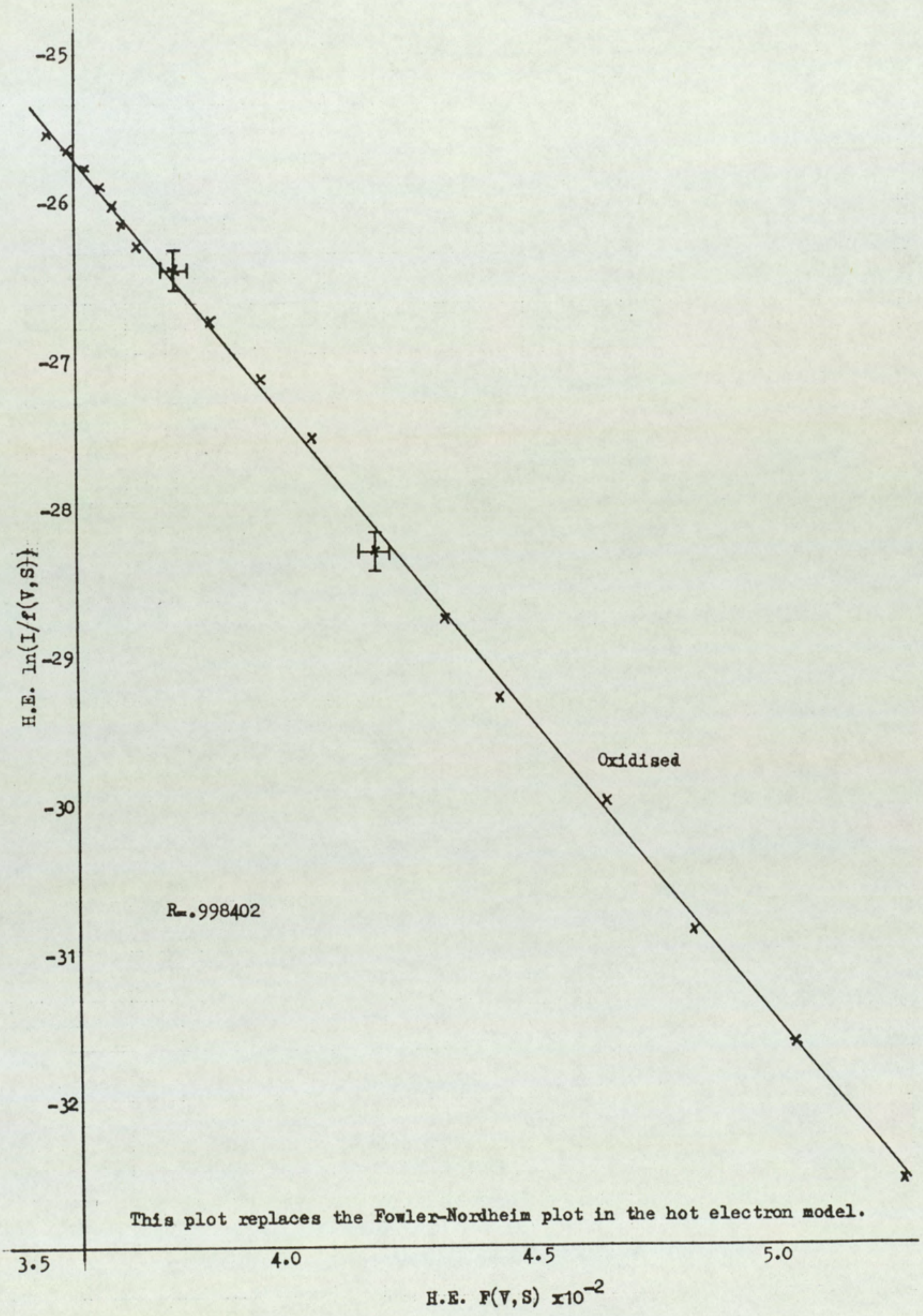

"HOT ELECTRON" PLOT FOR SPECIMEN (1) OXIDISED.

FIG 83.

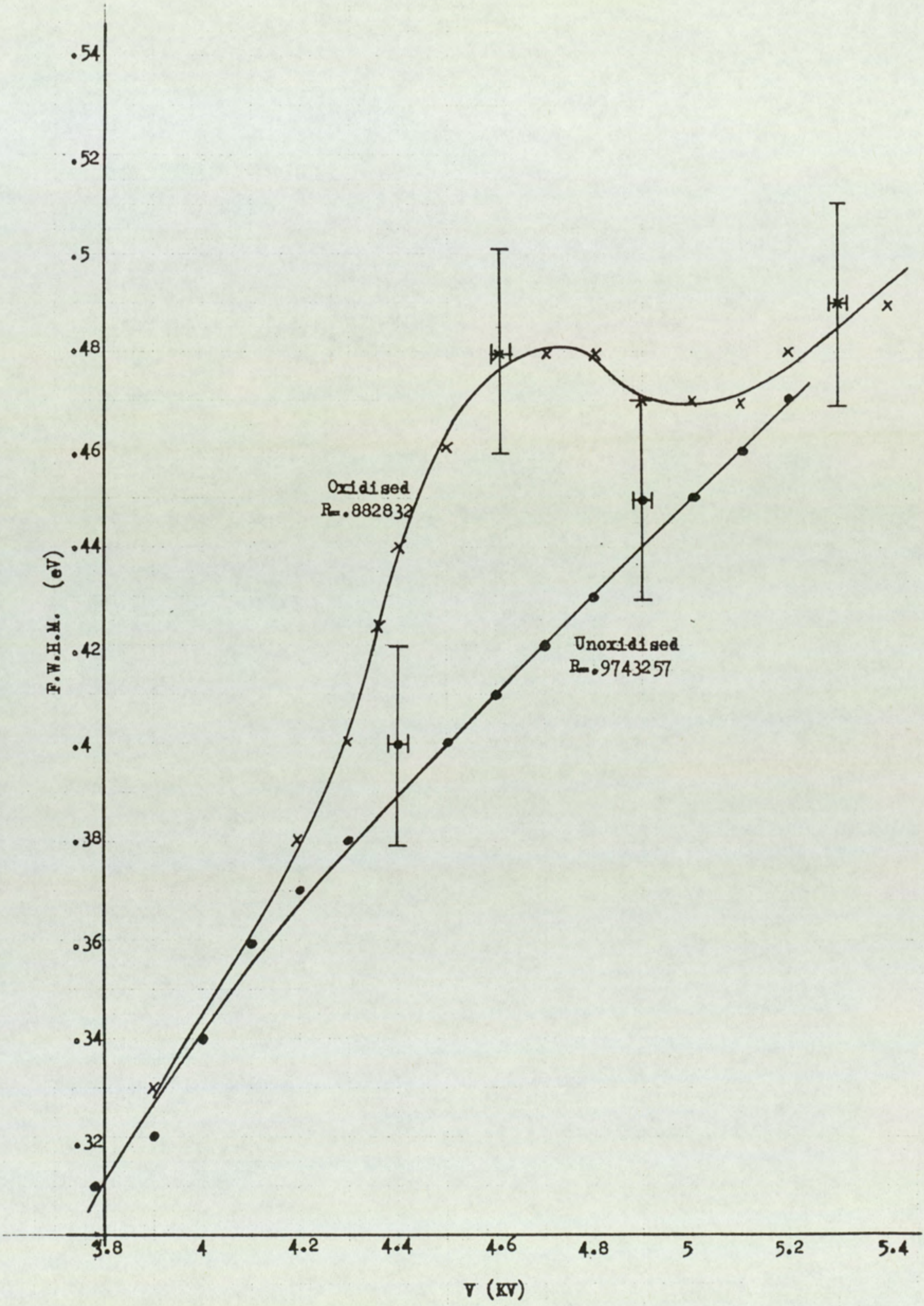

PLOT OF SPECTRAL F.W.H.M. AGAINST ANODE VOLTAGE : SPECIMEN (1)

FIG 84.

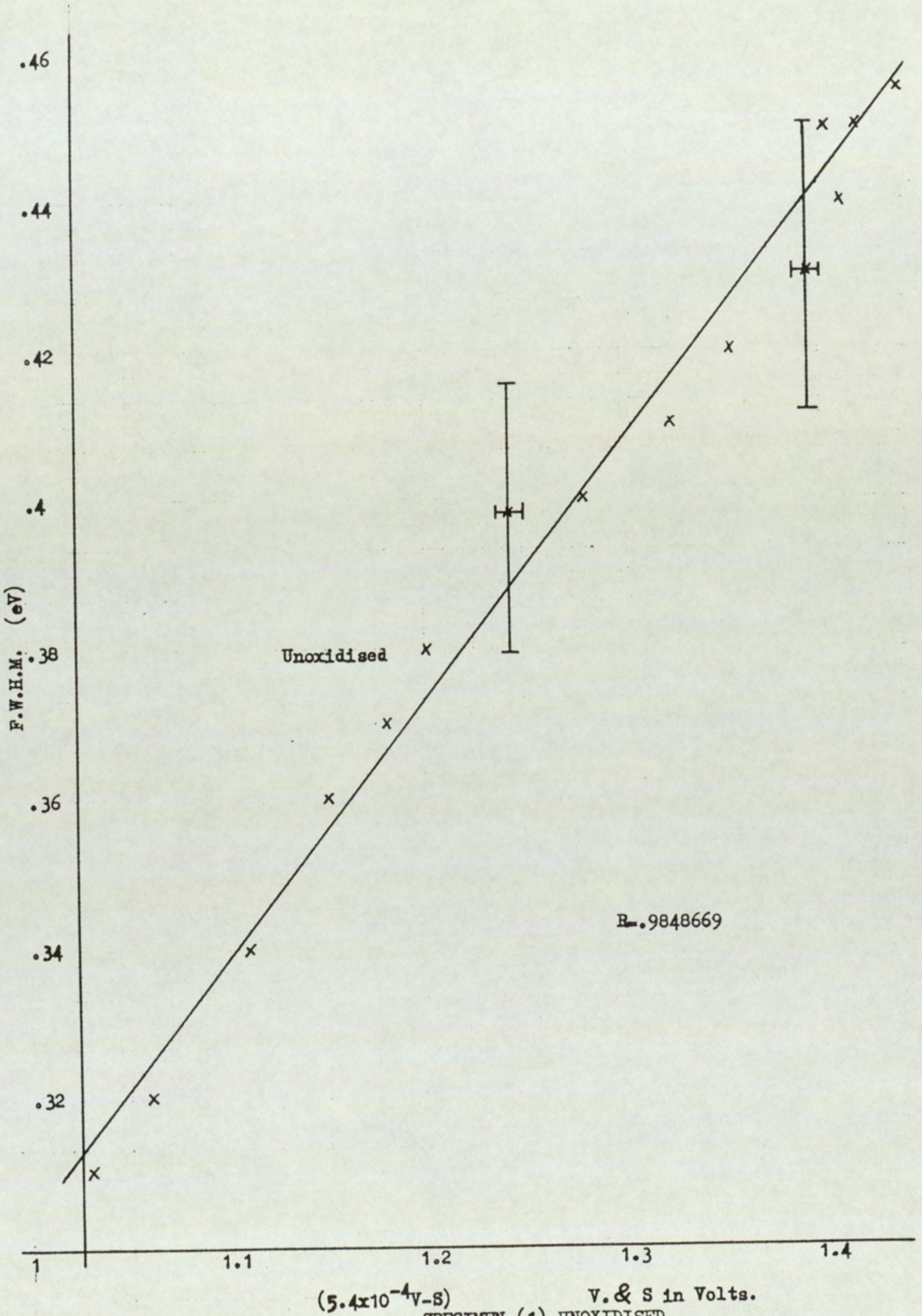

SPECIMEN (1) UNOXIDISED.

PLOT OF SPECTRAL F.W.H.M. AGAINST HOT ELECTRON ACCELERATING "POTENTIAL":

FIG 85.

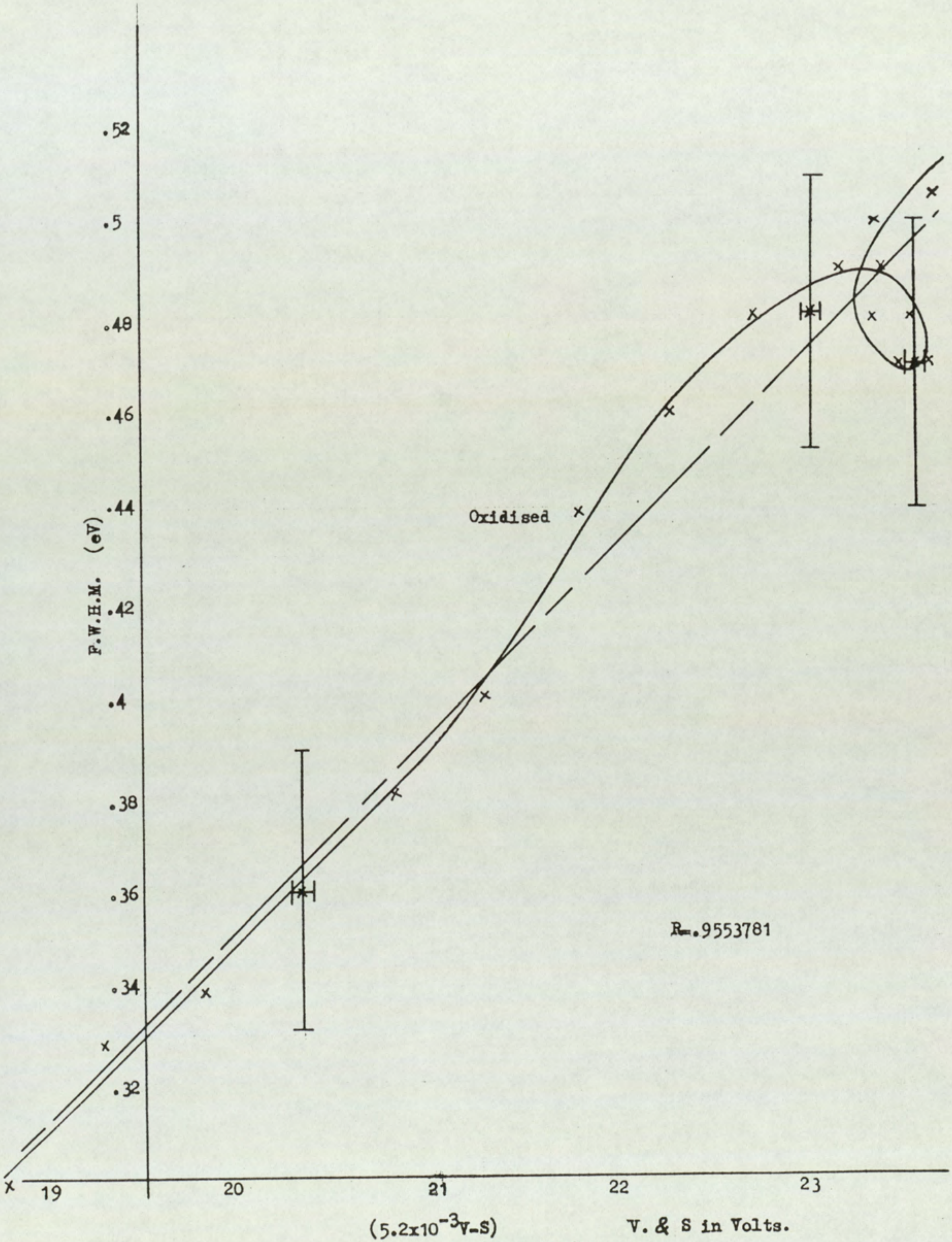

SPECIMEN (1) OXIDISED.
PLOT OF SPECTRAL F.W.H.M. AGAINST HOT ELECTRON ACCELERATING "POTENTIAL".

FIG 86.

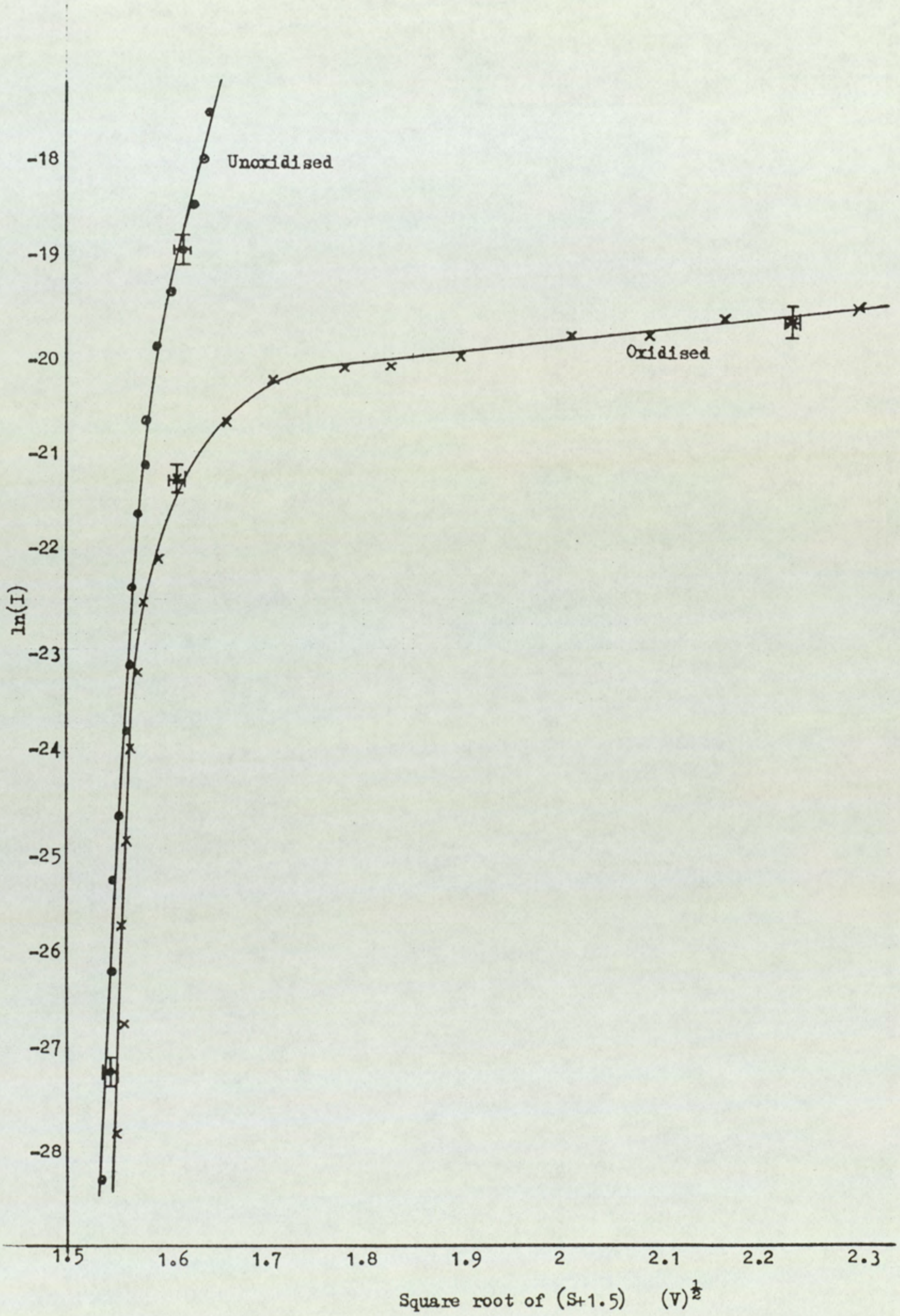

ELECTRODE LIMITED TO BULK LIMITED I-V CHARACTERISTIC FOR SPECIMEN (1).

FIG 87.

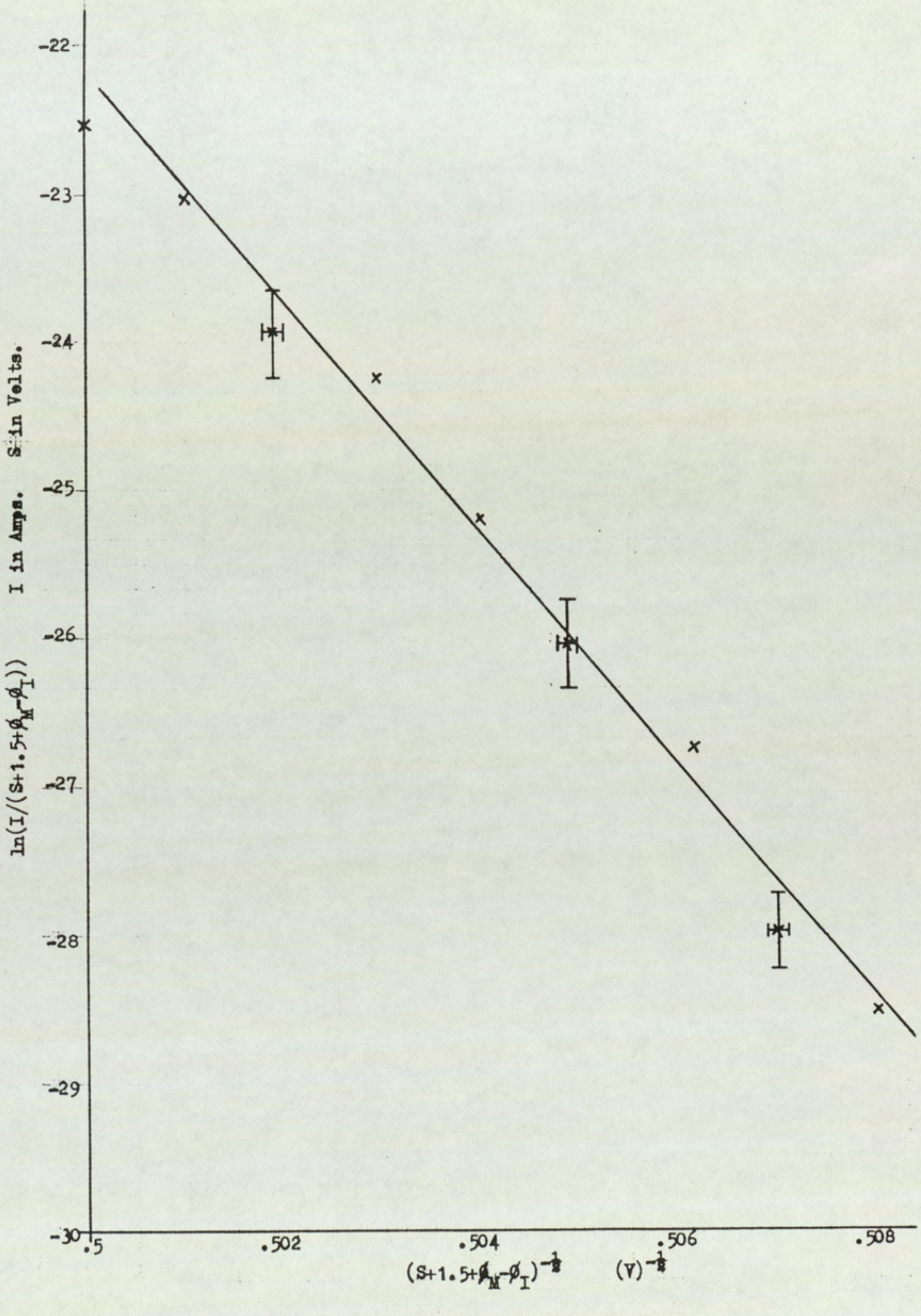

CONTACT LIMITED CHARACTERISTIC FOR SPECIMEN (1),UNOXIDISED.

FIG 88.

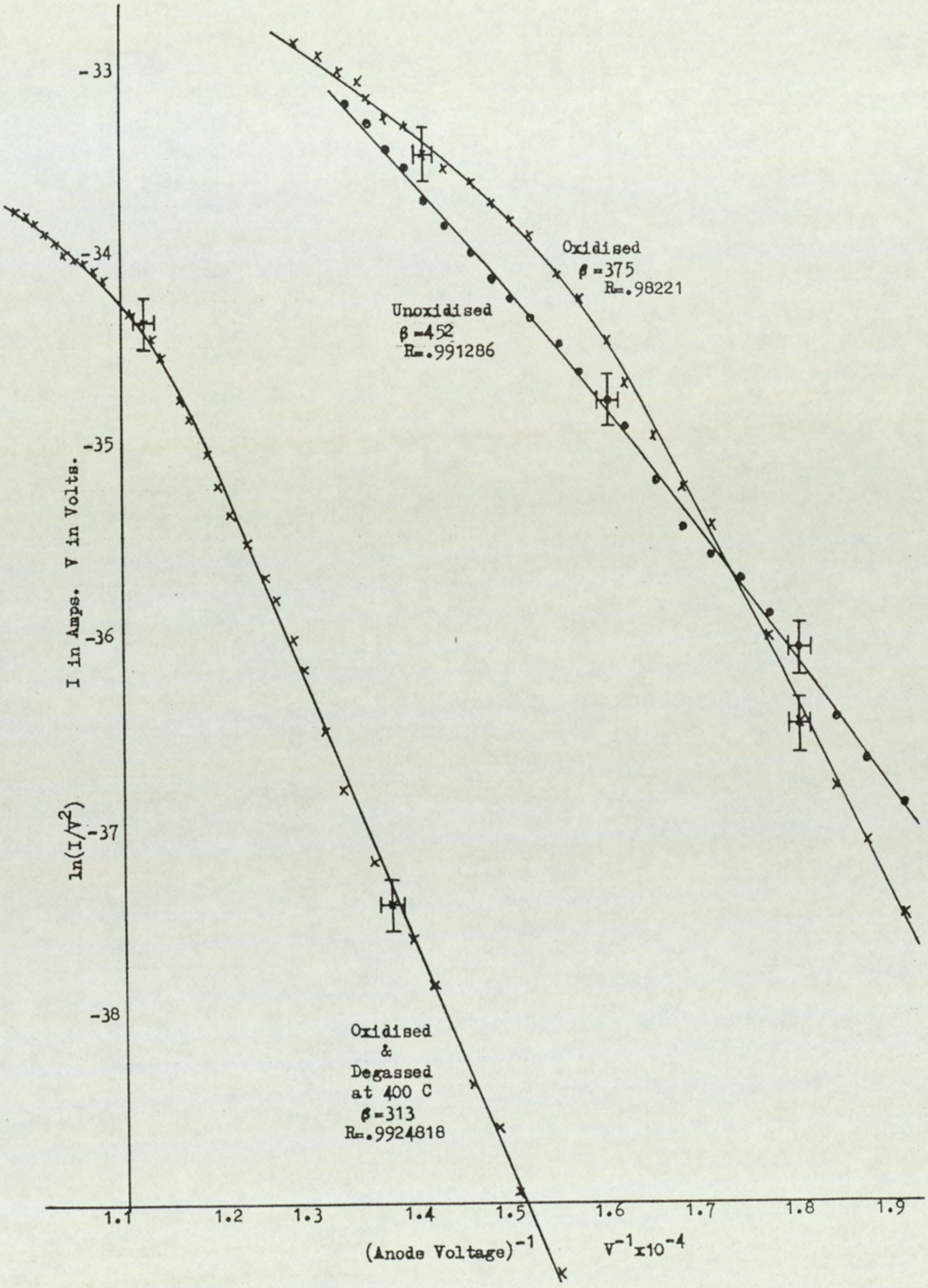

FOWLER-NORDHEIM PLOTS FOR SPECIMEN (2).

FIG 89.

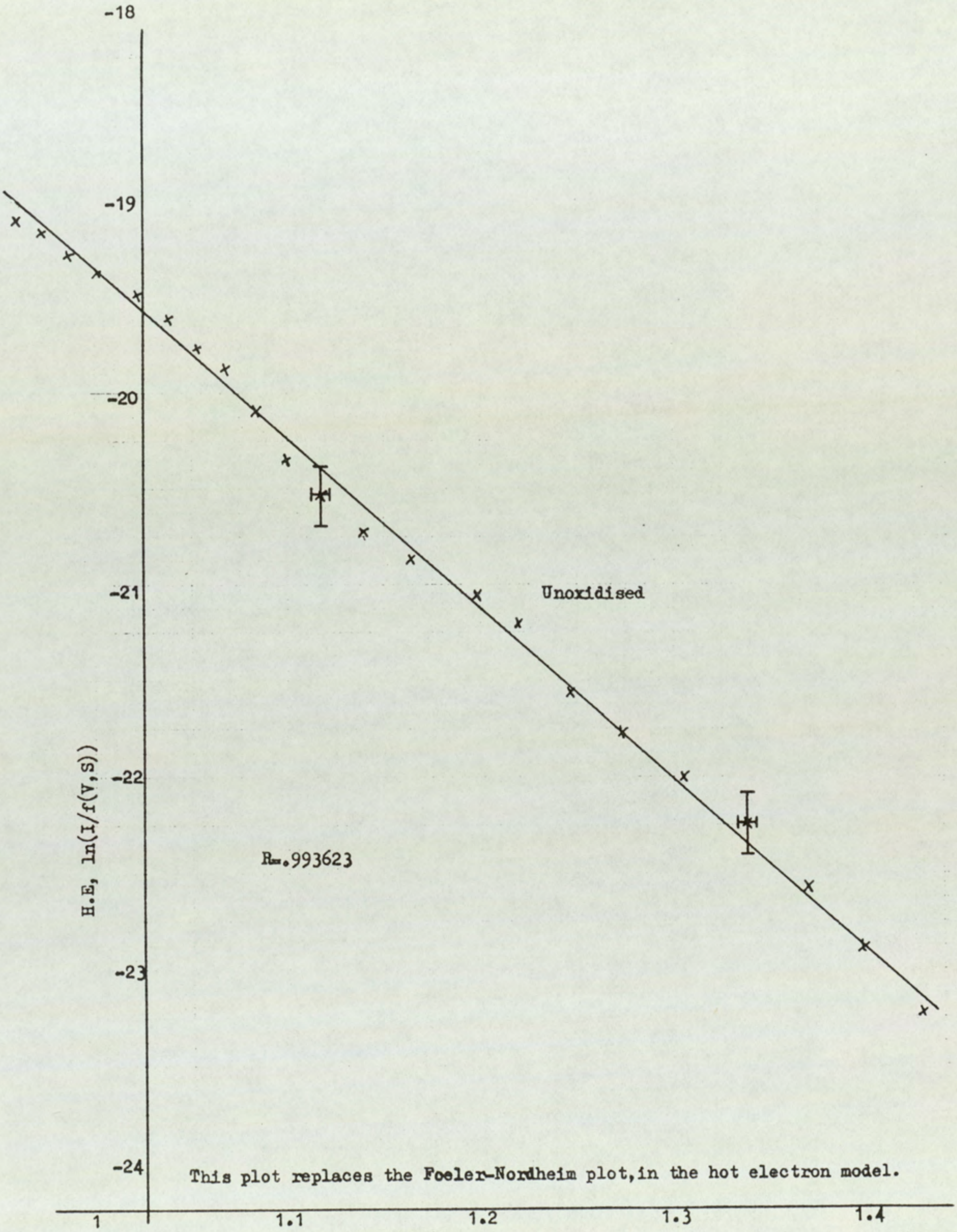

"HOT ELECTRON" PLOT FOR SPECIMEN (2), UNOXIDISED.

FIG 90.

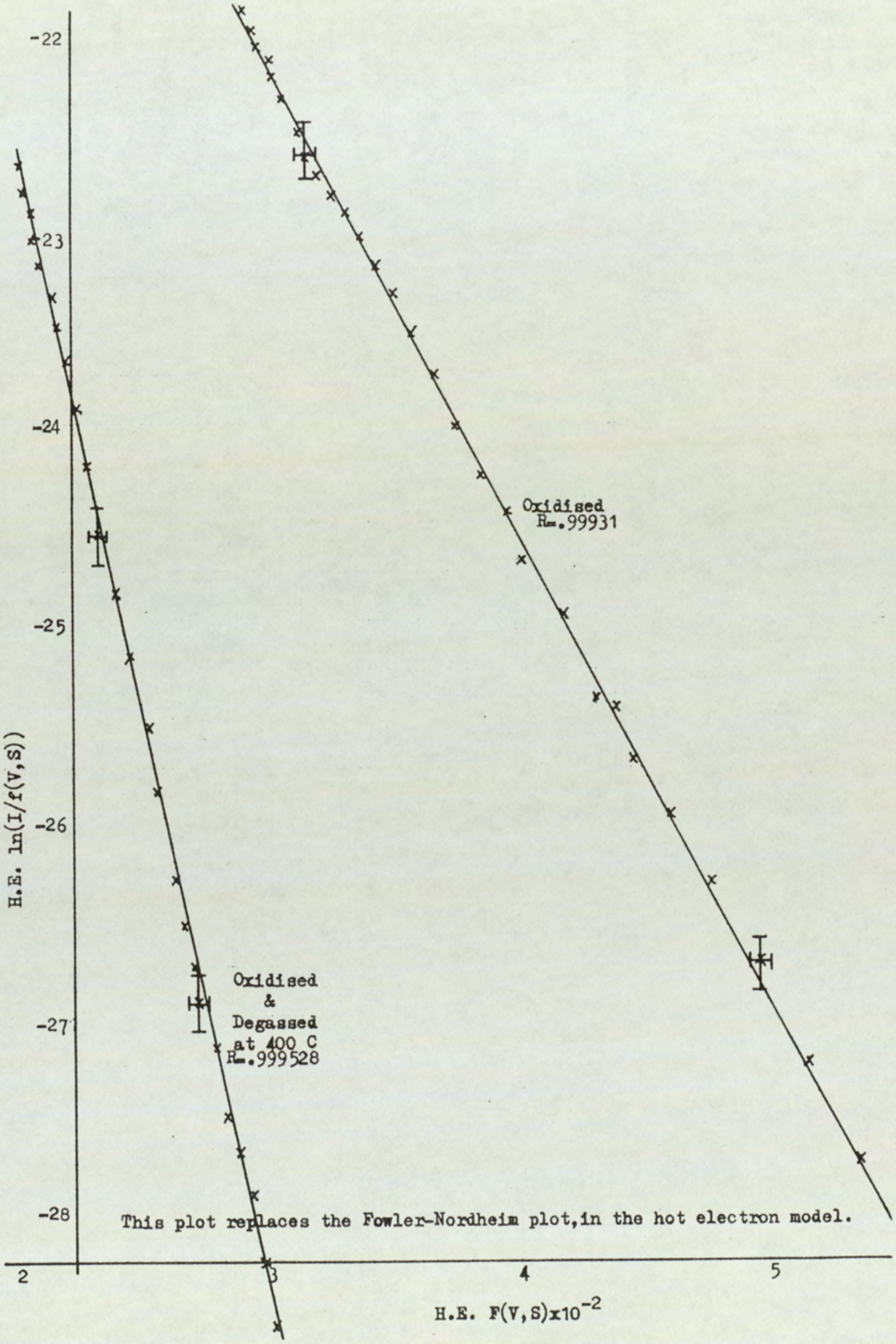

This plot replaces the Fowler-Nordheim plot,in the hot electron model.

"HOT ELECTRON" PLOT FOR SPECIMEN (2)

FIG 91.

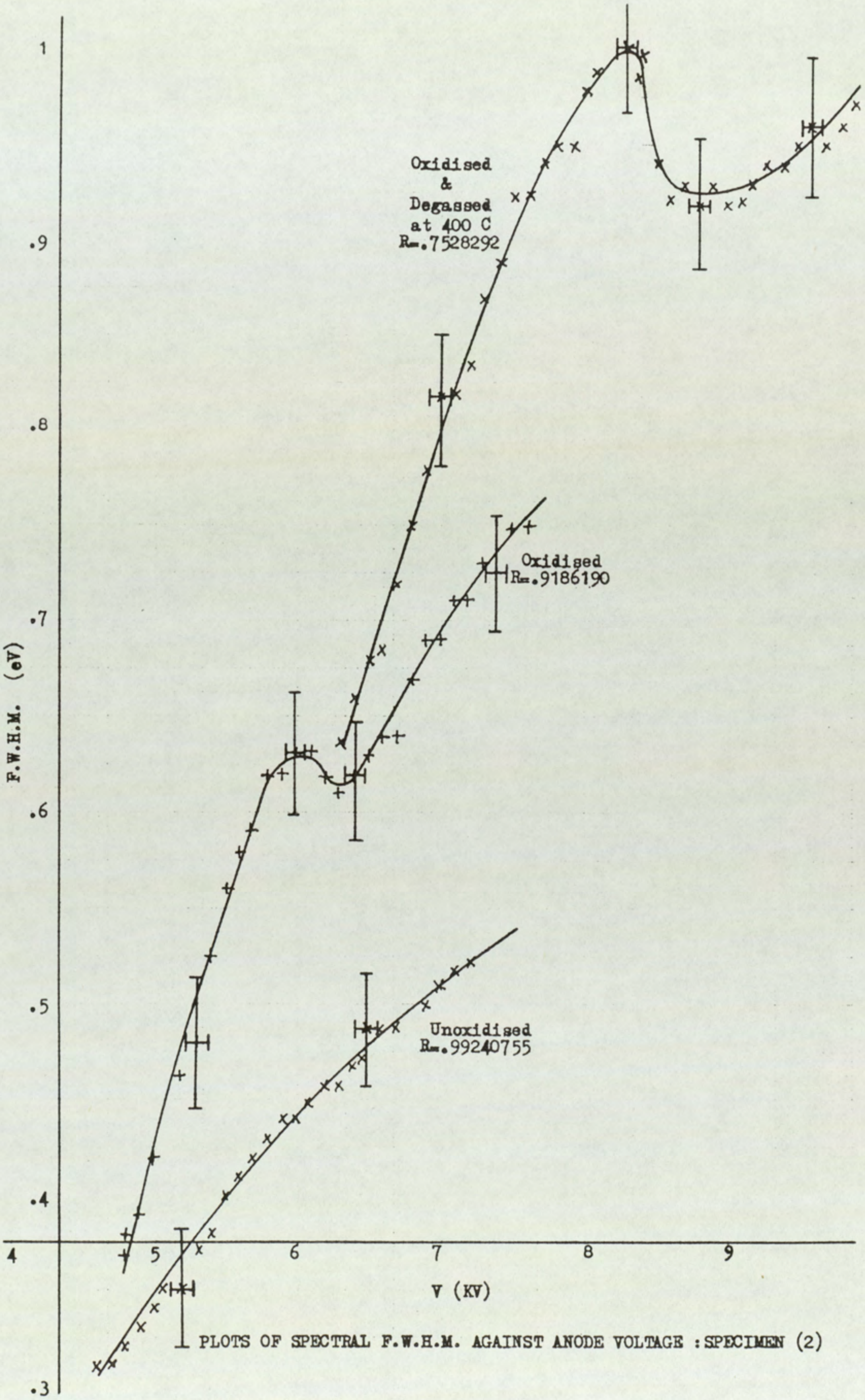

PLOTS OF SPECTRAL F.W.H.M. AGAINST ANODE VOLTAGE : SPECIMEN (2)

FIG 92.

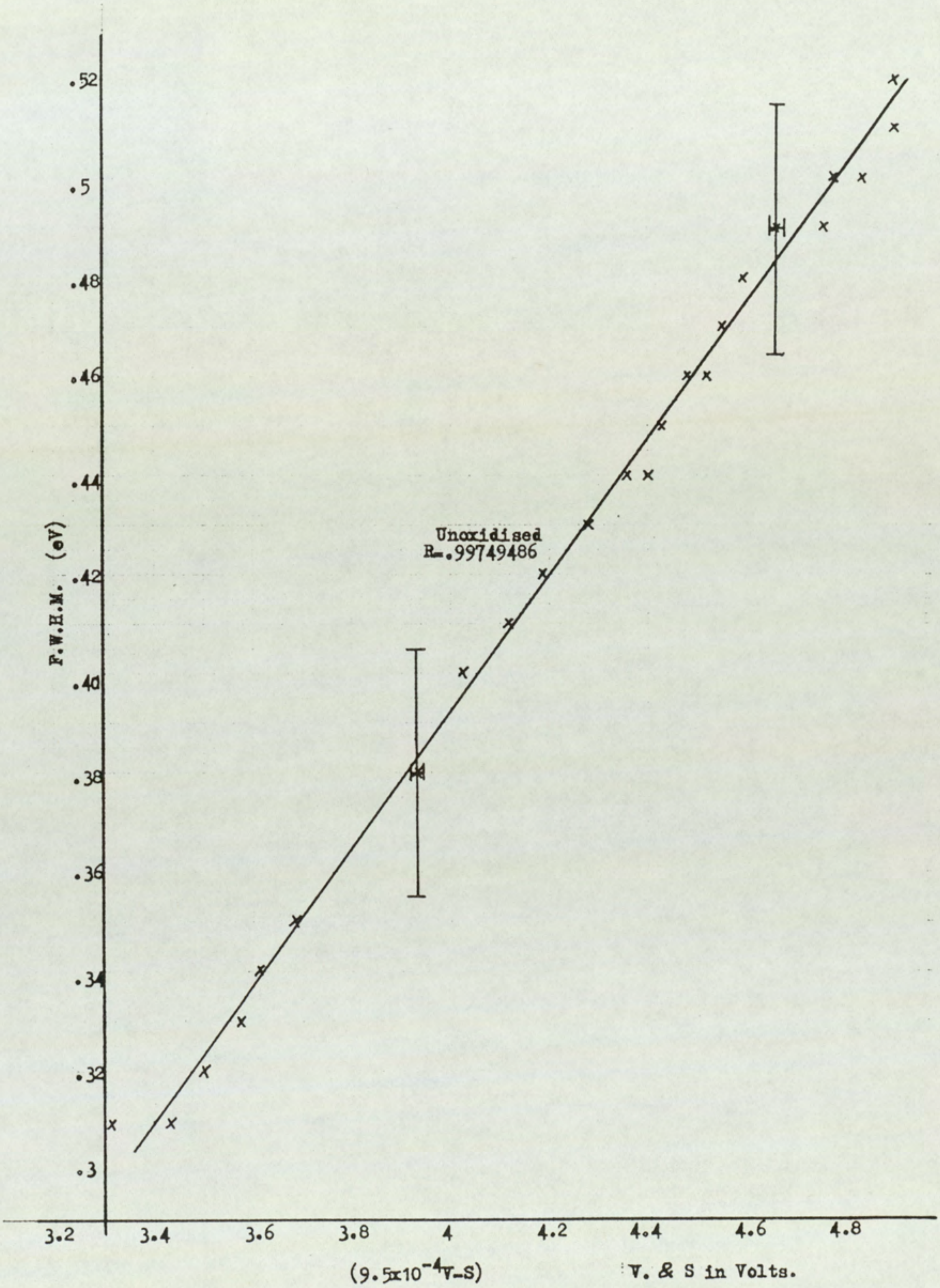

SPECIMEN (2) UNOXIDISED.
PLOT OF SPECTRAL F.W.H.M. AGAINST HOT ELECTRON ACCELERATING "POTENTIAL".

FIG 93.

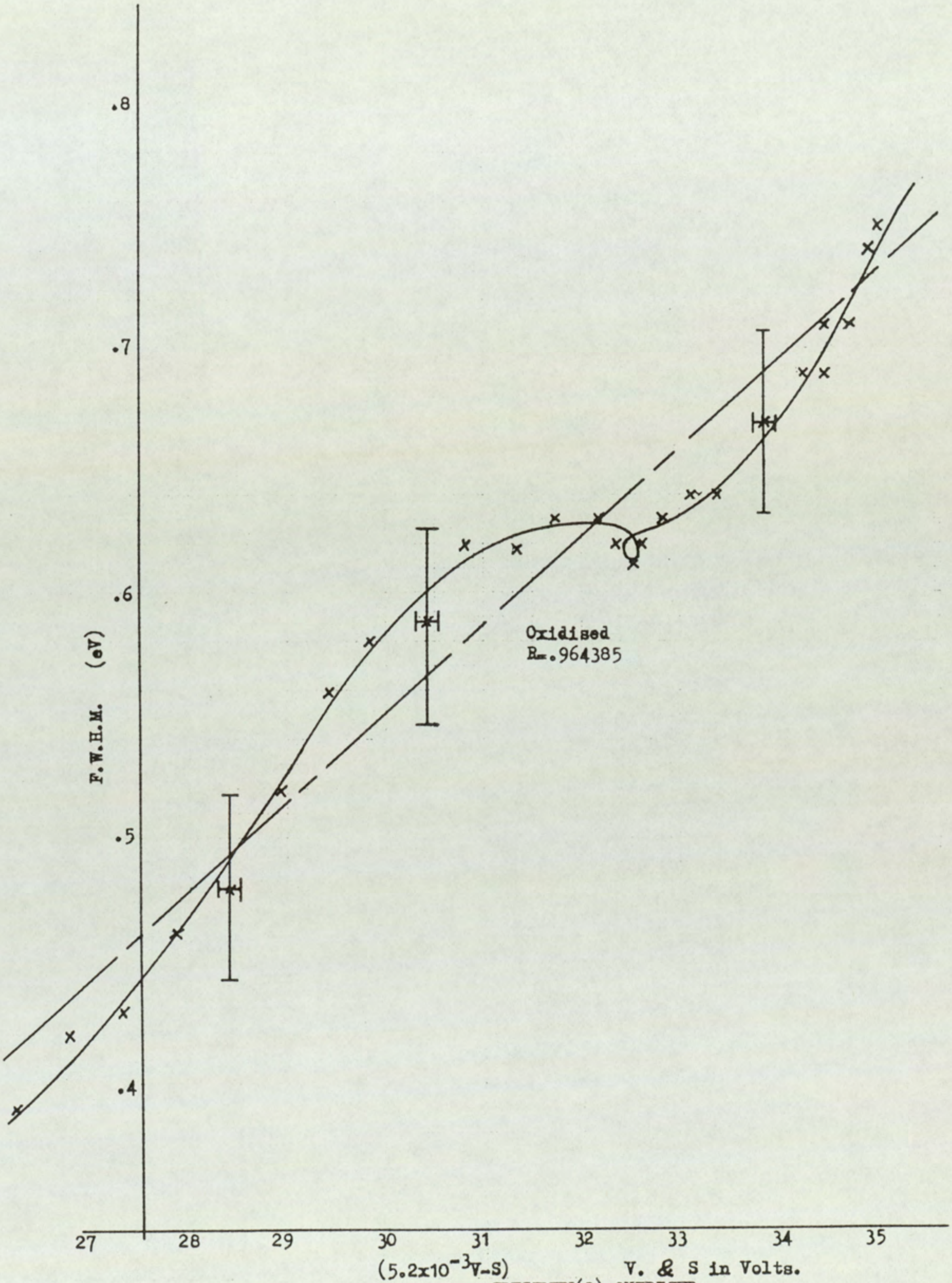

SPECIMEN(2) OXIDISED

PLOT OF SPECTRAL F.W.H.M. AGAINST HOT ELECTRON ACCELERATING "POTENTIAL".

FIG 94.

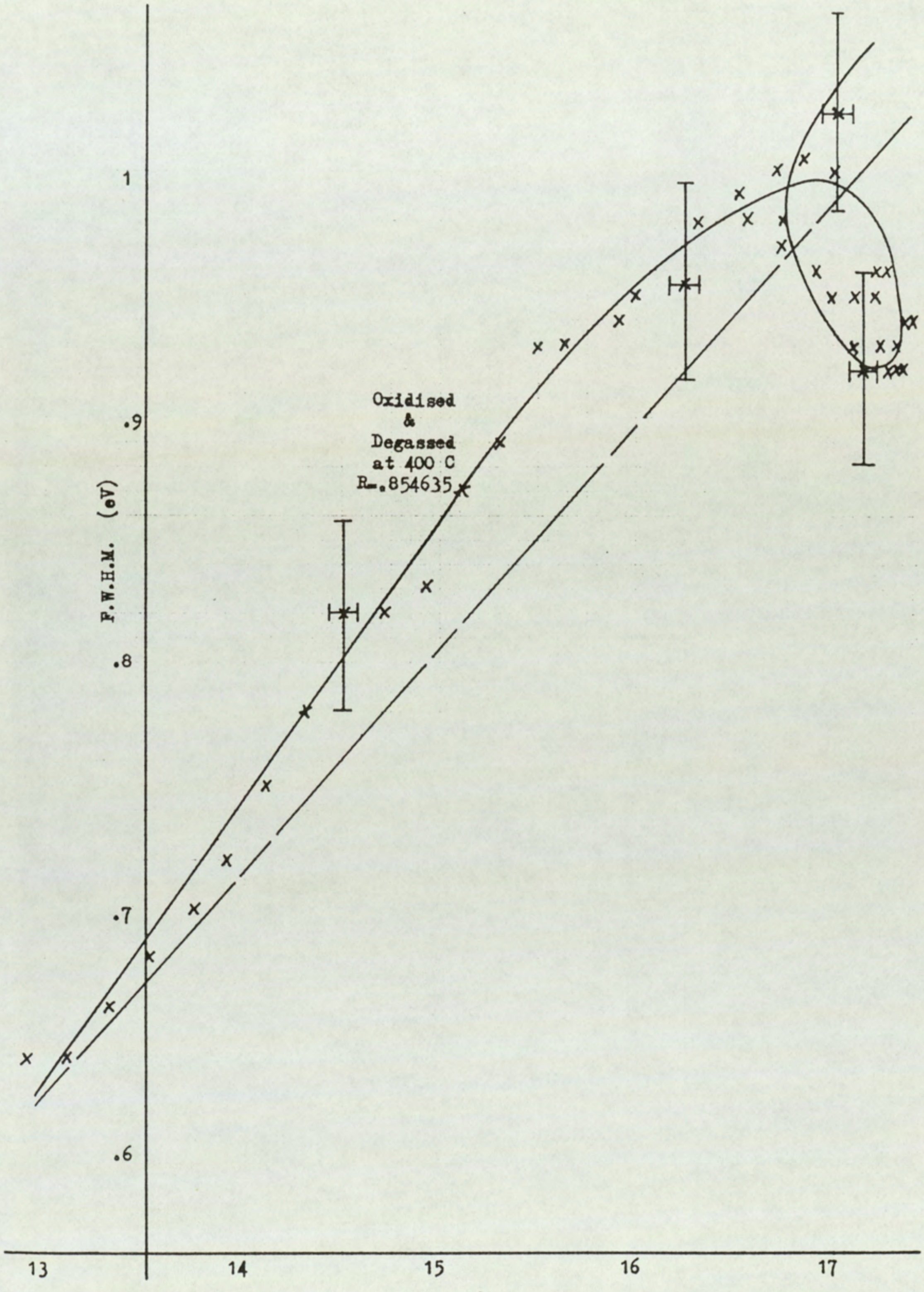

SPECIMEN (2) DEGASSED.
PLOT OF SPECTRAL F.W.H.M. AGAINST HOT ELECTRON ACCELERATING "POTENTIAL".

FIG 95.

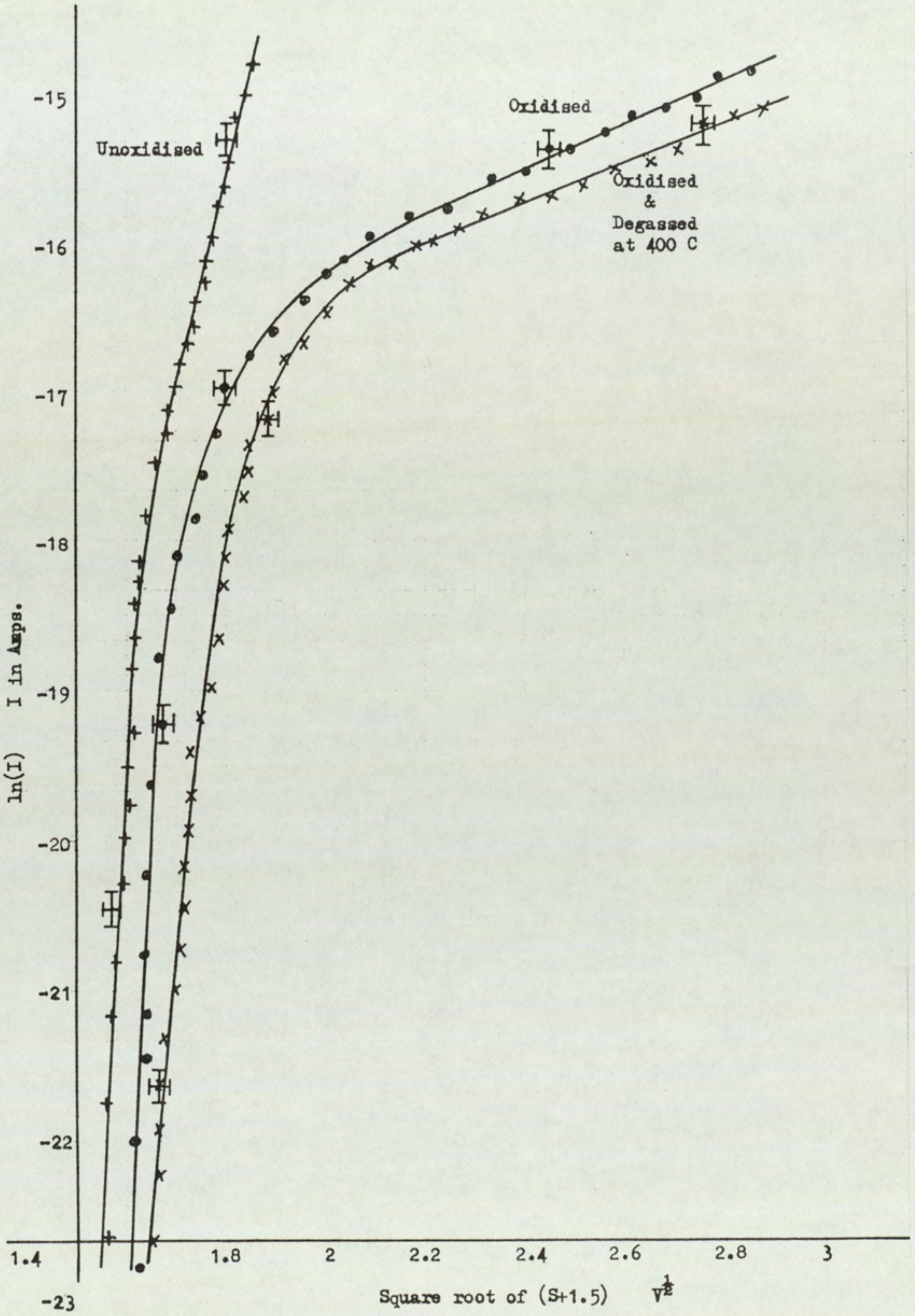

ELECTRODE LIMITED TO BULK LIMITED I-V CHARACTERISTIC FOR SPECIMEN (2).

FIG 96.

	Constants from the F.W.H.M. graph.			Constants from the Hot Electron plot.			Approximate values for the constants resulting from the Hot Electron model.				
Specimen	M_1	C_1	B_1	B_2	M_2	C_2	$V^*(V)$	m	$X^*(eV)$	a (m^2)	T_{max} (K)
1 unox	.345	-.042	$5.2x10^{-4}$	$7.4x10^{-4}$	-51.1	- 5.1	1.12	.099	5.06	$3.8x10^{-15}$	2700
1 ox	.038	-.404	$5.2x10^{-3}$	$7.6x10^{-3}$	-414	-10.8	11.7	.01	4.14	$1.2x10^{-15}$	2900
2 unox	.136	-.151	$9.5x10^{-4}$	$1.6x10^{-3}$	-76.4	-11.9	.26	.039	2.98	$2.8x10^{-17}$	3800
2 ox	.031	-.385	$5.6x10^{-3}$	$7.1x10^{-3}$	-237	-15.1	13.8	.0089	2.11	$2.2x10^{-17}$	3200
2 deg	.066	-.163	$2.3x10^{-3}$	$5.4x10^{-3}$	-573	-11.3	2.74	.015	8.59	$3.4x10^{-16}$	7800
3 unox	.067	-.612	$3.1x10^{-3}$	$3.3x10^{-3}$	-57.9	-13.9	8.9	.019	1.1	$1.6x10^{-17}$	2100
3 20 C	.069	-.941	$4.4x10^{-3}$	$6.1x10^{-3}$	-143	-14.7	13.4	.02	2.86	$6.4x10^{-18}$	5600
3 80 C	.079	-.562	$2.7x10^{-3}$	$2.6x10^{-3}$	-34.7	-14.3	6.74	.023	0.8	$7.2x10^{-18}$	1900

FIG 97. CONSTANTS CALCULATED USING THE HOT ELECTRON MODEL.
FOR SPECIMENS 1,2&3.

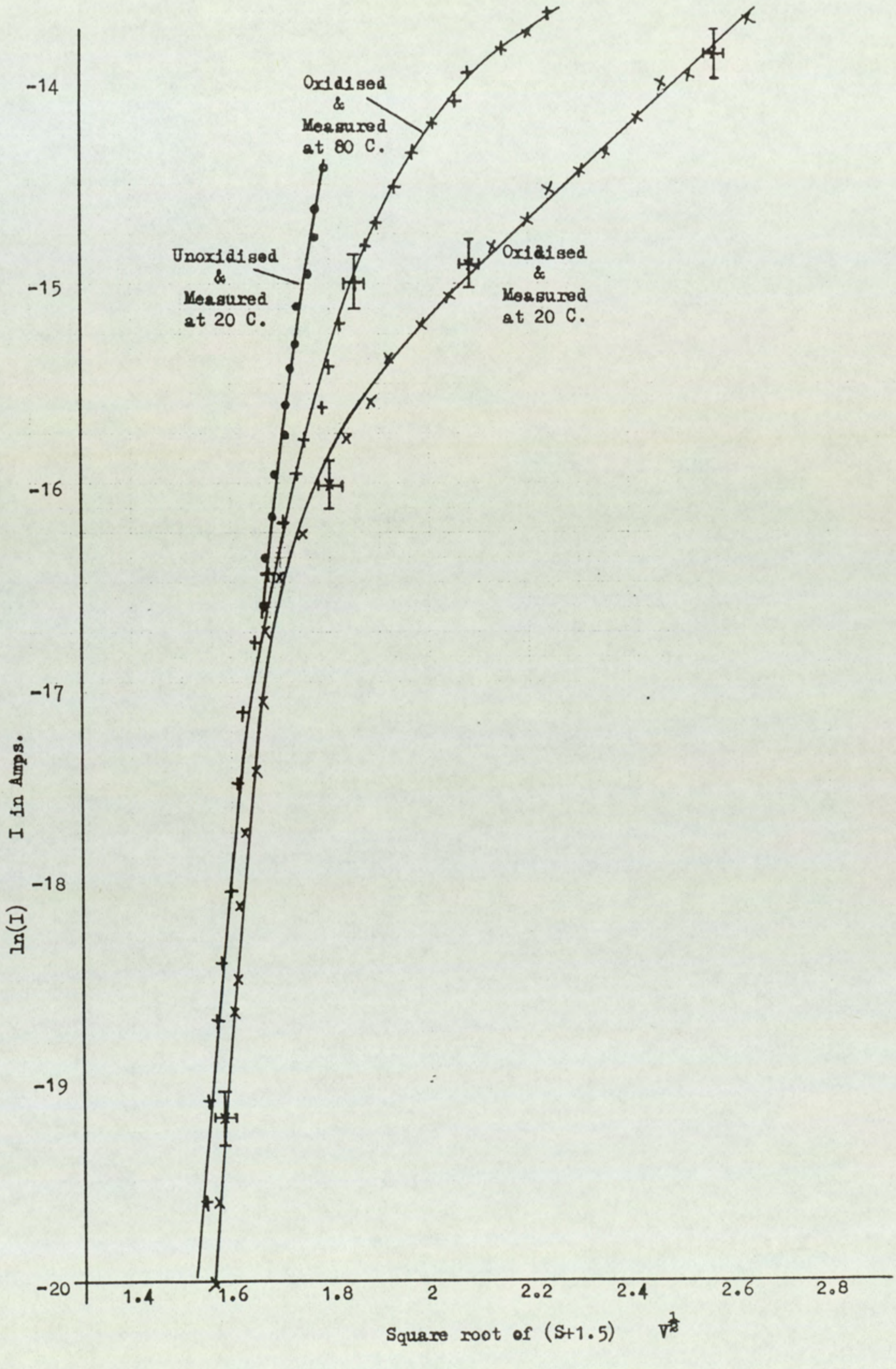

ELECTRODE LIMITED TO BULK LIMITED I-V CHARACTER ISTIC FOR SPECIMEN (3).

FIG 98.

density, although the respective points on the graphs are only just outside the combined errors in S and I. However, the large change in F.W.H.M. observed after degassing this specimen, which is shown in figure (92), indicates that the vacuum surface of the insulator has been markedly affected, as would be expected. The resulting increase in electron temperature given by equation 10 shows that the vacuum barrier height has been increased and this is also born out by subsequent calculations.

7.3. Evaluation of the Parameters Associated with the Hot Electron Model.

During the computer solution of equations 16 and 19 for the data just presented, it was found that the results were very insensitive to changes in the constant W. This was expected since W relates to the Schottky barrier height correction term which is only a small fraction of the actual barrier height and a slowly varying function of applied voltage. Accordingly, for subsequent calculations $W = \beta / (X^*)^2 = \cdot 8$ which seemed reasonable since β was expected to be ~ 5 and $X^* \sim 3$. For each of the three specimens the approximate values of the constants appearing in the hot electron model are tabulated in figure (97). From this, it will firstly be seen that the separately optimised B values relating to the hot electron & F.W.H.M. plots of equations 19 and 16 agree to within a factor of two. It will also be observed that the B values for the nominally unoxidised cases are considerably less than for the oxidised cases as expected, since this is the parameter directly related to the thickness of the insulating layer, i.e. $B = \dfrac{\beta\, d}{\varepsilon\, D}$.

All the other hot electron parameters have values of the order of those expected although no great accuracy is claimed largely due to experimental uncertainties in F.W.H.M and sub-site current determination. Thus the values of X^* would be expected to fall around the value for the insulator electron affinity X which would be estimated at about 2 to 3V. The 8.59 value for X^* does seem excessive but this is associated with the degassed specimen which also had a non typical spectral shape which may have complicated matters.

Values of V^* are in the volts to tens of volts range, which is consistent with the expected effect of stored surface charge. This data also gives the first estimates for M which is the proportion of the surface field accelerating potential energy retained by the hot electrons. Since there is no other data for comparison all that may be said in this case is that the values are not unreasonable.

Assuming values for the insulator thicknesses between $\sim 10^{-7}$ and $\sim 10^{-6}$m and values for the diameters of the conducting channels between $\sim 10^{-8}$ and $\sim 10^{-7}$m (which will later be shown to be reasonable) the emitting area would be expected to be $\sim 10^{-14}$ m^2. Hence several of the quoted emitting areas are very low, but in this context it will be noted from the logarithmic nature of equation 24 that the emitting area is the only parameter to depend directly upon the absolute value of emission current, while from chapter 6 it will be recalled that this had a high uncertainty. In addition it was noted when discussing the Richardson - Duschman relation of equation 11, that an error of about 30% was at present largely unavoidable when computing emission areas, at least in this simplified analysis.

An important result to come from this hot electron model is that the changes in slopes seen to occur in conventional F.N. plots and in plots of F.W.H.M. versus applied voltage, are manifestations of contact to bulk-limited transitions taking place within the insulating inclusions. Thus for bulk-limited conduction with charged traps, the slope of ln I versus S^* plot is given from equations 19 and 20 of chapter 4 as

$$\text{slope} = \frac{1}{kT_o}\left(\frac{e^3}{\pi\varepsilon_o\varepsilon d}\right)^{\frac{1}{2}} \qquad (28)$$

hence with $T_o = 300K$

$$(\varepsilon d)^{\frac{1}{2}} = \left(\frac{e^3}{\pi\varepsilon_o}\right)^{\frac{1}{2}} \frac{1}{kT_o \text{ slope}} = \frac{2{\cdot}9 \times 10^{-3}}{\text{slope}} \qquad (29)$$

Therefore from the "oxidised" plots of figures 87, 96, and 98, referring to specimens (1), (2) and (3) respectively, the values for ε d are: $\varepsilon d\ (1) = 7{\cdot}6 \times 10^{-6}m$, $\varepsilon d\ (2) = 4 \times 10^{-6}m$, $\varepsilon d\ (3) = 1{\cdot}9 \times 10^{-6}m$. If neutral traps are assumed these values must each be halved.

7.4. Geometrical Details of the Conducting Filament.

Some approximate calculations may now be carried out to relate the dimensions of the conducting filament to the various constants so far evaluated. Firstly an average value of B may be calculated from the values given in the table of figure (97) for the three specimens; viz.

$$\bar{B}\ (1) = 6{\cdot}4 \times 10^{-3}, \qquad \bar{B}\ (2) = 6{\cdot}35 \times 10^{-3}, \qquad \bar{B}\ (3) = 5{\cdot}25 \times 10^{-3}$$

secondly, intensification of the field within and around a conducting filament due to the altered potential distribution along its length and the increased electron density at the channel end, will result in an electric field pattern similar to that shown in figure (99a). Where the field intensification factor β used in the hot electron analysis relates the average electric field in the conducting filament to that inside the remaining insulator well away from the conducting region. In this respect it is somewhat

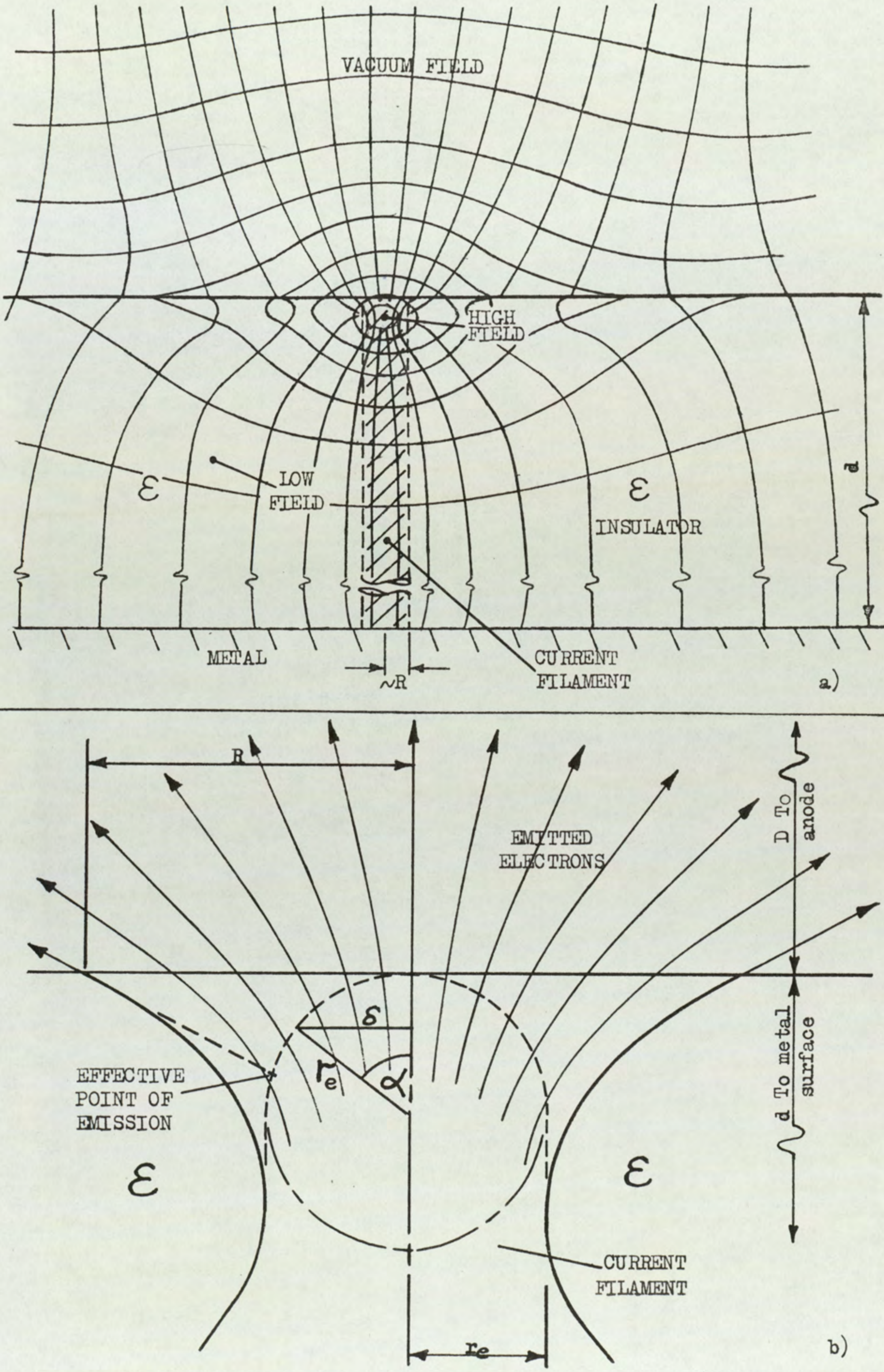

FIG.99. SCHEMATIC REPRESENTATIONS OF A POSSIBLE FIELD PATTERN AND AN ELECTRON EMITTING REGIME AT THE END OF A CONDUCTING CHANNEL.

different to the usual β factor encountered in metallic F.N. emission in that the latter refers to the average field just above the tip of a protruding metallic whisker. However, figure (99a) indicates that most of the field intensification actually occurs towards the vacuum interface of a conducting filament, and this is also born out by the energy band diagram of figure (79) since there is a much lower change in potential throughout the bulk of the filament than at its vacuum end. Hence the approximate relations for β, as derived for emitting metallic protrusions etc., may be applied to conducting filaments in order to obtain very approximate relations between the β factors and filament dimentions. For metallic emitters it has been shown (139,140) that the relation $\beta = \frac{h}{r} + 2$ is a good representation of the situation for most emitting geometries, where **h** is the height and r the radius of the protrusion creating the field enhancement. The field geometry which most closely resembles that of an emitting filament is produced by a metal sphere of radius r at a distance h from a flat metal plane (139, 140), the filament only having a metal-like electron density in the very high field region at its tip. Therefore, the sphere radius may be taken to be the radius r_e of the conducting filament in the high field region, and the distance h to be the thickness of the insulating inclusion d. However the β factor thus defined would apply to an insulator having a dielectric constant $\varepsilon \sim 1$ and where the ratio of the two fields expressed by β would refer to the local field in the filament tip to the gap field well away from the filament. Since an actual insulating inclusion will have $\varepsilon > 1$ the resulting β factor associated with the filament will be reduced by $\sim 1/\varepsilon$, hence

$$\beta \sim \frac{1}{\mathcal{E}}\left(\frac{d}{r_e} + 2\right) \qquad (30)$$

Referring now to figure (99b), which shows an enlarged region around the tip of a conducting filament, it will be seen that the channel current must diverge in order to satisfy Laplace's equation at the tip if the field also diverges there. This makes the radius R of the emitting area greater than r_e the radius of the conducting filament in the high field region, and a detailed investigation would have to be carried out to find the exact relationship. However, this has been estimated rather crudely from both diagrams in figure (99) to be $1{\cdot}5r_e < R < 2{\cdot}5r_e$ if the filament geometry is assumed to be correct. In addition the channel current must converge when entering the high field surface region, so that the radius of the filament in the low field region of the insulator bulk will probably be about equal to the radius of the emitting area R. Also from figure (99b) it will be noted that the "spherical" high field core at the end of a conducting filament may be represented as the effective electron emitter, where the extreme points of emission then correspond to points well down the side of the upper hemisphere. It is then possible to use this construction to obtain the radius Ra of the emitted electron beam when it strikes the anode. This is given by Chatterton (141) for metallic whisker emitters as

$$Ra \sim 2\left(D\beta\delta \operatorname{Sin}\alpha\right)^{\frac{1}{2}} + \delta(\beta)^{\frac{1}{2}} \qquad (31)$$

where δ is the radius of the effective emitting area, α is the emission cone internal half angle and D is the distance between the whisker tip and the anode. In this case it will be noted from figure (99b) that, for the filament tip high field region, $\alpha \sim 90^{\circ}$ when measured to the extreme points of emission and therefore $\delta \sim r_e$, thus

$$Ra \sim 2(D\beta r_e)^{\frac{1}{2}} + r_e(\beta)^{\frac{1}{2}} \qquad \text{or} \qquad \frac{Ra}{(\beta r_e)^{\frac{1}{2}}} \sim 2(D)^{\frac{1}{2}} + (r_e)^{\frac{1}{2}}$$

from which it will be seen that $Ra \sim 2(\beta D r_e)^{\frac{1}{2}}$ since $D \gg r_e$. In addition we have $r_e \sim R/2$ and the actual area of emission $a = \pi R^2$. All these equations may now be summarized as follows

$$\frac{\beta d}{\varepsilon D} = B \qquad (32) \qquad\qquad \beta \sim \frac{2}{\varepsilon}\left(\frac{d}{R} + 1\right) \qquad (33)$$

$$a = \pi R^2 \qquad (35) \qquad\qquad R_a \sim (2 D \beta R)^{\frac{1}{2}} \qquad (34)$$

where D is the specimen-anode gap; also from preceeding alalysis we have εd and B known approximately and estimates for the emitting areas. An upper value may be asigned to R_a by noting for the oxidised specimens that the electron image spot radii on the analysis phosphor screen were between 1•5 and 3 mm. Hence using an interfacing lens magnification of 60 and assuming negligible aberation a value of $Ra \sim 3 \times 10^{-5}$m results. While this system of equations and data is still not deterministic in the sense that all the unknown are at once fixed, it is self-consistent as will now be shown for specimen (1) oxidised. We have

$D = 5 \times 10^{-4}$m $\qquad$ $Ra \sim 3 \times 10^{-5}$m

$\varepsilon d = 7{\cdot}6 \times 10^{-6}$m $\qquad$ $B = 6{\cdot}4 \times 10^{-3}$

and assuming $\varepsilon = 4$, d is then $1{\cdot}9 \times 10^{-6}$ m

From equation 32 we have $\beta = 6.7$ which then gives from equation 33 $R \sim 1.5\times10^{-7}$m, while equation 34 implies $R \sim 1.63\times10^{-7}$m, finally equation 35 gives $a = 8.3\times10^{-14}\,m^2$. This value of a, obtained using the mean upper value of R_a, is about 70 times the estimated value given in the table of figure (97) which was obtained from the hot electron plots directly. This degree of missmatch between the two estimates of (a) is to be expected because a visual determination of R_a is implied in both methods : directly in the case of equations 34 & 35, and indirectly in the case of equation 22 through the estimation of sub-site current from the area of the image spot on the analyser phosphor screen. Other values may be tried for $\mathcal{E}$ but it will be found that at least one of the unknowns then becomes unrealistic. Values for the other oxidised specimens are

Specimen (2) $\mathcal{E}d = 4\times10^{-6}$, $B = 6.35\times10^{-3}$.

If $\mathcal{E} = 3$, $d = 1.3\times10^{-6}$m, $\beta = 7.3$ $R \sim 1.5\times10^{-7}$m, $a \sim 7.3\times10^{-14}\,m^2$

Specimen (3) $\mathcal{E}d = 1.9\times10^{-6}$, $B = 5.25\times10^{-3}$

If $\mathcal{E} = 3.5$ $d = 5.4\times10^{-7}$m, $\beta = 17$, $R \sim 5.3\times10^{-8}$m, $a \sim 8.8\times10^{-15}\,m^2$

In the case of the "unoxidised" specimens the values for $\mathcal{E}d$ are as yet unknown but values of B range from 0.1 to 0.5 of the "oxidised" values. In addition the electron image spot sizes were smaller and tended to fluctuate more, thus making measurements of their radii rather difficult, but values <1 mm were estimated. These facts taken together indicate that the "unoxidised" insulator thickness is probably of the order of 10^{-7}m. This is of course much greater than the ambient thickness of oxide coverage on copper, which is about 20 to 50 Å, thereby supporting the view that surface insulating inclusions are causing the emission.

Additional calculations could also have been made relating to the bulk and contact parameters of the insulator; however, this would have involved further assumptions regarding the insulator donor and trapping levels and also their respective densities which would not have been justified from present experimental data.

7.5. The Effects of Temperature.

Of the "constants" used in the preceeding equations, those most likely to be significantly affected by changes in the ambient temperature (T_o) are M, V^*, and X^*. Thus M, which represents that fraction of the potential energy in the surface accelerating field producing hot electrons at a temperature T, might be expected to fall slightly as the scattering cross section for electrons rises with ambient temperature; although the over-all effect may be overshadowed by the extra energy input from the hotter lattice. Next V^* accounts for those electrons trapped in surface states and at the bottom of the conduction band which modify the insulator surface potential. Depending on the depth of these energy states below the surface barrier peak, this parameter may be expected to remain reasonably constant for moderate temperature rises if the Fermi level at the surface does not move. For larger temperature rises however, V^* might at first be expected to fall as trapped electrons get thermally excited over the surface barrier. But if the insulator internal field conditions change as the temperature rises, produced for example by a decrease in S, then V^* would be expected to increase in compensation as the surface Fermi level moves to a higher equilibrium position. Lastly if the barrier height X^* can be taken as the insulator electron affinity, this would not be expected to be strongly temperature - dependent. On the other hand the degree of surface contamination from adsorbed gas~~s~~es etc., would be strongly dependent on temperature, hence it is likely that the effective value of X^* could change as gas desorption and surface re-structuring take place with changes in the ambient temperature.

A major effect of temperature on the other measured spectral parameters results from changes in the spectral shift voltage S. This essentially represents the voltage dropped across the insulator contact plus that dropped across the insulator bulk, the latter possibly being very current dependent. If the conduction is contact-limited, the value of S will represent a barrier thin enough for electron tunnelling which will be largely independent of temperature variations. For the bulk-limited case, a marked decrease in S results when the temperature rises as shallow donor or trapping centres throughout the bulk are thermally ionised, producing a change in the slope of a ln I versus $(S^*)^{\frac{1}{2}}$ plot. In spite of these observations the following analysis will assume that X^*, M and V^* remain constant for moderate changes in temperature. Therefore, the F.W.H.M. of a spectrum has been shown from equations 13 and 15 to be given by

$$\text{F.W.H.M.} = 3{\cdot}5\, M \left(B V - S + X - \phi_I - V^* \right) + 3{\cdot}5 \frac{kT_o}{e}$$

Hence on rearranging in terms of the ambient temperature T_o and shift S this gives

$$\text{F.W.H.M.} = 3{\cdot}5 \frac{k}{e} \left(T_o - \frac{M e}{k} S\right) + 3.5\, M \left(BV + X - \phi_I - V^*\right) \qquad (36)$$

which by introducing the constants

$$M_3 = 3{\cdot}5 \frac{k}{e} \qquad (37) \qquad\qquad C_3 = 3.5\, M\left(BV + X - \phi_I - V^*\right) \qquad (38)$$

and assuming that all the constants are known and with V held fixed, reduces to another straight line equation.

$$\text{F.W.H.M.} = M_3 \left(T_o - \frac{M\,e}{k} S \right) + C_3 \qquad (39)$$

having an independent variable $T_o - \frac{M\,e}{k} S$.

To the extent that S also does not vary with temperature, the slope of this equation is then M_3, i.e. $3{\cdot}5 \frac{k}{e} = 3\text{x}10^{-4}$ eV/K (40)

Finally the total emission current given by equation 19 may be written in the form

$$I = 1{\cdot}62 \text{ x } 10^{14} \; a\,M \frac{k^2}{e^2} \left(T_o - \frac{M\,e}{k} S + \frac{C_3}{M_3} \right)^2 \text{EXP} \left[\frac{-X^* + \left(\frac{e\,\beta\,V}{4\pi\varepsilon_0 D} \right)^{\frac{1}{2}}}{\frac{k}{e}\left(T_o - \frac{M\,e}{k} S + \frac{C_3}{M_3} \right)} \right] \qquad (41)$$

which indicates that the emission current increases with specimen temperature in a similar manner to that experimentally observed, although no quantitative assesment of this equation will be carried out.

The result given by equation 40 may now be checked against the data of figure (58) from chapter 6. Thus the plot of F.W.H.M. against specimen temperature resulting from this data, which is shown in figure (100), has a slope of $4{\cdot}6 \text{ x } 10^{-4}$ eV/K, although of course the F.W.H.M. measurements have a quite high uncertainty due to the interference of the second peak in the spectra. This value agrees fairly-well with that predicted by equation 40, i.e. $3 \text{ x } 10^{-4}$eV/K even though S can be seen to vary slightly.

The values of the hot electron parameters associated with specimen (3) are shown directly in the table of figure (97) without the supporting experimental plots, however, additional information for this specimen is presented in figure (98). This shows the contact to bulk- limited characteristic for a single sub-site at temperatures of 20°C and 80°C. As can be seen, the bulk-limited region for

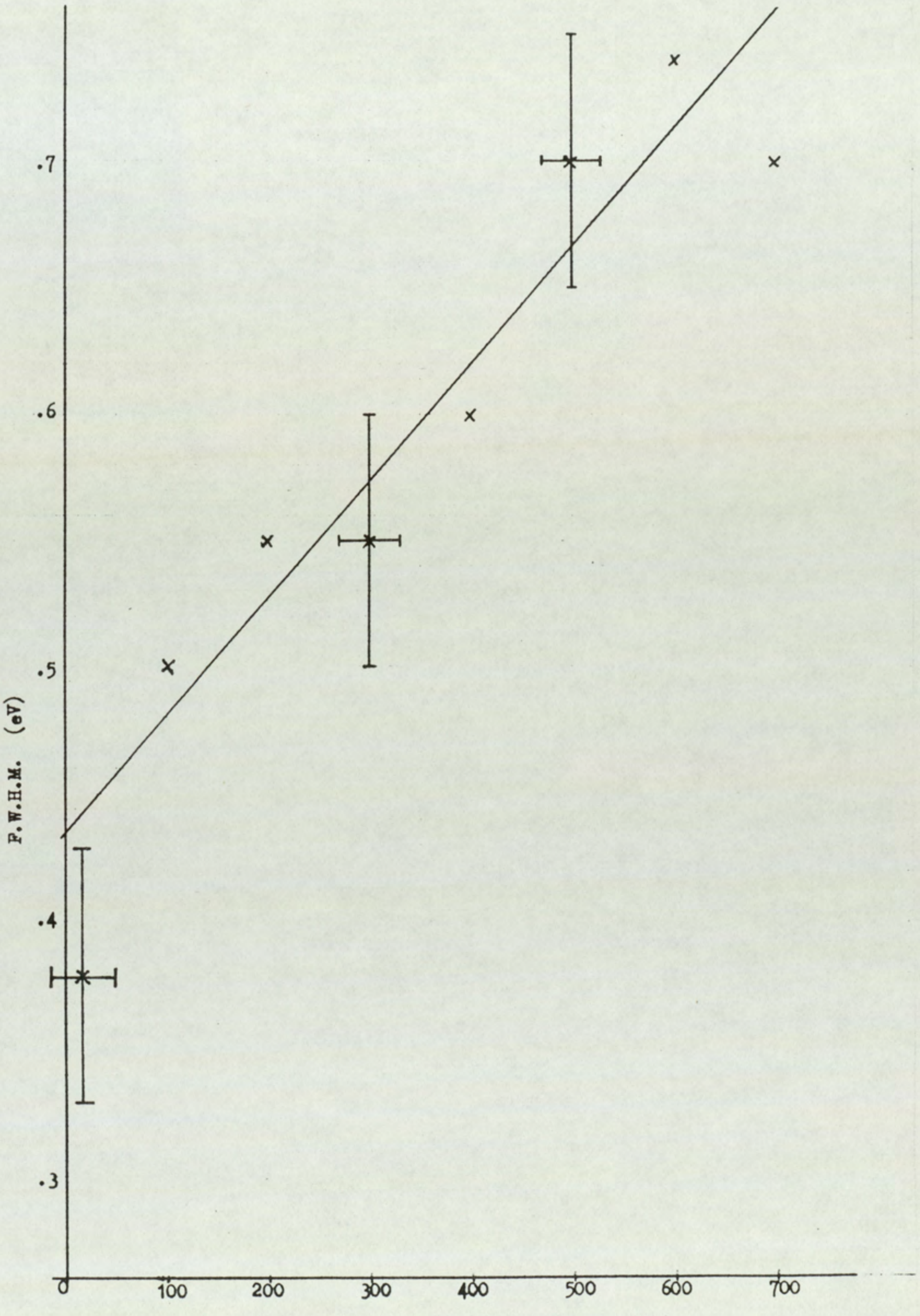

PLOT OF SPECTRAL F.W.H.M. AGAINST TEMPERATURE AT CONSTANT APPLIED FIELD

FIG 100.

the oxidised case has been reduced at the higher temperature to such an extent that the linear part no longer shows up in the field range covered. In fact the curve is tending towards the unoxidised contact-limited case as described by the equations for bulk and contact-limited conduction at higher temperatures, i.e. equations 14, 18, & 20 of chapter 4 sections 7b & 8. It will also be seen that the contact-limited region is independent of temperature as predicted, at least over the limited range 20 to 80°C. The gradual disappearance of the bulk-limited region noted above was associated with the decrease in spectral shift voltage S, which was described in chapter 6 section 9. This was also shown to have a long relaxation time as the specimen was cooled, which presumably was the time required for all thermally ionised donor centres and electron traps to refil with electrons, although several tens of minutes does seem rather a long time. Alternatively, some form of lattice restructuring may also be taking place, such as produced by the movement of oxygen vacancies or by ionic conduction; these processes would be expected to have long relaxation times.

7.6. Emission Site Instabilities.

At currents of $\sim 10^{-7}$ a sub-site may randomly switch on and off once in ~ 10s, while at a current of 10^{-6}A the rate might be once in ~ 1 S. These times are so long that the process is almost certainly thermally controlled. Hence, again assuming a cylindrical filament of cross-sectional area $\sim 10^{-14} m^2$ and length 10^{-6}m penetrating through a thick oxide film, the volume of the conducting channel is $\sim 10^{-20} m^3$. If this passes a current of 10^{-6}A it will have a bulk volt drop (S^*) of at least 1V, so that the power dissipated will be greater than 10^{-6}W, especially since this neglects the energy gained by the filament end from the hot electron accelerating field. Therefore the power density is $\sim 10^{+14} W/m^3$ which may be even greater for the unoxidised case and much greater if the filament area is very much smaller. Such a large power density should certainly be able to raise the conducting channel temperature at least a few tens of degrees. In addition, the current passing through a filament is governed by a positive feedback system, such that two conduction states are possible at the same value of field. Thus, the tip field enhancement associated with filamentary conduction means that there can be either a current giving field enhancement and hence more current or there is no current with no field enhancement. Therefore, the combined effect of these two phenomena may be able to explain the observed sub-site flicker. Hence, the actual filament temperature and the temperature of the hot electrons may become so great that the negative charge stored towards the insulator-vacuum boundary in trapping and surface states may be released and emitted in a current burst. This will lower the level of the bottom of conduction band to well below the top of the surface potential barrier, with the result that the emission current will cease. A short time then ellapses as the trapping states are refilled and the surface charge restored. The length of the off time being determined by the filament end capacitance associated with stored surface charge in series with the resistances of the insulator contact and bulk under reduced field conditions, since β would then be low. Once the conduction band has moved above the top of the surface barrier and emission current has started to flow again, β will suddenly increase and the process repeat itself. Finally, it should be noted that the very large power density occurring in a filament conducting with a current greater than $\sim 10^{-5}$A, must lead to some form of thermal breakdown with possible "explosive" rupturing of the surface region and hence ark initiation in the vacuum gap, i.e. as discussed by Cook (101) and observed experimentally by Hurley & Dooley.(40)

7.7. General Observations on the Hot Electron Model.

The hot electron model as presented so far can account for nearly all the experimentally observed phenomena, including many of so called "anomalous" ones. Thus the sharp discontinuities in F.N. plots are very probably due to changes in the number of sub-sites contributing to the measured current. These may vary in emissivity due to local changes in the surface barrier height X^* that result from variations in the adsorbed surface layers. This effect would be expected to decrease as the chamber pressure is lowered and particularly after thorough specimen degassing, as is experimentally observed. Changes in the conductivity of filaments could also be brought about by gas diffusion altering the electron trapping and donor levels. At higher current levels, filament heating will obviously complicate the situation and may produce bursts of thermally desorbed gasses or disrupt the conducting path by changeing the insulator structure. Whereas for sub-site currents greater than $\sim 10^{-7}$A the periodic switching phenomena will obviously contribute a large amount of noise to the measurements of total breakdown current.

The slightly curved and "saturating" F.N. plots that are frequently observed are necessary consequences in this hot electron model when contact to bulk-limited transitions occur, whilst electroluminescence may still be observed, although any holes produced by impact ionisation are not now a prerequisite for stable conduction. Site-switch-on and hysteresis phenomena are seen to result from the fact that β depends on the electron density in the conducting channel. During the initial field application β will be ~ 1 but this may suddenly rise to values up to ~ 10 when filament current starts to flow, which in-turn raises the current for no further increase in field. For stable conduction in this model both β and $\mathcal{E}$ have been assumed to be constant and the results seem to indicate that this was not unreasonable. However, for both very low currents, i.e $\ll 10^{-14}$A and for high currents, i.e. $\gg 10^{-5}$A this will not be the case, since β is most likely to be current dependent at low currents while $\mathcal{E}$ is more likely to vary at high currents as the conducting channel becomes metal-like. In this regard, the "b" sites described by Cox (25) and Hurley (26) are difficult to explain by the stable hot electron model. These sites have a negative slope resistance for currents $\sim 10^{-5}$A which may require a change in β, the cross channel area or $\mathcal{E}$ with field to explain them. It should also be particularly noted in this context, that the hot electron model and the insulator switching model described in chapter 4.3. are not mutually exclusive. Hence it may be, that as the filament current density as given by the hot electron model approaches that given by Peterson & Adler (113) for the insulator switching model, i.e. 10^{8} A/m^{2}, a gradual transition takes place from one mode of conduction to the other. For a filament cross sectional area $> 10^{-14}$m^{2} this would require a current $> 10^{-6}$A and this is just about the order of current at which the negative resistance region in "b" sites starts to occur. Further support for this proposition is obtained by noting that the double injection mechanism envisaged in the switching model, has been shown by Mott to lead directly to an S shaped I-V characteristic having a negative slope resistance region. Under these circumstances "b" sites need to be stable against thermally induced breakdown, and again the double injection model may be the reason since this requires the conducting channel to expand with increasing current, unlike the hot electron model which gives a constant filament cross sectional area.

CHAPTER 8.

CONCLUSIONS.

8.1. The Principal Experimental Findings.

Previous chapters have described a wide-ranging investigation into the nature of electron field emitting sites on broad area electrodes. Where the majority of the experimental work was carried out using a specially modified high resolution electron spectrometer to determine the energy distribution of the electrons emitted from these sites.

Results have generally confirmed the findings of other investigations, in that the general form of the observed spectra was fundamentally different from that expected for Fowler - Nordheim field emission. In particular the maximum of the distribution is always shifted at least 200-500 meV below the substrate metal Fermi level and the half width (F.W.H.M.) is always greater than $\sim$300 meV; both these values are considerably in excess of those expected for electrons which have quantum-mechanically tunnelled through a metallic work function barrier at room temperature. In addition, "broad-area spectra were very frequently double or multi-peaked. Following the instrumental developments described in this thesis, this latter observation has now been explained as being due to the overlap of the spectra from two or more sub-sites associated with a given site. While new types of data, in particular the maps of the emission current distribution in the anode plane, have indicated that what were thought to be isolated emission centres, are in fact just the points of strong emission from areas particularly prone to emit, and that these areas may be quite large i.e. up to $\sim 1\,(\mathrm{mm})^2$. It has also been shown that sub-sites switch on and off randomly with an average frequency determined by the magnitude of the sub-site current, thus explaining many of the erratic and non-linear measurements reported in the past.

These properties have been shown to be typical of the observations for all the electrode materials examined to date, as indeed are all the characteristics associated with emission sites. Hence most of the experimental work was undertaken using copper specimens for reasons of continuity with previous work and for ease of fabrication; copper is also a material widely used in high voltage technology.

8.2. Further Experimental Findings.

Experimental data resulting from observations of the electron energy distributions from individual sub-sites, on "unoxidised" and oxidised copper specimens, has provided a considerable amount of new information. This has enabled the variation of the peak shift of a spectrum with applied field to be related in detail to an energy band diagram which describes electron conduction through a surface "insulating" layer. Also, experiments at elevated temperatures have shown the existence of a previously unobserved phenomena, i.e. the decrease in spectral shift as the temperature is raised, which has reinforced the interpretation of prebreakdown emission currents in terms of contaminated insulating inclusions.

8.3. Theoretical Considerations.

Sequencesof electron energy spectra which were obtained over quite a wide range of applied anode voltages, i.e. for fields from ~ 6 to ~ 18 MV/m, have been found to contain sufficient information to validate the development of a sophisticated (quantitative) hot electron model of the emission process. As with previous emission models, this hot electron model assumes that emitted electrons originate from the vacuum surface of an insulating impurity, and that conduction from the metal substrate through the impurity layer or inclusion takes place in the form of very thin filaments.

Subsequent developments presented here are then natural consequences of the assumptions: a) that the shift in the peak of the electron energy spectrum results solely from the sum of the potentials dropped at the metal insulator contact and in the insulator bulk, and b) that the final emission must essentially be due to hot electrons passing over the insulator electron affinity barrier, as in earlier models. But it has been found during this analysis that the properties of contaminated insulators are sufficient to account for the observed phenomena without introducing additional complications, such as filament crystalisation or forming, to describe stable conduction. In this regard it differs from the previous "double injection" or switching model which required two hypotheses to adequately describe the situation. This new model has not only been shown to account for the known phenomena but has also been able to correlate several observations which were previously not thought to be directly related. In particular, it has been shown that slightly curved and "saturating" F.N. plots are produced by changes in the degree of spectral shift, and that these are consequences of a change from contact to bulk limited processes occuring in the insulating inclusions. The switching property of the emission sites, which was a major feature of the earlier "switching" model, may also be shown to be essentially a natural result of the fact that conduction takes place through very narrow filaments. This fact, together with the probable potential energy distribution in the conducting channel which results from the energy band diagram, enables a likely field pattern to be constructed for the whole filament. This automatically yields field enhancement around the conducting region which then enables the emitted current to be boosted for no further increase in the average field, thus giving an alternative explanation of the switch on effect.

On the basis of this model estimates may be made of several of the parameters and dimensions associated with the conducting filaments, and these have also been found to be of the orders expected or hinted at from other experiments, especially those concerned with simulated microparticle studies. The mathematical functions derived from the model, which represent the insulator contact and bulk I-V variations, have been found to agree with experiment over the range of applied field used. In this context, all previous models could only give qualitative estimates, the "double injection" or "switching" model in particular, since the presence of holes makes calculations very difficult with the strong likelyhood that other functions would result. The "switching or double injection" model may, however, provide the solution to the problem of current controlled "b" sites. Particularly since the physical requirements of this model are fulfilled for the currents at which negative filament resistance observed, if it is assumed that the filament dimensions are initially given by the new model at lower currents.

8.4. Summary of Achievements.

These findings may now be summarised as follows :

a) Broad area prebreakdown electron emmision sites have been found to consist of groups of emitting regions (sub-sites) which together may extend over quite large areas of the electrode surface.

b) Each sub-site may then switch on and off at a random rate determined by the sub-site current, or "explode" if the current is high enough to produce a breakdown event.

c) A quantitative model of the electron conduction process in contaminated insulating surface layers or inclusions has been found to account for the known experimental results and has also correlated and explained several sets of unexplained phenomena.

d) The characteristics of the emitted electron energy distributions have been analysed in detail and shown to provide a great deal of information on the properties of the insulating inclusions.

e) Thermal experiments have reinforced the interpretations obtained from the above model and extended the range of available data.

8.5. Suggestions for Future Advances.

A final positive aspect of the present investigation is that it has pointed to several potentially profitable lines of investigation. These include instrumental developments, more refined experimentation and further detailed theoretical work on the hot electron model.

Thus a major instrumental improvement that has still to be added to the spectrum analyser system, is some means of accurately measuring the emission current from an individual sub-site over the entire applied field range. At present this is only just satisfactory because measurement is based on the assesment of several indirect parometers, such as emission image spot size, and if this is not improved, future data will only be of limited use. Some form of data analysis facility could then be incorporated to ~~rapp~~ rapidly give the spectral parameters, such as the area under the curve, peak shift and F.W.H.M. etc.,with the prospect of an immediate mathematical analysis to derive the properties of the emitting insulating structure.

8.6. Further Experimental Work.

Experimentally, the possibilities now arise for carrying out very detailed spectral analyses of specimens in a systematic manner over a considerable field range, i.e. up to $\sim$ 40 MV/m and over a wide temperature range, i.e. up to 1000K. Where the new hot electron model enables much more meaning to be placed on the various measurements and equally important indicates what is to be expected to happen before an experiment is carried out. This is a much better situation than previously was the case, where it was easy to overlook a disturbing phenomena as an extraneous "statistical variation", especially whilst the origin of the double peaked spectra remained unexplained. As further data accumulates, it should be possible to judge whether the hot electron model as proposed so far is well enough defined or whether additional detailed work should be done.

8.7. Additional Theoretical Work.

It is likely that more theoretical work on the hot electron model will be found to be necessary, especially in relation to the definition of spectral F.W.H.M. since this may be already showing signs of being inadequate. Related to this is the problem of the position of the Fermilevel at the vacuum surface as the penetrating field and the stored "surface" charge vary. For simplicity of analysis the Fermi level position has been assumed to be constant during changes in the applied field etc., but this is probably not the case for large changes in field.

A valuable additional theoretical study would be a computer simulation of the electric field pattern in the vicinity of a conducting filament. This would take into account the potential energy distribution along the filament resulting from the energy band diagram and the assumed dimensions and parameters of the conducting channel. The current density is then not likely to be constant throughout the filament length since the field lines will converge towards the vacuum end. A better understanding may then be achieved of the thermal stability of the various regions, in particular the high field region towards the vacuum interface where energy input is greatest, which may then explain why some emission sites are thermally unstable, producing "a" sites, and others not producing "b" sites. The conduction transition into the negative resistance characteristic for "b" sites may then actually be shown to be produced as "double injection" or hole production sets in, as mentioned earlier.

REFERENCES.

REFERENCES.

1. R J Noer, Appl. Phys. A (Germany), A28 No1, 1-24, (1982).

2. R V Latham, High Voltage Insulation, (Academic Press, London), (1981).

3. R A Millikan & R A Sawyer, Phys. Rev., 12, 167-170 (1918)

4. R A Millikan & C C Lawitsen, Proc, Natl. Acad. Sci. (U.S.A), 14, 45-49

5. W S Boyle, P Kisliuk & L H Germer, J. Appl. Phys. 26, 720-725 (1955).

6. W P Dyke, J K Trolan, W W Dolan & G Barnes, J. Appl. Phys. 24, 570-576 (1953).

7. W P Dyke, J K Trolan, E E Martin & J P Barbour, Phys. Rev., 91, 1043-1054 (1953).

8. D Alpert, D A Lee, E M Lyman & H E Tomaschke, J. Vac. Sci. Tech., 1, 35-50 (1964).

9. R P Little & S T Smith, J. Appl. Phys, 36, 1502-1504 (1965).

10. H E Tomaschke & D Alpert, J. Vac. Sci. Tech., 4, 192-198 (1967)

11. R P Little & W T Whitney, J. Appl. Phys. 34, 2430-2432 (1963).

12. I Brodie, J. Appl. Phys., 35, 2324-2332 (1964)
13. I Brodie, J. Vac. Sci. Tech., 2, 2449-256 (1965)

14. R Gomer, J. Chem. Phys.,21, 293-303 (1965).

15. D K Davies & M A Biondi, J. Appl. Phys. 37, 2967-2977 (1966).

16. D K Davies & M A Biondi, J. Appl. Phys. 39, 2979-2990 (1968).

17. R Hawley & A A Zaky, Progress in Dielectrics. 7, 115-215 (1967).

18. H P S Powell & P A Chatterton, Vacuum,20, 419-429 (1971).

19. R V Latham, High Voltage Vacuum Insulation, Academic Press, London, 25-29 (1981).

20. L I Pivovar & V I Gordienko, Sov. Phys : Tech. Phys., 3, 2101-2105 (1958).

21. L I Pivovar & V I Gordienko, Sov. Phys.: Tech Phys.,7 908-912 (1963).

22. H P S Powell & P A Chatterton, Vacuum, 20, 419-429,(1971).

23. R H Good & E Muller, Encycl. Phys.,21, 176 (1956).

24. R Hackam & S K Salman, Proc. I.E.E., 119, 377-384 (1972).

25. B M Cox, C.E.G.B. Laboratory Note R/M/N 1021 (1979)

26. R E Hurley, J.Phys. D: Appl. Phys., 13, 1121-1128 (1980).

27. B M Cox, J. Phys. D: Appl. Phys., 8, 2065-2073 (1975).

28. R E Hurley & P J Dooley, J. Phys. D: Appl. Phys. 10, L195-L201 (1977).

29. N K Allen & R V Latham, J.Phys. D: Appl. Phys. 11, 11, L55-L57 (1977)

30. C S Athwal & R V Latham., Proc. IX-DE1V, Physica D E, 104C, (1981)

31. B M Cox & D E J. Wort, Vacuum, 22, 453-455 (1972)

32. B M Cox & W T Williams, J. Phys. D: Appl. Phys. 10, L5 - L9 (1977)

33. E E Donaldson & M Rocbinowitz, J. Appl. Phys. 34, 319-322 (1963).

34. A S Prokrovskaya-Soboleva, V Kraft, T S Borisova & L K Mazurova, Proc. 5th Int. Symp. Discharges and Elect. Ins. in Vac. Poznam, Poland, 105-109 (1972).

35. J T Maskrey & R A Dugdale, J. Sci. Instrum. 42,284-286 (1966).

36. G A Farrall, F G Hudda & R H Johnston, J. Appl. Phys., 50 3608-3614 (1979).

37. B N Klyarfel'd & A S Pokrovskaya-Soboleva, Sov.Phys., 15 149-152 (1970).

38. G F Alfrey & J B Taylor, Brit, J. Appl. Phys. 6, Scippl. 4, S 44 - S49 (1955).

39. R E Hurley, J. Phys. D: Appl. Phys., 12, 2247-2252 (1979).

40. R E Hurley & P J Dooley, Vacuum, 28, 147-149 (1978).

41. R E Hurley, J. Phys. D: Appl. Phys., 12, 2229-2245 (1979).

42. N K Allen & R V Latham, J. Phys. D: Appl. Phys. 11, L55-L57 (1978).

43. C S Athwal & R V Latham, J.Phys. D: Appl.Phys.,17,1029-1043 (1984).

44. W Schottky, Physik. Z.,14, 63. (1923).

45. R H Good & E W Muller, In "Handbuck der Physik" (Springer-Verlag, Berlin) 21, 176-231 (1956).

46. A G J Van Oostrom, Philips Res. Reports Suppl. No.1. (1966).

47. H C Miller, J. Franklin Inst., 289, 347-351 (1969).

48. R Haefer, Z. Physik., 116, 604-622 (1940).

49. W P Dyke, J K Trolan, W W Dolan & G Barnes, J. Appl. Phys. 24, 570-576 (1953).

50. W P Dyke, J K Trolan, E E Martin & J P Barbour, Phys.Rev., 91, 1043-1054 (1953)

51. H E Tomasche & D Alpert, J. Appl. Phys. 38, 881-883 (1967)

52. J E Henderson & R E Badgley, Phys.Rev., 38, 590 (1931)

53. J E Henderson & R K Dahlstron, Phys. Rev. 55, 473-481 (1939).

54. E W Muller, Z.Physik., 102, 734-761 (1936).

55. E W Muller, Z.Physik., 120, 261-269 (1943).

56. E W Muller & K Bahadur, Phys. Rev. 102, 624-631 (1956).

57. R D Young & E W Muller, Phys. Rev. 113, 115-120 (1959).

58. J W Gadzuk & E W Plummer, Rev. Mod. Phys., 45, 487-548 (1973).

59. R D Young, Phys. Rev. 113, 110-114 (1959)

60. L W Swanson & L C Crouser, Phys. Rev. 163, 622-641 (1967).

61. E W Plummer & A E Bell, J. Vac.Sci.Tech. 9, 583-590 (1972).

62. N Nicolaou & Modinos, Phys.Rev., B 11, 3687-3696 (1975).

63. N Nicolaou & Modinos, Phys.Rev.,B 13, 1536-1547 (1976).

64. A Modinos, Surf. Sci., 70, 52-91 (1978).

65. L W Swanson & L C Crouser, Phys. Rev. Lett. 19, 1179-1181 (1967)

66. N J Dionne & T N Rhodin, Phys. Rev., B14, 322-340 (1976)

67. N Rihon, Phys. Stat. Sol., A49, 697-703, (1978).

68. C Lea & R Gomer, Phys. Rev. Lett., 25, 804-806 (1970).

69. J W Gadzuk & E W Plummer, Phys. Rev. Lett. 26, 92-95 (1971)

70. J J Czyzewvski, Surf. Sci. 39, 1-20 (1973).

71. R Stratton, Proc. Roy. Soc., B68, 746-757 (1955).

72. R Stratton, Phys. Rev., 125, 67-82 (1962).

73. R Stratton, Phys. Rev., 135, A794-A805 (1964).

74. J Bardeen, Phys. Rev., 71, 717-727 (1947).

75. L M Baskin, Lvov & N Fursey, Phys. Stat. Sol., B47 49-62 (1971).

76. B F Lewis & T E Fischer, Surf. Sci., 41, 371-376 (1974).

77. J R Arthur Jr., J. Appl. Phys., 36, 3221-3227 (1965).

78. O H Hughes & P M White, Phys. Stat. Sol., 33, 309-316 (1969).

79. L T J Salman & E Braun, Phys. Stat. Sol., A16 527-532 (1973).

80. A Modinos, Surf. Sci., 42 205-227 (1973).

81. P Handler, J.Phys. Chem. Slids 44, 1-8 (1960).

82. W B Shepherd & W T Peria, Surf. Sci., 38, 461-498 (1973).

83. D E Sykes & E Barun, Phys. Stat. Sol., B69 K137-140 (1975).

84. N Rihon, Surf. Sci. 70, 92-100 (1978).

85. C B Duke & H E Alferieff, J.Chem.Phys. 46, 923-937 (1967).

86. E Merzebacher, Quantum Mechanics, (Wiley, New-York), 121-130 (1961).

87. E W Plummer & R D Young, Phys. Rev., B1, 2088-2109 (1970).

88. L W Swanson & L C Crouser, Surf. Sci.,23, 1-29 (1970).

89. E L Murphy & R H Good Jr.,Physical Rev., 102, No. 6, 1464-1473 (1956).

90. O W Richardson, The Emission of Electricity from Hot Bodies. (Longmans Green & Co., London) (1921).

91. W W Dolan & W P Dyke, Phys. Rev., 95, 327, (1954).

92. W W Dolan & W P Dyke. Adv. Electronics-Electron Phys., 8 90-180 (1956).

93. S G Christof, Phys.Stat. Sol., 17, 11-26, (1966).

94. A G Zhdan, M I Yelinson & V B Sandomirskiy, Radiotexhn I Elextron, 7, PP630 (1962).

95. N K Allen, B M Cox & R V Latham, J.Phys. D:Appl. Phys., 12, 969-977 (1979).

96. C S Athwall, Ph.D. Thesis, University of Ason Birmingham, England. (1981)

97. N K Allen & R V Latham, Proc. 8th Int. Symp. Disch. & Elec. Ins. in Vac., Alburquerque, B.3, 1-13 (1978).

98. N K Allen, Ph,D. Thesis, University of Aston, Birmingham, England, (1979).

99. A Septier, Proc. Workshop on RF. Superconductivity, Karlsruhe, pp. 56-76 (1980).

100. G Dearnaley, A M Stoneham & D V Morgan, Rep. Prog. Phys., 33, 1129-1191 (1970).

101. E L Cook, J. Appl. Phys., 41, 551-554 (1970).

102. G Dearnaley, Thin Solid Films, 3, 161-174 (1969).

103. T W Hickmott, J. Appl. Phys, 37, 4380-4388 (1966).

104. B Juttner, W Rohrbech & H Wolff, Proc. 5th Int. Symp., Disch. & Elec. Ins. In Vac., 65-69 (1972).

105. B Juttner, H Wolff & B Altrichter, Phys. Stat.Sol ,27, 403-412 (1975).

106. S Benzer, J.Appl. Phys., 20, 804-815 (1949).

107. S R Ovshinsky, Phys. Rev. Lett., 21. 1450-1453 (1968).

108. D Adler, M S Shur, M Silver & S R Ovshinsky, J. Appl. Phys. 51, 3289-3309 (1980).

109. K Homma, H K Henisch & S R Ovshinsky, J. Non-Cryst. Solids, 35 & 36. 1105-1110 (1980)

110. D Addler, Amorphous Semiconductors, (Buttersorth s ,London). (1972.)

111. D Adler, H K Henisch & N F Mott, Rev. Mod. Phys., 50 209-220 (1978).

112. N F Motts, Philos. Mag. 32, 159-171 (1975).

113. K E Peterson & D Adler, J. Appl. Phys., 47 256-263 (1976)

114. Solid Luminescent Materials, (J Wiley & Sons Inc. New York) (1948).

115. J G Simmons, J.Phys. D: Appl. Phys., 4. 613-657 (1971).

116. J G Simmons, Physical Rev., 166,No.3, 912-920 (1968).

117.. J G Simmons, Brit. J.Appl.Phys., 18 269 (1967).

118. J G Simmons, Phys. Rev., 155, 657, (1967).

119. A Braunstein, M Braunstein, G S Picus & C A Mead, Phys. Rev. Lett., 14, 519 (1965).

120. F L Schuermeyer, J. Appl. Phys., 37, 1998 (1966)

121. J F Frenkel, Phys. Rev., 54., 647 (1938).

122. R V Latham, Vacuum, 32, 137-140 (1982).

123. A G J Van Oostrom, Philips Research Reports Supplements, 1, 1-102 (1966).

124. C E Kuyatt & E W Plummer, Rev. Sci. Inst., 43, 108-111 (1972).

125. E Braun, R G Forbes, J Pearson, J M Pelmore & R V Latham, J. Phys. E : Sci. Inst., 11, 222-228 (1978).

126. N K Allen & R V Latham, J. Phys. D : Appl. Phys., 11, L55-L57 (1978).

127. E M Purcell, Phys. Rev., 54. 818-826 (1938).

128. J M Parker & R W Warren, Rev. Sci. Inst., 33, 948-950 (1962).

129. D W Heddle, R G Keesing & J M Kurega, Proc. Roy. Soc., A334, 135-147 (1973).

130. R D Young & C E Kuyatt, Rev. Sci. Inst., 39 1477-1480 (1968).

131. B Juttner, Proc., VI-DE IV, 101-106 (1974).

132. W Rogowski, Archiv. Für Elektrotechnik, 12. 1-15 (1923).

133. J Franks, British Patent No. 44718/73 (1973)

134. J Franks & A M Ghander, Vacuum, 24 , 489-491 (1974).

135. R K Fitch, M K Khorassany & T N mawlook, Proc. 7th.Int., Vac., Congr. & 3rd Int. Conf. on Solid Surfaces, Vienna, 285-288 (1977).

136. P D Davidse & L I Maissel, J Vac. Sci. Tech., 4. 33-36 (1967).

137. Nottingham, Phys. Rev., 59., 907 (1941).

138. A L Edwards, Statistical Methods 2nd Ed., (Holt, Rinehart & Winston Inc. London) (1967).

139. F Rohrbach, CERN Report, 71-5/TC-L (1971).

140. G E Vibrans, Tech. Report, 353, Lincoln Lab., MIT (NTISESDTDR 64-327) (1964).

141 P A Chatterton, Proc. Phys. Soc., (London), 88, 231-245 (1966).

ACKNOWLEDGEMENTS

This work would not have been possible without a grant from the Central Electricity Generating Board, whom I thank for their support. I would also like to thank both my Supervisor, Dr R V Latham, and Mr B Cox from the Central Electricity Research Laboratories, for many useful discussions during the course of the work, and Mr H Arrowsmith for making and assisting in the design of items of apparatus.

APPENDICES.

FIELD-INDUCED ELECTRON EMISSION FROM ARTIFICIALLY PRODUCED CARBON SITES ON BROAD-AREA COPPER AND NIOBIUM ELECTRODES

C.S. Athwal*, K.H. Bayliss**, R. Calder and R.V. Latham**
*LEP-VA Division, CERN, 1211 Geneva 23, Switzerland
**University of Aston, Birmingham B47ET, United Kingdom

Abstract

It has been experimentally demonstrated that micron-sized particles of graphite deposited on the surface of copper and niobium electrodes can promote the field emission of electrons in the range of 5-20 MVm^{-1}. From measurements of the current-voltage characteristic, electron spectrum and emission image of such sites, it has been concluded that electrons are emitted by a mechanism similar to that operating at the naturally occurring sites responsible for prebreakdown electron emission. A hot electron based metal-insulator-metal model is considered.

1. Introduction

There is a growing body of experimental evidence which strongly suggests that carbon, in certain forms, can promote the field emission of electrons at anomalously low fields, typically in the range of 5-20 MVm^{-1}. In particular, filamentary carbon fibres have been extensively studied as point field emission electron sources (1-4) and, in the form of a felt weave, as extended cold-cathode electron sources (5).Copious field emission has also been observed from bulk specimens of pyrolytic graphite (6), and from a carbon film deposited on an insulating substrate (7).There is also evidence from studies of prebreakdown electron emission from broad-area high voltage electrodes that carbon, as a localised impurity, can stimulate the emission of electrons in the same field range. For example, gold electrodes, which are known to have a high level of carbon contamination, have been observed to be strongly emissive (8), whilst more recently, electron emission sites have been shown to be located in the vicinity of surface carbon concentrations as identified by Auger analysis (9). Lastly there is evidence from vacuum arc studies that the initiation mechanism, which depends on a primary electron emission process, may be also associated with the presence of carbon concentrations (10).

On the basis of this evidence, and that discussed elsewhere (11), which emphasises the similarities between the electron and optical spectroscopic data obtained from the prebreakdown emission processes on high voltage electrodes and carbon fibre emitters, an investigation was initiated to create artificial carbon sites on broad-area metal electrodes and to determine how closely their emission behaviour simulates that of naturally occurring sites.

2. Experimental

2.1 Artificial site production

Two techniques have been developed, both very simple in concept. In the first, originally demonstrated with copper electrodes (12), a micromanipulator is employed to lower gently a finely sharpened pencil lead to a known position on the surface of a planar electrode that had previously been polished and ultrasonically cleaned in readiness for introduction to the vacuum system. By taking care to 'touch' the surface of the electrode only lightly it is possible to produce a faintly visible carbon spot of typical diameter ~ 0.2 mm. In the second and more recent technique, a fine glass capilliary tube is similarly used to deposit a ~ 0.5 mm drop of colloidal graphite (Aquadag) onto an electrode surface, which, after drying, typically leaves a visible deposit of somewhat smaller dimensions. At higher resolution, such deposits are found to consist of a random distribution of carbon particles of varying size and orientation; this is illustrated by the scanning electron micrograph of Figure 1 which shows a typical region of a 'pencil' spot. It is particularly important to note the bright appearance of the carbon particles, which suggests they are electrically insulated from the substrate metal electrode, i.e. similar to the appearance of naturally occurring sites (13).

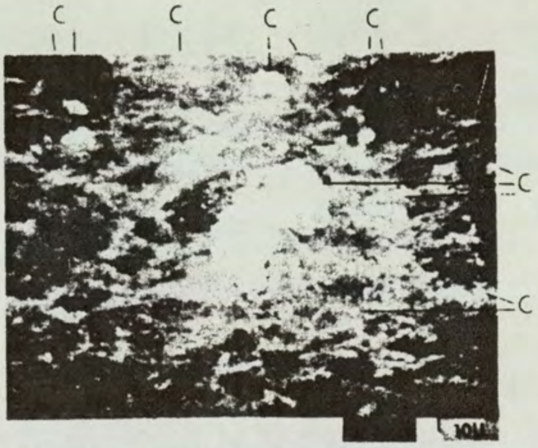

Fig. 1 A scanning electron micrograph of a 'pencil' site showing the randomly distributed carbon particles (labelled C).

2.2 Emission site characteristics

Using the experimental facilities previously developed for studying the emission properties of the sites that occur naturally on broad area electrodes (11,14-16), measurements have been made of the current-voltage characteristics, electron spectra and emission images for pencil and Aquadag sites on both copper and niobium electrodes. In all cases the most strongly emitting site was found to be at the location of the graphite deposit. However, no consistently reproducible difference in emission properties were identified between the two types of site on a given material, or indeed between a given type of site on the separate materials. Accordingly, the following examples of experimental data are to be taken as representative of all the systems studied.

Thus Figure 2 is a typical single-site current-field characteristic of the initial field cycling (i), together with the resulting reversible Fowler-Nordheim (F-N) plot (ii). This illustrates how the current from a virgin site initially increases in a very erratic and unstable manner from a near-zero current level (i.e. 10^{-11} A) to a level of ~ 10^{-7} A and then exhibits a spontaneous switch-on into a

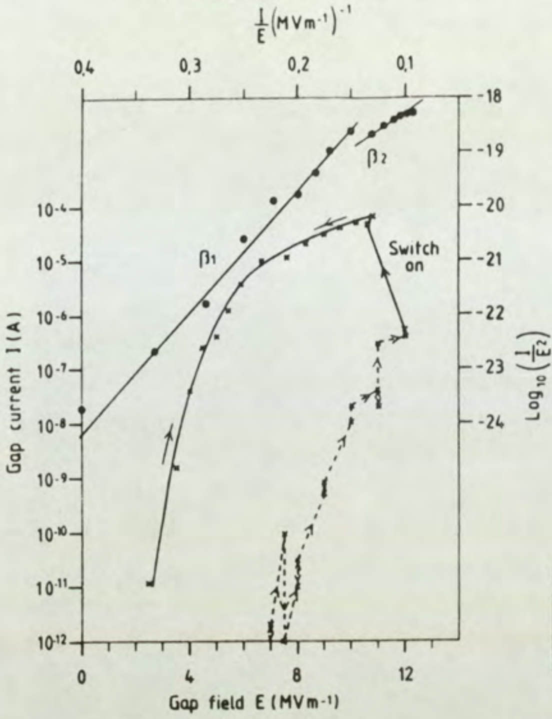

Fig. 2 A typical example of (i) the current-field characteristic (x) and (ii) the associated F-N plot (•) of a carbon site.

final and more stable emission mode that is subsequently reversible over the whole field range. It is to be noted that the hysteresis associated with the initial field cycling is so marked that whereas a field of ~ 9 MVm^{-1} was initially required to obtain a current of ~ 10^{-10} A, the same current could subsequently be drawn by a field of ~ 3 MVm^{-1} after the switch-on process. The F-N plot corresponding to the switched-on state can often be divided into two fairly clearly defined linear regions above and below current levels of ~ 10^{-6} A: typically, the low-field range is characterized by ß-values in the range 300-1200, whilst within the limited high field range one finds ß > 1000.In the plot of Figure 2, this parameter has the respective values $ß_1$~1000 and $ß_2$ ~1700.

Fig. 3 presents two electron spectra successively recorded at slightly different fields from an Aquadag site on a niobium electrode. This illustrates both how the spectra, with broad half-widths (> 0.3 eV), are shifted from the cathode Fermi level and how the emission can switch between a single-peak and multi-peak mode, i.e. in both respects exhibiting a behaviour similar to that observed for naturally occurring sites (11,17). As a consequence of this latter property, it generally proved difficult to measure systematically how the shift of a single peak spectrum varied with field. However, in the case of one pencil site, such a measurement was possible, and it revealed a behaviour broadly similar to that found for naturally occurring sites (18), i.e. where the shift increases rapidly with field. Lastly, Figure 4 is a typical projection image of the emission obtained from such sites, and reveals that, as with natural sites, the total current is derived from several independent sub-sites, each having its own characteristic single-peak spectrum (9,15). From a comparison of this image with that obtained from naturally occurring sites (9,15), known to consist of micron-sized particles (13), it can be concluded that the present emission originates from only a very small localized region of the carbon deposit, possibly just one of the particles. Multi-peak spectra are observed when the emission from two or more sub-sites is simultaneously collected by the spectrometer input aperture. Not revealed on this image is the other important observation, again common to natural sites, that each of the sub-sites intermittently switches on and off with time, with a mean frequency that tends to increase with the current drawn from the site (typically 0.5 Hz at 10^{-6}-10^{-7} A emission (9,15)). In fact, this 'flickering' of the emission image accounts for the ambient noise on the measured emission current.

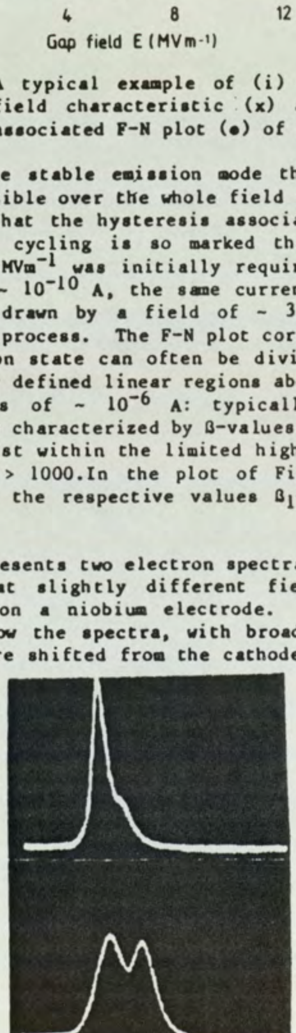

Fig. 3 Single and multi-peak spectra successively recorded at (a) 7.2 MVm^{-1} and (b) 8.4 MVm^{-1} from an Aquadag site on a niobium electrode.

Fig. 4 A projection image of the electrons field emitted from a carbon site (9,15).

3. Discussion

The central conclusion to be drawn from the above experimental data is that the emission characteristics of artificial carbon sites are in most respects very similar to those of naturally occurring sites. Thus they exhibit a switch-on phenomenon to give a subsequently smooth and reversible current-voltage characteristic with a linear F-N plot for fields up to ~ 10 MVm^{-1} having typical ß-values in the range 300-1200 (17). Similarly, there is an apparent equivalence between the electron spectra and emission images obtained from the two types of site. It now remains to discuss how carbon might promote the field-induced hot electron emission mechanism thought to operate at naturally occurring sites (11, 17-20). Two approaches have been considered: firstly, that it is a consequence of the physical properties of carbon, and secondly, that carbon, behaving as a conductor, plays some form of field enhancing geometrical role.

Carbon is a generic term used to describe a wide range of materials having very different physical and chemical properties (21). At one extreme, there are materials such as diamond and many hydrocarbon based 'cokes' that are electrically insulating whilst, at the other extreme, there are the chemically pure pyro carbons that can exist in either an amorphous 'glassy' form or in a highly orientated 'graphitic' form. There are numerous intermediate forms of carbon (e.g. turbostratic carbons) of which the degree of purity and graphitisation generally depends on the choice of organic precursor and the temperature to which it is heat-treated. Typically, temperatures in the range 2000-3000 K are required to achieve the purest forms of carbon. In the context of the present discussions of the field emitting properties of carbon sites, attention will be focussed on its highly-orientated graphitic form, since both pencil lead and colloidal Aquadag use this form of the material.

Graphite has the well-known layered structure consisting of stacked basal planes containing closely-packed, covalently bonded carbon atoms arranged in hexagonal rings. The separation between the basal planes (3.35 Å) is nearly 2.5 times the separation of the carbon atoms within the planes (1.42 Å), and they are only weakly bound together by Van der Waals forces. This means that they can readily cleave to form flake-like structures.

Another important consequence of this structure is that graphite exhibits a large anisotropy in its electronic properties: in particular, the ratio of c to a-axis electrical resistivities ρ_c/ρ_a can approach values ~ 5000 at 300 K and exceed 10^5 at ~ 5 K for highly orientated pyrolytic graphite (21) that has been thoroughly annealed to ~ 3000 K. However, for somewhat lower annealing temperatures (say 2000-2500 K), one still obtains a graphite-like structure with stacking of the carbon rings, although in this case they are randomly orientated about the c-axis. These structures also have a somewhat greater mean separation between the basal planes and this can lead to even higher values of the ρ_c/ρ_a ratio, possibly in excess of 10^4 where typically the basal plane resistivity ρ_a at 300 K has a value ~ 1500 μΩ cm. From this brief survey, it is evident that, even in the most favourable circumstances, the anisotropy of graphite never leads to a c-direction resistivity that is greater than that corresponding to a small bandgap semiconductor. Accordingly, it is difficult to envisage how graphite could support the necessary dielectric field penetration to sustain a hot-electron emission mechanism. It may be, however, that amorphous carbon (4) and binding agents (predominantly clay in pencil and organic additives in the case of Aquadag) play a crucial role: in fact, experiments are currently in progress to investigate this possibility.

A more plausible explanation of how graphite might stimulate the hot-electron emission mechanism previously proposed for insulating inclusions (11,17-20) stems from its flake-like structure (21). Thus, for the configuration schematically illustrated in Figure 5, the graphite flake is depicted as forming a metal-insulator-metal (MIM) structure, involving either the ambient surface oxide of the metal or, more likely, some anomalous insulating inclusion such as might be provided by the polishing medium or the non-metallic constituents of the pencil or Aquadag. According to this model the insulating-like material, sandwiched between the metal substrate and the overlaying conducting flake, will undergo a switching process similar to that described elsewhere (17) and occurring at some critical gap field in the range 5-20 MVm^{-1}. This will give rise to a flux of hot electrons that are projected through the flake into the vacuum as occurs in purpose fabricated MIM electron sources (22).

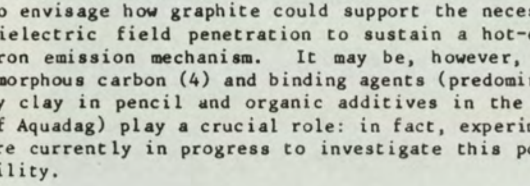

Fig. 5 A schematic illustration of how a conducting flake could form an MIM structure on the surface of an electrode with an accompanying field enhancing effect.

The three essential requisites of this model are (a) that the MIM structure should initially 'block' the exchange of charge as the external field is applied to the surface, so that the potential of the flake rises with respect to the substrate electrode; (b) that there is a geometrical enhancement of the field appearing across the junction resulting from the flake being effectively at the potential existing at, perhaps, a micron above the electrode surface (for the configuration illustrated in Fig. 5, the field across the 100 Å thick insulating layer could be many times larger than that existing across it without the flake), and (c) that the thickness of the overlaying flake should be ≲ 1000 Å so that the majority of the hot electrons are able to escape to the vacuum (22). The first requirement of a 'blocking' contact is apparently confirmed by the experimental evidence of Fig. 1, where the carbon particles appear to be charged, and therefore presumably electrically insulated from the substrate. This same evidence also suggests that the geometrical configuration of at least some of the particles could fulfil the second and third requirements. Thus it appears that the necessary conditions could well exist to promote a MIM hot-electron emission mechanism.

In conclusion, two further examples of indirect evidence supporting this model should be cited. Firstly, the anode probe technique of Athwal and Latham (13) for locating emission sites on broad-area electrodes frequently identified sites by X-ray spectroscopy as consisting of particles containing such metallic elements as aluminium and silver (19). These general findings have been recently confirmed by a similar experiment employing an Auger, rather than X-ray, analysis facility (23). Secondly, when a test electrode pair suffers a flash-over it is generally found that the electron emission is subsequently very much higher at a given field: the reason for this is dramatically illustrated in Figure 6, which shows the 'before' and 'after' emission site maps (9,15). On finally examining the surface of the cathode, it was found to be decorated by numerous particles of anode material; in this case stainless steel. It was therefore concluded that the proliferation of emission sites displayed in Figure 6b was a consequence of the creation of MIM structures by metal being 'splashed' from the anode onto suitable insulating regions of the cathode surface. Indeed, the degradation of the insulating properties of a vacuum gap due to the presence of metallic particles is well known (24).

(a) (b)

Fig. 6 Emission site maps (9,15) recorded at a constant field of 12 MVm^{-1} 'before' and 'after' a flash-over event between a 15 mm diameter copper cathode and a stainless steel anode. The proliferation of sites is thought to be associated with the 'splashing' of metal droplets of anode material onto the cathode surface.

From the technological point of view, the above findings have two important implications. Firstly, they indicate that the carbon concentrations which are known to exist at grain boundaries on broad-area electrodes (25) could be possible sources of field emission currents, and hence ultimately a limiting factor on the performance of high voltage electrodes. Secondly, brief mention should be made of a recent study associated with the electron loading of superconducting RF cavities (26), in which artifical carbon sites have been used to simulate effects of naturally occurring field emission sites.

Acknowledgements

Two of the authors (K.H. Bayliss and R.V. Latham) wish to thank the Science and Engineering Research Council and Central Electricity Generating Board of the United Kingdom for their support of this work. One of the authors (R.V. Latham) also gratefully thanks CERN and the University of Geneva for their support of a sabbatical year spent in these two institutions.

References

1. F.S. Baker, A.R. Holber and J. Williams, Nature, 239, 96-97, 1972.
2. C. Lea, J. Phys. D., Appl. Phys., 6, 1105-1114, 1973.
3. R.V. Latham and D.A. Wilson, J. Phys. E., Sci. Instrum., 15, 1083-92, 1982.
4. R.V. Latham and D.A. Wilson, J. Phys. D, Appl. Phys. 16, 455-63, 1983.
5. G.F. Erikson and P.N. Mace, Rev. Sci. Instrum., 54, 586-90, 1983.
6. R.E. Hurley, Private communication, 1978.
7. K.H. Bayliss, R.V. Latham, F. Jones and D.J. Mellor, Vacuum, to be published 1984.
8. R.E. Hurley, J. Phys. D, Appl. Phys. 12, 2229-2245, 1979.
9. K.H. Bayliss, Ph. D. Thesis, University of Aston, Birmingham, U.K., 1984.
10. B. Jüttner, Physica, 114B+C, 255-61, 1982.
11. R.V. Latham, IEEE Trans. Elec. Insul. EI-18, 194-203, 1983.
12. R.V. Latham, Private communication, CERN, May 1983.
13. C.S. Athwal and R.V. Latham, Physica, 104C, 46-49, 1981.
14. N.K. Allen, C.S. Athwal and R.V. Latham, Vacuum, 32, 325-332, 1982.
15. K.H. Bayliss and R.V. Latham, submitted for publication 1984.
16. N. Hilleret, Private communication, CERN, March 1983.
17. C.S. Athwal and R.V. Latham, J. Phys. D, Appl. Phys, 17, 1029-1043, 1984.
18. C.S. Athwal and R.V. Latham, Physica, 104C, 189-95, 1981.
19. R.V. Latham, High Voltage Vacuum Insulation: The Physical Basis, Academic Press, London and New York, 1981.
20. R.V. Latham, Vacuum, 32, 137-140, 1982.
21. I.L. Spain, Chemistry and Physics of Carbon, Vol. 16, pp.119-304, Mariel Dekker, New York and Basel, 1981.
22. Yu B. Yavkelevitch, Vacuum, 30, 97-107. 1980.
23. O. Fischer and P. Niedermann, Private communication, University of Geneva, May 1984.
24. J.J. Maley, J. Vac. Sci. Technol., 11, 892-895, 1974.
25. A. Septier, Proc. Workshop on RF Superconductivity, Karlsruhe, 1980, pp. 56-76.
26. C.S. Athwal and W. Weingarten, Int. CERN Report, 1984.

```
READY.

 10 PRINT"□"
 20 PRINT"THIS PROGRAM CALCULATES THE K-B
 30 PRINT:PRINT" COORDINATES FROM BASIC V,I,S DATA
 40 PRINT:PRINT
 50 PRINT"KB F(I,V,S)=LN(I/[BV-AS-E]↑2)":PRINT
 60 PRINT:PRINT"KB F(V,S)=(1-0.0017SQR(WV))/[BV-AS-E]":PRINT
 70 PRINT" WHERE W,B,E&A ARE CONSTANTS"
 80 PRINT:PRINT:PRINT"R IS THE STRAIGHT LINE FIT REGRESSION":PRINT:PRINT"COEFFIC
IENT"
 90 PRINT:PRINT
 100 PRINT"    PRESS ■RETURN■ TO CONTINUE!"
 110 GET C$:IF C$="" THEN 110
 120 IF ASC(C$)=13 THEN 160
 130 STOP
 140 PRINT
 150 PRINT
 160 PRINT
 170 DIM X(50),Y(50),S(50),L(50),M(50),A(50),H(50),J(50),K(50)
 180 PRINT "□":INPUT "HOW MANY SETS OF RESULTS";N:PRINT
 190 PRINT"TYPE IN THE";N;"SETS OF RESULTS":PRINT"IN THE FORM X,Y,S":PRINT
 200 PRINT"X IN 100VOLTS,Y IN AMPS,S IN VOLTS"
 210 FOR  I=1TO N:PRINT I;:INPUT X(I),Y(I),S(I):NEXT
 220 N2=1
 230 PRINT  :PRINT :PRINT
 240 N3=N2+14:IF N3<=N THEN 260
 250 N3=N
 260 PRINT" N"TAB(3)" X"," Y"," S"
 270 FOR I=N2 TO N3
 280 PRINTITAB(3)X(I),Y(I),S(I):NEXT
 290 PRINT:PRINT "ARE THE RESULTS SHOWN CORRECT? Y OR N"
 300 GET A$:IF A$="" THEN 300
 310 IF A$="N" THEN 350
 320 IF A$<>"Y"THEN 290
 330 IF N3=N GOTO 430
 340 N2=N3+1:PRINT"□":GOTO 240
 350 PRINT:INPUT "WHICH SET OF RESULTS IS INCORRECT";I:PRINT
 360 IF I> N THEN 390
 370 IF I-INT(I)<>0 THEN 390
 380 IFABS(I-INT(I+.00001))<.0001THEN410
 390 PRINT"□□TYPE THE INTEGER IN COLUMN 1 OPPOSITE  "
 400 PRINT"THE INCORRECT RESULTS";:INPUT I:GOTO 380
 410 PRINT"TYPE THE CORRECT RESULTS FOR X(";I;") AND Y(";I;") AND S(";I;")";
 420 INPUT X(I),Y(I),S(I):GOTO 260
 430 PRINT:PRINT"TO CHANGE B,PRESS A KEY AND INPUT DATA, OTHERWISE PRESS RETURN"
 440 FOR I=1 TO N:X(I)=100*X(I):NEXT
 450 PRINT:PRINT:PRINT"TYPE IN THE VALUES FOR A,E,W&B*E-3 ":PRINT:PRINT:PRINT
 460 INPUT A,E,W,B
 470 B=B*.001:FOR I=1 TO N
 480 K(I)=0.0017*SQR(W*X(I))
 490 A(I)=B*X(I)-A*S(I)-E
 500 L(I)=LOG(Y(I)/A(I)/A(I))
 510 M(I)=(1-K(I))/A(I):NEXT
 520 S1=0:S2=0:X1=0:X2=0:Y1=0:D3=0:Y2=0
 530 FOR I=1 TO N
 540 X1=X1+M(I):Y1=Y1+L(I):X2=X2+M(I)*M(I):S1=S1+M(I)*L(I):Y2=Y2+L(I)*L(I):NEXT
 550 D=N*X2-X1*X1:F=N*S1-X1*Y1:C=(X2*Y1-S1*X1)/D:G=N*Y2-Y1*Y1:M=F/D
 560 R=F/SQR(D*G)
 570 PRINT"E=";E;" B=";B;" R=";R
 580 GET K$:IF K$=""THEN 580
 590 IF ASC(K$)=13THEN 610
 600 IF ASC(K$)<>13THEN INPUT"NEW B=";B:GOTO0470
 610 IF C<0 THEN 630
 620 PRINT"□":PRINT" Y = (";M;"* X)+";C:GOTO 640
 630 PRINT"□":PRINT" Y = (";M;"* X)";C
 640 FOR I=1 TO N
 650 D2=(M*M(I)+C-L(I))↑2:S2=S2+D2
 660 IF D2<D3 THEN 680
 670 D3=D2:Z=M(I)
 680 NEXT
 690 D3=SQR(D3): M2=SQR(S2/(N-2))*SQR(N/D):C2=SQR(S2/(N-2))*SQR(X2/D)
 700 M3=M2/SQR(N):C3=C2/SQR(N)
 710 PRINT:PRINT"A=";A;" W=";W;" E=";E;" B=";B;" R=";R
 720 PRINT:PRINT"STANDARD DEVIATION OF M";M2
 730 PRINT"STANDARD DEVIATION OF C";C2
 740 PRINT:PRINT"THE STANDARD ERROR OF M";M3
 750 PRINT"THE STANDARD ERROR OF C";C3
 760 PRINT:PRINT"THE MAXIMUM DEVIATION IS":PRINT D3;"WHEN X="Z
 770 PRINT
 780 PRINT"PRESS RETURN TO CONTINUE"
 790 GET P$:IF P$=""THEN 790
 800 IF ASC(P$)<>13THEN 790
 810 PRINT
 820 PRINT" N"TAB(6)"KB F(I,V,S)"TAB(24)"KB F(V,S)"
 830 FOR I=1 TO N
 840 PRINTITAB(8)INT(L(I)*1000)/1000TAB(24)M(I):NEXT
 850 PRINT
 860 PRINT:PRINT"TO CHANGE THE VALUE OF A,E&B PRESS RETURN"
 870 PRINT"FOR PRINTOUT PRESS P"
 880 GET X$:IF X$=""THEN 880
 890 IF ASC(X$)<>80THEN 450
 900 FOR I=1 TO N:H(I)=LOG(Y(I)):J(I)=SQR(S(I)+1.5):NEXT
 910 OPEN1,4
 920 CMD 1
 930 PRINT"A=";A;" W=";W;" E=";E;" B=";B;" R=";R;"  Y=";M;"X+(";C;")"
 940 PRINT:PRINT"  V"TAB(12)"I"TAB(15)"S";
 950 PRINTTAB(9)"KB F(I,V,S)"TAB(12)"KB F(V,S)":PRINT
 960 FOR I=1 TO N
 970 PRINTX(I)TAB(6)Y(I)TAB(8)S(I);
 980 PRINTTAB(10)INT(L(I)*1E5)/1E5TAB(10)INT(M(I)*1E6)/1E6
 990 NEXT
 1000 PRINT:PRINT"STANDARD DEVIATION OF M IS ";M2
 1010 PRINT"STANDARD DEVIATION OF C IS ";C2
 1020 PRINT:PRINT" V"TAB(10)"LN(I)"TAB(11)"SQR(S+1.5)"TAB(14)"[BV-AS-E]"
 1030 FOR I=1 TO N
 1040 PRINTX(I)TAB(5)INT(H(I)*1E5)/1E5TAB(8)INT(J(I)*1E5)/1E5;
 1050 PRINTTAB(14)INT(A(I)*1E5)/1E5
 1060 NEXT
 1070 PRINT#1:CLOSE1
 1080 GOTO 860
```

```
READY.


READY.

 10 PRINT"□▩▩▩"
 20 PRINT"   THIS PROGRAM CALCULATES THE FWHM"
 30 PRINT:PRINT" COORDINATES FROM BASIC V,I,S DATA"
 40 PRINT:PRINT
 50 PRINT" THAT IS V(FWHM) & [BV-AS]":PRINT
 60 PRINT"  WHERE B,A ARE CONSTANTS"
 70 PRINT:PRINT:PRINT"R IS THE STRAIGHT LINE FIT REGRESSION":PRINT:PRINT" COEFFI
CIENT"
 80 PRINT:PRINT"▩▩"
 90 PRINT"    PRESS ▩RETURN■ TO CONTINUE!"
 100 GET C$:IF C$="" THEN 100
 110 IF ASC(C$)=13 THEN 150
 120 STOP
 130 PRINT
 140 PRINT
 150 PRINT
 160 DIM X(50),Y(50),S(50),L(50),M(50),A(50)
 170 PRINT "□":INPUT "HOW MANY SETS OF RESULTS";N:PRINT
 180 PRINT"TYPE IN THE";N;"SETS OF RESULTS":PRINT"IN THE FORM X,S,Y":PRINT
 190 PRINT"X IN 100VOLTS,S IN VOLTS,Y IN VOLTS"
 200 FOR  I=1TO N:PRINT I;:INPUT X(I),S(I),Y(I):NEXT
 210 N2=1
 220 PRINT  :PRINT :PRINT
 230 N3=N2+14:IF N3<=N THEN 250
 240 N3=N
 250 PRINT" N"TAB(3)" X"," S"," Y"
 260 FOR I=N2 TO N3
 270 PRINTITAB(3)X(I),S(I),Y(I):NEXT
 280 PRINT:PRINT "ARE THE RESULTS SHOWN CORRECT? Y OR N"
 290 GET A$:IF A$="" THEN 290
 300 IF A$="N" THEN 340
 310 IF A$<>"Y"THEN 280
 320 IF N3=N GOTO 420
 330 N2=N3+1:PRINT"□":GOTO 230
 340 PRINT:INPUT "WHICH SET OF RESULTS IS INCORRECT";I:PRINT
 350 IF I> N THEN 380
 360 IF I-INT(I)<>0 THEN 380
 370 IFABS(I-INT(I+.00001))<.0001THEN400
 380 PRINT"□□TYPE THE INTEGER IN COLUMN 1 OPPOSITE  "
 390 PRINT"THE INCORRECT RESULTS";:INPUT I:GOTO 370
 400 PRINT"TYPE THE CORRECT RESULTS FOR X(";I;") AND S(";I;") AND Y(";I;")";
 410 INPUT X(I),S(I),Y(I):GOTO 250
 420 PRINT:PRINT"TO CHANGE B,PRESS A KEY AND INPUT DATA, OTHERWISE PRESS RETURN"
 430 FOR I=1 TO N:X(I)=100*X(I):NEXT
 440 PRINT:PRINT:PRINT"TYPE IN THE VALUES FOR A,B*E-3 ":PRINT:PRINT:PRINT
 450 INPUT A,B
 460 B=B*.001:FOR I=1 TO N
 470 A(I)=B*X(I)-A*S(I)
 480 L(I)=Y(I)
 490 M(I)=A(I):NEXT
 500 S1=0:S2=0:X1=0:X2=0:Y1=0:D3=0:Y2=0
 510 FOR I=1 TO N
 520 X1=X1+M(I):Y1=Y1+L(I):X2=X2+M(I)*M(I):S1=S1+M(I)*L(I):Y2=Y2+L(I)*L(I):NEXT
 530 D=N*X2-X1*X1:F=N*S1-X1*Y1:C=(X2*Y1-S1*X1)/D:G=N*Y2-Y1*Y1:M=F/D
 540 R=F/SQR(D*G)
 550 PRINT"A=";A;" B=";B; " R=";R
 560 GET K$:IF K$=""THEN 560
 570 IF ASC(K$)=13THEN 590
 580 IF ASC(K$)<>13THEN INPUT"NEW B=";B:GOTO460
 590 IF C<0 THEN 610
 600 PRINT"□":PRINT" Y = (";M;"* X)+";C:GOTO 620
 610 PRINT"□":PRINT" Y = (";M;"* X)";C
 620 FOR I=1 TO N
 630 D2=(M*M(I)+C-L(I))↑2:S2=S2+D2
 640 IF D2<D3 THEN 660
 650 D3=D2:Z=M(I)
 660 NEXT
 670 D3=SQR(D3): M2=SQR(S2/(N-2))*SQR(N/D):C2=SQR(S2/(N-2))*SQR(X2/D)
 680 M3=M2/SQR(N):C3=C2/SQR(N)
 690 PRINT:PRINT"A=";A;" B=";B;" R=";R
 700 PRINT:PRINT"STANDARD DEVIATION OF M";M2
 710 PRINT"STANDARD DEVIATION OF C";C2
 720 PRINT:PRINT"THE STANDARD ERROR OF M";M3
 730 PRINT"THE STANDARD ERROR OF C";C3
 740 PRINT:PRINT"THE MAXIMUM DEVIATION IS":PRINT D3;"WHEN X="Z
 750 PRINT
 760 PRINT"PRESS RETURN TO CONTINUE"
 770 GET P$:IF P$=""THEN 770
 780 IF ASC(P$)<>13THEN 770
 790 PRINT
 800 PRINT" N"TAB(8)"V(FWHM)"TAB(21)"[BV-AS]"
 810 FOR I=1 TO N
 820 PRINTITAB(8)INT(L(I)*1000)/1000TAB(24)M(I):NEXT
 830 PRINT
 840 PRINT:PRINT"TO CHANGE THE VALUE OF A,B PRESS RETURN"
 850 PRINT"FOR PRINTOUT PRESS P"
 860 GET X$:IF X$=""THEN 860
 870 IF ASC(X$)<>80THEN 440
 880 OPEN1,4
 890 CMD 1
 900 PRINT"A=";A;" B=";B;" R=";R;"  Y=";M;"X+(";C;")"
 910 PRINT:PRINT"  V"TAB(11)"S"TAB(12)"V(FWHM)"TAB(9)"[BV-AS]"
 920 FOR I=1 TO N
 930 PRINTX(I)TAB(6)S(I)TAB(12);
 940 PRINTINT(L(I)*1E5)/1E5TAB(10)INT(M(I)*1E6)/1E6
 950 NEXT
 960 PRINT:PRINT"STANDARD DEVIATION OF M IS ";M2
 970 PRINT"STANDARD DEVIATION OF C IS ";C2
 980 PRINT#1:CLOSE1
 990 GOTO 840
```